District-Scale Ground Heat Exchange Performance with Fiber Optic Distributed Temperature Sensing

By

Adam Louis McDaniel

A thesis submitted in partial fulfillment of the requirements for the degree of

Master of Science

Geological Engineering

At the

University of Wisconsin-Madison

2017

District-Scale Ground Heat Exchange Performance with Fiber Optic Distributed Temperature Sensing

By

Adam Louis McDaniel

Approved by

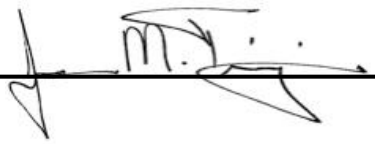

James M. Tinjum

Acknowledgements

I would like to thank the members of my advising committee—Professors James Tinjum, Dante Fratta, and David Hart—for their constant advice, guidance, and patient redirection of my work. It was Professor Tinjum who gave me my first opportunity to combine my passions for studying the earth and protecting it with sustainable energy systems as an undergraduate researcher on the Energy Geotechnics research team. Since that first opportunity, countless doors have been opened by Professor Tinjum's diligent efforts and trust in my abilities. Without Professor Dante Fratta, the minutiae of fiber optic distributed temperature sensing would remain a mystery and this work would never have been possible. Professor David Hart was nearly always working by my side on field assignments where we shared many conversations about engineering and life. His perpetual optimism and excited pursuit of discovery often reminded me why I chose to be a geological engineer.

I owe the greatest debt of gratitude to my parents, Matthew and Julie McDaniel. Their unflinching support has been the greatest source of my resolve in the face of the inevitable challenges of life. They instilled in me great wonder at the world around me, and equipped me with the ability to believe in myself and the virtue of hard work to satisfy that curiosity. Their countless sacrifices for my benefit spur me forward when my own determination for self-improvement has temporarily abandoned me. They showed me from an early age the relational nature of life, a lesson which, to this day, is the secret to any of my successes. Phil, my brother, and life-long partner in seeing just how far we can push the boundaries of life, merits special mention as my motivation to chase science as far as it will lead me down the path of discovery. Clair Kurzynski, thank you for your understanding and sacrificial heart, inspiring me to be a better man, and walking with me on this adventure.

There are far too many names to thank individually within the geotechnical engineering family, but Xiaodong "Buff" Wang deserves special mention as an exceptionally gifted laboratory manager who has provided invaluable assistance in assembling, repairing, and re-repairing instrumentation of all forms. Among student research cohorts, Lauren Thomas must be especially thanked for her outstanding contributions to this research through her willingness to invest long hours calibrating fiber data and for never giving up in the face of exceptionally high expectations. Ayse Özdoğan-Dölçek, Matthew Walker, Matthew Harper, Eleanor Bloom, Ian Atkins, Levi Mitchell, Maxwell Brennan, and Kevin Hernandez—the other student members of the Energy Geotechnics research team—have my sincerest thanks for spending countless hours sharing

their expertise, and for never being afraid to suggest a new idea or challenge an old one. Thank you to Christian Herrera, who provided the mechanical engineering expertise necessary to construct a customized thermal response test that became the basis for an important part of my research. Thank you to all my graduate student peers who were always willing to lend a helping hand, and provide a fun, yet productive atmosphere at work.

The Illinois State Geological Survey and its members provided the financial means to develop and share my work among geologic minds of the highest caliber. Yu-Feng “Forest” Lin and Andrew Stumpf in particular provided expert guidance and treated me with the highest hospitality on my many visits to their fine campus. Thank you to Epic Systems for their extremely generous sharing of resources and willingness to collaborate to increase both academic and industry understanding of the geothermal resource. General Heating & Air Conditioning, Bertram Drilling, Teel Plastic, Rygan Inc., Silixa, and Morse Group are also acknowledged for their support in installing instrumentation and advising instrumentation design at the Epic field site.

Thank you to NSF Geothermal and Energy Geotechnics (Award # 1156674) for sponsoring my undergraduate research. Any opinions, findings, and conclusions or recommendations expressed in this material are those of the authors and do not necessarily reflect the views of the funding organizations.

Table of Contents

List of Figures

List of Tables

Chapter 1: Introduction

Ground-source heat pumps (GSHP) systems have great potential as an energy-efficient alternative to conventional space heating and cooling systems. The basic principal behind GSHP technology is cyclical energy storage in the subsurface—energy injection into the ground during summer to cool buildings, and extraction of that same energy during winter to provide space and water heating. When operating properly, efficiently transferring energy within a GSHP system is operationally more efficient than burning fossil fuels to produce single-use heat in the winter, or using low-efficiency air conditioner units when air temperatures are warmer. Due to high initial borefield costs, the installation of a GSHP system is often controlled by its payback period—the time until operational savings has accumulated to equal the additional capital investment. There exists some debate about true GSHP effectiveness and efficiency due to historic case studies where there was difficulty in accurately predicting lifetime performance. This difficulty stems from the inherent complexity of subsurface heat transfer. The subsurface chosen for energy storage is often comprised of distinct geologic units that may vary widely in properties that drive heat transfer; such as mineral constituents, grain orientation, density, porosity, saturation, groundwater flow, fractures, and voids. Due to the multitude of variables in play and the practical difficulties in observing subsurface processes, there is a lack of robust quantification of how heat is transferred in the subsurface.

This work begins in Chapter 2 with an Introduction that describes the fundamentals of GSHP systems, overviews the design and predictive methodology, and provides thorough background on the primary tool used in this study to advance subsurface heat transfer mechanisms: fiber optic distributed temperature sensing (DTS). Previous work using DTS as a tool to investigate GSHP performance is described, paying special attention to the development of the distributed thermal response test (DTRT) for *in situ* measurement of distributed heat

transfer. Finally, a short case study is presented that highlights the tangible benefits of understanding the distributed nature of subsurface heat transfer.

Chapter 3 presents an in-depth study on the calibration of a fiber optic DTS network installed in a district-scale borefield at Epic Systems in Verona, WI. DTS is a powerful tool with great advantages that also requires a significant investment of time and resources to realize its full potential. Among expanding environmental monitoring applications, the installation of an 11.2-km network of buried fiber optic cables for long-term monitoring is a demanding DTS application that has a unique set of obstacles to achieving consistently accurate temperature data. The design of a dynamic, double-ended, centralized, and remotely accessible calibration routine is carefully described. As an increasingly popular tool, DTS has significant discussion in literature regarding calibration techniques. This paper seeks to build contribute to that discussion to document a novel method of splice and cable end-point location, and to use long-term calibrated results to consider optimal combinations of calibration baths, compare how calibration parameters vary in space in time, and discuss the importance of combing forward and reverse signals in a double-ended configuration.

The results of the DTS calibration within Epic's borefield 4 are presented in Chapter 4. One of the largest borefields of its kind, borefield 4 has exceptional potential for economic and environmental benefits. The heat injection and extraction loads into borefield 4 were monitored from January 2015 through March 2017 and found to be heavily imbalanced towards heat injection. The net heating loads and heterogeneous sedimentary bedrock of borefield 4 with variable thermophysical properties and groundwater conditions provides an optimal field laboratory to study subsurface heat transfer mechanisms. Rock cores from the geologic units found in borefield 4 were analyzed in the laboratory by Meyer (2013) for thermal conductivity using guarded-comparative-longitudinal heat flow experiments (ASTM E1225) and specific heat capacity using "coffee-cup calorimetry." Estimates of bedrock density, porosity, and hydraulic

conductivity were taken from the Dane County Regional Flow Model (Parsen et al. 2016). These thermophysical and hydraulic bedrock properties were used as a basis of interpretation for distributed subsurface heat flow rates, as observed by the fiber optic temperature monitoring.

Chapter 5 of this thesis focuses on the design and implementation of a DTRT to analyze *in situ* distributed thermal properties of heterogeneous lithology in central Illinois. A pilot borehole was drilled, cored, and installed with fiber optics within the u-pipe ground heat exchanger (GHX), grouted between the GHX and the borehole wall, and 5 m beneath the GHX. The cores were measured in the laboratory for thermal conductivity using a KD2-Pro Thermal Properties Analyzer (Decagon Devices), gravimetric water content by ASTM D2216-10, and bulk density by ASTM D7263-09. The custom-made rig was designed to conduct both a conventional TRT and a DTRT. The conventional TRT data analysis presented by Raymond et al. (2011) and an error minimization technique were used to find average 'effective' subsurface thermal properties. A novel analogy to the Molz et al. (1987) impeller-meter pumping test for distributed hydraulic conductivity was used to calculate thermal conductivity during the heat injection portion of the TRT. Thermal conductivities from the laboratory testing, 1-m-resolution fiber data, and fiber data sectioned by heat transfer rates were compared to known geologic conditions. Distributed heat decay was observed after the conclusion of the test to investigate differential cooling processes.

Appendices 1 through 5 document related research that was performed, but not to the extent of a stand-alone paper as in the case of Chapters 3 through 5. Appendix 1 summarizes work to quantify energy flows at Epic's campus at the building, intermediate campus, and total campus scales. Appendix 2 documents Epic's total campus energy balance and provides comments on the current state of that research. Appendix 3 investigates the performance of a traditional u-pipe and a coaxial GHX installed nearby Epic's borefield 4 using fiber optics and traditional ΔT methods. Appendix 4 describes an investigative study performed on the overheated

borefield of the Wisconsin Institutes for Discovery (WID) building. Appendix 5 provides documentation of Epic remote connection methodology and calibration Matlab scripts.

Chapter 2: Background

2.1 Ground-Source Heat Pumps

Ground-source heat pumps (GSHP) are a growing source of space heating and cooling. Worldwide GSHP energy capacity has increased from 85 PJ in 2005 to 325 PJ in 2015, which is equivalent to ten 1000-MW nuclear or coal power plants (Lund and Boyd 2015). A GHSP uses an exchanger fluid within a pipe network to transfer energy between the surface and the subsurface for space heating and cooling to buildings. When air temperatures are high and building cooling is desired, energy is injected into the ground for storage. When air temperatures are low and heating is desired in buildings, the exchanger fluid is used to harvest that same energy from the ground. Because ground heat exchange relies on a principle of storing energy in a relatively constant-temperature heat sink/source and re-accessing energy with a thermally advantageous carrier fluid, significant economic and environmental efficiency advantages exist over conventional sources of heating and cooling. The coefficient of performance (COP) of a properly designed and installed GSHP system is three or greater, meaning that for every 1 unit of electrical energy input used to run the system, ≥ 3 units of heat energy are extracted or rejected. This is in stark contrast to the maximum 1:1 ratio of electrical resistance and fossil fuel heating. In practice, even “high efficiency” coal power plants have significant energy waste, and are at best 50 to 55% efficient (Bugge et al. 2006). Despite these inherent inefficiencies, fossil fuels made up 81.5% of all forms of U.S. energy consumption in 2015 (EIA 2016).

The two main GSHP system components are heat pumps and ground heat exchangers (GHX). Heat pumps function by collecting heat from surrounding air, water, or ground; concentrating it; then redistributing it to an area for space heating or domestic water heating. A

heat pump can also work in reverse by collecting heat from inside a building and pumping it outside. Heat pumps are most efficient when they are collecting energy from a constant temperature source (Omer 2008). GHXs in the US are typically a sealed loop made of high-density polyethylene (HDPE) piping that is located below a ground or water surface. Common configurations of the GHX piping are trenched horizontal loops, spiral horizontal loops, vertical loops (u-tube or coaxial), and submerged loops in a pond. In general, horizontal and submerged loops provide less capacity for a smaller initial investment, while vertical loops provide the highest heat transfer capacity per unit of surface area (Wu et al. 2014) at a higher initial investment.

Vertical GSHPs are typically installed in boreholes 23 m to 92 m in depth that are spaced 4.6 m to 6.1 m apart that are sized for 17.4 to 52.2 kW of energy transfer per meter of pipe (Omer 2008). GHX borefields are typically sized to match 60 to 70% of the max building loads to prevent overdesign (Tarnawski et al. 2009), which may look quite different depending on the application. For example, three GHXs may provide sufficient capacity for a one family residence (Bloom and Tinjum 2016); 18 are needed for a three-story, 1530 m^2, office building in Germany (Luo et al. 2015); 81 were installed at a 30,600 m^2 campus research center in Madison, WI (Herrera 2016); 1400 were needed at 16,000-student West Chester University (Helmke et al. 2016); and 3600 were installed at 22,000-student Ball State University (Siliski et al. 2016). District-scale borefield systems (>500 GHX) bring about their own unique challenges and opportunities. Chief among these is the potential for borefields to overheat because of year-after-year cooling-dominated loads (Florea et al. 2017). As more energy is injected into the subsurface than is extracted, the ground temperature increases, water temperatures exiting the borefield will increase, and the efficiency of heat pumps will be negatively impacted (Li et al. 2009). In a district-scale borefield, the near-field (local volume surrounding individual GHXs) for a particular GHX will overlap with others, and cross-contamination will multiply the negative effects of overheating in the far-field (bulk borefield area). By sheer magnitude, district-scale borefields have greater potential to create

thermal perturbations and disturb ecosystems from their natural state. Elevated temperatures may cause bacteria to grow or harmful chemicals, such as arsenic, to become soluble and impact aquifers. District-scale GSHP borefields also have the greatest potential to provide the greatest efficiencies and economic and environmental benefits when designed and operated optimally.

The installation of a borefield is the most significant added cost in a GSHP system because the heat pump or chiller replace similar thermodynamic units and the HVAC distribution system is largely the same. Because the initial investment in GSHP systems is the highest cost, the project viability is dependent on the payback period—or the time at which the savings in operational costs have accumulated to offset the additional installation cost. In Wisconsin, the payback period is 9–10 years when the systems are used for offices and schools (Energy Center of Wisconsin 2010). Operational costs are highly dependent on local fuel mix and cost (Blum et al. 2010) and are minimized with balanced building loads and a proper operational schedule designed around sustainable practices. Compared to traditional systems, maintenance costs can be cut in half, and operational costs can be a quarter of what they otherwise would be (Omer 2008). Reduction in capital costs by optimal borefield design can provide the greatest opportunity to decrease payback periods and increase the economic viability of a GSHP project. To accomplish this, borefields must be constructed to provide sufficient current and future heating and cooling capacity, without oversizing to a point where the capital costs become economically infeasible.

2.2 Design and Performance Prediction

Lifetime heating and cooling ground heat exchange performance has proven difficult to predict and systems have deviated from expected design performance, leading to poor environmental and economic outcomes (Magraner et al. 2010, Knudson 2013). Economic viability and payback periods are highly sensitive to energy extraction and rejection rates that deviate from design values (Garber et al. 2013). Due to the importance of accurate load prediction and appropriate

system sizing, many predictive models have been developed and used to size GSHP systems (Nagano et al. 2006, Sayyaadi et al. 2009, Puttagunta et al. 2010). These models are predominately based in well-developed thermoeconomic optimization principals (Bejan et al. 1996) that often focus on the performance of the mechanical GSHP components and the associated capital, operational, and fuel costs of the system. In contrast, heat transfer in the subsurface is commonly estimated with static and conservatively estimated effective parameters that represent the entire borehole and assume one homogenous unit.

A Thermal Response Test (TRT) is the current, widely used, and industry accepted assessment tool used for *in situ* quantification of GHX thermal performance to calculate subsurface parameters used in system design. A conventional TRT quantifies heat transfer in a pilot GHX by supplying a known heating load and measuring the exchanger flow rate and ΔT from the GHX inlet to outlet. *In situ* heat exchange capacity and 'effective borehole thermal conductivity' are calculated and can then be used to supplement and refine model results for improved design. Typical analysis (Puttagunta et al. 2010, Luo et al. 2015) of these results relies on a line-source heat model (Zeng et al. 2002). Ingersoll et al. (1954) first applied the line-source equation (Eq 1.) to model a GHX as an infinite line source of energy, transferring heat radially away from the borehole in a finite medium.

$$T - T_0 = \frac{q}{2\pi\kappa}\int_n^\infty \frac{e^{-\beta^2}}{\beta}\,d\beta = \frac{q}{2\pi\kappa} I(n) \tag{1}$$

Where T is ground temperature [K], T_0 is initial ground temperature [K], q is the heat transfer rate per length of the GHX [W m^{-1}], r is the distance from the pipe center [m], λ is the effective subsurface thermal conductivity, κ is thermal diffusivity [m^2 s^{-1}], ρ is the effective subsurface density, t is the time since the onset of heat injection [s], and β is an integration variable equal to

(2)

$\frac{r}{2\sqrt{\kappa(t-t^*)}}$. When n ≥ 2, $I(n)$ has tabulated solutions presented in Ingersoll et al. (1954). When n < 2, Eq 2. Is used to approximate $I(n)$.

$$I(n) = 2.303log10\frac{1}{n} + \frac{n^2}{2} + \frac{n^4}{8} + 0.2886$$

A similar analytical method, the cylindrical source solution, is based on one-dimensional radial heat conduction originating in a cylinder surrounded by an infinite homogenous medium. Eq. 3 was originally developed by Carslaw and Jaeger (1947) and refined to its current form by Kavanaugh (1985).

$$T - T_0 = \frac{q}{\lambda} G(\kappa, t, r_b, r) \quad (3)$$

Where all variable definitions for Eq. 1 hold, and r_b is equal to the outer pipe radius [m]. The expression $G(\kappa, t, r_b, r)$ is known as the "Geometry-function," which has estimated solutions tabulated in literature (Kavanaugh 1985 and Hellström 1991)

Both the line-source and cylindrical solutions make the following simplifying assumptions:

1. Geology surrounding the borehole is homogenous.
2. Advective heat transfer from groundwater interaction is negligible.
3. Heat flow is 1-D in the radial direction.
4. Ground temperature is constant with depth.

Each of these four assumptions may cause a mechanism of subsurface heat flow to be missed. The first assumption of borehole homogeneity forces effective average borehole properties. While an effective borehole capacity and thermal conductivity may be enough to provide rough estimates of sizing and general design specifications, it fails to provide insight into how subsurface heat transfer varies with depth. The second and third assumptions place all causality for heat

transfer on 1-D radial conduction, which may overestimate its importance while underestimating vertical conduction and advective groundwater heat flow effects. Assumption four is particularly troubling in long-term district-scale installations that have the energy capacity to significantly change ground temperature with depth and time. For a true understanding of GSHP system performance to advance, methodologies are needed to quantify the distributed nature of subsurface heat transfer and address individual variables which drive subsurface heat transfer.

Thermophysical properties will vary with depth and location in a GHX borefield. Thermal conductivity, specific heat capacity, and density will vary between geologic units and even between them, creating thermofacies that would have been previously indistinguishable by traditional grouping methodologies. Distributed quantification of subsurface thermophysical properties by coring and laboratory measurements may allow predictions of long-term heat exchanger performance to be made with greater confidence (Walker et al. 2015), albeit at much greater cost.

Heat flow may also be controlled by hydrologic properties—porosity and hydraulic conductivity—which vary with depth (Dehkordi and Schincariol 2014, Diao et al. 2004, Hecht-Mendez et al. 2013). Water has a higher thermal conductivity than air, so saturated rock conducts heat better than unsaturated rock (Horai and Simmons 1969, Zimmerman 1989, Clauser and Huenges 2013, Meyer 2013). In addition, significant heat can be transported by groundwater flow itself in the form of advection (Özdoğan-Dölçek, A. 2015). The magnitude of this advective heat flow and direction can be estimated by measuring water levels with piezometers and the hydraulic conductivity of the porous medium.

Despite the fundamental understanding that heat transfer in the subsurface varies with depth, a lack of validated quantification of these effects (particularly using multiple lines of evidence) has contributed to the simplifying assumptions of homogenous ground. As a result,

GSHP designers may conservatively overdesign the system with general estimates of effective subsurface thermal conductivity and capacity. TRTs support accurate borefield sizing by providing *in situ* average ground properties as a temporary solution to site-specific design. However, ignoring differential behavior for convenient average solutions does not allow for improving future designs that may also be affected by subsurface heterogeneities. To further investigate distributed subsurface behavior, a tool is needed that can feasibly provide long strings of temperature data with sufficient spatial and temporal resolution to describe heat transfer within and around a GHX.

2.3 Fiber Optic Distributed Temperature Sensing

Distributed temperature sensing (DTS) was first developed in the early 1980's (Hartog 1983) and the oil industry was the first to apply at field scale. Companies installed cables both within and surrounding oil and gas pipelines as a means of leak and fire detection (Kersey 2000). In this early application, the temperature and spatial resolutions were poor; however, oil companies only needed to detect large spikes in temperature over broad areas. As the advantages of temperature sensor networks became evident, effort was spent on technological advancement to improve instrument accuracy and resolution. By the early 2000s, robust calibration could achieve temperature and spatial resolutions of 0.01 °C and 1 m (Henninges et al. 2003).

In recent years, the scientific community has taken advantage of these improvements in DTS technology that have provided finer temporal, spatial, and temperature resolutions. With the onset of these capabilities, environmental monitoring applications of DTS have rapidly expanded. Such applications include investigations into groundwater/surface water interactions (Lowry et al. 2007, Slater et al. 2010, Blume et al. 2013, Xiang et al. 2016), distributed subsurface hydraulic properties (Bahr et al. 2011, Read et al. 2013), soil moisture content (Steele-Dunne et al. 2010, Sayde et al. 2010, Striegl et al. 2012) lake thermal stratification (Suárez et al. 2011, Arnon et al. 2016, Lucas et al. 2016), illicit sewer connections (Schilperoort et al. 2009, Hoes et al. 2009),

snow pact coverage (Tyler et al. 2008), boundary layer height (Thomas et al. 2011, Keller et al. 2011), and forest canopy coverage (Bense et al. 2016). Researchers have also used the advantages of DTS to explore geothermal resource potential by installing fiber optics inside boreholes to observe temperature gradients (Cottingham et al. 2013), investigating *in situ* subsurface thermophysical properties (Henninges et al. 2005, Freifeld et al. 2008), and monitoring ground heat exchanger performance (Fujii et al. 2009, Beier et al. 2012, Acuña et al. 2013).

Fiber optic DTS uses the interaction of laser light within fiber optic cables to monitor temperature along the length of the cable. An interrogator generates light pulses that propagate through a silica glass fiber, and interacts with the constituent molecules of that medium. If the photon/constituent molecule collision does not occur at a wavelength near medium resonance, a scattering event forms. There are three predictable scattering events know as Rayleigh, Brillouin, and Raman (Figure 1, Bao and Chen 2012). Rayleigh scattering is a linear and elastic scattering process that returns light of similar wavelength and intensity of the incident light pulse. This elastic scattering occurs when the kinetic energy of the photons are conserved through the collision (Suárez et al. 2011). Brillouin scattering is an inelastic scattering event that creates two pulse events of unique wavelengths above and below the wavelength of the incident light (Hausner et al. 2010). Raman scattering is also an inelastic event that occurs when a portion of incident light is adsorbed and emitted at alternate wavelengths due to the loss or gain of energy with the electrons in the fiber molecules. This research uses Raman-based DTS. During a Raman scattering event, Stokes backscatter is created when a photon excites a molecule at its

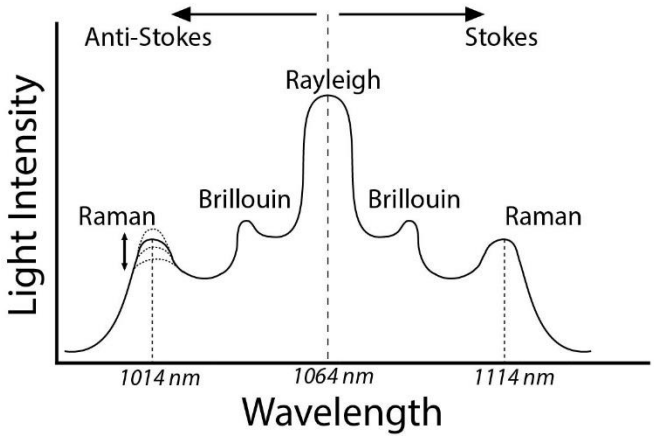

Figure 1: Three types of backscattered light after a photon collision

base vibrational state and bumps the molecule to the next highest vibrational state by the addition of energy. Anti-stokes backscatter is the result of a constituent molecule receiving energy from the photon and releasing it at a lower vibrational and energy state (Suárez et al. 2011). The ratio of photons in the Anti-stokes and Stokes states, defined in Eq. 4, is a function of the temperature at which the scattering event occurred (Smith and Dent 2005), where P_s is the power of the stokes signal, P_{as} is the power of the Anti-stokes signal, and z is length along the fiber.

$$R(z) = \frac{P_S(z)}{P_{As}(z)} \tag{4}$$

Interrogators use lasers to generate pulses of light for typically 10 to 20 ns at a known wavelength that propagate down a fiber optic cable (Suárez et al. 2011). This wavelength is commonly near 1064 nm, which is above the visible light spectrum (400 to 700 nm). A fiber optic cable consists of a glass core encapsulated by glass cladding with a higher index of refraction to allow for total internal reflection. Typical multimode DTS cables have a 50-µm-diameter glass core and a 125-µm-diameter cladding. In all fiber optic cables, light encounters impurities in the core's crystal structure and molecular inclusions (commonly GeO_2) to create scattering events (Selker et al. 2006a). At these backscatter events, a fraction of the incident light propagates back to the integrator. The interrogator is equipped with a high-precision photodiode that measures the amplitudes of the Stokes and Anti-stokes Raman backscatter. Because of the temperature dependence of the ratio of these intensities, these light amplitude measurementss can be converted into temperatures. The distance along the fiber to which an individual temperature belongs is calculated by time-domain reflectometry using the speed of light within the glass fiber which varies between $1.7 \cdot 10^8$ and $2.0 \cdot 10^8$ m s^{-1} (Suárez et al. 2011). Assuming a light speed of $2.0 \cdot 10^8$ m/s and a sampling interval of 20 ns, the spatial resolution obtained is 2 m, meaning that a temperature calculated at 5 m is in truth an average temperature of the fiber between 4 and 6

m. The spatial resolution will continue until the end of the fiber or until light intensity attenuates, which is dependent on the initial power of the laser and signal losses in the fiber.

Fusion splicing is the typical method for conjoining two separate fiber optic cables to create one continuous signal pathway. This type of splicing consists of precisely aligning the glass cores of the two fibers (mechanically assisted) and applying focused heat to fuse the two glass cores together. Either by darkening of the glass or misalignments of the cores, a step loss in signal strength often occurs across these splices. If this step loss in signal is not correctly identified and corrected, temperatures reported by DTS will have an erroneous offset for the remainder of temperature measurements after the splice. Step losses in signal may also occur with cable impingements, sharp bends that undermine total internal reflection, or the physical connectors (typically E2000) between the fiber and the interrogator. Hausner and Kobs (2016) provides an in-depth discussion on identifying and correcting for step losses

The interrogator may be set up for single- or double-ended measurement. In the single-ended setting, light pulsates from one end of a fiber optic cable for the prescribed duration, creating one profile before moving to the next fiber. In the double-ended setting, each fiber optic

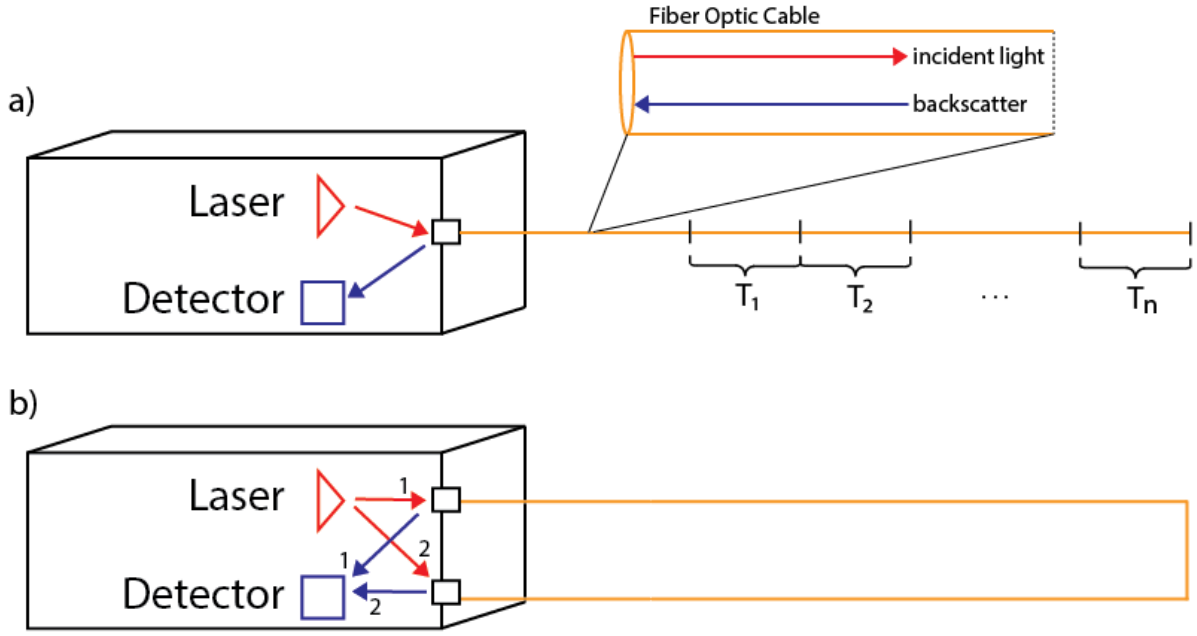

Figure 2: a) Single-ended and b) double-ended interrogator configurations.

cable is looped back and reattached to the interrogator so that both ends of the fiber will propagate light sequentially from path 1 to path 2 in Figure 2b. In this way, the interrogator can receive two sets of light intensity data for the same fiber. Due to the sampling methodology in double-ended configurations, the signal near the middle of the fiber will have the lowest noise-to-signal ratio, and will thus provide more accurate temperature measurements near the middle of the cable (van de Giesen et al. 2011). Each monitoring mode has its own strengths and weaknesses and the choice of monitoring mode at an installation can dramatically affect the temperature accuracy achieved (Krause and Blume 2013). The light intensity ratios must be decoded to provide strings of temperature data along the cable either by the manufacturer default calibration routine, or a manual calibration procedure. The parameters that describe the relationship between the Stokes/Anti-stokes ratio and temperature are prone to vary with the operating temperature of the

interrogator, the quality and consistency of the power supply, mechanical variance within the equipment, and localized strain in the fiber (Hausner et al. 2011). An internal calibration routine relies on a coil of fiber and several thermometers within the interrogator. The signal within the coil is calibrated to the average of the internal thermometers. In some applications, the internal calibration routine can provide acceptable accuracy of these parameters, while in other applications a manual calibration scheme is needed.

A field installation was used to test the efficacy of the default calibration on a Sentinel DTS-LR Interrogator (Sensornet) on a heavily spliced (8 splices) double-ended fiber optic loop within a district-scale geothermal borefield. Default calibration temperature data from the loop was observed to contain data a step-offset after splices. Before any heat exchange had occurred, two 140 m boreholes installed with fiber should have provided nearly identical temperature profiles. However, a 0.5 °C shift in temperature was observed. Additionally, the absolute ground temperature presented by the default calibration did not align well with the 9 to 11 °C temperature range expected in southern WI (USGS, 1920), suggesting that the other splices before the fiber entered the borefield were also creating a temperature offset. The temperature shifts shown in the data provided strong evidence that the default calibration was unable to correct for step losses at splices.

It has been noted (Selker et al. 2006, Tyler et al. 2009) that rapid shifts in ambient temperature may cause errors in the default calibration. To test the Sentinel interrogator's sensitivity to this, a gas heater was used to rapidly raise the temperature of the underground vault that houses the interrogator. The internal temperature of the interrogator elevated from 10 °C to 25 °C between 8am and 10am. Fig. 4 shows the resulting failure of the default calibration to accurately handle the change in air temperature that was created. The rapid heating created a temperature gradient within the interrogator that caused the average internal thermometer temperature to not be truly representative of the true average fiber temperature. Both data sets measured the same environment inside of the GHX, and should nearly overlap. However, a shift of nearly -6 °C is observed (Figure 3). While this is an extreme example, temperature fluctuations occur on a smaller scale from diurnal temperature swings and weather patterns that could create a similar bias. A server box with a temperature set-point controlled fan was installed around the interrogator to counteract ambient temperature swings. Although the diurnal temperature swings were muffled by the server box to less than 0.5 °C, these temperature swings still created appreciable biases in the default calibration output.

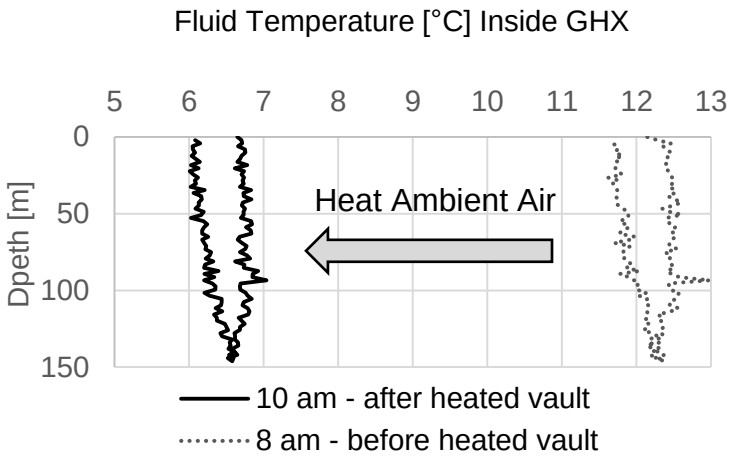

Figure 3: U-pipe temperature profiles before and after ambient heating.

Manual calibration requires that the DTS user create an experimental setup in which multiple sections of each fiber optic cable are at a known temperature. Eq. 5 governs the

relationship between the ratio of light intensities, temperature, and the calibration parameters (Hausner et al. 2011):

$$T(z) = \frac{\gamma}{ln\frac{P_s(z)}{P_{As}(z)} + C - \Delta\alpha * z} \quad (5)$$

where γ, C, and Δα are the calibration parameters. γ represents the shift in energy between a photon at the wavelength of the incident laser and the scattered Raman photon and is defined as $\gamma = \hbar\Omega/k$ K (van de Giessen et al. 2012); where $\hbar = 6.62 \cdot 10^{-34}$ m^2 kg s^{-1} is Planck's constant, Ω ≈ 1013 Hz (for a typical 1064-nm laser) is the frequency difference between incident light and backscattered light, and $k = 1.38 \cdot 10^{-23}$ m^2 kg s^{-2} K^{-1} is the Boltzmann constant. While γ ≈ 470 K theoretically should not change, the instrument's ability to read differential frequency may change as physical components within the interrogator change with time, temperature, vibration, etc. This reading is an extremely sensitive input as a wavelength shift difference of 1 nm changes γ by about 10 K. The calibration parameter C corrects for physical variations within the interrogator. It is common practice to fix γ at an optimal value for the data set, thus allowing C to absorb all variation that γ would have created (van de Giessen et al. 2012). Δα is the differential attenuation between the Stokes and anti-Stokes signal. Both signals attenuate at different rates during travel back from a scattering event. Δα must be accounted for to accurately recover the ratio of signals at the scattering event (Hausner et al. 2011). There are several methodologies to calculate the calibration parameters. Hausner et al. (2011) provides an in-depth discussion on single-ended methods (light propagation through the fiber in a single direction), while van de Giessen et al. (2012) discusses double-ended methods.

All calibration processes refer to the determination of the three unknown variables C, γ, and Δα. The most straightforward way to accomplish this is by designing an experimental set-up with three known temperatures at three different positions along the fiber optic cable. Sections of

fiber at a known temperature are better than point measurements as they allow for multiple reference points and increase the signal-to-noise ratio. This is most often accomplished by coiling a section of fiber of at least ten times the length of the spatial resolution (Tyler et al. 2009). Under these conditions, three values of T(z) are known from the external temperature measurement, and three values for Ps(z)/Pas(z) are taken from the DTS outputs. Eq. 2 may then be thrice restated with the known values specified to provide a system of three equations with three unknowns. The calibration variables are then calculated using linear regression techniques. Once the calibration parameters are specified, the light intensity ratios provided by the interrogator for the remainder of the cable length can be converted to temperature.

There are many considerations and associated adjustments beyond this most basic simultaneous parameter calculation calibration process. To begin, it is important to understand that, although mathematically interdependent, each calibration parameter represents a unique physical truth that may vary differently over time and space. γ, as a combination of physical constants, should not change in time or space. C will change in time as the physical conditions around and within the interrogator change. Δα will change in space, as the rate of differential attenuation is a physical property of the glass core of a fiber optic cable, and may change in time as the environmental conditions around a fiber change. When using multiple fiber optic cables that may have been manufactured under slightly different conditions (even from the same manufacturer), Δα should be calculated separately between splices to calculate true differential attenuation with greater precision.

A calibration may be static or dynamically recalculated in time. A static calibration involves calibrating a DTS system at one fixed point in time and applying those calibration parameters over the duration of the DTS data collection. This method requires less experimental consideration and capital cost of time and resources to apply the calibration. However, static calibrations assume that the ambient conditions around the interrogator (C) and the fiber (Δα) are constant in time to

an extent that their variance does not introduce significant bias into the calibration. In this research, a manual static calibration fell far short of the needed accuracy and precision of the research questions. Other DTS interrogators exist that rely on other interrogation principles (such as frequency domain sampling) that may be calibrated statically with lasting accuracy. DTS that relies on Raman backscatter and time domain reflectometry in environmental applications should be calibrated dynamically. While keeping two or more temperature baths at different temperatures over time can be an operational challenge, it will at-worst provide a static calibration, and at-best recalibrate the system for each change in ambient condition, thus minimizing data bias. Beyond fully static or fully dynamic calibrations, there may be intermediate combinations. The most common combination is to fix γ in time, find Δα as a function of the entire cable length and fix it in time, and recalculate C dynamically to account for all time variation in the calibration.

Single-ended calibration techniques are only able to calculate one value of Δα for a fiber. In contrast, by utilizing double-ended calibration, a unique Δα can be calculated at each data acquisition point z independently of temperature references (van de Giesen et al. 2012). This procedure also allows for robust correction of step losses incurred by splicing and different Δα values of different fiber sections. Additionally, if Δα is calculated using only the light intensity data with a double-ended configuration, the calibration regime requires only two unique temperature reference sections to solve for the remaining two calibration variables. Another methodology to calculate the differential attenuation of a fiber is to use the calibration bath itself. If the bath is truly at a uniform and constant temperature, any change in the Stokes/Anti-stokes intensity ratio from a coil within that bath would be due to differential attenuation. Eq. 6 presented in Hausner et al. (2011) and derived from Beer's Law under constant temperature conditions, shows that if $ln\frac{P_S}{P_{As}}$ is plotted as a function of position (z), the slope of the linear relationship is the differential attenuation of the fiber.

$$ln\frac{P_S}{P_{AS}}(z_2) = ln\frac{P_S}{P_{AS}}(z_2) + \Delta\alpha * (z_2 - z_1) \quad (6)$$

This method for calculating differential attenuation is limited in two respects. First, Δα for that small portion of the cable is subsequently applied to the entire fiber, which is especially a problem when multiple fibers are spliced together. Secondly, the magnitude of erroneously reported temperature changes from Δα are so small that the absolute uniformity of the temperature bath is critical to the calculation. In practice, this can be quite difficult to achieve. Water changes buoyancy with temperature and naturally stratifies in the presence of a temperature gradient. Small circulation pumps are often used to provide mixing; however, within an insulated calibration bath, submerged circulations pumps can provide electrical resistance heating, which will preferentially heat the bath beginning with the area immediately surrounding the pump. Additionally, boundary effects must be considered. Convection resistances at the interaction of the calibration bath wall and fluid will create a temperature shift. Calibration coils that rest on this boundary will have a bias towards the wall temperature and not all of the change in fiber reported temperatures will truly be from differential attenuation. For these reasons, it is extremely important to design a calibration bath that can provide a uniform temperature around the entirety of all calibration coils.

Fiber optic distributed temperature sensing is a tool with great advantages that also requires a significant investment of time and resources to realize its full potential. Once designed, a calibration routine can become fully automated with minimal maintenance needed. By running from a central interrogator, and having a single continuous sensor that also provide telemetry, all data is centrally collected with minimal disturbance of the conditions being monitored. In demanding environmental applications that require high degrees of accuracy and precision, design must be made with ability to analyze large data sets. While often difficult, this is certainly possible and made easier by a multitude of worldwide organizations that sell DTS systems and

offer support. One organization in particular, the Center for Transformative Environmental Monitoring Programs (CTEMPs) has dedicated resources to advancing understanding and aiding in the implementation of DTS.

2.4 Distributed Thermal Response Tests

A distributed thermal response test (DTRT, Acuña and Palm 2013) uses a fiber optic temperature probe within a GHX during a TRT to observe differential subsurface heat transfer. Freifeld et al. (2008), pioneered this concept by using a resistance heater in a borehole to create a thermal perturbation and monitor the subsequent temperature decay with DTS. Due to difficulty in fixing the fiber optic cable location in the well, sharp differences in temperature with depth were observed while the heater was energized due to varying fiber optic cable proximity to the heating element. The DTS collected temperature decay data that was inverted by a radial heat flow model to calculate thermal diffusivity and then distributed thermal conductivity of the subsurface with estimates of distributed specific heat capacity (i.e., the amount of energy required to raise the temperature by 1 degree of a unit mass of a material).

Fujii et al. (2009) enhanced the DTRT with fiber optics in the supply side of the GHX, and compared the distributed decay temperature data to a traditional TRT. Two tests were performed, one within mostly homogenous granite down to 63 m, and another in weathered tuff down to 100 m. The cylindrical source function was used with inlet and outlet temperatures and flowrate to find subsurface thermal conductivities (λ_{ss}) of 2.74 W m^{-1} K^{-1} (granitic) and 1.27 W m^{-1} K^{-1} (tuff). The DTRT used a multi-layer analytical model to find distributed thermal conductivity with depth. At both sites, despite relatively homogenous subsurface lithology, the distributed data was able to capture depths of distinct thermal conductivities allowing for determination of thermal stratigraphy. In particular, for both tests, the presence of ground water increased local thermal conductivity. The average thermal conductivities found with the DTRT methods were 2.56 W m^{-1} K^{-1} (granitic)

and 1.21 W m^{-1} K^{-1} (tuff), which were validated by their small difference from the traditional TRT results.

Beier et al. (2012) and Acuña and Palm (2013) expanded the DTRT further by placing fiber within both a coaxial and standard u-tube GHX configuration to study the effects of pipe configuration on heat transfer during a heat injection period. Beier et al. (2012) developed a distributed analytical model for inverting temperatures in the late stages of the heat injection to calculate borehole resistance with the true circulating water temperature from the fiber optics rather than using the mean approximation of the inlet and outlet water temperatures. The focus of Acuña and Palm (2013) was the use of *in situ* distributed temperature data at the borehole wall to compare between piping configurations at different exchanger fluid flow rates. Results indicated that coaxial GHXs may provide lower thermal resistance than standard u-tube GHXs when comparing the heat exchanger as a hole, but localized resistances can be higher because of the lack of thermal contact between the fluid in the annulus and the inner pipe. They conclude that more DTRTs must be performed to gain complete understanding of GHX piping configuration. Recently, a DTRT was performed on a GHX within an overheated geothermal field as a diagnostic tool to analyze differential heat decay with depth (Herrera 2016). Thermal conductivities were found using a layered analytical model called the “cross-contours” method that varied all input parameters (e.g., borehole resistance, thermal conductivity, subsurface density, etc.) and found the combination that minimized the error. Thermal conductivities were segmented to match geologic sections and found that different formations exhibited differential thermal conductivities.

Distributed thermal response tests have shown the ability to provide insight on distributed subsurface heat transfer. However, the pool of successful tests is small, and experimental methodology and data analysis techniques vary. Further testing and research is needed to enhance this tool that has shown promise to decrease uncertainty and increase optimization potential in future GSHP installations.

2.5 District-Scale Borefield Case Study

Academic or commercial campuses are particularly well-suited to benefit from the long-term increased economic and environmental efficiencies of a district-scale GSHP borefield. The following case study on a hypothetical district-scale borefield at such a campus in Verona, WI is presented to demonstrate tangible benefits from the consideration of heterogeneous subsurface heat transfer.

To increase the accuracy of ground thermal properties, a preliminary TRT was conducted at the Epic System's site to a depth of 115 m. The average effective thermal conductivity of the subsurface is 3.3 W m^{-1} K^{-1}. Building loads can be matched by a 500-GHX borefield, each 115 m deep and spaced 6 m apart in a 20 x 25 grid pattern. With this design, 57175 m of vertical GHX piping is needed. A conservative installation cost of $32.81 per m of GHX (Rafferty 2015) brings the capital cost of installation to $1.87 million.

Consider that a preliminary DTRT was conducted and distributed thermophysical properties were found (Figure 4). The distributed results reveal that the bottom 35 m of each GHX would be installed in the least thermally conductive rock present at the site. With this foresight, the borefield design could be adjusted to avoid the Tunnel City Formation with 80-m GHXs, with

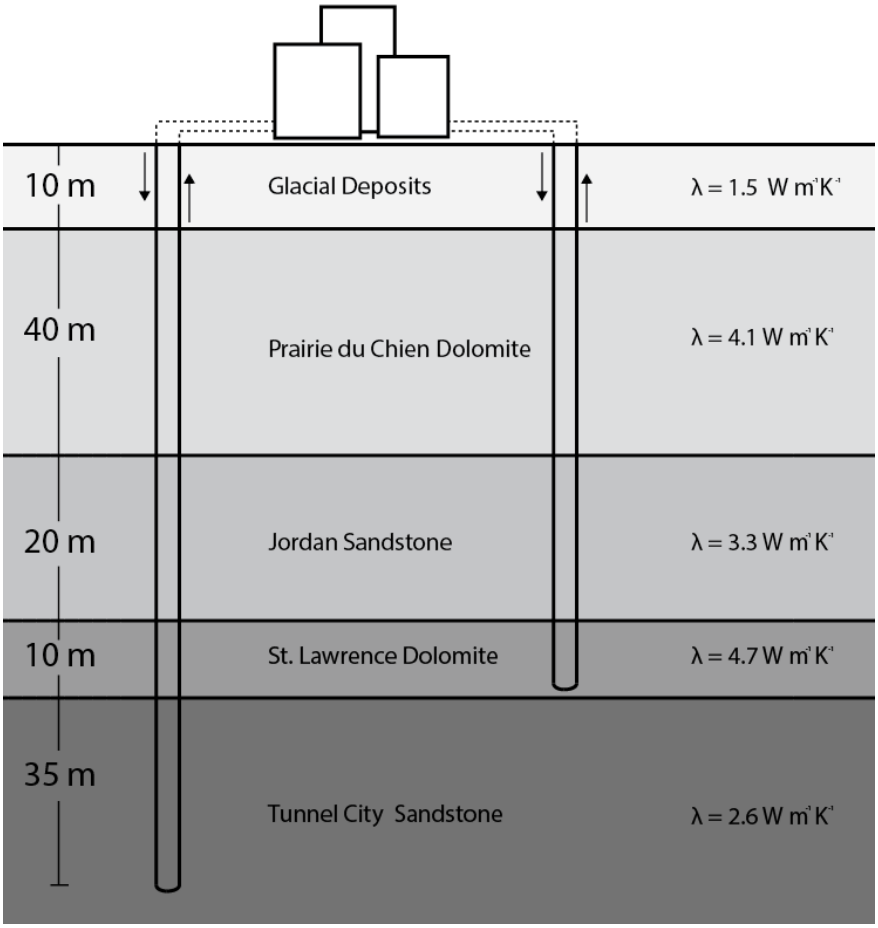

Figure 4: Distributed thermophysical properties from a hypothetical DTRT in Verona, WI.

a new average borehole thermal conductivity of 3.65 W m^{-1} K^{-1}. The DTRT also hinted at the benefits of ground water flow of the shallow aquifer, by showing a jump in thermal conductivity beneath the water table. To match the same building loads, 600 80-m-deep GHXs were required, now in a 60 x 10 pattern elongated perpendicular to ground water flow. Overall pipe length with this new design is 47,500 m, over 9.5 km less GHX length than the original design. The new cost installation is $1.55 million, or $320,000 less than the previous design based on homogenous properties.

This district-scale borefield replaced an HVAC system comprised of natural gas heating in the winter and air-to-air heat exchange cooling in the summer. The cost of natural gas was fixed at the present cost of $0.00088 per kWh (EIA 2017), and electricity was supplied at rates of

$0.14 per kWh in the summer and $0.13 per kWh in the winter (MGE 2017). Applying a conservative GSHP cooling COP of 2.5 and a heating COP of 3.0 the operational cost savings of installing the GSHP borefield was approximately $180,000 per year. Quantifying the current HVAC system as a sunk cost, the payback period was calculated based on how long it would take these operational savings to accumulate to the capital cost of installation. If using the borefield design from a traditional TRT with homogenous effective properties, the payback period is 10.4 years. With the aid of the more optimally designed borefield from DTRT insights, the payback period is reduced to 8.6 years.

While this study is hypothetical, the scenario is very real. The geology in south-central Wisconsin is well documented by the Wisconsin Geological and Natural History Survey (WGNHS 2005). In place of conducting a DTRT, distributed thermophysical properties were compiled for this case study using laboratory core measurements and a review of literature values (Meyer 2013). Industry standard borefield design software (Ground Loop Design 2016) was used to match building loads with borefield design. The results describe a situation where a 144-h DTRT with minimal financial investment may provide enough novel information to save $320,000 of project costs, and 1.8 years on the investment payback period.

Chapter 3: Dynamic Calibration of a Permanent Distributed Temperature Sensing Network

Distributed temperature sensing (DTS) is a technique that uses the interaction of laser pulses with silica to continuously sense temperature along the length of fiber optic cables. The temporal and spatial resolution of DTS makes it an excellent technique for monitoring the performance of a district-scale geothermal exchange borefield. These types of systems require assessing how heat is transferred through complex geologies under varying heat demands. Subsurface trenching and grouted vertical borehole installation is a demanding application in which proper calibration of the DTS response is needed to achieve meaningful results. A calibration routine developed in response to site-specific challenges and constraints is systematically presented and analyzed. In applications where DTS arrays are long (e.g., more than 5 km), many splices are present (e.g., more than 4), individual fiber segments have various lengths and configurations, and continuous sensing is required for long periods of time (e.g., more than a year), a highly-involved calibration methodology is required. For these reasons, a long-term, dynamic, double-ended, centralized, and remotely accessible calibration routine is developed and evaluated to provide novel insight on calibration considerations. Results show that different combinations of calibration baths may change calibration accuracy, and over-determination in the calculation of calibration parameters provide greater accuracy. Fixing the γ calibration parameter does not appreciably change accuracy but does provide a buffer against error from variations in calibration bath temperatures. Differential attenuation varied by up to 25% between discrete fiber sections and should be calculated for each array section to prevent errors generated from applying just one attenuation coefficient value for the entire fiber array. Dynamically calculated differential attenuation may vary systematically with time and space, and the intrinsic noise associated with this variation is dependent on the environment the fiber is in as well as the optical properties of the fiber itself. In a double-ended configuration, the consideration

of whether the forward, reverse, or some combination of all light data is used will affect the robustness of the calibration over time. Each of these results may assist in thoughtful consideration of calibration design at future DTS installations facing similar challenges.

3.1 Introduction

Fiber-optic Distributed Temperature Sensing (DTS) is a method of temperature sensing that provides temperature measurements along kilometers of a fiber-optic cable. To accomplish this, an interrogator unit sends pulses of light of a known frequency down a fiber optic cable. Impurities in the silica core of the fiber optic create scattering events where energy is exchanged between the light and the glass medium. The interrogator records the time of arrival and intensity of the scattering event. The time of arrival locates the position of the scatter event along the length of the fiber through time domain reflectometry. The backscattered event includes two distinct portions of the inelastic Raman spectra scattering: the Stokes and anti-Stokes signals (Bao et al. 2012). While both signals return at predictably shifted frequencies, the Stokes signal amplitude is temperature independent, while the anti-Stokes signal is strongly related to the temperature at which the scattering event occurred. Therefore, the ratio of these two signals can be used to produce a temperature measurement. Using the averaging of scattering events and time domain reflectometry, the temperature profiles along the entire length of the fiber optic cable are created. For a more complete discussion of the science behind DTS the reader is referred to Selker et al. (2006) and Bao et al. (2012).

Originally used by the oil and gas industry for leak and fire detection (Kersey 2000), coarse temperature spatial and temporal resolutions provided adequate data profiles. In the past ten years, however, significant advancements made in DTS technology has allowed for temporal resolutions of 0.01 °C, spatial resolutions of 0.35 m, and temporal resolutions of 1 Hz (Silixa 2017). With the onset of these capabilities, environmental monitoring applications of DTS have rapidly expanded. Such applications include investigations into groundwater/surface water

interactions (Lowry et al. 2007, Slater et al. 2010, Blume et al. 2013, Xiang et al. 2013), distributed subsurface hydraulic properties (Bahr et al. 2011, Read et al. 2013), soil moisture content (Steele-Dunne et al. 2010, Sayde et al. 2010, Striegl and Loheide 2012) lake thermal stratification (Suárez et al. 2011a, Arnon et al. 2016, Lucas et al. 2016) illicit sewer connections (Schilperoort and Clemens 2009, Hoes et al. 2009), snow pack coverage (Tyler et al. 2008)), boundary layer height (Thomas et al. 2011 and Keller et al. 2011), and forest canopy coverage (Bense et al. 2016). Similar to the motivation behind this study, researchers have also used the advantages of DTS to bury fiber optics in grouted boreholes looking for temperature gradients (Cottingham et al. 2013), investigate *in situ* subsurface thermophysical properties (Henninges and Huenges 2005, Freifeld et al. 2008) and ground heat exchanger performance (Fujii et al. 2009, Beier et al. 2012, Acuña and Palm 2013).

DTS systems come with an internal calibration routine that converts the raw Raman spectra into temperature values. The internal calibration depends on comparing light intensity data from a coil of fiber within the instrument to temperature measurements of that same coil by a precise thermistor. However, the user must take care to avoid data bias that may arise from using these internal calibration routines. When the ambient temperature around the interrogator varies, the propagation of heat waves across the calibration coil and thermistors within the interrogator will cause a time-dependent shift in the calibration parameters. This potential for data bias has been previously identified (Suárez et al. 2011b) and it is recommended that the problems may be minimized by placing the interrogator in a temperature controlled box. Splices and associated sudden loss of signals also pose a challenge for internal calibration routines. Each fusion splice at an installation has the potential to introduce systematic bias and temperature shifts in each data set. Although it is possible with some interrogators to program splice locations, the quality (and effect on backscattered data) of any two fusion splices are rarely identical and difficult to assess. Due in part to these considerations, many environmentally monitoring users of distributed temperature sensing opt for the control of a manual calibration technique. Manual calibration

uses Eq. 7 to convert the ratio of Stokes $P_S(z)$ and anti-Stokes $P_{aS}(z)$ signal intensities into temperatures values while also assess manual splice identification and correction (Farahani and Gogolla 1999).

$$T(z) = \frac{\gamma}{\ln\big(R(z)\big) + C - \Delta\alpha z}$$

$$R(z) = \frac{P_S(z)}{P_{aS}(z)} \tag{7}$$

This method relies on creating reference sections of the fiber at known temperatures. The reference sections allow for the explicit calculation of three calibration parameters: γ, C, and Δα. γ represents the shift in energy between a photon at the wavelength of the incident laser and the scattered Raman photon and is defined as $\gamma = \hbar\Omega/k$ [K] (van de Giesen et al. 2012); where $\hbar = 6.62 \cdot 10^{-34}$ [m^2 kg s^{-1}] is the Planck's constant, $\Omega \approx 10^{13}$ Hz (for a typical 1064 nm laser) is the frequency difference between incident light and backscattered light, and $k = 1.38 \cdot 10^{-23}$ [m^2 kg s^{-2} K^{-1}] is the Boltzmann constant. While γ ≈ 470 [K] theoretically should not change, the instruments ability to read differential frequency may change as physical components within the interrogator change with time, temperature, vibration, etc. A wavelength shift difference of 1 nm changes γ by about 10 [K]. The calibration parameter C corrects for physical variations within the interrogator. General practice is to fix γ at an optimal value for the data set, thus allowing C to absorb all variations that γ would have created (van de Giesen et al. 2012). Δα is the differential attenuation between the Stokes and anti-Stokes signal. Δα must be accounted for to accurately recover the ratio of signals at all scattering events (Hausner et al. 2011). There are several methodologies to calculate the calibration parameters. Hausner et al. (2011) provides an in-depth discussion on single-ended methods (i.e., light propagation through the fiber in a single direction), while van de Giesen et al. (2012) discuss double-ended methods (i.e., intermittent propagation of light from

both directions. This methodology requires a loop with both ends attached to the interrogator). Krause and Blume (2013) present a compelling case for thoroughly understanding the choices and making an informed decision on which calibration routine to use as the selection may greatly impact the accuracy and precision of the DTS measurements. Hausner and Kobs (2016) provide detailed insight into the process of correcting step losses in signal and the effects that this correction may have on temperature calculations using the manual calibration technique.

Recent studies have built on the understanding of manual calibration techniques by applying these fundamental principles to project-specific applications, each with its own set of requirements and constraints (Hausner et al. 2011, van de Giesen et al. 2012). Many different interrogators, integration times, spatial resolutions, fiber-optic cables, and calibration baths have been utilized with both single and double-ended installations. Each case study provides strengths and weaknesses of the calibration methodologies. However, one common thread in all these applications is the short-term nature of data collection. Most studies continuously collect data for days to weeks, with only a few extending to months or years. Even studies with permanent fiber installed often only intermittently collect data. Perhaps a reason for the lack of long-term DTS installation are the challenges posed by maintaining continuous data collection and dynamic manual calibration which is necessary as the response instrument drift (Tyler et al. 2009).

This study provides an example of a long-term dynamic calibration of a complex fiber-optic network buried within a low temperature geothermal borefield. Due to the complex nature of the fiber installation, many fusion splices were performed without known locations of splices or lengths of buried fiber. Additionally, physical access to the interrogator was generally restricted. These conditions allowed for an opportunity to develop alternate solutions to the previously documented considerations, such as locating splices and specifying fiber lengths, as well as a remotely controlled calibration routine. By performing a dynamic calibration over the course of years, valuable insight was gained in considerations for optimizing calibration methodologies.

3.2 Materials and Methods

3.2.1 Field Site

The campus of a southern Wisconsin company relies on low-enthalpy ground heat exchangers to supply space heating and cooling and domestic hot water heating for nearly all the campus buildings. This campus has 15 office buildings that house over 10,000 employees. Due to the heat generated during the daily use of the buildings, yearly building HVAC loads are cooling dominated. To provide these loads, this company has constructed four district-scale geothermal borefields and a cooling pond. The borefields provide a combined cooling capacity of 48.5 MW (with borefield 4 yielding more than 50% of this capacity), while the cooling pond provides an additional capacity of 4.2 MW. The total system flow is 3.8 m^3/s. Because of the predominant cooling loads, the first two geothermal fields that were constructed initially experienced a net inflow of energy in yearly cyclic loads, which greatly increased the temperature of the borefields. Heat exchanger and heat pump efficiencies decreased dramatically, and operational costs went up. To improve the operation of the system, the company added additional capacity with the last two fields, allowing the older fields to cool as well as to better distribute the future heating loads. However, it was recognized that simply constructing new borefields each

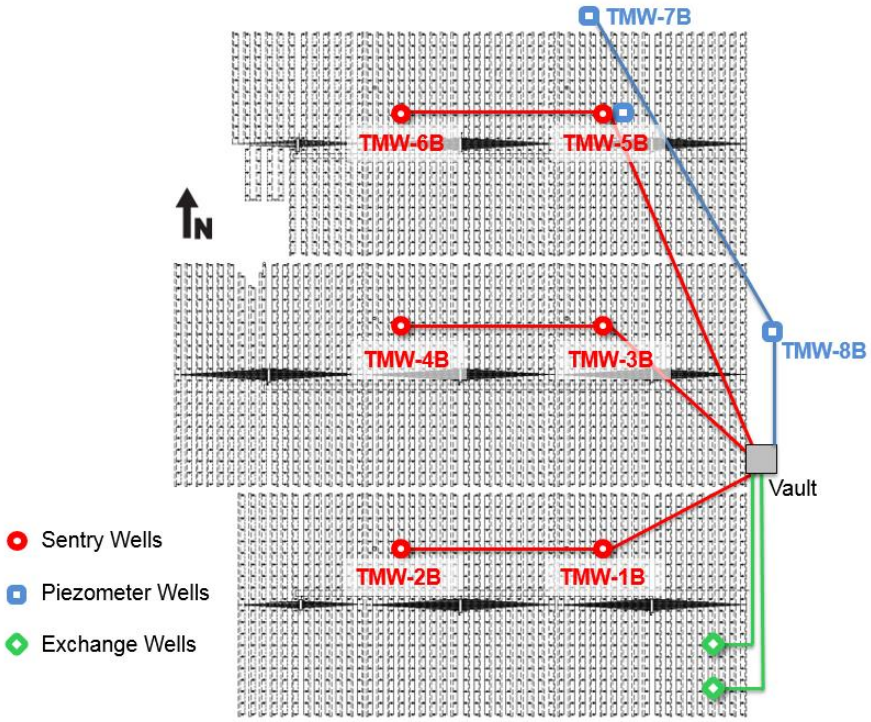

Figure 5: DTS network installed to monitor borefield 4.

time a field overheats is not a sustainable solution. For these reasons, further information was required to better evaluate the long-term heat transfer mechanisms in a heterogeneous subsurface, which was the overall goal of this research project. Figure 5 shows the complex DTS network that was installed in the newest borefield 4 to investigate the mechanisms of subsurface heat flow. The fiber optic loops that will be discussed in this paper are temperature monitoring wells (TMW) 1 through 8.

3.2.2 Instrumentation

A Sensornet Sentinel DTS-LR interrogator with a 16-channel multiplexor was used for this research. This interrogator provides up to 0.01-°C temperature resolution, 1-m spatial resolution over 10 km of fiber (Sensornet 2015). Fiber-optic cables were multi-mode 50/125 μm OM2 ClearCurve Plenum Orange, 2 mm outer diameter. Connectors were E2000 APC. All fiber optics were protected by 6.35-mm-diamter HDPE plastic piping to avoid differential stress or pinching in the fiber which would result in signal loss. Two PT100 Platinum Thermistors (±0.25 °C) (Sensornet, 2015) were connected directly to the Sentinel interrogator to collect continuous calibration bath temperatures and pair it to the appropriate fiber data.

The DTS interrogator was installed in a subsurface 10 m by 10 m by 5 m concrete vault that functions as an electrical switch hub and maintenance point for borefield 4. This vault was chosen for its proximity to the borefield, preexisting electrical capabilities, and for the buffer it provides the interrogator from environmental conditions. To test this buffer, internal temperature of the interrogator and air temperature of the vault were monitored for two weeks to quantify what environmental conditions were indeed felt by the interrogator. Although the signal was muted by the vaults insulation, the interrogator did show daily degree temperature swings mimicking diurnal air temperature patterns. As suggested by Suárez et at. (2011a), a further buffer was created in the form of a temperature-controlled server box. A remote connection was developed that allows complete control of the DTS interrogator, as well as instantaneous data collection and calibration.

3.2.3 Default Calibration Analysis

Previous studies have utilized default calibrations on interrogators (Yilmaz and Karlik 2006, Henderson et al. 2009), and achieved project-sufficient results. Likewise, the default calibration of the Sentinel interrogator was first explored for this work, and potential data bias was flagged at several sources. Despite the temperature-controlled server box, the interrogator was still exposed to buffered ambient air temperature changes and erroneous temperature shifts were observed during the most rapid of these events. Additionally, the large number of splice-work in the array—46 fusions splices and 53 fibers spread over the seven loops—was challenging to appropriately correct using the default calibration. Figure 6 provides a schematic of one such loop and the resulting effect of uncorrected splices. Two splices between two monitoring wells caused a drop in the Stokes and anti-Stokes signal intensities and created a coupled shift in the R(z) values that was manifested as a temperature offset of ≈ 1 [°C] on the east and west sides of the borefield at any depth recorded. The profile presented in the figure was taken as background data before any

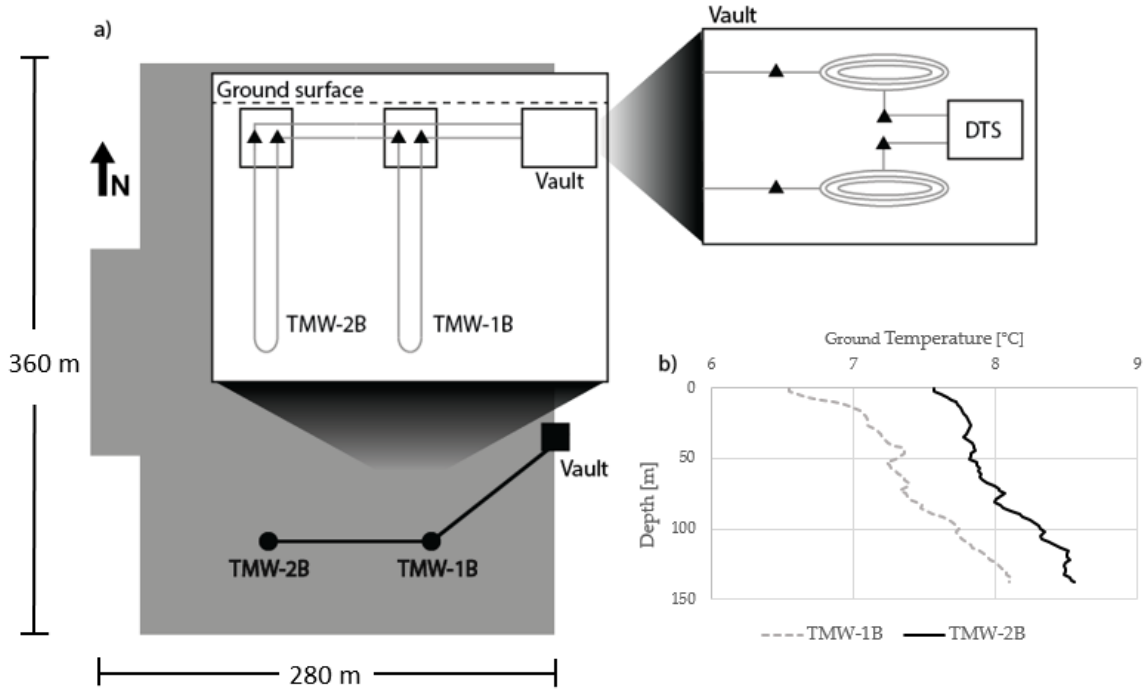

Figure 6a) Splice locations represented by triangles in 1 of 7 loops and b) the resulting temperature shift caused by two of these splices in the default calibration data.

heat injection into the borefield, and has no immediate physical explanation besides the signal offset. Manual calibration was required to correct for these data biases.

3.2.4 Manual Calibration Set-up

A double-ended, dynamic, centralized, and remotely accessible manual calibration was developed. Two 0.110 m^3 insulated water baths, ambient and heated, were installed in the vault to keep all calibration equipment centrally located for ease of access (Figure 7). Small pumps were used to promote mixing and prevent thermal stratification in the baths. An aeration tube was used for the ambient bath while a submersible pump was placed in the heated bath to provide additional energy through electrical resistance heating. Each fiber loop has a coil in both the ambient and the heated bath, is buried in communication trenches until reaching the sentry wells, returns in trenches, and again as a coil in both baths. The recommended length of fiber within a calibration bath is ten times the spatial resolution (Tyler et al. 2009). However, even fewer data points than ten may be available due to boundary effects of fiber crossing a sudden temperature change. As a result, some early baths only use 3-5 data points for calibration, while later baths have much longer coils and use up to 18 data points.

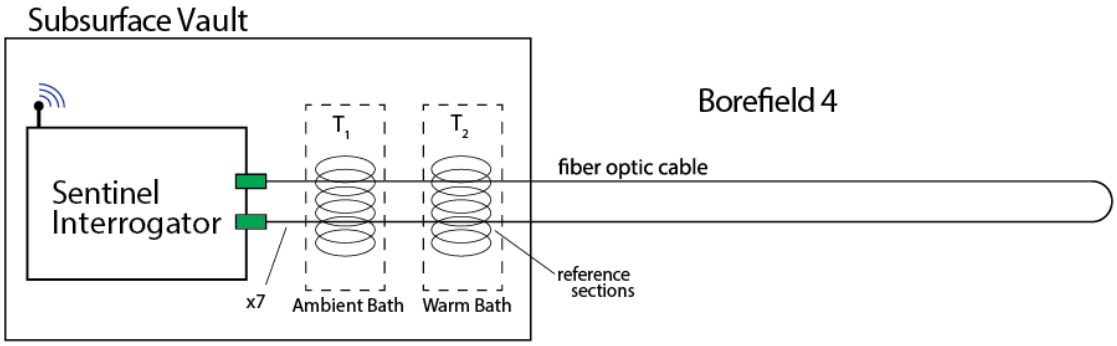

Figure 7: Schematic of double-ended, dynamic, centralized, and remotely accessible manual calibration.

Double-ended configuration was chosen over single-ended for the ability to calculate local differential attenuation $\Delta\alpha$ independently of calibration at any fiber section (Δz) desired by comparing the forward ($\Rightarrow$) and reverse ($\Leftarrow$) Raman spectra data (van de Giesen et al. 2012):

$$\int_{z}^{z+\Delta z} \Delta\alpha(z')\,dz' = \frac{ln\left[\frac{P_S(z+\Delta z)}{P_{aS}(z+\Delta z)}\right]_{\Rightarrow} - ln\left[\frac{P_S(z)}{P_{aS}(z)}\right]_{\Rightarrow} + ln\left[\frac{P_S(z+\Delta z)}{P_{aS}(z+\Delta z)}\right]_{\Leftarrow} - ln\left[\frac{P_S(z)}{P_{aS}(z)}\right]_{\Leftarrow}}{2} \quad (8)$$

Single-ended configurations assume a constant Δα over the entire length of a cable. However, Δα may differ in individual cables and over time, which must be quantified. To accomplish this, Eq. 8 was used with a Δz equal to the 1-m spatial resolution. Subsequently, local differential attenuations were optimized on a single cable between splices by the piecewise method described in van de Giesen et al. (2012). Δα was recalculated with each data trace to allow cable Δα values to vary over time. The decision to use a double-ended configuration also provided increased signal-to-noise ratio in the farthest sections of the loops (Krause and Blume 2013). This is of great benefit for the study as most temperature monitoring wells are located at the largest distances from the interrogator.

Dynamic calibration was chosen when a static calibration was first analyzed and temperature drift of over 0.5 [°C] was observed in only the first week of data collection. The dynamic calibration uses the calibration baths to recalculate all three calibration parameters γ, C, and Δα for each raw data output. For a given data interval to be calibrated, the mean of γ values is taken, fixed, and the calibration process is repeated solving only for C.

3.2.5 Fiber Length and Splices using Data Signals

When using a double-ended configuration, the total length of the fiber optic cable (i.e., from connector to connector) is required to match the forward signal to its correct reverse counterpart. In the simplest case, if no splices exist and the continuous cable is labeled, a user can simply record fiber lengths at each connector. When exact cable lengths are unknown, as is the case of this study, the signal itself can be used to find fiber lengths. Forward and reverse data can be oriented by finding the same temperature event (such as a calibration bath) in both traces. This

method can be complicated by asymmetric loops and an unknown length of fiber within the interrogator for default calibration. If the internal calibration coil length is unknown, it can be determined by using a single-ended configuration once with both connectors attached, and once with one connector unplugged. The difference in the lengths of these data traces will be equal to the internal length of the fiber. For this study, an alternate method of matching the forward and reverse signals was developed that required no change in configuration, and no site visit.

An original guess was made for the endpoint of the fiber based on the length of a double-ended signal and a length estimation of 50 m for the internal calibration coil. Using this endpoint, Eq. 8 was used to calculate local differential attenuation with Δz = 1 m along the length of the signal. Figure 8a shows the resulting signal for the incorrect endpoint which can be defined by high variability and spikes of attenuation (Figure 8a). In Eq. 8, these spikes represent large differences between signals in the forward and reverse direction. Here, when the two traces are not aligned, these locations represent a signal loss or temperature change that is not also seen at that same location in the paired trace. Consequently, these spikes are excellent first order estimations for locating fusion splices along the cable. To find the correct endpoint, a simple

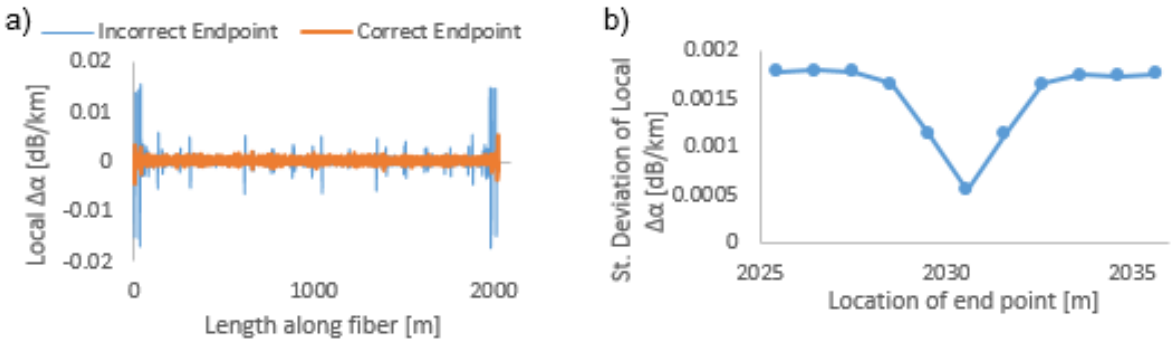

Figure 8a) Local DA for a correct and incorrect endpoint and b) a clear minimum in noise at the correct endpoint.

parametric study was performed, systematically varying the endpoint in both directions until the spikes and noise in the signal were muted. Figure 8b quantifies the noise from the parametric study and shows a clear minimum in signal noise at the correct endpoint.

3.2.6 Correction of Step Losses

Once potential splice locations were specified, further investigation was required to determine if the local spike were caused by sharp changes in temperature, splices, or other lost signal mechanisms such as pinches or fiber bends. Each spike was recorded and the location of the fiber was investigated in the raw Stokes and anti-Stokes signals. Since the anti-Stokes signal is more sensitive to temperature changes than the Stokes signal, a large signal anti-Stokes change in signal, and a muted Stokes change in signal suggests a change in temperature as the cause of the spike and was thus uncorrected. If the jump in signal had a similar magnitude in both Raman spectra signals, the spike was judged to be a loss in signal that required correction.

The magnitude of the signal loss has a spatial effect that varies in width depending on the splice quality and signal strength before the splice. The ratio R(z) is held constant across the splice width (creating a constant temperature), and the shift that was needed to match the temperature before and after the splice was applied to every temperature after the splice. This method and correction must be repeated for each splice on a cable, as well as in both the forward and reverse directions before the R(z) ratio can be used to create calibrated temperature profiles. This method was adapted from Hausner and Kobs (2016) where this method is described in detail.

3.2.7 Calibration Bath Over-determination

Although there are many methods for calibration (Selker et al. 2006, Hausner et al. 2011, van de Giesen et al. 2012) most calibration methodologies use the minimum necessary calibration baths to perform calibration and include one extra bath for validation and to report precision, accuracy, and repeatability (Tyler et al. 2009, Suárez et al 2011a, and Hausner et al. 2011). In the double-ended configuration, $\Delta\alpha$ is calculated independently of calibration baths, only two calibration baths are needed to solve for the remaining parameters: γ and C. Alternatively, if γ was to be taken as a physical constant and fixed prior to calibration, only one bath would be needed to find C. In this study, two baths in each loop provided over-determination of the system

of equations. Therefore, many combinations of baths were available and each would suffice for calibration but they may yield different accuracies. To investigate which bath combination would be optimally suited for this long-term deployment, a study was performed to compare accuracy between combinations. Least-squared regression was used in all cases to solve for calibration parameters. Root mean square error (RMS) residual of calibrated temperatures in all bath instances for one loop were compared over five months. Summary of the results are summarized in Table 1. Shaded values on the right side of Table 1 represents baths not used for calibration. Using only two calibration baths (sufficient but not overdetermined) yielded the worst calibration. This study also brought up the possibility of false accuracy. For example, in the fourth configuration, the two calibration baths in use both yielded RMS residuals less than 0.2 [°C]; however the validation baths that were not included in calibration had RMS residuals of 1.3 [°C] and 0.82 [°C], which is considerably higher. The instances of fiber in the hot baths also consistently performed worse that the ambient baths. The higher temperature gradients within the calibration bath lead to a higher possibility of thermal stratification and highlight the importance of uniform calibration baths. RMS residual was minimized using all four calibration baths, leading to the selection of maximum over-determination for the calibration of this study.

Table 1: Parametric study of calibration baths used and resulting RMS residuals of all baths.

	Baths Used				Error Analysis				
	Amb 1	Hot 1	Hot 2	Amb 2	1 RMSE	2 RMSE	3 RMSE	4 RMSE	Avg RMSE
1	x	x			0.138	0.149	1.265	0.759	0.578
2			x	x	0.814	1.241	0.093	0.065	0.553
3		x		x	0.810	0.277	1.253	0.236	0.644
4	x		x		0.169	1.305	0.191	0.818	0.621
5	x	x	x		0.130	0.631	0.643	0.794	0.550
6	x	x		x	0.419	0.271	1.275	0.372	0.584
7	x		x	x	0.419	1.283	0.139	0.407	0.562
8		x	x	x	0.821	0.589	0.640	0.192	0.560
9	x	x	x	x	0.403	0.624	0.623	0.397	**0.512**

3.3 Results

3.3.1 Instrument Calibration Parameters

Tabulating the calibration parameters over time and with changing bath temperatures provided useful insight into calibration best practices. Figure 9 illustrates some of these key insights from the calibration of loop TMW12 (Figure 6) from May to October 2016. Any pair of calibration baths provides data to determine parameters γ and C, and if either or both calibration temperatures change, γ and C should change accordingly to maintain the proper calibration. Past studies (Selker et al. 2006, Suárez et al. 2011a, Tyler et al. 2009) suggest bracketing recorded fiber temperatures with calibration bath temperatures so the calibration interpolates the measured temperature. Our results support this recommendation, as well as show the increased noise in the parameter γ when the temperature difference between the calibration bath is small (e.g., results before 6/24 on Figure 9a).

On 6/24, the submersed circulation pump was replaced with an aeration tube in the ambient calibration bath to allow the temperature to drop. During the relatively sharp temperature drop (9 [°C] in 48 h, 13 [°C] in 96 h), γ changed from 492.7 to 482.1 [K] while C changed from 1.33 to 1.30. The calibration parameters rapidly shifted and took 96 h to recover to a new equilibrium. As

previously discussed, there is no physical explanation for variability in γ, as it is comprised of a combination of physical constants, while C is meant to correct for changes in the calibration regime. However, the dynamic calibration allows γ to vary in response to changes in calibration bath temperature, which also caused an associated drop of approximately 1 [°C] in the calibrated temperatures along the fiber. Accordingly, after the initial calibrations are performed in which γ and C are both allowed to vary, the mean of γ over that time is found and fixed for a recalibration. Results of the calculation of C before and after fixing γ are shown in Figure 9b. C still responds to the ambient bath temperature changes on 6/24, although to a much smaller degree than it did with a variable γ calibration. C values with a fixed γ calibration also have appreciably less noise (i.e., standard deviation drops by an order of magnitude) than when γ is variable. The temperature shift seen in the calibrated temperatures when γ varies in smoothed out and not present with the fixed γ calibration.

To investigate the effect of fixing γ on temperatures and ensure that the calibration remains valid, an error analysis was performed. For the same fiber and period shown in Figure 9, the RMS residual between calibrated fiber temperatures of the calibration coils and externally measured calibration bath temperatures was calculated in each of the four calibration baths at each time step and averaged to report a single value. Once each RMS residual was found, Eq. 9 was used to calculate the differences in residuals between the fixed and variable γ calibration methods.

$$Residual\ Difference = \frac{RMS\ Residual_{var} - RMS\ Resisual_{fix}}{RMS\ Residual_{fix}} 100 \quad (9)$$

Table 2 documents the resulting differences in total accuracy by fixing γ or allowing it to vary. The residual difference went down slightly in two baths, and slightly increased in two compared with a fixed γ. When all four baths are combined, fixing γ caused the total RMS residual to increase by 0.31%. The slight increase was well worth the lowering in the noise of the input parameters

and the removal of a step change in temperatures coinciding with the change in ambient bath temperature.

Table 2: Difference in RMSE residual with fixed vs variable gamma, in both instances of the hot and ambient baths.

	Hot 1	Amb 1	Amb 2	Hot2
Forward	1.9%	-1.7%	-0.6%	-0.8%
Reverse	1.6%	-1.5%	1.4%	-1.8%
Combined	1.6%	-2.7%	1.7%	-3.1%
Bath Avg.	1.7%	-2.0%	0.8%	-1.9%

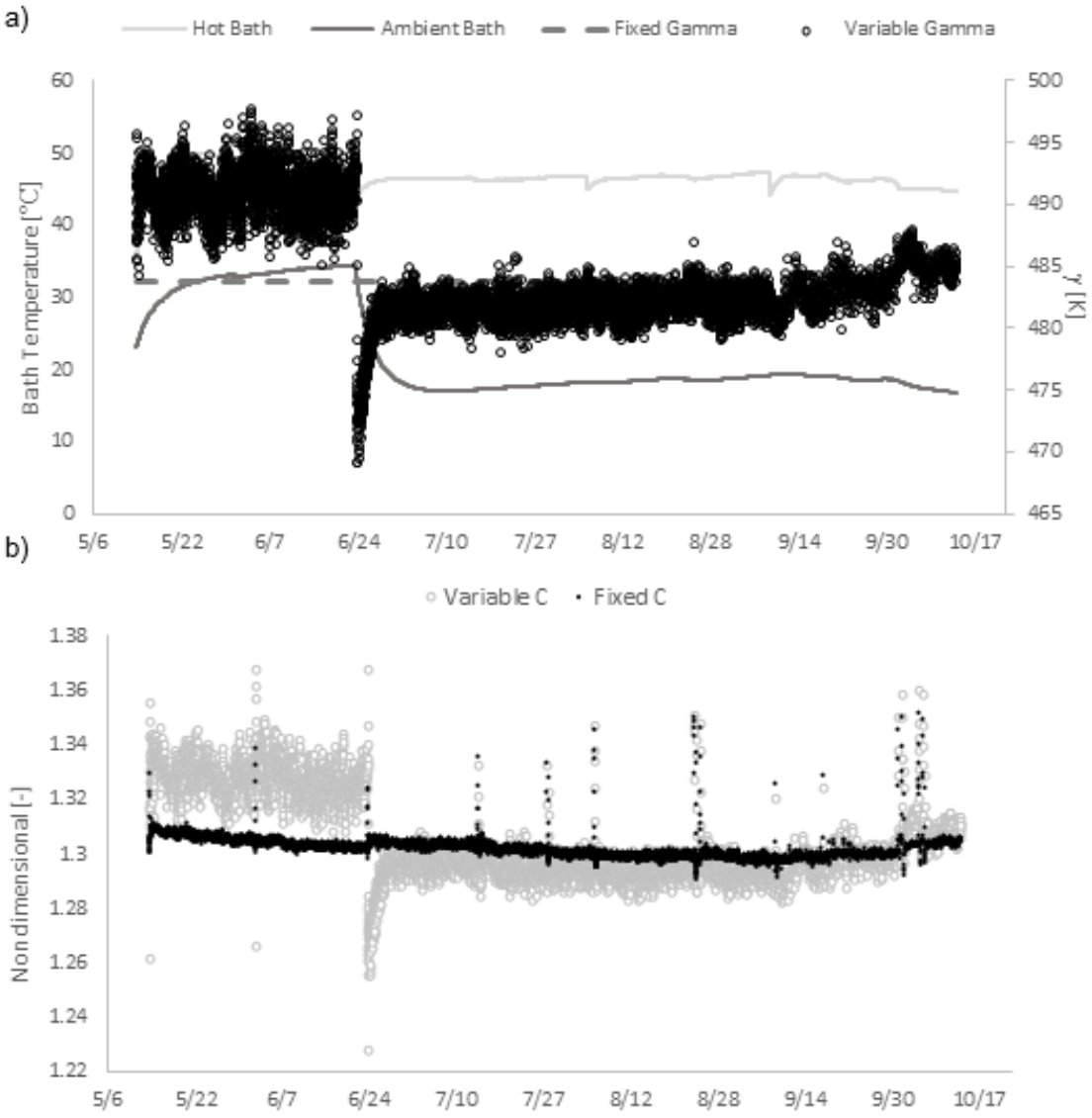

Figure 9a) Fixed and variable gamma with calibration bath temperature and b) C with fixed and variable gamma.

3.3.2 Differential Attenuation

Differential attenuations (Δα) were calculated and tabulated for four loops, each with seven sections. The first and last sections correspond to calibration coils and did not provide an accurate estimation of Δα due to their short lengths and sharp changes in temperature. The remaining fiber sections are labeled as follows: 2 – trenched to the first sentry well, 3 – grouted in the first sentry well, 4 – trenched between sentry wells, 5 – grouted in the second sentry well, 6 – trenched back to the interrogator vault. A fusion splice separates each of these sections, which also physically differentiates where fibers may have different optical properties and should be analyzed independently. Figure 10 supports the hypothesis that differential attenuation may exhibit appreciable variation within individual cable sections, either due to different manufacturing or environmental conditions (e.g., physical location). The lowest value for differential attenuation is from section 5 of loop TMW78 and has a value of $4.69 \cdot 10^{-05}$ dB/km. Conversely the largest differential attenuation value comes from section 3 of loop TMW34 and has a value of $6.30 \cdot 10^{-05}$ dB/km.

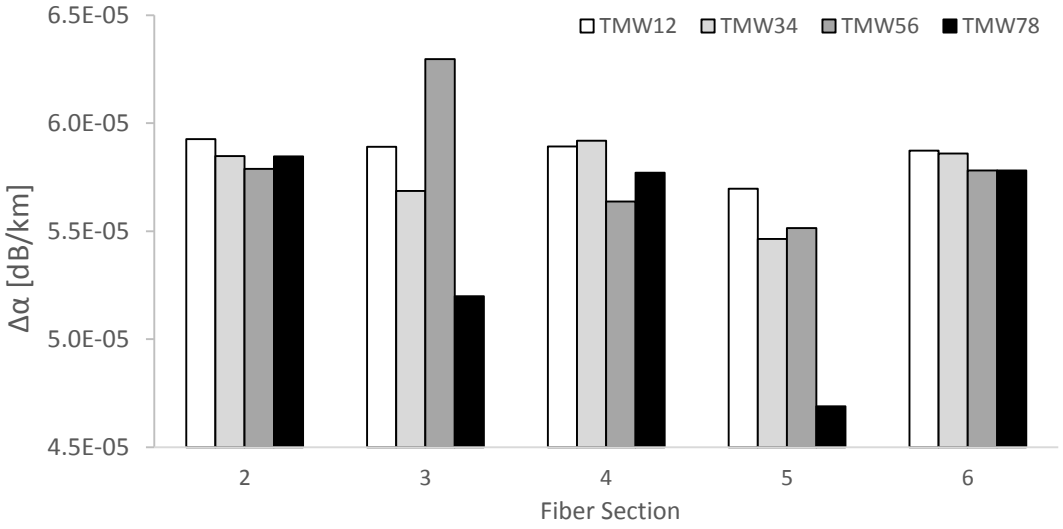

Figure 10: Differential attenuation long-term averages by fiber spliced together.

Another significant result is the difference in variability between sections buried in trenches (two, four, and six: less variable) and fibers grouted into sentry wells (three and five: more variable). Although the grouted fibers are protected by 6.35-mm-diamter HDPE piping, they are still subject to long-term light propagation that may change the glass properties of the fiber core over time. Figure 11 shows an example of a trend seen in several of the grouted fibers: differential attenuation cyclically varying in time. Although not seen in every fiber, this result supports dynamically calculation of differential attenuation. In this example, if Δα had been calculated at the beginning of data collection and fixed, $5.80 \cdot 10^{-05}$ dB/km would have been applied to the indefinite future when the true value became as low as $5.25 \cdot 10^{-05}$ dB/km. However, it can also be observed in Figure 11 that there is noise introduced into the signal by recalculating Δα dynamically, the magnitude of which varies across fiber and with integration time in a single fiber. From the beginning of data collection on 5/13 to 9/8, integration time is 240 s. From 9/8/ to 10/13, integration time increases to 300 s, and from 12/3 onward the integration time has remained constant at 600 s. Figure 12 shows the standard deviation of dynamically calculated differential attenuation of a single loop by integration time and individual section. While the standard deviation (noise) of the signal does slightly decrease with longer integration times, a significantly larger difference is due to the fiber itself. Interestingly, the grouted fibers (sections three and five) have the lowest (and near equal) noise, and the trenched fibers (sections two, four, and six) each have different and greater amounts of noise. Sections three and five belong to the same batch of fiber. Less is known of the origins of fiber sections two, four, and six as they

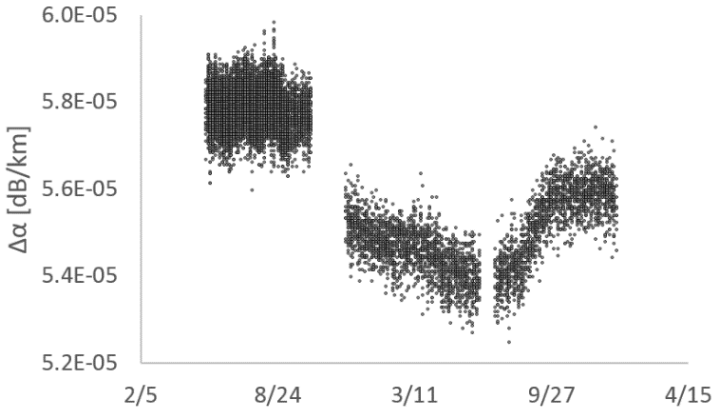

Figure 11: Differential attenuation of section 5 of loop TMW12 from 03/2015 to 03/2017; showing a cyclic pattern.

were purchased and installed by a contractor, which may explain why these fibers exhibit differential amounts of noise when Δα is dynamically calculated.

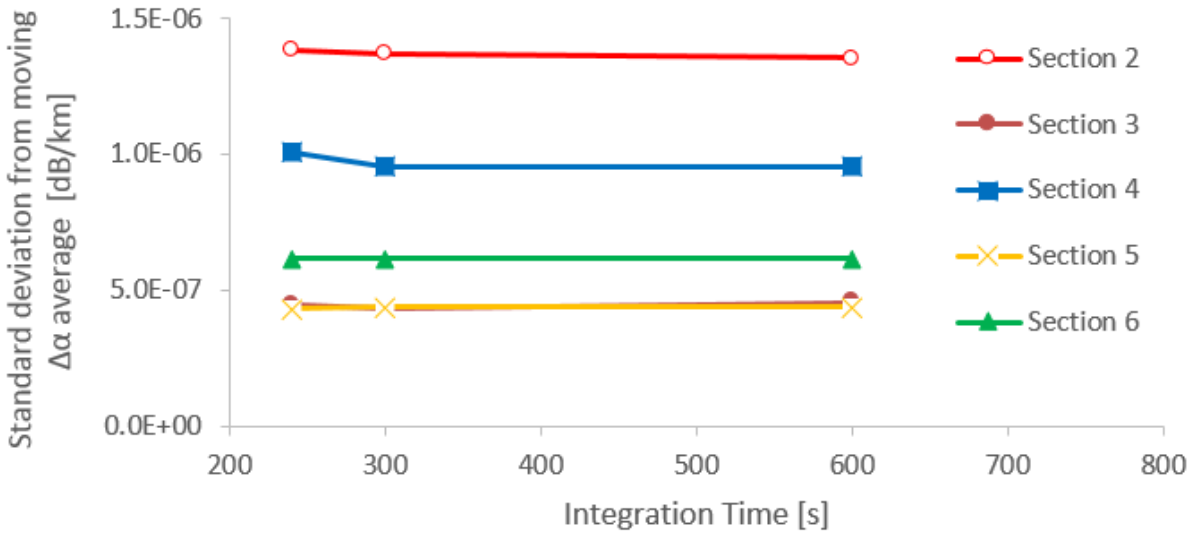

Figure 12: Loop TMW12 noise in differential attenuation by section and integration time.

3.3.3 Forward and Reverse Signals

In double-ended configurations, the Raman spectra data are collected in both the forward and reverse directions. In the default calibration of interrogators, data traces are combined with an automatic routine to output temperature profiles. However, in the case of manual calibration the user must decide how to combine the forward and reverse signals to achieve optimal calibration. One aspect of interest is the behavior of a splice, which can vary both in magnitude and splice width between the forward and the reverse directions. The mechanisms behind this difference are not well understood, however, it is possible to imagine light attenuation through an imperfect fusion splice differing with propagation direction.

To investigate how to best combine the forward and reverse data strings, data were first calibrated in the forward and reverse directions independently, and the temperatures were compared by forward alone, reverse alone, and arithmetic mean of forward and reverse directions. Table 3 summarizes the results of all four calibration baths in all four loops averaged

over the entire data collection period (May 2015 to January 2017 for TMW12 and from December 2015 to January 2017 for all others). For all loops, the combined RMS residuals of all four baths were worse than when only using the forward data. This may be a result of splice widths being found only in the forward direction and subsequently also applied to the reverse direction, leading to incorrect signal loss corrections. Interestingly, even though the reverse calibration was often less accurate than the forward calibration, the mean temperature from both provided the lowest RMS residuals in all loops but TMW12. The TMW12 loop has calibration coils of 10 m compared to the 30 m calibration coils in the other three loops. Because of this, data points from the fiber that were taken to be within the calibration bath may be closer to the boundary effects and may still be points slightly affected by the sampling resolution crossing a sharp temperature change. Baths in the forward direction go from the hot bath to the ambient bath before the borefield and from the ambient bath to the hot bath after the borefield. By definition the reverse traces have signals that pass through these baths in the reverse direction. If the data points in loop TMW12 calibration coils are still transitioning from temperatures before the bath, and these temperatures are different in the forward and reverse direction, the RMS residuals of that bath will be affected as is shown in the data.

Time averaged values of RMS residuals in baths do not tell the whole story, however. Forward, reverse, and combined calibrations all have time-varying values of RMS residuals, as seen in Figure 13. The trends here show that the forward RMS residuals become much lower in the summer, while the reverse RMS residuals becomes much higher in the summer, also raising the combined calibration RMS residual values. By dynamically calibrating and monitoring the forward, reverse, and combined calibrations, it may be possible to implement a calibration regime that switches between which trace is used to optimize accuracy year-round. Monitoring the accuracy of the forward, reverse, and combined calibration options also provides a continuous feedback for potential improvements in the calibration. The seasonal variation in RMS residuals

hints at how the calibration robustness may be affected by the ambient air or bath temperature and suggests the points chosen from calibration within the calibration coils could be improved.

Table 3: RMSE Residuals in all calibration baths using forward, reverse, or both calibrations.

	TMW12	TMW34	TMW56	TMW78
Hot 1				
Forward	0.50	0.40	0.72	0.49
Reverse	0.93	0.34	0.98	1.06
Combined	0.70	0.27	0.23	0.32
Ambient 1				
Forward	0.48	0.39	0.66	0.45
Reverse	0.95	0.34	0.93	1.04
Combined	0.70	0.23	0.17	0.32
Ambient 2				
Forward	0.42	0.42	0.70	0.47
Reverse	0.88	0.31	0.95	0.92
Combined	0.64	0.24	0.21	0.26
Hot 2				
Forward	0.54	0.39	0.68	0.46
Reverse	0.91	0.33	1.00	1.02
Combined	0.72	0.26	0.18	0.32

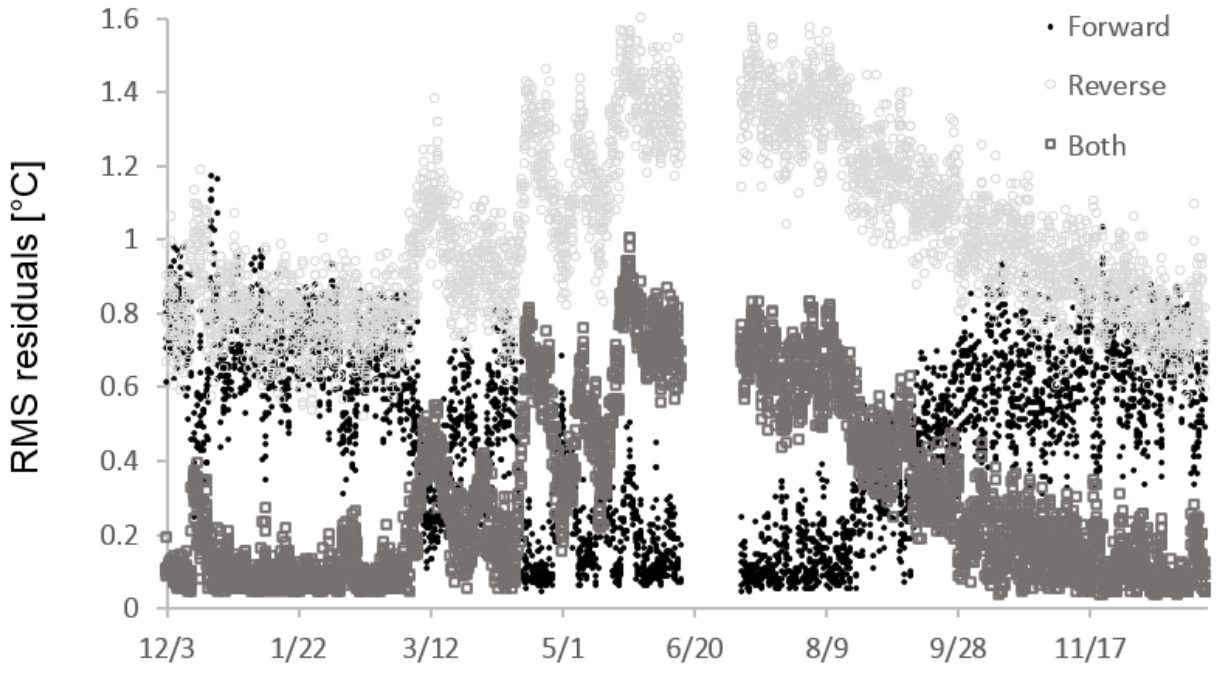

Figure 13: Forward, reverse, and combined RMSE values for TMW78 over 1 year.

3.4 Discussion

The instrumentation of a district-scale subsurface geothermal exchange field provided a challenging application for fiber optic distributed temperature sensing and provided a suitable field laboratory to investigate calibration considerations for a long-term, dynamic, centralized, and remotely accessible routine. Many of these considerations arose in response to project-specific challenges, but the insight gained from this work may be applicable to future installations that have similar goals and will therefore encounter comparable challenges.

The subsurface nature of the fiber optic network made it highly difficult for in-person physical verification of fiber lengths, and splice locations for this research. Although splice location and corrected in single-ended configurations is well documented (Hausner and Hobs 2016), this work presented a novel methodology to locate splices in a double-ended configuration using the forward and reverse signal and Eq. 8. Used in conjunction with double-end splice considerations (van de Giesen et al. 2012), this method may provide an additional option for increased confidence in splice handling when physical verification is not feasible. Similarly, several methodologies exist for correctly matching the forward and reverse light traces in a double-ended configuration (van de Giesen et al. 2012), however these methods often involve physically unplugging one end of a fiber. When this is not possible, the method described in this paper provides an additional line of evidence to find or support a known matching of the forward and reverse traces.

The effort to simplify the installation lead to one interrogator in a centralized location, with one each fiber-optic cable having a reference coil in a hot and an ambient bath before entered the borefield, as well as another reference coil in each upon returning from the borefield. By calculating $\Delta\alpha$ independently of the calibration baths, any combination of two, three, or all four calibration bath instances could be used to specify the remaining two calibration parameters, γ and C. Current practices suggest using two baths to calibrate, and using any remaining baths

instead to validate the calibration and provide an accuracy calculation. We researched this approach by systematically varying which calibration baths were used over the same time period with the same fiber and found that the choice of which baths are used for calibration and which are used for validation affect the accuracy of the results. In particular, the validation baths will have lower accuracy than the baths used for calibration, and the more reference sections that are used for the calibration, the greater the calibration accuracy becomes. In this study, the most over-determined solution of all four baths yielded the greatest accuracy; although that may not be true for every installation, it is worth posing the question for future installations if greater accuracy can be achieved by adding or removing reference sections from the solution of the calibration parameters.

Past work (van de Giesen et al. 2012) have fixed γ at an optimal value to better represent the physical truth that γ is a constant. Here, we have investigated the effect of this method and found that the RMS residual of the calibration baths both minimally increase and decrease, while the overall RMS residual slightly decreases by fixing γ. However, fixing γ also significantly decreases the variability and noise in the third calibration parameter, C, which is manifested in a calibration that is more resistant to changing temperatures in the calibration bath. A small decrease in accuracy for the ability to maintain calibration through the changing of calibration bath temperatures is a worthy trade off in long-term installations where keeping a true constant bath temperature is infeasible.

Differential attenuation is can be calculated at the sampling resolution of a double-ended data collection routine. It is often discussed that different fibers that are spliced together should be considered as having unique optical properties and Δα values (Selker et al. 2006, Hausner et al. 2011, van de Giesen et al. 2012). This work not only supports this hypothesis with highly variable Δα values between fiber sections, it also finds that Δα may change in time. Often γ is seen as the fixed parameter, C is seen as the parameter that may vary with time, and Δα values are seen to vary across distance but are fixed with time (van de Giesen et al. 2012). However, data in this

work suggests that Δα may systematically vary in time in magnitudes great enough to introduce significant error if Δα values are held constant over time. A primary benefit to holding Δα constant in time is the complete reduction in noise and by dynamically recalculating Δα, another source of signal noise is introduced to the calibration. This noise is of a smaller magnitude than the time-dependent variance in the signal, meaning there is still an overall increase in accuracy by dynamic Δα recalculation. After investigation, the noise introduced by this method is more dependent on the optical properties of the fiber and its environmental conditions than the routine's integration time.

Double-ended routines provide forward and reverse Raman spectra data that could both be used to create calibrated temperatures once the calibration parameters have been specified. It is up to the user to determine which trace (or combination of traces) may be best for a specific research site. Lessons from this work indicate the possibility of combining the traces to achieve a better accuracy than either trace can alone. Location and correction of splices and choice of appropriate reference coil data points in both the forward and reverse directions further dictate accuracy. Forward- or reverse-only data may be calibrated at a lower investment of time and resources, while still achieving meaningful temperature results for project-specific constraints.

A long-term, dynamic, centralized, and remotely accessible calibration routine does require many thoughtful considerations. With these considerations, accuracies greater than the default interrogator calibration are possible, with greater understanding and control of results.

Chapter 4: Long-term District-scale Geothermal Exchange Borefield Monitoring with Fiber Optic Distributed Temperature Sensing

Fiber optic distributed temperature sensing is used for long-term monitoring of a geothermal exchange borefield to quantify the role of groundwater flow and distributed thermophysical properties on subsurface heat transfer and storage. District-scale borefields subject to a sustained imbalance in heating and cooling loads have experienced yearly subsurface temperature increases that may, without corrective action, eventually lead to diminished borefield performance. Laboratory testing of bedrock thermophysical properties and on-site piezometric groundwater flow measurements of two aquifers are used to interpret distributed subsurface temperature patterns. Saturated rock in the phreatic zone heats and cools faster than dry rock. A laterally continuous layer of highly voided rock near the bottom of a dolomite formation repeatedly correlates with expedited cooling that highlights the importance of groundwater advection. The presence of clay mineral constituents in other sandstones and shaley formations lead to lower laboratory measurements of thermal diffusivity and lower hydraulic conductivities leading to poor local heat transfer rates. An optimal borefield design to counteract overheating would maximize contact with a saturated, voided or fractured, clay-constituent-free sedimentary bedrock. As the pilot study on a long-term FO-DTS monitoring of a district-scale borefield, this research provides a template for future work to advance and discover more borefield optimization techniques.

4.1 Introduction

From 2000 to 2010, world energy consumption increased by 23%, and energy consumption is projected to grow by 48% between 2012 and 2040 (EIA 2016). Meanwhile, burning of fossil fuel has been directly tied to the exponential increase in atmospheric CO_2 levels since the Industrial Revolution (Etheridge et al. 1996). Fossil fuels—such as coal, petroleum, and

natural gas—account for 78% of world energy use (EIA 2016). CO_2 concentrations are at a record high of 406 parts per million (Tans and Keeling 2017) and, at the current growth rate, the consumption of fossil fuels alone is projected to increase emissions by 34% by 2040 (EIA 2016). Extensive climate research has demonstrated the connection between increased GHG concentrations and global temperature rise, shifting snow and rainfall patterns, and extreme climate events, among other effects (EPA 2017). The superposition of these issues and concerns has created urgent global pressure to develop and integrate efficient renewable energy solutions such as space heating and cooling by geothermal exchange. The World Economic Forum (2012) indicates that annual spending of $700 billion on renewable power, low-carbon transport, and energy efficiency is needed to meet the United Nations goal to mitigate the effects of global warming.

Ground-source heat pump (GSHP) systems are low enthalpy systems used for space heating and cooling with elevated thermodynamic efficiencies and decreased emissions compared to conventional fossil fuel temperature control. Research has shown 38% CO_2 emissions savings compared to a domestic gas boiler in the UK (Jenkins et al. 2009), a 35–72% reduction (depending on regional fuel fix) in Germany (Blum et al. 2010), and a decrease of 33 to 50% globally (Fridleifsson et al. 2008). In the US, space heating and cooling accounts for 48% of residential energy use, 66% if water heating is included (EIA 2009). With the adoption of more properly designed and operated GSHP systems, overall demand for energy is reduced, while decreasing harmful emissions and spurring local economic development because these systems are designed, drilled, manufactured, and installed with domestic resources and talent.

GSHP systems in the US typically include ground heat exchangers (GHXs) that have a sealed loop made of high-density polyethylene (HDPE) piping that is buried in the ground and connected to a heat pump through which a carrier fluid is circulated. Common configurations of the GHX piping are trenched horizontal loops, spiral horizontal loops, vertical loops, and

submerged loops in a pond. In general, horizontal and submerged loops provide less capacity for a smaller initial investment, while vertical loops provide higher heat transfer capacity per unit of surface area (Wu et al. 2014) for a higher initial investment. Vertical GSHPs are typically installed in boreholes 23 m to 92 m in depth that are spaced 4.6 m to 6.1 m apart and that are sized for 17.4 to 52.2 meters of pipe per kW of energy transfer (Omer 2008). GHX borefields are typically sized to match 60 to 70% of the max building loads to limit overdesign (Tarnawski et al. 2009). For example, three GHXs may provide sufficient capacity for a single family residence (Bloom and Tinjum 2016); 18 were needed for a three-story, 1530 m^2, office building in Germany (Luo et al. 2015); and 81 were installed at a 30,600 m^2 campus research center in Madison, WI (Herrera 2016) to provide cooling for a server system. When loads are increased to the next order of magnitude, district-scale geothermal borefields are needed.

Currently, district-scale borefields supply the heating and cooling needs of many university and commercial campuses such as the 16,000-student West Chester University with 1,400 GHX (Helmke et al. 2016); 22,000-student Ball State University with 3,600 GHX (Siliski et al. 2016); and 10,000-employee Epic Systems with 6172 GHX, the subject of this work. District-scale systems bring about their own unique challenges and opportunities. Chief among these is the potential for borefields to overheat because of year-over-year cooling-dominated loads (Florea et al. 2017). As more energy is injected into the subsurface than is extracted, the ground temperature increases, and the efficiency and capacity of the borefield will be negatively impacted (Li et al. 2009). Because of the significant impact borefield temperature has on ground heat exchange and heat pump efficiencies, analytical and numerical models have been developed to characterize subsurface heat flow by including heterogeneous thermophysical properties of the rock (Walker et al. 2015), understanding the impact of hydrology (Diao et al. 2004, Samuelson et al. 2011, Florea et al. 2017), and modeling potential overheated borefield remediation strategies (Özdoğan-Dölçek et al. 2015). While this work has pushed forward understanding of key heat transfer

variables, the GSHP design manual published by the American Society of Heating, Refrigerating, and Air-Conditioning Engineers (ASHRAE) states that “a major missing component in current design method is long-term field-monitored data, which are needed to further validate the design method so that the effects of water movement and long-term heat storage are more fully addressed.” This work directly aims to fill that need with the implementation of fiber optic Distributed Temperature Sensing (DTS).

DTS is a technique that utilizes the interaction of laser light with the silica core of a fiber optic cable and time-domain reflectometry principles to calculate the temperature of the cable at discrete sections of the fiber. In recent years, the scientific community has taken advantage of improvements in DTS technology that have provided finer temporal, spatial, and temperature resolution. With the onset of these capabilities, environmental monitoring applications of DTS have rapidly expanded. Such applications include investigations into groundwater/surface water interactions (Lowry et al. 2007, Slater et al. 2010, Blume et al. 2013, Xiang et al. 2016), distributed subsurface hydraulic properties (Bahr et al. 2011, Read et al. 2013), soil moisture content (Steele-Dunne et al. 2010, Sayde et al. 2010, Striegl et al. 2012) lake thermal stratification (Suárez et al. 2011, Arnon et al. 2016, Lucas et al. 2016), illicit sewer connections (Schilperoort et al. 2009, Hoes et al. 2009), snow pact coverage (Tyler et al. 2008), boundary layer height (Thomas et al. 2011, Keller et al. 2011), and forest canopy coverage (Bense et al. 2016). Similar to the motivation behind this study, researchers have also used the advantages of DTS to encase fiber optics in grouted boreholes looking for temperature gradients (Cottingham et al. 2013), investigate *in situ* subsurface thermophysical properties (Henninges et al. 2005, Freifeld et al. 2008), and GHX performance (Fujii et al. 2009, Beier et al. 2012, Acuña et al. 2013).

4.2 Materials and Methods

Epic Systems is a healthcare software company in Verona, WI that has an expanding campus that houses approximately 10,000 employees in 19 office buildings. Overall, Epic's campus approaches energy neutrality via the use of a 10-MW-capacity wind farm, 1.5-MW-capacity in solar panels, and district-scale geothermal heating and cooling. Epic has four district-scale borefields with 6,172 u-pipe GHXs that provide 48.5 MW of cooling capacity and a cooling pond with 1,300 coiled loops that provide 4.2 MW of cooling for limited intervals. Borefield 4, the newest addition, provides the largest portion of the heating and cooling with 2,596 GHX that provide 25.6 MW of cooling capacity. At 360 m (north-south) by 280 m (east-west) by 152-m-deep, borefield 4 has approximately 15.4 million m^3 of rock to offer as a thermal battery. Borefield 4 has been instrumented with temperature monitoring wells (TMW) with fiber-optic loops down to the base of the borefield. Sentry wells (red circles in Figure 14) are instrumented with fiber loops grouted in direct contact with the ground. Sentry wells are drilled in the center of a square of 4 GHX, meaning each GHX would be 4.2 m away at a 45° angle. Piezometer wells (blue squares in Figure 14) are equipped with a piezometer screen in the shallow aquifer, a piezometer screened in the deep aquifer and a fiber optic loop installed to the base of the borefield. Both piezometers are equipped with a levelogger (Solinst) to measure the piezometric surface and water temperature over time.

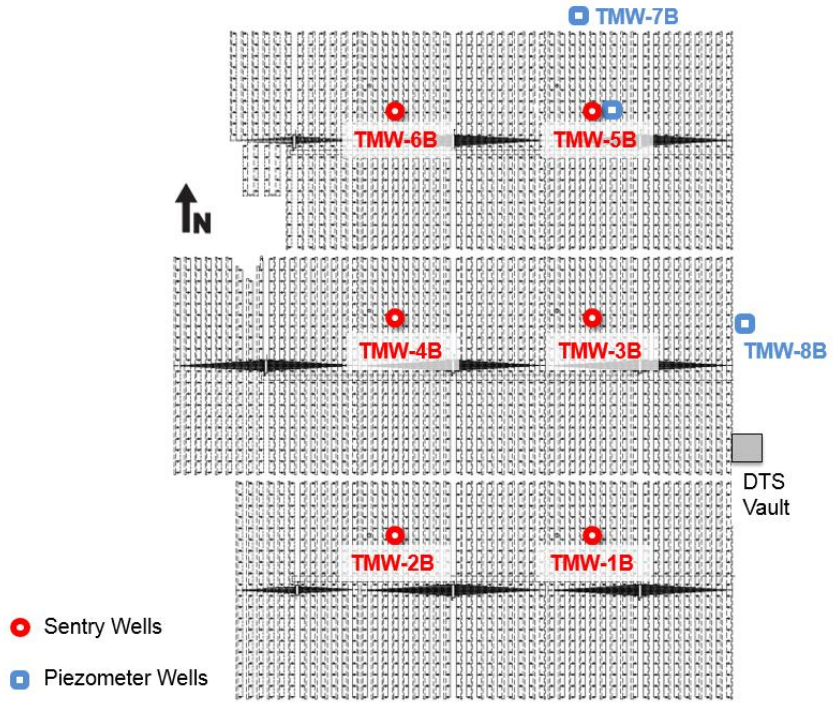

Figure 14: DTS wells installed to monitor borefield 4.

A Sensornet Sentinel DTS-LR interrogator with a 16-channel multiplexor was placed in a 10 x 10 x 5 m subsurface vault on the east side of the borefield that functions as an electrical control hub for geothermal operations. This interrogator can provide 0.01 °C temperature resolution, 1-m spatial resolution over each these loops (Sensornet). Fiber-optic cables were multi-mode 50/125 µm OM2 ClearCurve Plenum Orange, 2-mm outer diameter, with E2000 APC connectors. All fiber optics were protected by 6.35-mm HDPE piping to avoid differential stress or pinching in the fiber which would result in signal loss. Temperatures were calibrated by a dynamic, double-ended, centralized and remotely accessible manual routine (McDaniel et al. 2016). Accuracy of calibrated temperatures varied over time between 0.05 to 1.0 °C with a long-term average of 0.36 °C. The calibration methodology is fully described in McDaniel et al. (2017).

The operational heating and cooling loads of the borefields and pond have been tracked since January 2015. Borefield 4 activation was carried out in three phases. The 840 GHXs that make up phase 1 were activated in the southern third of the field on 10/25/14. 967 GHX in phase 2, and

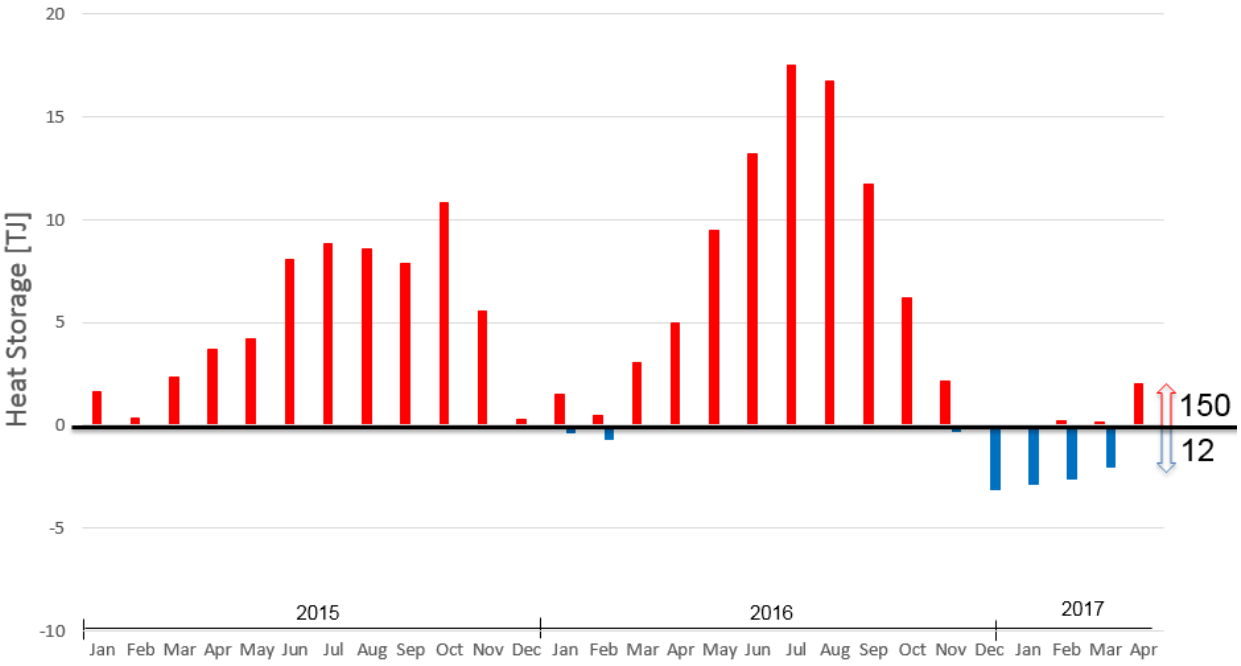

Figure 15: Borefield 4 operational heating and cooling.

789 GHX in phase 3, comprising the northern two thirds of the borefield, were activated on 9/23/15. Fiber-optic data monitoring the southern half of the field from TMW-1B and TMW-2B became operational 5/13/15, just under seven months after heat injection began. Phases 2 (TMW-3B and TMW-4B) and 3 (TMW-5B and TMW-6B) activated in mid-September, 2015, with their subsequent fiber-optic monitoring phases launching on December 3rd, 2015.

Operational decisions of how to split the heating and cooling demand between all four available borefields and the pond are informed by returning exchange water temperatures as well as field temperature data from thermistor strings in borefields 1-3 and the fiber data in borefield 4. In cooling mode, heat pumps run at higher efficiencies at lower entering water temperatures, so it is optimal to split up the load to accomplish the highest overall temperature drop over the fields before the water is returned to the buildings. However, optimal present performance must not be achieved at the cost of a greater decrease in future performance. When borefield 4 was first activated, it had the largest heat transfer capacity (53% of system capacity), and also had the lowest ground temperature of 10 to 11 °C. Since it could provide the greatest temperature drop, and highest efficiency for the heat pumps, most of the heat was directed towards borefield 4 during the 2015 cooling season. Because of cooling-dominated building loads at Epic, the heating season is limited to only the coldest month or two in the winter. In the temperate months of early spring, the pond is utilized as the primary energy sink to allow the borefields to recover before the next cooling season. However, even with this remediation-minded operational schedule, from January 2015 through April 2017, 150 TJ of energy had been injected into borefield 4, while only 12 TJ had been extracted (Figure 15). Over the same period, the campus-wide cooling load was 307 TJ and the heating load was 140 TJ. While the campus-wide loads were imbalanced, borefield 4 was bearing the largest portion of the imbalance. Monitoring the temperature of the borefield with fiber optics allows for informed operational decisions regarding the optimization of using

borefield 4 as the primary heat sink for this imbalance while maintaining the field temperature as long as possible to reserve heat sink capacity for the future and keep heat pump efficiencies high.

Beyond operational decision making, distributed temperature sensing with fiber optics can provide data resolution to correlate subsurface temperatures to specific geologic and hydro-geologic conditions and enhance understanding of the controlling variables in subsurface heat transfer. TMW-2B, TMW-5B, and TMW-8B were logged with gamma, electrical resistance, imaging, heat pulse, and calipers to document the lithology of borefield 4.

Borefield 4 is located approximately one kilometer west of the terminal moraine of the Green Bay Lobe of the Wisconsin glaciation between 26,000 and 10,000 years ago (Dott and Attig 2004). Just inside the Driftless Area of no glacial influence, the region is home to unique ecosystems, scenic views, and significant topographical relief. Borefield 4 itself is located beneath a hill 10 m higher in the southeast corner than in the northwest corner.

The bedrock history of south-central Wisconsin is predominately a recording of a series of carbonate, sandstone, and shale depositions in response to sea level regressions and transgressions from the Upper Cambrian to the Lower Ordovician 550 to 450 billion years ago (Figure 16, Clayton and Attig 1990). Beneath a 10-m layer of gravel and sand fill at the surface, the first bedrock encountered at borefield 4 is the Oneota Dolomite formation of the Prairie du Chien group. This formation is characterized by the presence of chertz nodules, oolites, and predominantly hard dolomite. The next 10 m are the clean quartzose sandstones of the Jordan formation, which abruptly contains no chert, oolites, or dolomite. Beneath the Jordan formation, is an unconformity, then the St. Lawrence formation. The interbedded siltstone and dolostone of the St. Lawrence formation produce the highest thermal conductivity of any layer at borefield 4. The next 35 m are characterized as the Tunnel City Formation by the clay and feldspathic cements that bind the sand particles. These cements conduct heat at slower rates than quartz and lower the overall thermal conductivity of the Tunnel City Formation. Underlying the Tunnel City is the Wonewoc sandstone. Similar to the Jordan Formation, the Wonewoc is composed primarily of clean quartz-rich sandstone. At the bottom of borefield 4, some GHXs interact with the Eau Claire formation, which is a dolomitic, fossiliferous and glauconitic shaley sandstone with the lowest thermal conductivity of any unit at borefield 4.

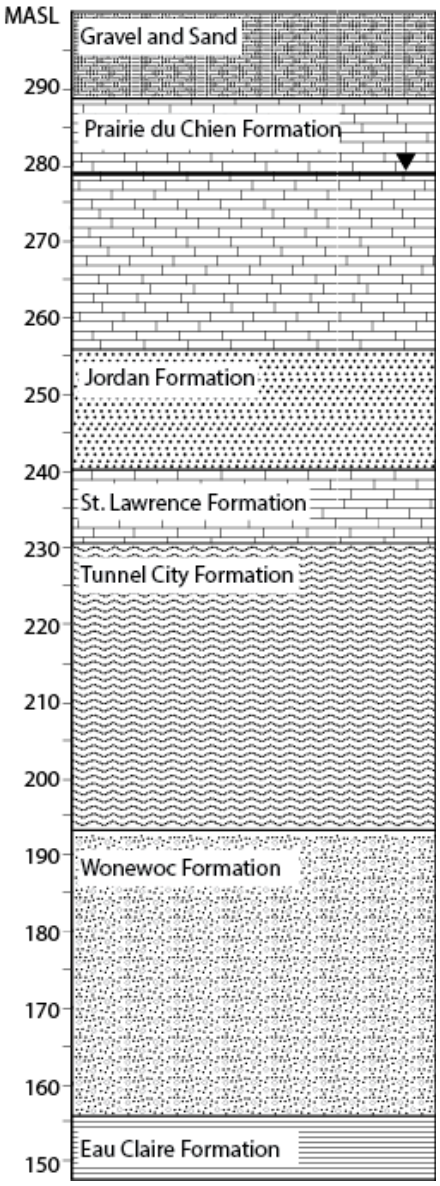

Figure 16: Borefield 4 geologic profile.

When discussing thermal conductivities, conduction through the mineral constituents of a rock is considered. The thermal conductivity of quartz is generally 4 to 7 W m^{-1} K^{-1}, and dolomite is 4 to 6 W m^{-1} K^{-1} (Clauser and Huenges 2013). The relative abundance of these minerals in a rock formation relative to cementitious material and pore fluid is the primary determinant of rock thermal conductivity. Water has a thermal conductivity of 0.6 to 0.7 W m^{-1} K^{-1}(Ramires et al. 1995), while the thermal conductivity of air is an order of magnitude smaller at approximately 0.024 to 0.026 W m^{-1} K^{-1} (Montgomery 1947). In general, less voids means a higher thermal conductivity, and presence of water in the voids rather than air will increase a rock's bulk thermal conductivity.

In modeling and designing GSHP fields, thermal conductivity is often given primary importance (Ground Loop Design 2016). However, the true parameter that describes how heat moves throughout a medium is a combination of thermal conductivity (λ), specific heat capacity (C_p), and density (ρ): thermal diffusivity, as defined:

$$\kappa = \frac{\lambda}{\rho\, C_p} \tag{10}$$

The presence of groundwater flow is also expected to affect the heat transfer capacity of rocks in the form of advective heat transfer. There are two separate aquifers beneath borefield 4; the shallow aquifer is composed of the rocks above the Tunnel City Formation, and the deep aquifer is composed of the units beneath the Tunnel City. In the shallow aquifer, the water flows south-westerly towards the nearby Sugar River. In the deep aquifer, water flow oscillates between also flowing south-westerly towards the Sugar River under equilibrium conditions and flowing south-easterly towards a nearby municipal well during pumping. The average deep aquifer flow direction between pumping and non-pumping conditions is southern.

Rocks with high hydraulic gradients and conductivities may transport more heat by advective flow. The Prairie du Chien formation has significant voids and fractures which promote

groundwater flow. Similarly, the Tunnel City formation is fractured near the middle, separating an upper and lower formation that have significantly less groundwater flow than the middle. The shaly Eau Claire formation is an aquitard that acts as a hydraulic barrier beneath the Wonewoc, and will likely not allow downward adjective heat flow. Table 4 contains a complete list of thermophysical and hydraulic properties of the rock units in borefield 4. Three null hypotheses come from these predictive properties that will be tested against the fiber-optic temperature data.

1) Saturated rock will conduct heat faster than dry rock.
2) Groundwater flow will create advective heat transfer.
3) Rocks with higher thermal diffusivities will heat and cool down faster.

Table 4: Thermal conductivity, specific heat capacity, density, thermal conductivity, porosity, horizontal and vertical hydraulic conductivity of formations found at borefield 4.

	λ [W m^{-1} K^{-1}]	C_p [J kg^{-1} K^{-1}]	ρ [kg m^{-3}]	κ [mm^2 s^{-1}]	n [%]	K_h [m day^{-1}]	K_v [m day^{-1}]
Gravel and Sand	1.5	800	1800	1.04	15	0.450	0.004
Prairie du Chien	4.14	832	2678	1.86	5	4.115	0.030
Jordan	3.30	821	2135	1.88	22	0.091	0.003
St. Lawrence	4.67	872	2678	2.00	5	18.288	0.003
Tunnel City	2.59	891	2446	1.19	13	0.305	0.500
Wonewoc	3.82	900	2650	1.60	10	1.740	0.300
Eau Claire	1.84	795	2477	0.93	5	0.005	0.001

4.3 Results

The following temperature data provides an unprecedented view of thermal stratigraphy in a heating district-scale borefield. This data was used in conjunction with independently verified thermophysical and hydrogeological conditions to test preexisting hypotheses and develop new ones from unexpected results. There are two gaps in the otherwise continuous data stream due to loss of interrogator power: 10/13/15 to 12/3/15 and 6/15/16 to 7/8/16.

TMW-1B data (Figure 18) strongly support the hypothesis that subsurface heat transfer is heterogeneous. The first 5 m of the gravel and sand fill are highly impacted by seasonal air temperature variation. Beneath this, the dry Prairie du Chien dolomite is slow to heat and cool until the water table, where there is a noticeable increase in the rate of heat transfer. Just beneath the water table at a depth of 30 m, temperature decreased 2 to 3 °C more than the surrounding rock during a neutral time of heat injection/extraction. This portion of the Prairie du Chien unit was reported by the drillers to have significant voids, which is both difficult for drilling and would be expected to locally increase ground water flow. The borehole imaging log (Figure 17) verifies the presence of a 0.4-m-diameter void at this depth and a void of similar diameter at 22 m bgs. Since the void above the water table is thermally insignificant and the void beneath the water table causes cooling, a strong case can be made for increased groundwater flow causing the extra cooling. Beneath the Prairie du Chien Formation, the Jordan, St. Lawrence and Tunnel City heat up relatively homogenously. The Wonewac, however, appears to heat up and cool down slightly more rapidly than the rest of the units. The Wonewac has an average to low thermal diffusivity compared to the other units, but does represent the beginning of a deep aquifer and the onset of advective heat transfer. The very bottom of the borefield shows a localized vertical temperature gradient, suggesting heat flow to the undisturbed (cooler) ground beneath the bulk volume of borefield 4.

Figure 17: 360 degree view of the 0.4 m void just below the water table at 30 m bgs.

The TMW-1B sentry well temperature response is delayed from the operational schedule of heat injection and extraction. This is an expected response as the sentry well is just over 4 m

away from the four nearest GHXs and a thermal wave will move very slowly from the near-field to far-field. In the 2015 cooling season, the sentry well temperatures increased from 11 °C to approximately 15 °C. During the following heating season, borefield 4 was used sparingly, as energy was purposely drawn from the other three borefields as a remediation strategy to cool their bulk ground temperatures. In this 3-month period of limited use, ground temperatures decreased by no more than 2 °C, before again heating up to 15 °C during the 2016 cooling season. During the subsequent heating season of December 2016 through March 2017, a net 10.7 TJ was extracted from borefield 4, which was enough to cool the field back to approximately 14 °C.

TMW-2B (Figure 19) provides a second observation into a similar subsurface environment. On the west side of the field, the ground surface is at an elevation approximately 10 m lower than TMW-1B. As a result, TMW-2B does extend into the Eau Claire shale at the base of the borefield. The 8 m of shaley lithology was expected to create a thermal barrier at the base of the borefield. TMW-2B data supports this by displaying a slightly decreased vertical gradient at the base of TMW-2B. The Tunnel City Formation stands out as showing relatively low rates of heat transfer. The presence of feldspathic and clay-rich cementitious materials create lower rock thermal diffusivity. These same interstitial materials lower hydraulic conductivities and the potential for advective heat flow. Interestingly, the borehole imaging log displays voids beneath the water table at 29 and 34 m bgs that do not appear to be thermally significant. One possible explanation is a lack of interconnectedness of these voids that would limit ground water flow.

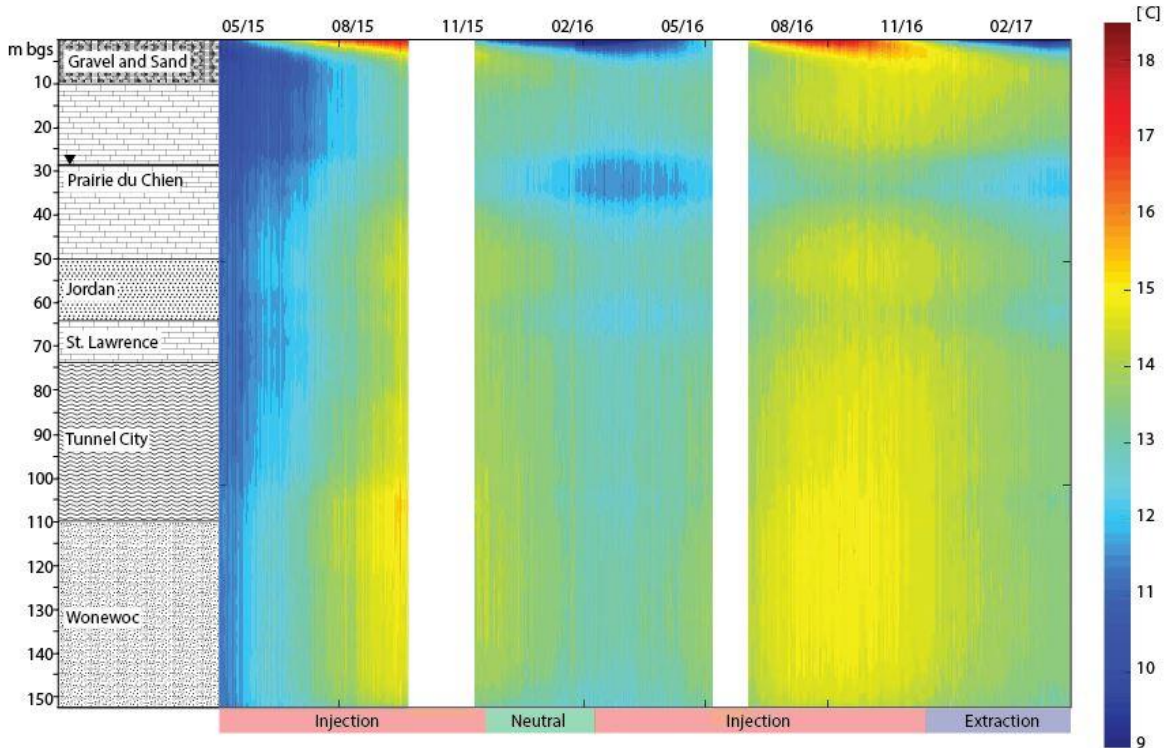

Figure 18: TWW-1B temperature monitoring.

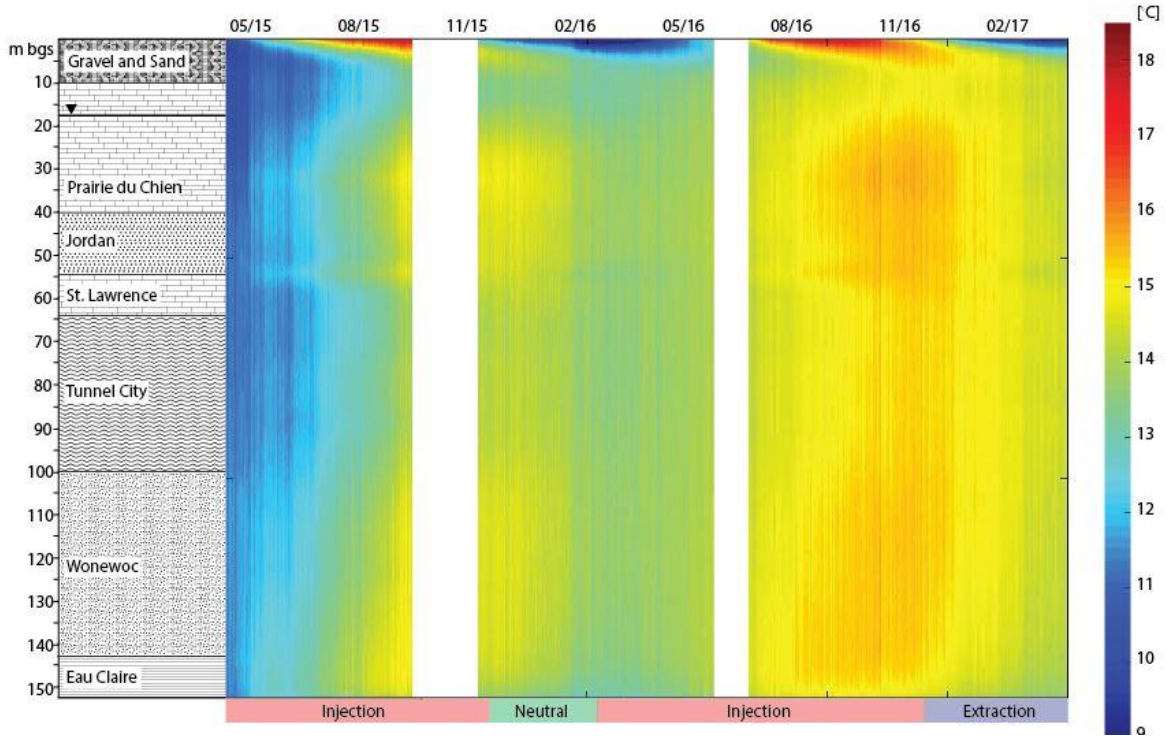

Figure 19: TMW-2B temperature monitoring.

TMW-3B (Figure 20) and TMW-4B (Figure 21) begin data collection during an intermittent period of heating and cooling, 2.5 months after phase 2 and 3 activation, which is why temperatures are already elevated. The heating of dry Prairie du Chien dolomite above the water table lags behind in both temperature monitoring wells, which provides additional evidence for lower diffusivity in dry rock. Season surface effects are again visible and punctuated by a sharp decrease in temperature in October 2016, which correlates with the onset of snowfall. The voided window at the lower half of the Prairie du Chien appears to create faster cooling in the 2016/2017 heating season, more so observable in TMW-3B than TMW-4B. TMW-4B again displays the relatively low heat movement in the Tunnel City formation, while TMW-3B displays a more homogenous heat flow in all units beneath the Prairie du Chien formation.

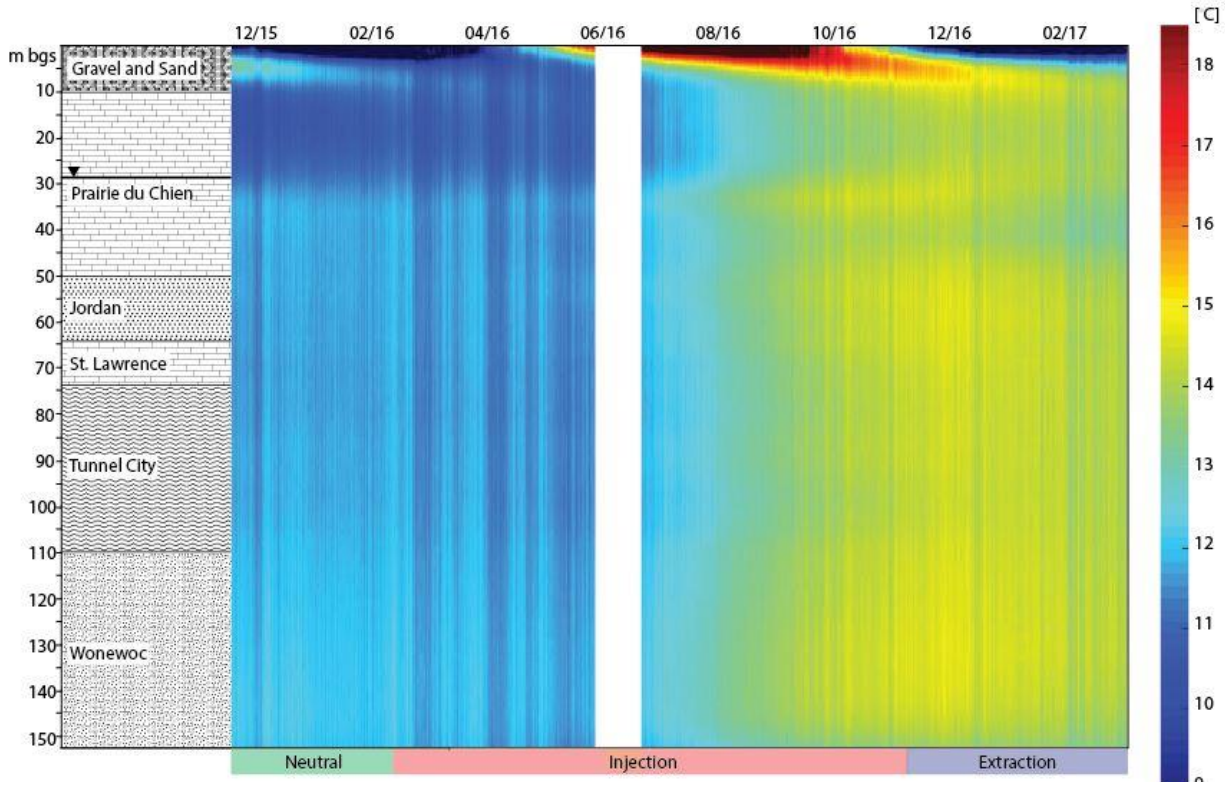

Figure 20: TMW-3B temperature monitoring.

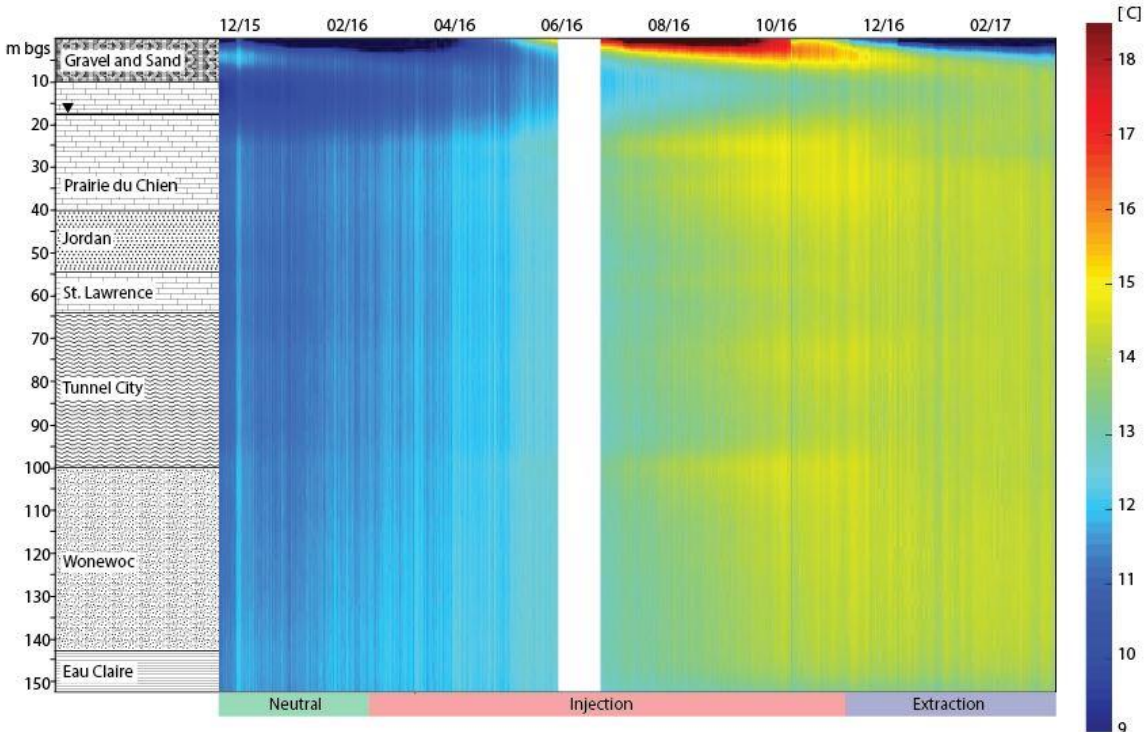

Figure 21: TMW-4B temperature monitoring.

TMW-5B (Figure 23) and TMW-6B (Figure 22) display the temperature development for phase 3—the northern third of borefield 4. The same season surface effects and low heating above the water table are again seen. TMW-5B clearly displays the cooling effects of the voids near the base of the Prairie du Chien dolomite while TMW-6B does not make a compelling case for cooling due to groundwater flow through voids at the expected depth. TMW-6B is drilled 20 m shorter to match the depths of the GHX in the northwest corner of the field. These boreholes were drilled shorter to avoid the weak rock at the base of the Wonewoc sandstone that was causing borehole collapse and slow and expensive drilling. TMW-5B displays approximately homogenous heating beneath the voids of the Prairie du Chien formation. TMW-6B, however, shows the most local variation in heat flow in the entire field. Four distinct (depth) windows of preferential heat flow exist: the base of the Prairie du Chien (30 m bgs), the interface between the Jordan and St. Lawrence (48 m bgs), at the top of the Tunnel City (65 m bgs), and in the middle of the Wonewoc (115 m bgs). While some of these localized heat flows support previous trends (e.g., heating in

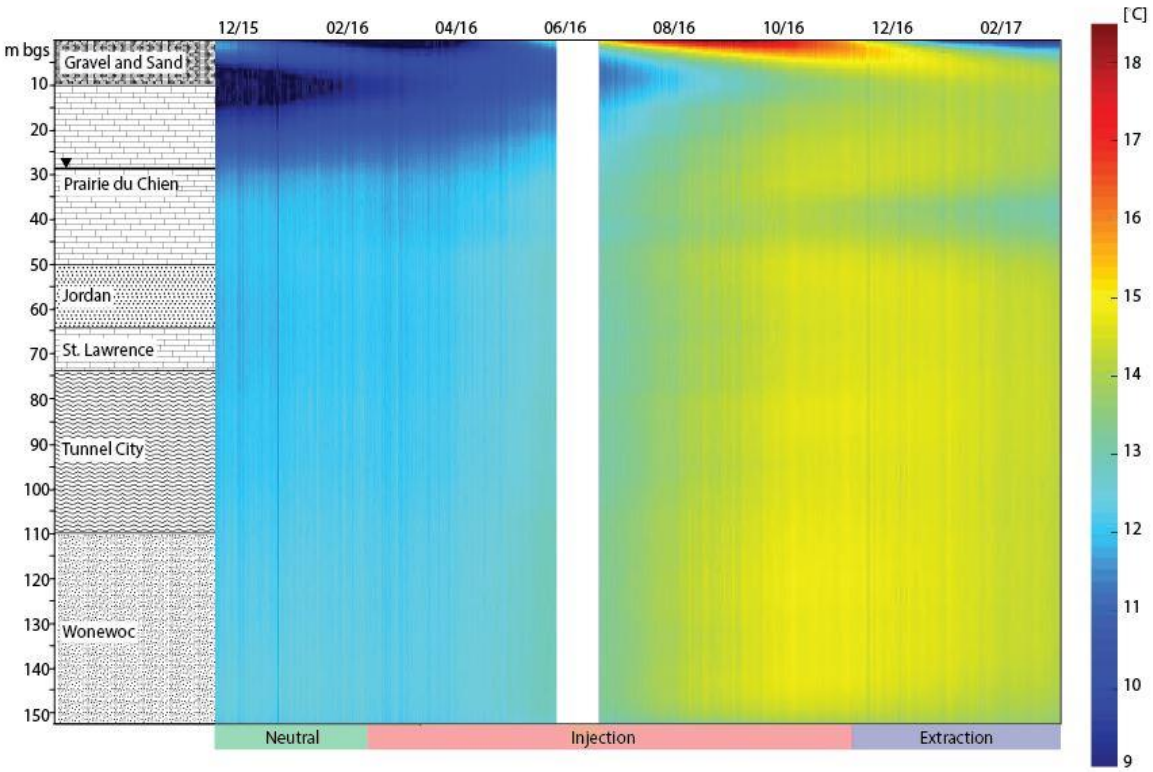

Figure 23: TMW-5B temperature monitoring.

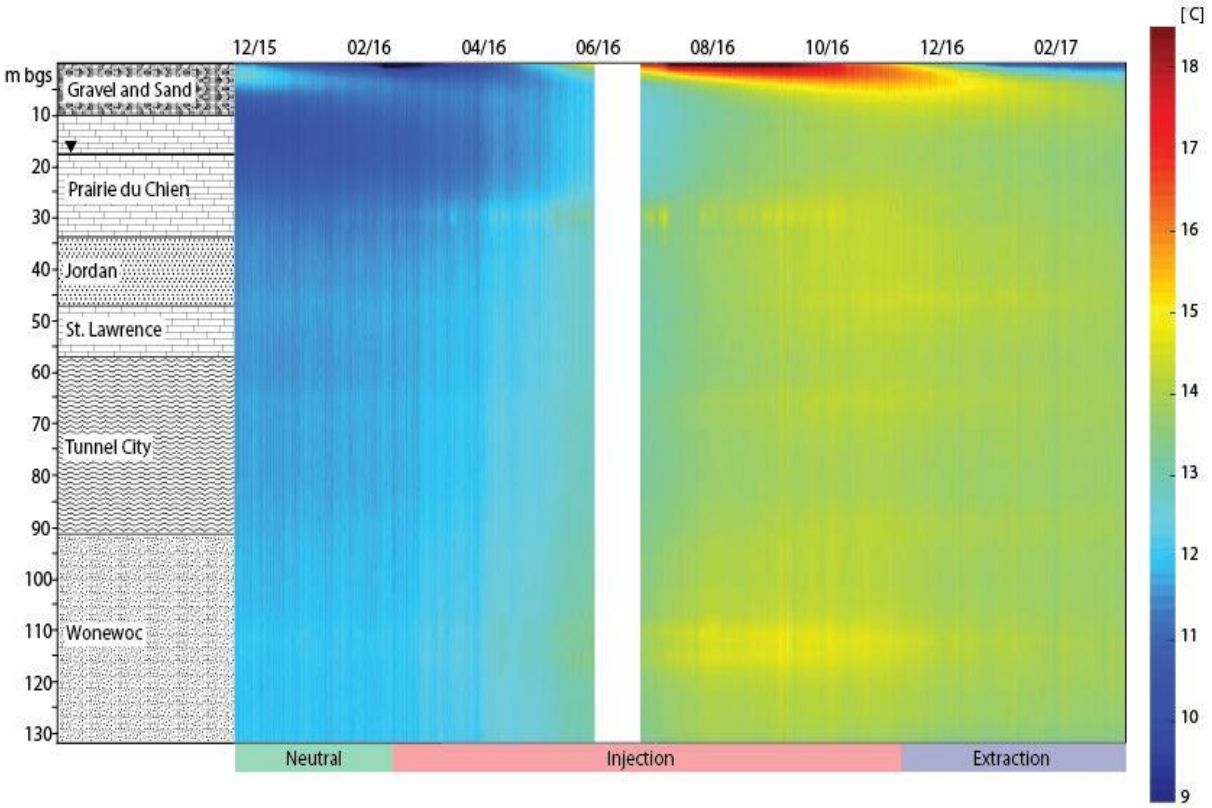

Figure 22: TMW-6B temperature monitoring.

quartz-rich Wonewoc), some are in stark contrast to what was previously seen (e.g., heating at

the voided region in the Prairie du Chien). This provides insight that thermal stratigraphy may not abide by conventional geological principles of lateral continuity.

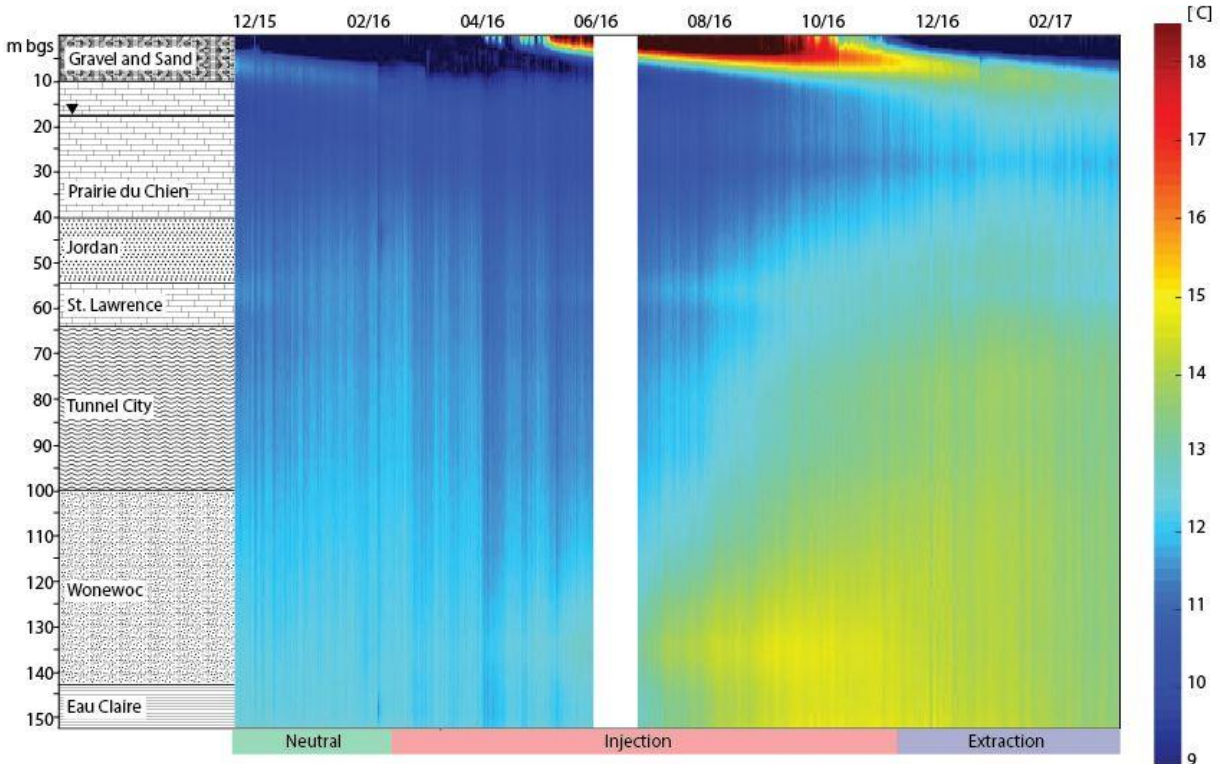

Figure 24: TMW-7B temperature monitoring.

TMW-7B (Figure 24) and TMW-8B (Figure 25) are the only two sentry wells that are outside the bulk volume of borefield 4. They are each paired with two piezometers and are meant to describe the interaction between groundwater flow and borefield heating. TMW-7B is located just north of borefield 4 by 2 to 3 m. Recall that the shallow aquifer flows southwest toward the Sugar River, and the deep aquifer oscillates flow between southeast during pumping and southwest during equilibrium conditions. In all of those conditions, groundwater will flow past TMW-7B and then to the borefield. As a result, TMW-7B provides a suitable field condition for direct comparison of heat flow from conduction and groundwater advection. In the shallow aquifer, temperature data suggests groundwater flow has moved heat south and reduced the heating due to conduction to < 1 °C over the entire monitoring period. In the deep aquifer, where groundwater

flow is oscillating and may have less overall movement, the effects of conduction are more apparent as the Wonewoc formation has heated by 1 to 2 °C more than the shallow aquifer.

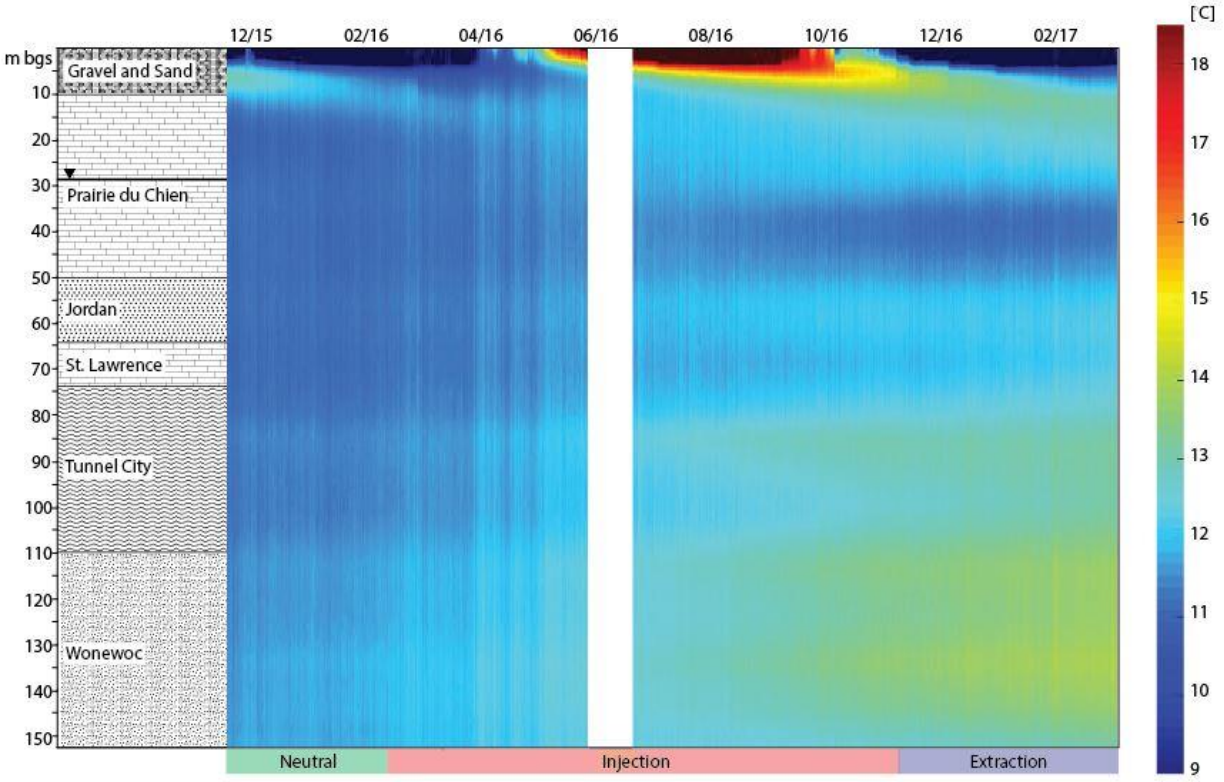

Figure 25: TMW-8B temperature monitoring.

TMW-8B, which is 3 to 4 m east of borefield 4, shows the least overall heating of any TMW. The deep aquifer and the Wonewoc does show the most heating. While municipal pumping is occurring, groundwater flow will be flowing southeast and groundwater from the field may be advecting heat away from the field and towards TMW-8B. The cooling effects of groundwater through the voids at the base of the Prairie du Chien are again evident here. The relatively small impact the borefield has had during 1.5 years of operation on a well less than 5 m away provides significant evidence that groundwater temperature and quality will not be significantly influenced beyond the boundaries of the borefield.

4.4 Discussion and Conclusions

The results of this research begin to answer the ASHRAE design manual (ASHRAE 2011) call for long-term field-monitored data to further validate the district-scale borefield design method so that the effects of water movement and long-term heat storage are more fully addressed. The methodology presented here to design such a monitoring system provide proof of concept and lay the foundation for future adaptations, each with their own set of unique challenges and considerations. Each new case study will continue to increase understanding of subsurface heat transfer mechanisms by monitoring district-scale borefields in new lithologic, hydrologic, and thermophysical settings. Site-specific results from Epic's large-scale borefield 4 provide novel thermal stratification insight in sedimentary bedrock in the presence of groundwater flow.

The temperature data from all eight TMWs supported the hypothesis that saturated rock will transfer heat more effectively than dry rock on the district-scale. This hypothesis was based on the thermal conductivity of water (Ramires et al. 1995) being an order of magnitude higher than the thermal conductivity of air (Montgomery 1947), and laboratory measurements of saturated rock yielding higher bulk thermal conductivities than dry rock (Meyer 2013 and Parsen et al. 2016). The shallow water table was monitored for the duration of this study and found to vary by 2 to 3 m. In all eight TMWs, dry rock above the water table heated up more slowly than the same rock saturated beneath the water table. For this reason, an optimal borefield design will minimize GHX length in the vadose zone and maximize GHX length in the phreatic zone. An optimal borefield would also avoid the possibility of local water table cones of depression from pumping that would create more dry rock and lower the borefield heat transfer capacity.

Groundwater flow was observed as an important mechanism for heat transfer within a borefield. Voids in the Prairie du Chien Dolomite consistently showed expedited cooling during neutral or heat extraction loading. Voids and fractures in sedimentary rock are known to provide

localized groundwater flow that is orders of magnitude greater than the same lithology without voids or fractures. In a district-scale borefield with the potential to overheat, highly fractured sedimentary units could provide a channel for heat removal from the field. The TMWs outside of the borefield provided insight that groundwater advection and conduction both drive heat transfer, and one can dominate the other based on relative magnitudes. Whether the heat transfer is desired or not, this experimental data shows that advective heat transfer from groundwater flow can be a non-negligible variable that should not be ignored in models or design software.

Thermophysical properties calculated from laboratory testing were expected to control heterogeneous heat flow at the borefield scale. Observations were made that the Tunnel City Formation and Eau Claire Shale had lower thermal diffusivity values and were also slower to increase temperature with energy injection. However, these units both had lower hydraulic conductivities and were the two aquitards present in the stratigraphic profile, so it is difficult to correlate lower temperatures specifically to less advective heat transfer from groundwater flow, lower thermal diffusivity, or a combination of both variables. Borefield 4 provided thermal diffusivity values that did not vary much more than a factor of two at the most extreme. Hydraulic conductivities, varied by up to five orders of magnitude (common in sedimentary rock). While thermal diffusivity may affect near-field heat flow, groundwater advection has displayed heat transfer capacity to remove energy from the bulk borefield volume, and decrease the far-field temperature. For this reason, ground water advection may be the more important design parameter than differential thermal diffusivity when designing against overheating within district-scale borefields.

Chapter 5: Distributed Thermal Response Test to Analyze Thermal Properties in Heterogeneous Lithology

A fiber optic distributed thermal response test (DTRT) conducted in well-documented heterogeneous geology is combined with laboratory thermophysical measurements of cores and novel data analysis techniques to provide a holistic picture of subsurface heat transfer including absolute magnitudes of distributed thermal conductivity (useful for modeling) and subsurface trends of heat transfer (useful for designing GHX borefields). In conventional TRT analyses, the subsurface environment is homogenized, which poorly reflects the reality of complex and heterogeneous lithology. Using analogies to well-developed hydrogeological tests and a novel error minimization technique, the effective borehole thermal conductivity of 2.0 W m^{-1} K^{-1} is well constrained and used a basis for distributed thermal conductivity calculation from *in situ* distributed temperature sensing that are verified against laboratory testing of core samples that have a weighted borehole average of 2.05 W m^{-1} K^{-1}. High thermal conductivities (≈ 3.0 W m^{-1} K^{-1}) are observed in the shallow Tiskilwa and Pearl Formations, while deeper units characterized by mudstone and coal seams display much lower thermal conductivities (≈ 1.5 W m^{-1} K^{-1}). Thermal decay data after the test has completed shows coal seams diffuse heat more slowly than the surrounding units. By observing the true variable nature of subsurface heat flow, it may be possible to optimize the design of future geothermal installations. District-scale borefields that commonly contend with overheating and desire high subsurface heat transfer rates may find additional value from knowledge of which geologic units to include (e.g., Quartz-rich Pearl Formation) or which to avoid (e.g., coal seams).

5.1 Introduction

Worldwide, the installed energy capacity of Ground-source heat pumps (GSHPs) has increased from 85 PJ in 2005 to 325 PJ in 2015 (Lund and Boyd 2015), which is equivalent to ten

1000-MW nuclear power plants. Further gains can be made by optimizing the design and layout of new geothermal borefields, which is the most expensive and variable capital component of a GSHP system. These systems must be carefully designed to provide capacity for design heating and cooling loads while minimizing the capital cost of installation. However, lifetime heating and cooling operating performance has proven difficult to predict and systems have deviated from expected design performance, leading to poor environmental and economic outcomes (Magraner et al. 2010, Knudson 2013). Economic viability and payback periods are highly sensitive to energy extraction and rejection rates that deviate from design values (Garber et al. 2013). Due to the importance of accurate load prediction and appropriate system sizing, many predictive models have been developed and used to size GSHP systems (Nagano et al. 2006, Sayyaadi et al. 2009, Puttagunta et al. 2010). These models are predominately based in well-developed thermoeconomic optimization principals (Bejan et al. 1996) that focus on maximizing the mechanical component heat transfer performance while minimizing capital, operational, and fuel costs. Long-term trends in subsurface heat exchange are traditionally secondary, if considered at all. However, treating the earth as an infinite heat source or sink at a constant temperature has proven to be an oversimplification, especially in district-scale systems.

Thermal Response Tests (TRT) are used to quantify *in situ* ground heat exchanger (GHX) thermal performance. A conventional TRT quantifies heat transfer in a pilot GHX by supplying a known heating load and measuring the exchanger flow rate and ΔT from the GHX inlet to outlet. *In situ* heat exchange capacity and effective borehole thermal conductivity are then used to supplement and refine model inputs for design. Typical analysis (Puttagunta et al. 2010, Luo et al. 2015) of these results relies on a line-source heat model (Zeng et al. 2002) that assumes that boreholes are infinitely long, heat flows only axially away from the borehole, lithology is homogeneous, and advective heat transfer by groundwater is neglected. Heterogeneous geology, varying thermophysical properties, and ground water flow are realities that will affect the

performance of the vast majority of GSHP installations in ways that are difficult to quantify with assumptions of homogenous conditions. Distributed quantification of subsurface thermophysical properties can be accomplished by coring and laboratory testing (Meyer 2013), and input into distributed analytical solutions to decrease uncertainty in GSHP performance (Walker et al. 2015). Numerical modeling can incorporate these distributed properties and groundwater flow to predict true three-dimensional heat flow (Özdoğan-Dölçek 2015). To complement these methods, *in situ* distributed temperature data is needed to validate model results and refine future analytical and numerical methods.

Fiber optic distributed temperature sensing (DTS) has been used to measure distributed thermophysical properties during a TRT (Fujii et al. 2009, Beier et al. 2012, Acuña and Palm 2013). DTS is a technique that uses the interaction of laser light with the silica core of a fiber optic cable and time-domain reflectometry principles to calculate the temperature of the cable at discrete sections of the fiber. In recent years, the scientific community has taken advantage of improvements in DTS technology that have provided finer temporal, spatial, and temperature resolutions in environmental and infrastructure applications (Selker et al. 2006).

A distributed thermal response test (DTRT, Acuña 2013) uses a fiber optic temperature probe within a GHX during a TRT to observe differential subsurface heat transfer. Freifeld et al. (2008), pioneered this concept by using a resistance heater in a borehole to create a thermal perturbation and monitor the subsequent temperature decay with DTS. Inverted temperature data and a radial heat flow model were used to create a profile of thermal conductivities with depth. Fujii et al. (2009) enhanced the DTRT with fiber optics in both the supply and return side of the GHX, during heat injection and decay in a mostly homogenous volcanic bedrock. Even so, the DTRT found thermal conductivity varied with depth. The DTRT was expanded even further by placing fiber within both a coaxial and standard u-tube GHX configuration (Acuña and Palm 2013) to study the effects of pipe configuration on heat transfer. Recently, a DTRT was performed on

a GHX within an overheated geothermal field as a diagnostic tool to analyze differential heat decay with depth (Herrera 2016).

This work combines a conventional TRT and a DTRT in a borehole surrounded by well-documented heterogeneous lithology to study the extent to which a DTRT can provide *in situ* distributed thermal properties. A novel approach is used for DTRT data analysis that extrapolates hydrogeological pumping test concepts (Raymond et al. 2011), and statistically minimized model error to achieve an effective borehole thermal conductivity, λ_{ss}, of 2.0 W m^{-1} K^{-1}. This effective conductivity is used as the basis of a distributed subsurface analysis based on an analogy to the Molz et al. (1989) impeller meter pumping test for distributed hydraulic conductivity.

5.2 Materials and Methods

5.2.1 Site Geology

The DTRT was conducted in a borehole completed at the University of Illinois at Urbana-Champaign (UIUC) Energy Farm. The geologic record at the site shows multiple cycles of deposition and erosion occurring over the past 300 million years. Glacial and proglacial deposits of at least two glacial cycles (the Middle to Late Pleistocene glaciations; Curry et al. 2011) overlie an irregular bedrock surface where Pennsylvanian-age mixed marine and terrestrial coal-bearing sedimentary strata (i.e., cyclothems) outcrop within the Illinois basin (Rosenau et al. 2013). An approximately 60-m-thick sequence of unconsolidated glacial and postglacial sediments, including glacial till, outwash, and lake sediment overlies an upland adjacent to the Mahomet Bedrock Valley (Figure 1Figure 26); (Ismail and Stumpf 2014). Within this sequence, the

lowermost horizons of a truncated interglacial soil marks the boundary between the two glacial cycles. The upper 3 m of the sequence contains fine-grained windblown material (loess) capping reworked sand, silt and gravel (alluvium), and glacial outwash along a postglacial river draining a recessional moraine situated just north of the site. An erosional unconformity separates the glacial sequence from the limestone bench or platform (Shelburn Formation, Rosenau et al. 2013). The heterogeneous geology encountered at the site provides an excellent field laboratory to assess a DTRT's ability to differentiate varying thermophysical properties with depth.

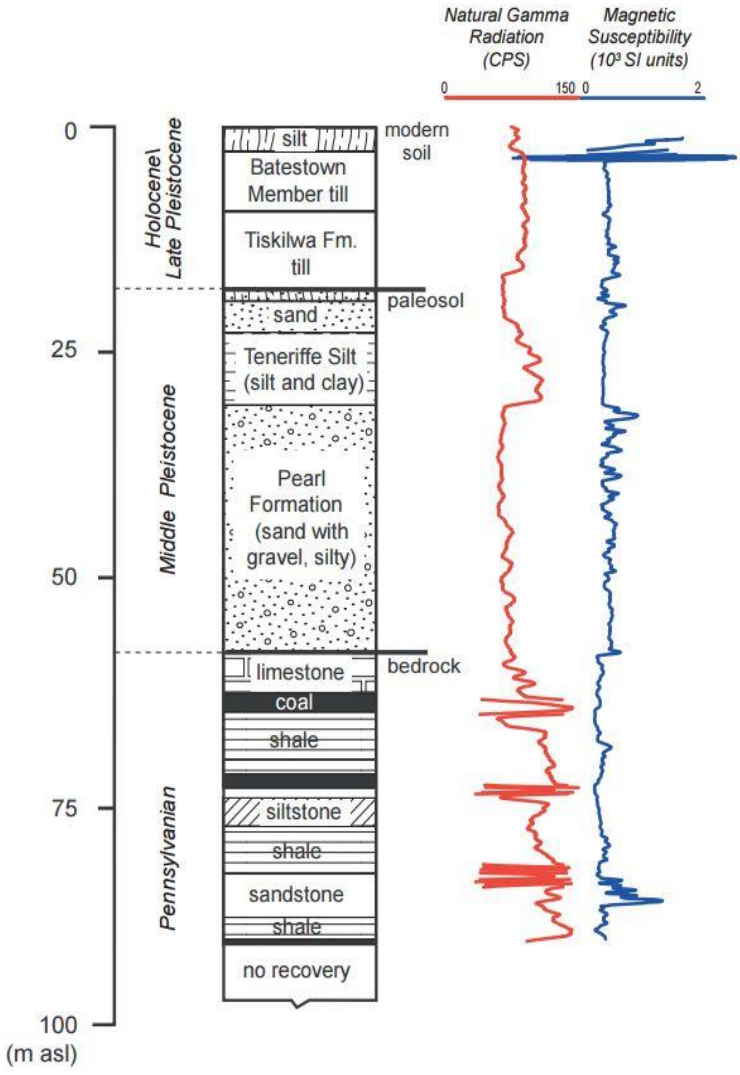

Figure 26: Borehole log for DTRT in Urbana, IL.

5.2.2 DTRT Materials

A 16.5-cm-diameter borehole was advanced to a depth of 97.5 m below ground surface (bgs). The borehole was cased from 0.75 m to 2.9 m bgs to prevent caving of the surface material. Continuous core was extracted from the borehole by mud-rotary techniques. The core was subsampled in the field and samples retained for later thermal conductivity, density, and moisture content measurements. The subsamples (27 in total) were taken at regular depth intervals, immediately sealed in airtight bags and refrigerated to maintain *in situ* moisture content and prevent oxidation. All subsurface fiber optic cables were first threaded through 6-mm-diameter plastic tubing for protection against pinching, pressure head, and repeated impacts caused by flow. One continuous fiber optic cable was threaded inside both the supply and return side of the GHX piping. As the GHX was lowered into the borehole, a second fiber optic cable was installed in the grout. The GHX piping was lowered to a depth of 91.4 m bgs, with the external fiber place an additional 6 m below the GHX to thus observe the vertical temperature gradient beneath an operational GHX. A 4.5 m^2 service shed was constructed on top of the borehole to house the TRT rig, fiber optic calibration baths, and interrogator. Once this protection was in place, calibration coils and connectors were fusion spliced to each of the four ends of the fiber optic cables, and the interrogator was used to propagate a laser signal down each cable to observe signal strength and ensure signal telemetry.

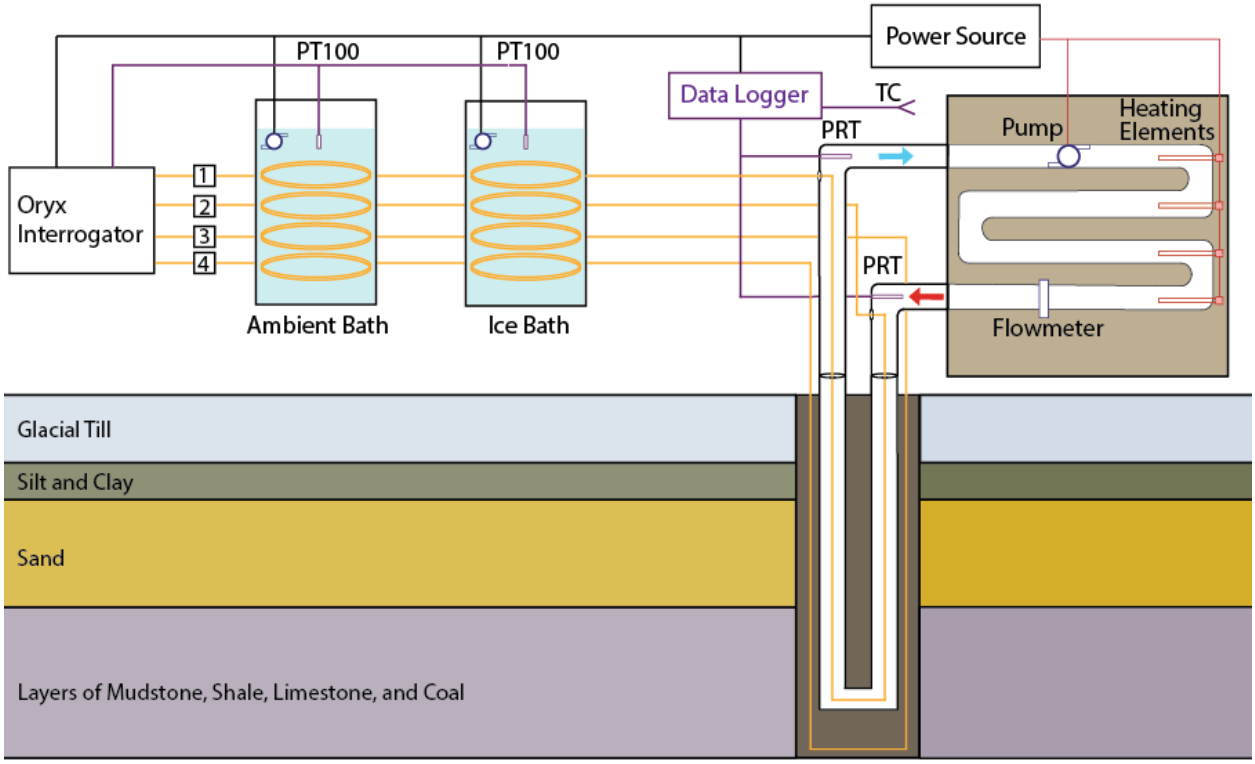

Figure 27: Custom DTRT apparatus and DTS calibration.

A custom TRT apparatus was constructed (Figure 27) to provide both the conventional TRT and the DTRT analysis. The heat injection portion of the TRT test lasted 72 h, and decay of the heat perturbation was monitored for the subsequent 2.5 weeks. The TRT rig is attached to the supply and return sides of the GHX to create close-loop flow. A Grundfos Alpha 15-55F/LC (Grundfos, Bjerringbro, Denmark: ± 0.07 $m^3 h^{-1}$) circulation pump was set at a constant flow rate of 1.1 $m^3 h^{-1}$. A positive displacement flowmeter (Master Meter, Mansfield, Texas: ± 2%) was used to verify the pump flowrate by time-averaging cumulative readings during the TRT. The flowmeter calculations consistently yielded a flowrate of 1.07 m^3 hr^{-1}. The TRT piping was filled with water and deaired by adding water through a valve at the highest point in the rig, and opening air valves at sequentially higher values of hydraulic head. Four electric resistance water heaters rated at 4500, 2000, 2000 and 1440 W provide the approximately 9940-W heat injection rate into the water exchange fluid. A set of thermostats were wired to each of the heater elements, providing an

automatic off-trigger if the water temperature exceeded a specified maximum of 75 °C. Temperature measurements are made at the inlet and outlet of the TRT rig using two Hart Scientific standard platinum resistance thermometers (PRT, Fluke Corporation, Everett, WA: ± 0.001 °C). The PRTs were wired to a CR3000 data logger (Campbell Scientific, Logan, UT: ± 2.85μΩ) using a four-wire configuration to eliminate the voltage drop contributed by the leads of the current source. A type-T (copper-constantan) thermocouple was attached to the data logger to monitor the air temperature of the shed. Temperature was sampled at a rate of 1 Hz and averaged by the data logger to record the average temperature each minute for the duration of the test.

An Oryx interrogator (Sensornet, London, UK) was used for the fiber optic DTS data analysis. The Oryx machine provides temperature resolution as fine as 0.01 °C, spatial resolution of 1 m, and sampling interval of 10 s. A variable sampling interval was employed: 1 min for the first hour of the test, 30 min for the remaining 71 h, 1 min for the first 12 h of the decay test, 30 min for the next 60 h, and 6 h for the remaining 2 weeks of the decay test. 20 m coils of fiber were placed in each of two insulated 66-L coolers filled with water that served as calibration baths. The first calibration bath was allowed to come to thermal equilibrium with the ambient temperature, while the second bath was continuously replenished with ice. Both baths were circulated by small pumps to avoid thermal stratification, and externally monitored for temperature by PT100 Platinum Thermistors (Sensornet: ±0.25 °C). Calibration baths were used for confirmation of the default Oryx calibration.

5.3 Data Analysis

Recent work (Raymond et al. 2011) has provided a method of TRT data analysis based on a direct analogy from hydrogeological pumping tests. The error between experimental and model-predicted GHX inlet and outlet water temperatures is minimized to constrain effective thermophysical properties of the (assumed homogenous) subsurface—the most important of

which is borehole effective thermal conductivity. A method exists (Molz et al. 1989) for determining hydraulic conductivity in sections of a borehole during a pumping test if the volumetric water flow of that section is known. By similar analogy, a DTRT provides distributed temperature, and the heat flow of a section between any two temperatures is also known, which allows for the calculation of distributed thermal conductivity. Both the conventional TRT data analysis and the DTRT analogy are used to analyze the data from this TRT.

5.3.1 Laboratory Samples

Thermal conductivities of core samples were measured with a KD2-Pro Thermal Conductivity Analyzer (Decagon Devices, Pullman, WA: ±10%). Depending on lithification and shear strength of the sample, a soil probe or a drill and a rock probe with thermal grease was used. The ends of highly lithified samples were smoothed with a rock grinder so the KD2-Pro probe would sit flush with the sample face. Before a measurement was taken, the sample was allowed to equilibrate to room temperature for at least 2 h. 6 to 12 repeated measurements were made on a single sample. The KD2-Pro software provides an error value that describes the quality of the contact between the probe and the sample. The thermal conductivity values below the 25th and above the 75th percentile were not considered. The arithmetic mean of the remaining values was taken to be the representative sample thermal conductivity.

5.3.2 Conventional TRT

Raymond et al. (2011) applies well-developed borehole pumping test solutions to the line-source heat model. Eq. 11 is an expression of the line-source model in radial coordinates around a borehole.

$$\Delta T(r_{bh}, t) = qR_{bh} + \frac{q}{4\pi\lambda_{ss}} \int_{u}^{\infty} \frac{e^{-u}}{u} du \tag{11}$$

$$u = \frac{r^2}{4a_{ss}t} \quad and \quad a_{ss} = \frac{\lambda_{ss}}{\rho_{ss} C_{p,ss}}$$

To arrive at this solution, the ground is assumed to be semi-infinite and at an initial homogenous temperature $T(r,t = 0) = T_0$. As is fully developed in pumping test data analysis, an infinite Taylor series can accurately estimate the integral in Eq. 11 (Theis 1935). Raymond et al. (2011) uses the Theis solution to the fourth factorial, and inputs the initial ground temperature (T_0), subsurface thermal conductivity (λ_{ss}), subsurface density (ρ_{ss}), subsurface specific heat capacity ($C_{p,ss}$), borehole thermal resistance (R_{bh}), volumetric flow of exchanger water (Q_w), water temperature at GHX inlet (T_{in}), and water temperature at GHX outlet (T_{out}) to solve for model temperatures. The error between and model and experimental T_{in} and T_{out} data is minimized by varying input parameters (particularly λ_{ss}) once the other parameters are well-constrained. Background fiber optic temperature profiles were taken prior to the TRT, and although temperature did increase with depth due to the natural geothermal gradient, the average temperature of these profiles was taken to be T_0. The effective density ρ_{ss} and specific heat capacity c_{ss} of the ground were estimated based on a weighted average of literature values of each lithological unit (Meyer 2013). The borehole resistance was determined using the software package Ground Loop Design™, which inputs the borehole geometry, and the thermal conductivity of the grout (λ_{grt} = 0.71 W m^{-1} K^{-1}). Q_{water} was taken from the cumulative flowmeter and T_{in} and T_{out} were taken from the PRTs.

Line-source data analysis performed on previous TRTs has shown the earliest data in the heat injection sequence also has the poorest conformity to the model (Gehlin 2005) and error is decreased by using temperature data when $t \geq 5r_{bh}^2 a_{ss}^{-1}$ (Eklof and Gehlin 1996). Temperature data from all heat injection times were initially used and compared to the model fit without the early data. The error between the experimental data and the model decreased appreciably, so early data ($t \leq 5r_{bh}^2 a_{ss}^{-1}$) was excluded from the data analysis.

5.3.3 Distributed TRT

With an effective borehole thermal conductivity (λ_{ss}) from the conventional TRT analysis, distributed thermal conductivity can be calculated from the distributed fiber optic data and an analogy to the work of Molz et al. (1989), in which a method for determining vertically distributed horizontal hydraulic conductivity during a borehole pumping test is presented. The effective borehole hydraulic conductivity must be first known from a conventional pumping test. An impeller meter is used to measure the discharge distribution with depth and Eq. 12 is used to calculate horizontal hydraulic conductivity at any interval where the volumetric discharge of water is known. A direct thermal analogy of this equation can be made in Eq. 13. In place of an impeller meter, the fiber optic temperature measurements and the volumetric flow of water and Eq. 14 can be used to measure incremental heat flow away from the GHX. Eq. 13 is only valid when the heat flow from the GHX is at steady state. Raymond and Lamarche (2013) suggests an alternate approach in which data can be used once the heat injection into subsurface layers has become constant. For this TRT, subsurface heat injection rates become nearly constant in the first several hours of the test. To ensure the best model fit possible, only data after a characteristic time, t_D, of 5 was used as the more conservation estimate of steady state conditions.

$$\frac{K_i}{\bar{K}} = \frac{\Delta Q_{w,i}/\Delta z_i}{QP_w/B} \tag{12}$$

$$\frac{\lambda_i}{\lambda_{ss}} = \frac{\Delta Q_{H,i}/\Delta z_i}{QP_H/B} \tag{13}$$

$$\Delta Q_{H,i} = (T_2 - T_1) * Q_w * \rho_w * C_{p,w} \tag{14}$$

$$t_D = \frac{\lambda_{ss} * t}{C_{p,ss} * \rho_{ss} * r_{bh}^2} \tag{15}$$

5.4 Results

5.4.1 Core Measurements

The thermal conductivity, moisture content, and bulk density measurements of core specimens are presented in Table 5. Of particular interest, the two intact coal samples have values of 0.32 and 0.36 W m^{-1} K^{-1} and a third sample of interbedded black shale and coal has a thermal conductivity value 0.87 W m^{-1} K^{-1}, which is lower than a sample of siltstone–shale at 1.12 W m^{-1} K^{-1}. Generally, among specimens other than coal, thermal conductivities increase with depth. Samples of the same lithology have similar thermal conductivities compared to samples taken across lithologic boundaries, which supports the hypothesis that the lithology affects thermal conductivity and, therefore, a heterogeneous geology will return a complex heat flow. For example, the Tiskilwa Formation (sandy till) has a mean thermal conductivity of 2.69 W m^{-1} K^{-1}, while the Teneriffe Silt (silt/loess) samples only a few meters deeper in the subsurface have a mean thermal conductivity of 1.52 W m^{-1} K^{-1}. The subsurface effective thermal conductivity (weighted average) from the laboratory measurements is 2.05 W m^{-1} K^{-1}.

Lithologic similarities extend beyond thermal conductivity. All core specimens from the Pearl Formation have bulk densities in a tight range of 1.52 g cm^{-3} to 1.84 g cm^{-3} and gravimentric moisture contents from 22.4% to 25.8%. The two siltstone specimens have identical bulk densities of 2.68 g cm^{-3}. The highest variability was seen in three mudstone specimens, which varied in both density (2.10, 3.04, and 4.23 g cm^{-3}) and moisture content (12.5, 10.2, and 9.0%). Low shear strength in all three mudstone specimens led to cracking and shear failure while being drilled for thermal conductivity measurements.

Table 5: Laboratory testing results of core specimens (UT = unnamed tongue).

Depth [m]	Thermal Conductivity [W m^{-1} K^{-1}]	Moisture Content [%]	Bulk Density [g cm^{-3}]	Unit / Lithology
0.5	1.27	31.0	0.68	Peoria Silt
1.5	1.87	22.7	1.49	Peyton Formation
4.1	2.01	11.4	3.59	Batestown Member
9.6	2.67	12.3	2.58	Tiskilwa Formation
13.0	2.34	12.8	1.89	Tiskilwa Formation
14.6	3.07	7.4	3.67	Tiskilwa Formation
20.6	2.33	24.5	1.80	Pearl Formation
24.2	1.55	26.5	1.26	UT, Teneriffe Silt
26.7	1.56	28.4	2.00	UT, Teneriffe Silt
35.8	2.51	24.5	1.56	UT1, Pearl Formation
43.7	2.16	22.4	1.62	UT2, Pearl Formation
44.7	2.34	25.3	1.52	UT2, Pearl Formation
51.1	2.25	25.8	1.84	UT2, Pearl Formation
59.8	3.19	3.0	2.93	Bankston Fork Limestone
62.9	2.52	7.5	2.48	Anna Shale
64.0	0.32	11.0	1.52	Herrin Coal
66.1	-	12.5	2.10	mudstone
69.5	2.27	9.1	2.60	shale
73.0	0.36	12.9	1.34	Springfield coal
74.2	-	10.2	3.04	mudstone
75.7	3.20	4.7	2.68	siltstone
81.9	1.40	6.9	2.34	Excello Shale
83.5	-	9.0	4.23	mudstone
88.0	-	7.0	1.78	shale
89.4	2.98	5.5	2.68	siltstone

5.4.2 Conventional TRT Analysis

The results of the conventional TRT (Figure 28) show a remarkably smooth increase in water temperature at both the inlet and outlet of the GHX. This occurrence, despite diurnal and anthropogenic ambient temperature fluctuations, suggests that the platinum resistance thermometers were well-insulated from ambient effects and are representative of the inlet and outlet water temperatures. In less than 10 min from the beginning of heat injection, the supply water temperature is approximately 8.5 °C hotter than the return water. This ΔT steadily decreases for the duration of the heat injection to just above 7 °C after 72 h. Since the absolute supply and return temperatures continue to increase, and the flow rate remains constant, the rate of energy injection into the exchanger water remains greater than the heat exchanged in the subsurface, meaning that true steady state conditions are not reached in this TRT. A characteristic time of 9.7 h was calculated from Eq. 15 (t_D = 5) with iteratively updated model parameters. Only temperature data after this time was used in the analysis. To minimize the error between the experimental data and the model, subsurface specific heat capacity, borehole thermal resistance, and effective thermal conductivity were systematically varied and the sum of

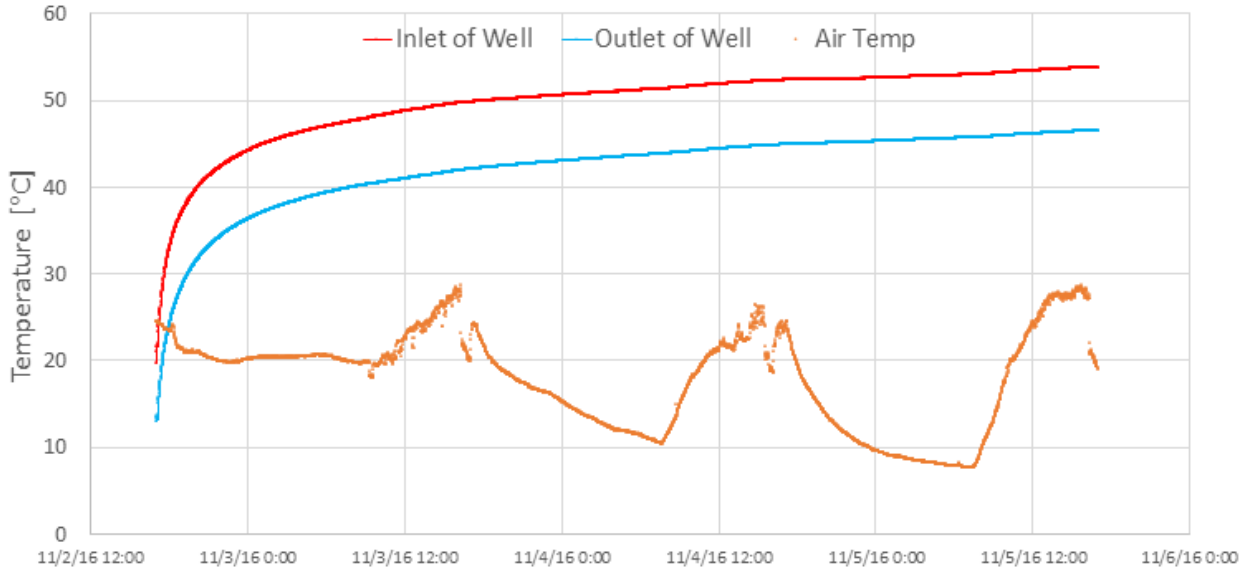

Figure 28: Conventional TRT results during heat injection.

the squared residuals between data were recorded. The results (Table 6) show that there is a global minimum of model best fit at a pairing of $C_{p,ss}$ = 920 J kg^{-1} K^{-1}, R_{bh} = 0.18 m K W^{-1}, and λ_{ss} = 2.0 W m^{-1} K^{-1}. This value is 2.5% lower than the weighted average of thermal conductivities found by the laboratory measurements.

Table 6: RMS residuals between model and experimental temperature data.

Effective Borehole Thermal Conductivity λss [W m-1 K-1]

Rbh [m K W-1]	1.4	1.5	1.6	1.7	1.8	1.9	2.0	2.1
0.10	680	1018	1389	1777	2174	2574	2971	3363
0.11	380	636	932	1253	1589	1933	2279	2624
0.12	172	345	567	821	1096	1384	1679	1977
0.13	55	146	293	480	694	927	1171	1421
0.14	30	38	111	231	384	561	754	957
0.15	97	22	21	73	166	286	428	584
0.16	255	97	22	7	38	103	194	303
0.17	504	264	114	33	3	12	51	114
0.18	845	522	299	150	59	12	0.6	16
0.19	1278	872	574	358	206	104	41	9
0.20	1802	1314	941	659	445	288	173	94

Effective Subsurface Specific Heat Capacity Cp_{ss} [J kg-1 K-1]

Rbh [m K W-1]	420	520	620	720	820	920	1020	1120
0.10	1132	1548	1938	2305	2648	2971	3276	3565
0.11	722	1061	1389	1701	1997	2279	2548	2803
0.12	405	666	930	1189	1439	1679	1910	2132
0.13	178	363	563	768	971	1170	1365	1553
0.14	44	151	288	439	595	754	911	1066
0.15	0.47	31	104	201	311	428	548	670
0.16	49	2.0	12	55	118	194	277	366
0.17	189	65	12	0.9	17	52	98	153
0.18	420	219	102	38	8.0	0.6	10	32
0.19	743	465	285	167	89	41	14	1.8
0.20	1158	802	559	387	263	173	109	64

5.4.3 Heat Injection

In Eq. 14, if T_2 is taken as the inlet temperature and T_1 is taken as the outlet temperature from the PRTs, the heat flux calculated is equal to the rate of heat injection into the ground by the GHX. Alternatively, T_2 can be taken as the first fiber temperature on the supply side and T_1 the final fiber temperature on the return side. The nature of fiber optic sampling is such that when the fiber passes through a sharp temperature transition, there will be a signal lag before the fiber signal represents the true temperature. The spatial width of this signal lag to recover 90% of the temperature spike is often referred to as the spatial resolution of the fiber (Selker et al. 2006). In this case, the spatial resolution was 4 m, which led to the removal of the first 4 m of the supply leg and the last 4 m of the return leg. However, the heat injection rates recorded by the thermistors and the fiber optics (Figure 29) show that similar rates of total heat injected in the subsurface. This total heat injected into the borehole at any measurement in time (QP_H) is an input into the distributed thermal conductivity analysis. The total rated power of the heating elements is 9940 [W]. In the first 7 h, both the fiber and the thermistors show a subsurface heat injection greater than this rate of power into the water. The most likely explanation for this spike is a lower flow rate of exchanger water during the beginning of the test. Since flow rate was measured by cumulative flow averaged over time, a period of lower flow would give the water more subsurface resonance time, but the calculations would still include an erroneously high flow rate, which would artificially inflate heat injection rates. After this initial period, the heat injection

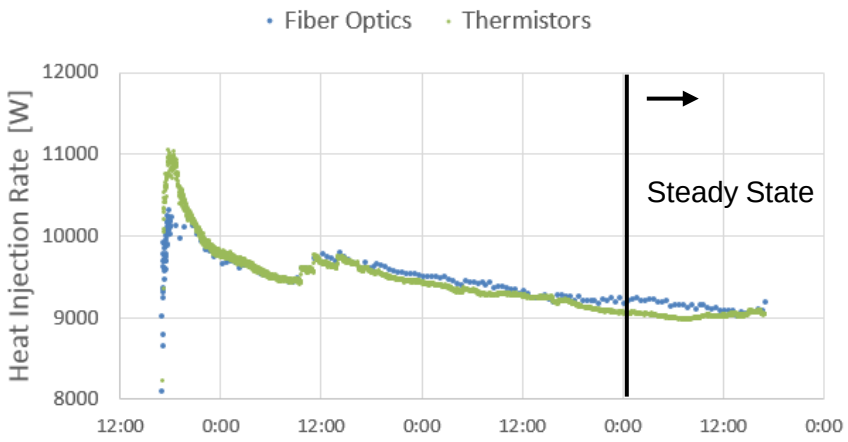

Figure 29: DTRT heat injection rates by fiber and thermistor measurement.

rate remained below the rated heater power and decreased at a decreasing rate; the only exception to this was the evening of the second day when sudden step increases in power occur, which is attributed to a spike in generator power supply. From this data, the pseudo-constant heat injection is reached at 55 h into the heat injection at midnight of the second day. Only fiber optic data in the steady state period of 55 h to 72 h was used for the DTRT analysis.

5.4.4 Distributed Thermal Response Analysis

Conventional TRT results provide valuable insights into effective borehole parameters but do not collected any data along the length of the GHX were the heat transfer has occurred. The distributed nature of DTS fills this gap at 1-m spatial resolution. The simplest analysis of this data is to observe the temperatures from the fiber within the GHX at one snap-shot in time. In Figure 30 this has been captured for the GHX profile 20 min before the end of the heat injection. The hotter side of the profile represents the supply side of the GHX as the exchanger fluid is continually losing temperature in the direction of flow as it rejects heat into the subsurface. The fiber optic data shows a ΔT of 7.1 °C entering the GHX at 52.4 °C, and leaving at 45.3 °C. The water at the bottom of the GHX is 48.3 °C, meaning 4.1 °C is lost on the supply side, and 2.9 °C is lost on the return side of the GHX. This is expected, as heat flow is driven by

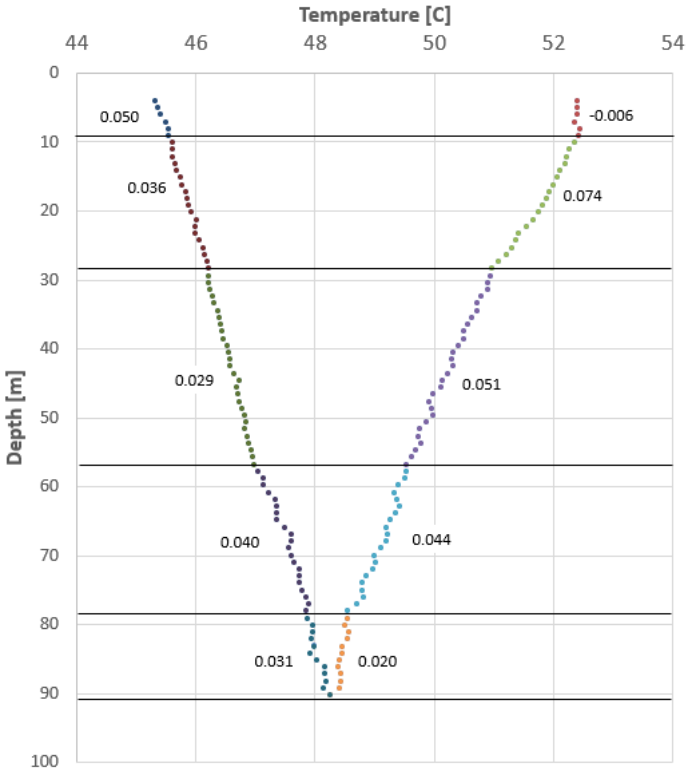

Figure 30: DTS profile of GHX at 71 h into heat injection with dT/dl sections.

a temperature gradient (Fourier 1822), and the supply side has the larger temperature gradient between the water temperature and the subsurface.

By this same relationship, the change in temperature with length along the GHX, $\left[\frac{dT}{dl}\right]$, is directly proportional to the heat flow away from the GHX at that location. When analyzing this dataset, $\left[\frac{dT}{dl}\right]$ was positive at some depths, suggesting a heat flow towards the GHX. As suggested in other literature Freifeld et al. (2008), this localized increase in temperature may be indicative of the variable radial distance of the fiber optic cable from the center of the GHX pipe. To avoid erroneous local heat flow from this effect, $\frac{\Delta T}{\Delta l}$ was calculated in segments that have similar $\left[\frac{dT}{dl}\right]$ values. These segments, and their corresponding least-squared regression $\left[\frac{dT}{dl}\right]$ values are shown in Figure 30.

5.4.5 Distributed Heat Injection

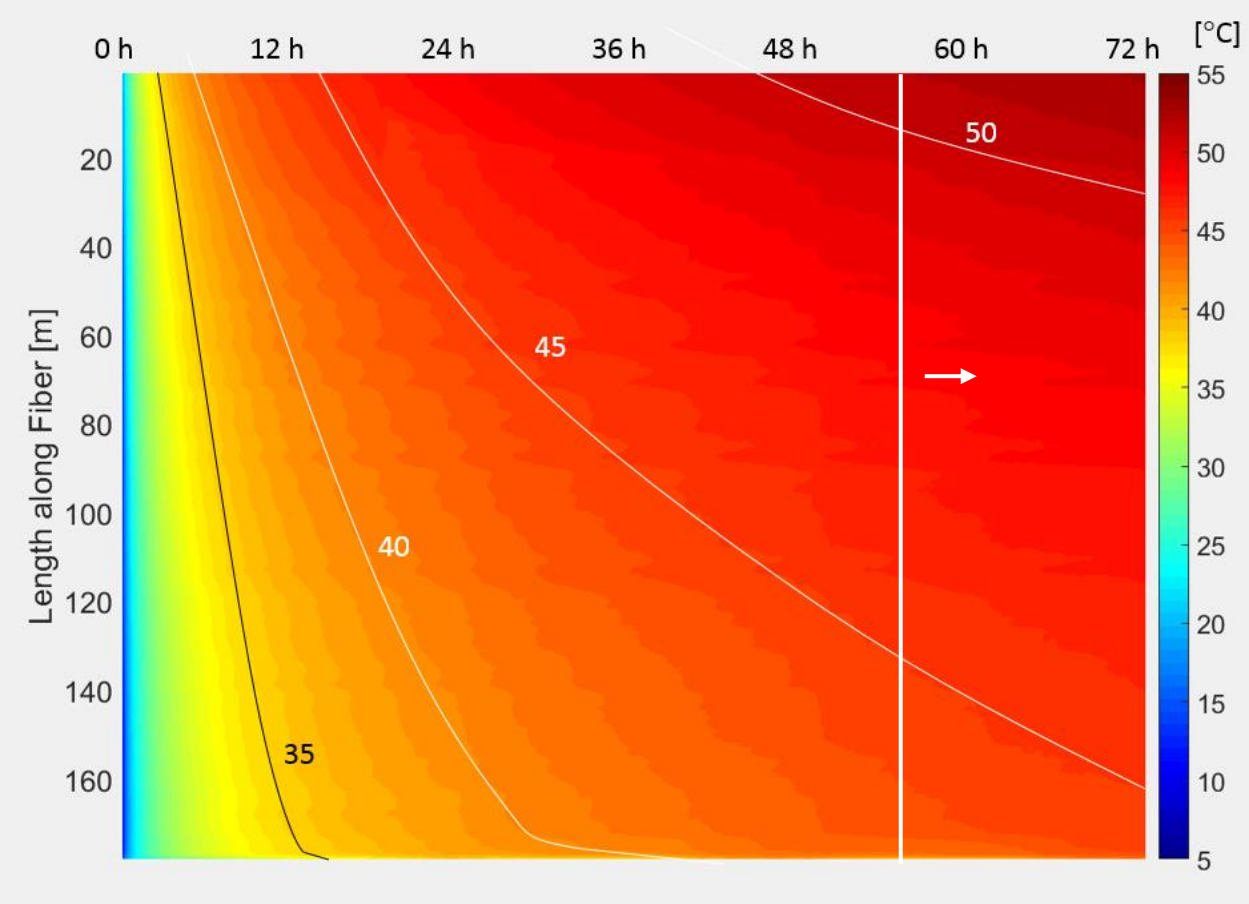

Figure 31: Fiber optic temperature profiles with the GHX during the 72-h heat injection.

Figure 31 shows the entirety of fiber optic data throughout the 72-h heat injection stage of the DTRT. The non-linear contours in this plot suggest that there is heterogeneous heat flow in the subsurface. Only temperature data after steady state heat flow has been achieved is used for the adapted Molz et al. (1989) analysis. By observation of total heat injection rates, psuedo-steady state occurred at 55 h. Using this data and Eq. 13, the thermal conductivity of the subsurface was evaluated at a resolution of 1 m. Since Eq. 13 assumes a constant temperature gradient between the water temperature and the subsurface, the thermal conductivity on the supply and return side were averaged; much in the same way as mean water temperature is often used in GHX modeling (Özdoğan-Dölçek 2015). Intrinsic noise in this signal is created because the fiber is not secured

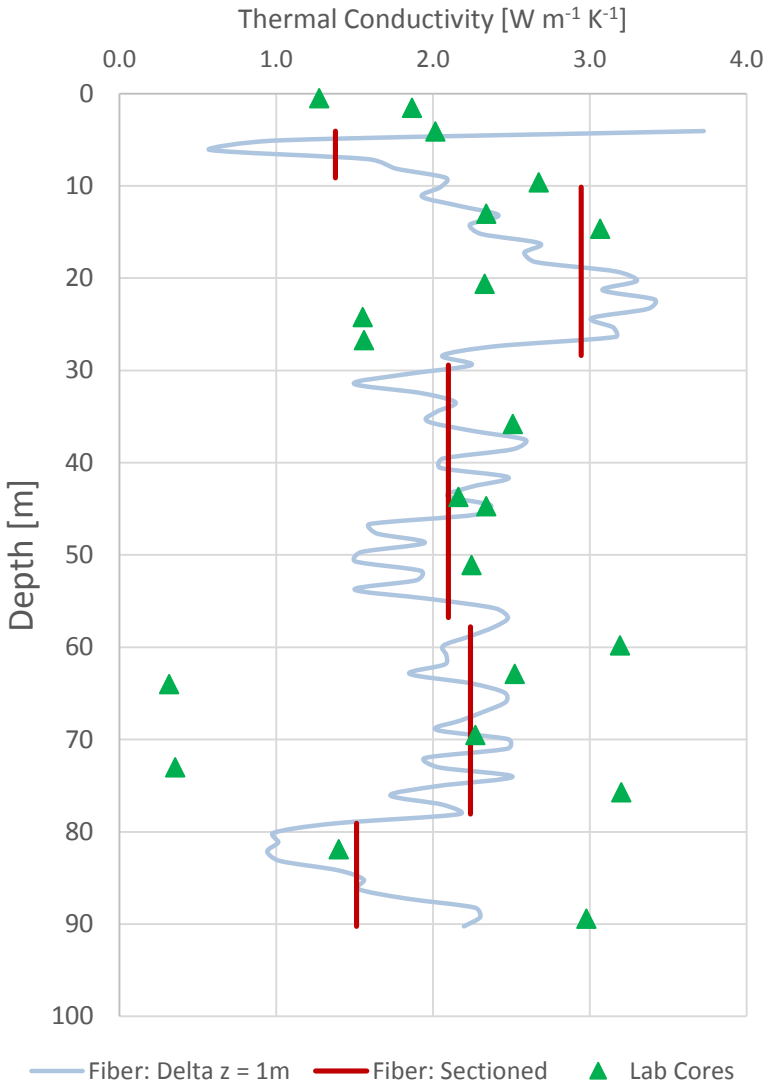

Figure 32: Thermal conductivity with depth from DTS at 1-m resolution, DTS section by dT/dl, and laboratory core measurements.

within the GHX and might provide local changes in temperature that do not fully represent heat flow, but also the position of the fiber. A moving average filter was used over the raw temperatures to smooth out these localized signal perturbations. The heat flow interaction between the supply and return side may also create local gradients that do not reflect heat flow by thermophysical properties, but are driven by Fourier's Law. The high thermal conductivities (≈ 3.0 W m^{-1} K^{-1}) of 15–25 m bgs agree with the higher laboratory measurements in the Tiskilwa and Pearl Formations

(≈ 2.5 W m^{-1} K^{-1}). Below 25 m bgs, the thermal conductivities decrease by ≈ 1.0 W m^{-1} K^{-1} in the Teneriffe Silt until 30 m bgs. This trend is also seen in the laboratory measurements (1.55, 1.44, and 1.56 W m^{-1} K^{-1}, respectively). Between depths of 33 and 58 m in the Pearl Formation, the fiber data shows values are consistently 0.5 to 0.75 W m^{-1} K^{-1} lower than the laboratory values. From 58 m bgs to the bottom of the tubing at 91 m (300 feet) bgs, the measurements were made in bedrock, which contains repeating sequences of shale, coal, and siltstone that vary significantly in their thermophysical properties. The fiber also shows a higher variability at this depth with a lower average, which may be expected because of the coal and shale. The two downward spikes of thermal conductivity near the bottom of the profile are at the same depths that produced coal cores that had thermal conductivities of 0.32 and 0.36 W m-1 K-1. The relatively high thermal conductivity at the bottom of the well may be a result of vertical heat flow to the relatively cooler subsurface beneath the well.

3.4.2 Distributed Heat Decay

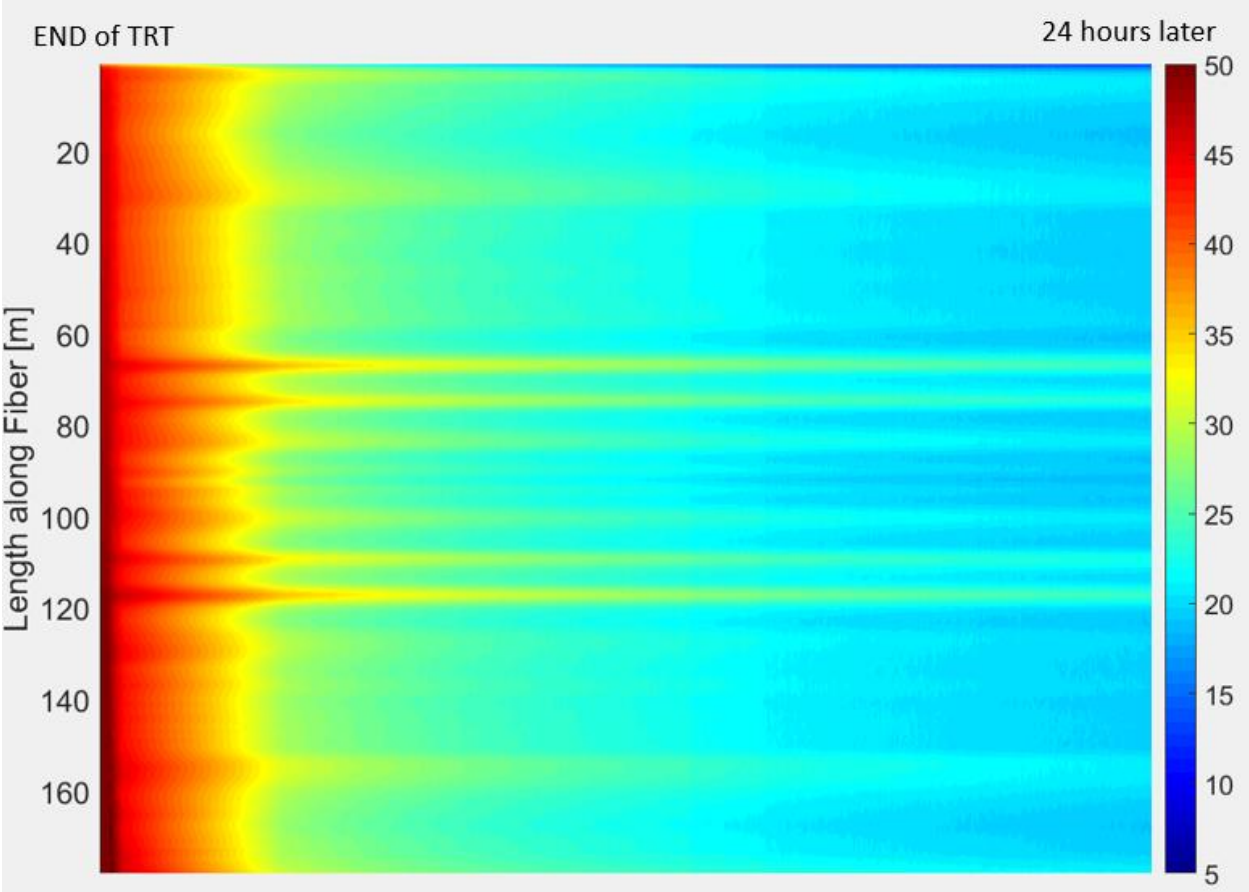

Figure 33: DTS profiles in the GHX during the first 24 h of heat dissipation. 0-90 m is the supply side, and 90-180 m is the return side.

After the heat injection portion of the DTRT was complete, the fiber optic system continued collecting temperature data for 2 weeks to quantify heat dissipation. Figure 33 shows the first 24 h of the GHX water temperature during the decay stage. The rate of heat dissipation is not homogenous with depth. In particular, there are certain sections of depths that dissipate heat at a lower rate. While the rate of heat dissipation is controlled by thermal diffusivity, $\alpha = \lambda/(\rho \cdot Cp)$, thermal diffusivity is be used as a proxy for thermal conductivity in this analysis since $\alpha = f(\lambda,\rho,Cp)$ and the specific heat capacity of the core samples have not been measured. The spike in slower heat diffusion at depths between 25 and 30 m correlates nicely with the depths of the Teneriffe Silt, whose core samples show a thermal conductivity value of approximately 1.5 W m^{-1} K^{-1}. The

two most notable depths of low heat diffusion are at depths of 64 and 73 m—the depths of the coal seams. The thermal decay profile can also be used to calculate distributed conductivity directly as was done in Freifeld et al. (2008). With distributed specific heat capacity (C_p) and density (ρ) from laboratory testing on the core specimens, the temperature data can be inverted to calculate thermal conductivity. During cooling, conduction of heat tends to homogenize local heat gradients inside and around the GHX. This may decrease the intrinsic noise created by the location of the fiber in the GHX and allow for greater resolution in distributed thermal conductivity calculations.

5.5 Discussion and Conclusions

This work adds to the current scientific understanding of distributed thermal response tests by conducting the test in an area of well-documented heterogeneous geology and applying new methods of data analysis to better calculate distributed thermal conductivity. The combination of a conventional TRT, laboratory thermophysical measurements of cores, and DTRT provide a holistic picture of subsurface heat transfer that captured both the absolute magnitudes of distributed thermal conductivity (useful for modeling) and subsurface trends of heat transfer (useful for designing GHX systems). Multiple lines of evidence (i.e., laboratory measurements and *in situ* fiber results led to higher confidence in results and greater evidence to support correlation between observed heat flow and known geological conditions.

Raymond et al. (2011) documented a pumping test analogy for analysis TRT data. This solution was used within a parametric study that varied key input parameters to fit valleys and absolute minimums of error between model and experimental data. From this analysis, model fits were optimized at extremely low errors that provided an effective subsurface thermal conductivity that only varied from the independent laboratory measurements by 2.5%. Secondly, a novel method of data analysis was presented based on the Molz et al (1989) impeller meter method for distributed hydraulic conductivity. One DTRT rig outfitted was used to supply all inputs for both

the Raymond et al. (2011) and the Molz et al. (1989) analogies, which provide important insight into the mechanisms of subsurface heat transfer.

Three different sources of distributed thermal conductivity with depth—1-m-resolution fiber, fiber data sectioned by geology and $\left[\frac{dT}{dl}\right]$, and laboratory measurements—while providing their own valuable insight, are particularly useful when viewed together. Of the three methods, the laboratory measurements of thermophysical properties are the most accurate estimation of absolute thermal conductivity magnitudes, which are valuable inputs into analytically and numerical models. However, laboratory core measurements cannot describe other *in situ* heat flow mechanisms such as groundwater advection, and come at a high time and monetary cost. The 1-m-resolution fiber data lends the best insight into true differential subsurface heat transfer. Heat transfer trends with depth are observed with the highest spatial resolution despite some signal muting to filter out noise. Removal of all spatial averaging from the 1-m-resolution fiber data achieves high local accuracy from the fiber data, but produces a noisy signal. The combination of the laboratory measurements and the 1-m-resolution fiber data between the depths of 60 and 75 m developed the hypothesis of an *in situ* feedback loop of heat flow. The laboratory measurements show oscillating thermal conductivity values with depth between the high conducting shale and limestone, and the poor conducting coal seams. The 1-m-resolution fiber data does reflect this variability, but with a muted signal. We hypothesize that the higher conducting layers heat up faster than the coal, and by Fourier's Law, the temperature gradient may induce vertical heat flow from other layers as well as preferential heat flow from the GHX towards the coal. This feedback loop would make higher conductivity layers move less heat, and lower conductivity layers conduct more heat, yielding the muted signal observed in the 1-m-resolution fiber data. The fiber data sectioned by $\left[\frac{dT}{dl}\right]$ and correlated to geology can give the best insight into optimizing the design of future borefields. The bottom 10 m of this test borehole—

comprised of siltstone, mudstone, and shales—has a low $\left[\frac{dT}{dl}\right]$, thus a low heat injection rate. In planning GHX design for future GSHP systems in this geology, there may be significant heat transfer gains by drilling more boreholes that are 10 m shallower to avoid this low heat transfer zone.

Appendix 1: Epic Campus Energy Flows

Human beings are constrained to a narrow range of ambient temperature comfort. When we are outside this comfort zone, or even near the fringes, our actions are greatly impacted. The Lawrence Berkeley National Laboratory conducted a study and found that there is an optimal temperature for workplace productivity: 72° F. Every degree away from that optimal correlates to a 1.25% decrease in productivity (Seppänen et al. 2006). For large companies such as Epic, an improperly set thermostat could have disastrous consequences to net productivity. In an effort to prevent such a drop in productivity and revenue, Epic has spent a great deal of money to create a remote space heating and cooling system that ensures each employee works in a comfortable temperature environment to his/her own preference. In fact, at Epic it is possible for each employee to set the temperature of their personal office with one click of the mouse from anywhere on the Epic network by opening the Epic internal homepage, Guru, and clicking the blue down arrow for office cooling or red up arrow for heating (Figure 34). This smart system is even attached to window sensors that will not allow adjustments if the windows are open. When

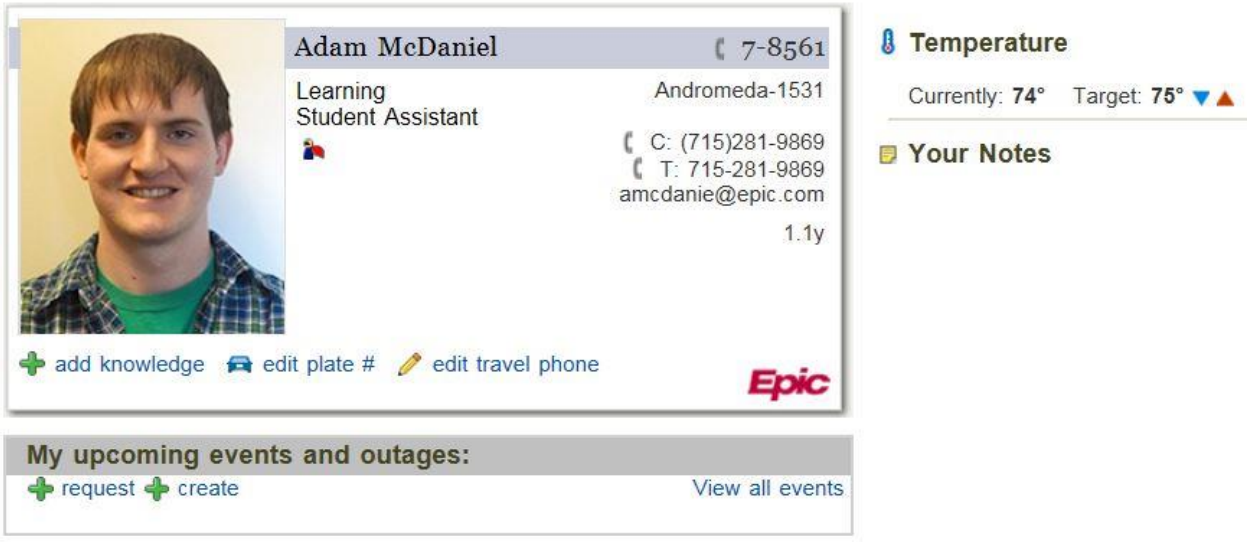

Figure 34: Example employee profile on Epic's internal homepage.

employees are asked to share office space with another employee, as is often the case for student assistants, it was not uncommon for office temperature control struggles to occur.

Epic's facilities and building management teams monitor and track these internal heat flows closely. A centralized data collection network, *Cimplicity*, collects, analyzes, and archives huge amounts of HVAC data for real time feedback. Beyond the employee control of personal offices, the majority of Epic buildings are automatically temperature controlled through *Cimplicity* feedback and controls. Many of these internal heat flows are being recorded and sent via .csv files emailed to almcdaniel@wisc.edu. These files are named Geo_Data_YYYY-MM-DD to convey the date of origin and contain a data point collected every 15 minutes throughout the day. Each morning at 01:00 the compiled data from the previous day is sent. This data has been collected each day from 01/01/2015 to the submittal of this thesis on 05/05/2017. At times, the automated email was not sent, and Bryan Lane (an Epic contractor who helped compile the spreadsheet), was emailed and able to provide the appropriate data. As the occurrence of missing emails lessen, and contact with Bryan became more difficult, it became common practice to simply copy the previous day's data to fill the gap of a missing day.

The data collected has evolved over time. The first four months of data collection included the following: Borefield 1-4, supply and return temperatures (°F), and flowrates (gpm). A supply and return temperature (°F) for the pond, and two flow rates. The two flow rates are provided as the pond is split into two distinct sections, however, the flow is in series between these two sections and the average of both flowrates should be paired to the temperature data for energy injection calculations. Geowater flow (gpm), supply and return temperatures (°F) were provided for each of the six buildings (Andromeda, Borealis, Cassiopeia, Deneb, Endor, Fomalhaut, and Ganymede) in Campus 1 (also known as the Prairie Campus). For the purposes of clarity, the term "Epic's Campus" will refer to the entirety of every building on Epic property in Verona, WI, and intermediate-campus will refer to groups of buildings known as campuses that will be followed

by a numeric label. The geowater flow rate (gpm) and supply and return temperatures (°F) were provided at the intermediate-campus scale for Campus 2 (aka Central Park campus), Campus 3 (aka Farm Campus), and Campus 4 (aka Authors Campus). Geowater flowrates (gpm) and supply and return temperatures are provided separately for Deep Space (DS, Epic's 10,000 person capacity auditorium), the Learning Center (LC, Epic's snake-like building comprised of dozens of lecture halls for customer classes), and Utility Building 3 (UB3, the building that houses Epic's servers and data center). The amperage of each of the pump's in Epic's pump house that move geowater throughout the campus are recorded (amps). This data was originally intended to be paired with voltage to calculate input power required to move the geowater. Each borefield and the pond valve open percentage (100 – open, 0 – closed) is reported to provide an indication of operational usage between borefield and pond resources. The flowrates (gpm) and supply and return temperatures (°F) for one u-pipe and one coaxial GHX (that are also installed with fiber) are provided. Figure 35 provides an example of what calculations could be performed on this data to gain insight about multi-scale heat flows on Epic's campus.

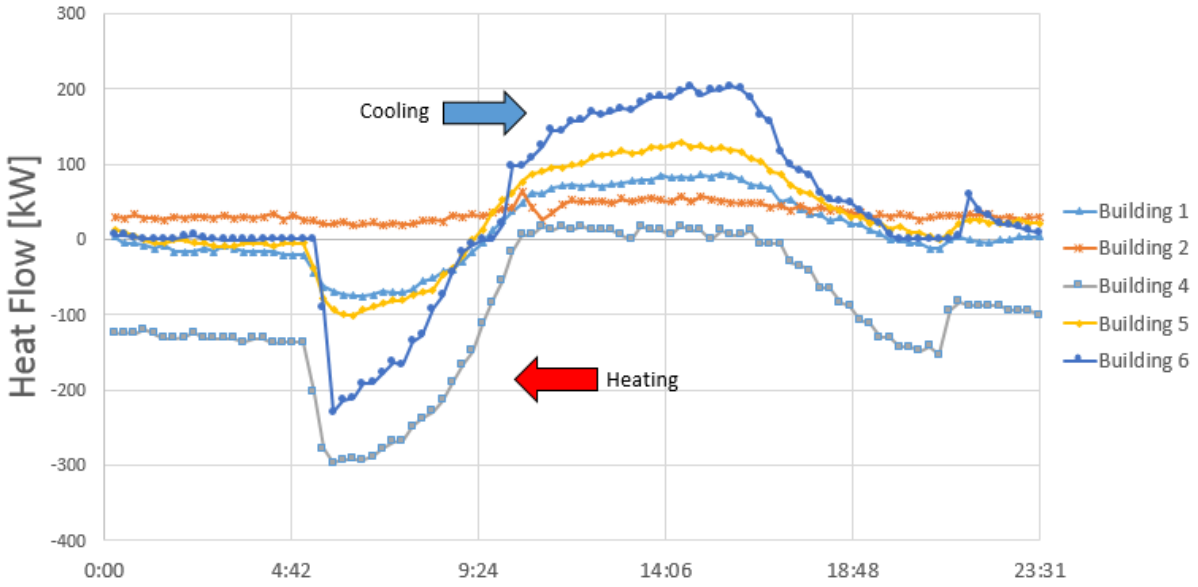

Figure 35: Campus 1 building heat flows on 01/13/2015.

The remainder of the data collected during the first four months is the mechanical energy needed to run the geosystem. All remaining units are average kW over the previous 15 minutes before the measurement was taken. Five columns called Geo Bus A,B,C,D,F represent groups of pumps in the pump house. The individual pump amperage (previously discussed) was included because some of these Geo Bus groups contain borefield and campus pumps, which was inconvenient to lump together during energy balances. A schematic of the pump house electric power connections (Figure 37) and piping diagram (Figure 36) are available below.

Campus 1 and 2 mechanical energy use is given individually by building, and also includes a data point for the each campus' Central Energy Plant (CEP), which houses some heat pumps and chillers for those two campuses. The mechanical energy for Learning Center, Deep Space, and UB3 are each provided. A second data point is needed for UB3, labeled UB3 Shared, which is simply a second needed data point to include all mechanical input that came from a different

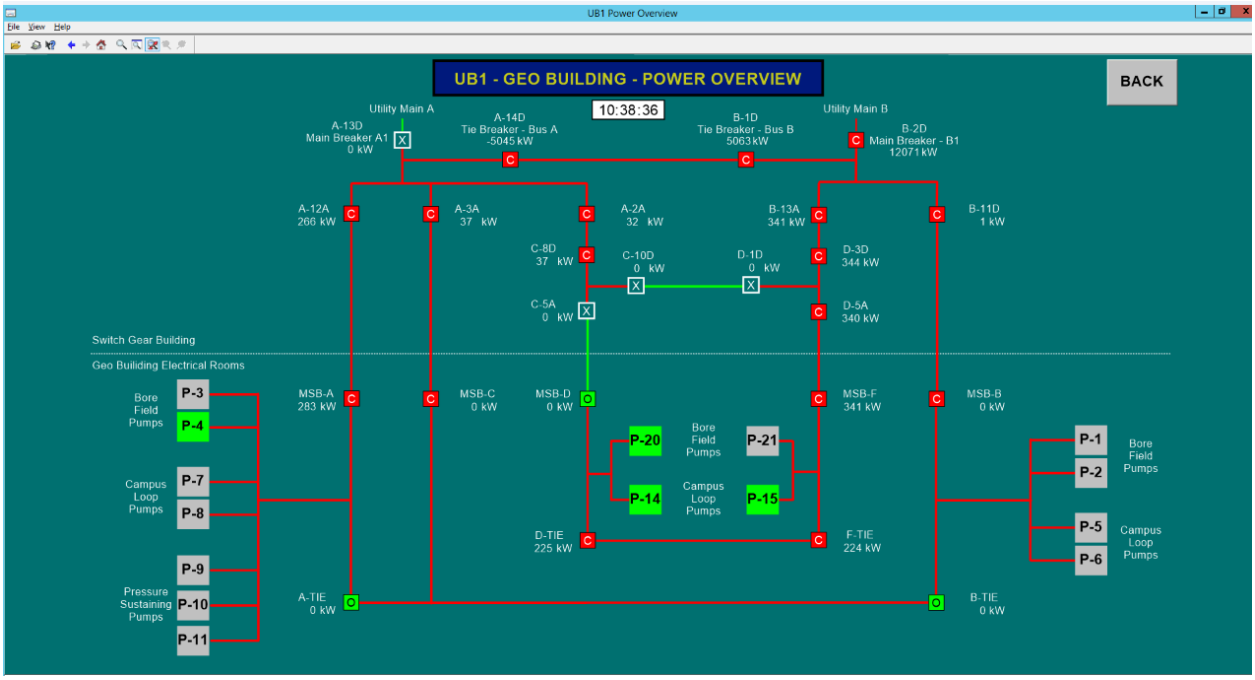

Figure 37: Epic pump house power connection diagram.

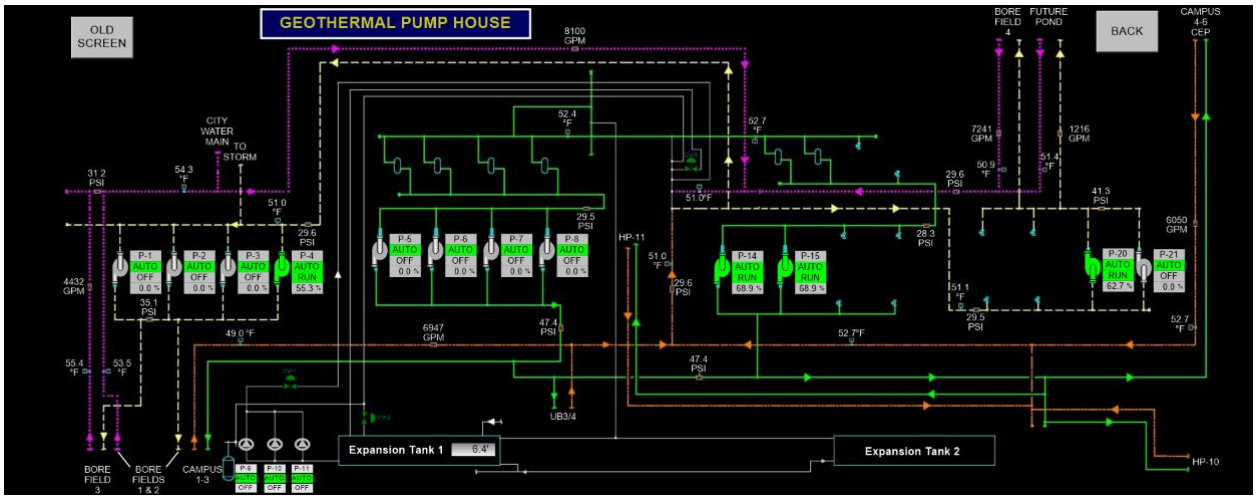

Figure 36: Epic pump house piping diagram.

breaker. Campus 3 and 4 provide only CEP mechanical energy, which house all of the heat pumps, chillers, and circulation pumps for their respective campuses. As a final note, elevators

are also included in each building-specific report for mechanical energy, which by Epic's estimate adds approximately 5% of additional energy.

With these data points, it was originally attempted to calculate a campus-wide COP for the geothermal exchange system. Eq. 16 and Figure 38 provide the inputs for this calculation, while Figure 39 shows initial 2015 results from this calculation method.

(16)

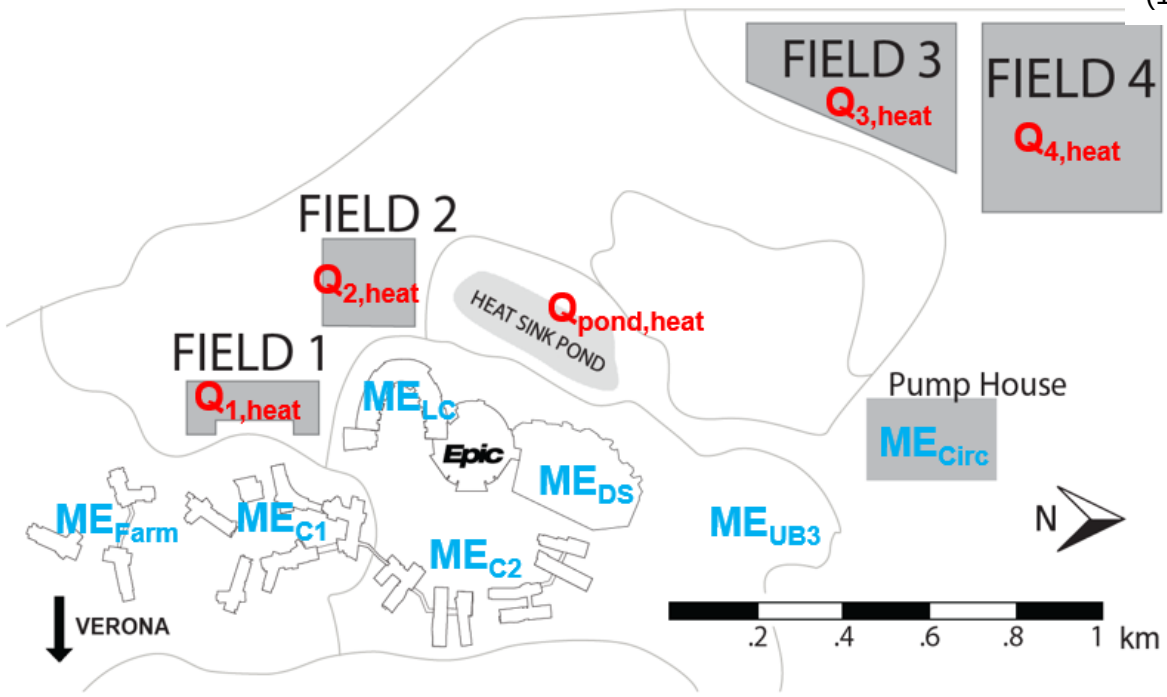

Figure 38: Epic campus geothermal COP inputs.

$$\frac{Q_{1,heat} + Q_{2,heat} + Q_{3,heat} + Q_{4,heat} + Q_{pond,heat}}{ME_{C1} + ME_{C2} + ME_{Farm} + ME_{LC} + ME_{DS} + ME_{Circ} + ME_{UB3}} = \frac{Q_{geothermal}}{ME_{geothermal}} = COP$$

It was determined through communication with Epic facilities staff that this form of calculation did not provide a complete analysis of the benefits of the geothermal system, because of a feature known as 'simultaneous mode'. This feature allowed individual buildings or intermediate campuses to heat and cool simultaneously, reusing one unit of energy (brought or removed by the geowater) multiple times in a useful manner. As a result, the .csv files were

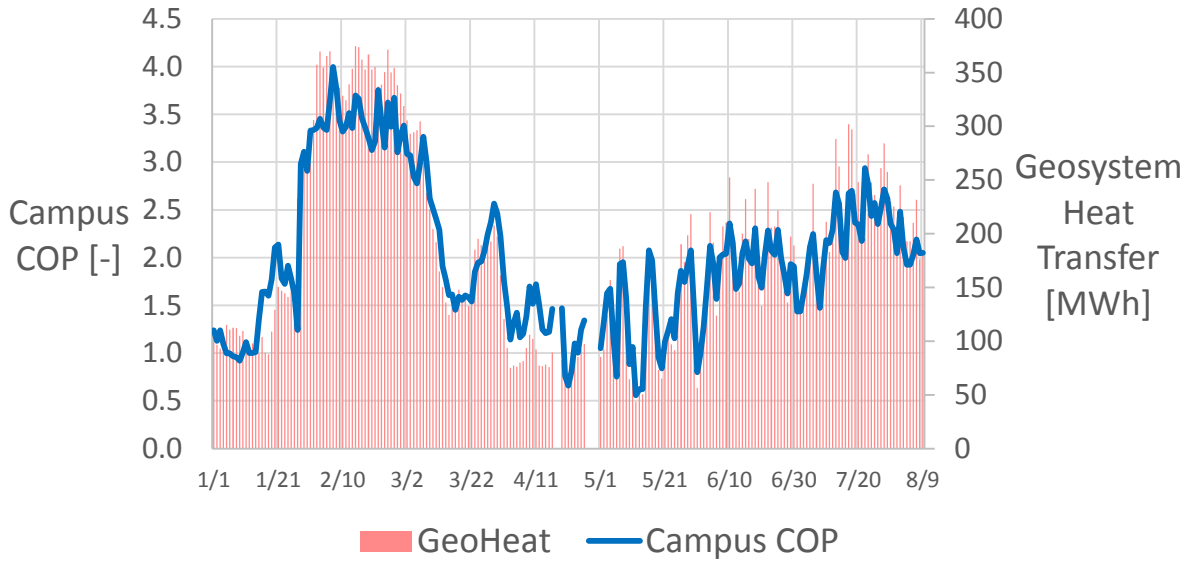

Figure 39: Epic campus geothermal COP results in 2015.

modified as of 05/01/2015 to include data for hot water supply and return temperatures (°F), chilled water supply and return temperatures (°F), and flowrates within building loops (gpm). At this point, there was not sufficient mechanical thermodynamic systems knowledge to continue analyzing and drawing useful conclusions from this data. It is my hope that Uzoma Mmeje, a mechanical engineering Ph.D. candidate at UW-Madison that has been introduced to this material, will continue this research to a more complete measure of campus geothermal efficiencies on multiple scales. The following is a Matlab script written to collect the data from the emailed spreadsheets, analyze it, and output meaningful reports each month.

```
%%Borefield Heat Flow, Internal Building Heat Flow, and Mechanical Energy
%%Tracking Script - Adam McDaniel 5/9/15
clear
close all
clc

%%Define the number of excel files and number of datapoints pulled from
%%each one.
path = cd('E:\MCDAN FLASH\Research\GeoExchange\Epic Operations
Data\Operations\Geo Data\2017\Months\Apr\');  %%ENTER HERE THE FOLDER NAME
WHERE FILES ARE STORED
listgeofiles = dir('*.csv');
numgeofiles = numel(listgeofiles); %%number of days/excel files to read.
datapoints = 96; %number of datapoints in the given file - datapoint every 15
minutes for 1 day (24*4)

%%Define Relevant Constants - Metric Units
Rho = 999.6018;    %%kg/m^3, taken at 11 [C] - average temperature of water
Cp = 4.186; %%kJ/kg*C



%%Borefield Heat Flow Section


%%Predefine Loop Vector Sizes
%%Borefield 1
BF1ST = zeros(datapoints,numgeofiles);
BF1RT = zeros(datapoints,numgeofiles);
BF1F = zeros(datapoints,numgeofiles);
BF1Q = zeros(datapoints,numgeofiles);
BF1 = zeros(numgeofiles,1);
%%Borefield 2
BF2ST = zeros(datapoints,numgeofiles);
BF2RT = zeros(datapoints,numgeofiles);
BF2F = zeros(datapoints,numgeofiles);
BF2Q = zeros(datapoints,numgeofiles);
BF2 = zeros(numgeofiles,1);
%%Borefield 3
BF3ST = zeros(datapoints,numgeofiles);
BF3RT = zeros(datapoints,numgeofiles);
BF3F = zeros(datapoints,numgeofiles);
BF3Q = zeros(datapoints,numgeofiles);
BF3 = zeros(numgeofiles,1);
%%Borefield 4
BF4ST = zeros(datapoints,numgeofiles);
BF4RT = zeros(datapoints,numgeofiles);
BF4F = zeros(datapoints,numgeofiles);
BF4Q = zeros(datapoints,numgeofiles);
BF4 = zeros(numgeofiles,1);
%%Pond
P10ST = zeros(datapoints,numgeofiles);
P10RT = zeros(datapoints,numgeofiles);
P11ST = zeros(datapoints,numgeofiles);
P11RT = zeros(datapoints,numgeofiles);
```

```
PF = zeros(datapoints,numgeofiles);
PQ = zeros(datapoints,numgeofiles);
Pond = zeros(numgeofiles,1);
%%Total Heat from geothermal system by Day
GeoHeat = zeros(numgeofiles,1);


%%Geowater to Outside of Buildings Section


%%Building 1
C1_B1_ST = zeros(datapoints,numgeofiles);
C1_B1_RT = zeros(datapoints,numgeofiles);
C1_B1_F = zeros(datapoints,numgeofiles);
C1_B1_Q = zeros(datapoints,numgeofiles);
C1_B1_Q_Daily = zeros(numgeofiles,1);
%%Building 2
C1_B2_ST = zeros(datapoints,numgeofiles);
C1_B2_RT = zeros(datapoints,numgeofiles);
C1_B2_F = zeros(datapoints,numgeofiles);
C1_B2_Q = zeros(datapoints,numgeofiles);
C1_B2_Q_Daily = zeros(numgeofiles,1);
%%Building 3
C1_B3_ST = zeros(datapoints,numgeofiles);
C1_B3_RT = zeros(datapoints,numgeofiles);
C1_B3_F = zeros(datapoints,numgeofiles);
C1_B3_Q = zeros(datapoints,numgeofiles);
C1_B3_Q_Daily = zeros(numgeofiles,1);
%%Building 4
C1_B4_ST = zeros(datapoints,numgeofiles);
C1_B4_RT = zeros(datapoints,numgeofiles);
C1_B4_F = zeros(datapoints,numgeofiles);
C1_B4_Q = zeros(datapoints,numgeofiles);
C1_B4_Q_Daily = zeros(numgeofiles,1);
%%Building 5
C1_B5_ST = zeros(datapoints,numgeofiles);
C1_B5_RT = zeros(datapoints,numgeofiles);
C1_B5_F = zeros(datapoints,numgeofiles);
C1_B5_Q = zeros(datapoints,numgeofiles);
C1_B5_Q_Daily = zeros(numgeofiles,1);
%%Building 6
C1_B6_ST = zeros(datapoints,numgeofiles);
C1_B6_RT = zeros(datapoints,numgeofiles);
C1_B6_F = zeros(datapoints,numgeofiles);
C1_B6_Q = zeros(datapoints,numgeofiles);
C1_B6_Q_Daily = zeros(numgeofiles,1);
%%Campus 1 Total
C1_Q = zeros(datapoints,numgeofiles);
C1_Q_Daily = zeros(numgeofiles,1);
%%Campus 2
C2_ST = zeros(datapoints,numgeofiles);
C2_RT = zeros(datapoints,numgeofiles);
C2_F = zeros(datapoints,numgeofiles);
C2_Q = zeros(datapoints,numgeofiles);
C2_Q_Daily = zeros(numgeofiles,1);
%%Learning Campus
```

```
LC_ST = zeros(datapoints,numgeofiles);
LC_RT = zeros(datapoints,numgeofiles);
LC_F = zeros(datapoints,numgeofiles);
LC_Q = zeros(datapoints,numgeofiles);
LC_Q_Daily = zeros(numgeofiles,1);
%%Learning Campus
DS_ST = zeros(datapoints,numgeofiles);
DS_RT = zeros(datapoints,numgeofiles);
DS_F = zeros(datapoints,numgeofiles);
DS_Q = zeros(datapoints,numgeofiles);
DS_Q_Daily = zeros(numgeofiles,1);
%%FARM "internal"
FARM_ST = zeros(datapoints,numgeofiles);
FARM_RT = zeros(datapoints,numgeofiles);
FARM_F = zeros(datapoints,numgeofiles);
FARM_Q = zeros(datapoints,numgeofiles);
FARM_Q_Daily = zeros(numgeofiles,1);
%%Total Buildings
Buildings_Q_Daily = zeros(numgeofiles,1);

%%UBENDvsRYGAN
UBEND_ST = zeros(datapoints,numgeofiles);
UBEND_RT = zeros(datapoints,numgeofiles);
UBEND_F = zeros(datapoints,numgeofiles);
UBEND_Q = zeros(datapoints,numgeofiles);
UBEND_Q_Daily = zeros(numgeofiles,1);
UBEND_avgF_Daily = zeros(numgeofiles,1);
UBEND_running_ST = zeros(numgeofiles*datapoints,1);
UBEND_running_RT = zeros(numgeofiles*datapoints,1);
UBEND_F_running = zeros(numgeofiles*datapoints,1);
RYGAN_ST = zeros(datapoints,numgeofiles);
RYGAN_RT = zeros(datapoints,numgeofiles);
RYGAN_F = zeros(datapoints,numgeofiles);
RYGAN_Q = zeros(datapoints,numgeofiles);
RYGAN_Q_Daily = zeros(numgeofiles,1);
RYGAN_avgF_Daily = zeros(numgeofiles,1);
RYGAN_running_ST = zeros(numgeofiles*datapoints,1);
RYGAN_running_RT = zeros(numgeofiles*datapoints,1);
RYGAN_F_running = zeros(numgeofiles*datapoints,1);

%%Internal Building Heat Flow Section


%Internal Campus 1 Building 1
INT_C1B1_HWS = zeros(datapoints,numgeofiles);
INT_C1B1_HWR = zeros(datapoints,numgeofiles);
INT_C1B1_F = zeros(datapoints,numgeofiles);
INT_C1B1_Q = zeros(datapoints,numgeofiles);
INT_C1B1_Q_Daily = zeros(numgeofiles,1);
%Internal Campus 1 Building 2
INT_C1B2_HWS = zeros(datapoints,numgeofiles);
INT_C1B2_HWR = zeros(datapoints,numgeofiles);
INT_C1B2_F = zeros(datapoints,numgeofiles);
INT_C1B2_Q = zeros(datapoints,numgeofiles);
INT_C1B2_Q_Daily = zeros(numgeofiles,1);
%Internal Campus 1 Building 4
```

```
INT_C1B4_HWS = zeros(datapoints,numgeofiles);
INT_C1B4_HWR = zeros(datapoints,numgeofiles);
INT_C1B4_F = zeros(datapoints,numgeofiles);
INT_C1B4_Q = zeros(datapoints,numgeofiles);
INT_C1B4_Q_Daily = zeros(numgeofiles,1);
%Internal Campus 1 Building 5
INT_C1B5_HWS = zeros(datapoints,numgeofiles);
INT_C1B5_HWR = zeros(datapoints,numgeofiles);
INT_C1B5_F = zeros(datapoints,numgeofiles);
INT_C1B5_Q = zeros(datapoints,numgeofiles);
INT_C1B5_Q_Daily = zeros(numgeofiles,1);
%Internal Campus 1 Building 6
INT_C1B6_HWS = zeros(datapoints,numgeofiles);
INT_C1B6_HWR = zeros(datapoints,numgeofiles);
INT_C1B6_F = zeros(datapoints,numgeofiles);
INT_C1B6_Q = zeros(datapoints,numgeofiles);
INT_C1B6_Q_Daily = zeros(numgeofiles,1);

%%Internal Campus 2 Total Hot Water
INT_C2TOT_HWS = zeros(datapoints,numgeofiles);
INT_C2TOT_HWR = zeros(datapoints,numgeofiles);
INT_C2TOT_F = zeros(datapoints,numgeofiles);
INT_C2TOT_Q = zeros(datapoints,numgeofiles);
INT_C2TOT_Q_Daily = zeros(numgeofiles,1);
%%Internal Campus 2 Total Chilled Water
INT_C2TOT_CHWS = zeros(datapoints,numgeofiles);
INT_C2TOT_CHWR = zeros(datapoints,numgeofiles);
INT_C2TOT_CWF = zeros(datapoints,numgeofiles);
INT_C2TOT_CWQ = zeros(datapoints,numgeofiles);
INT_C2TOT_CWQ_Daily = zeros(numgeofiles,1);
%%Internal Campus 2 Building K (Kouhotek) Hot Water
INT_C2K_HWS = zeros(datapoints,numgeofiles);
INT_C2K_HWR = zeros(datapoints,numgeofiles);
INT_C2K_F = zeros(datapoints,numgeofiles);
INT_C2K_Q = zeros(datapoints,numgeofiles);
INT_C2K_Q_Daily = zeros(numgeofiles,1);
%%Internal Campus 2 Building K (Kouhotek) Chilled Water
INT_C2K_CHWS = zeros(datapoints,numgeofiles);
INT_C2K_CHWR = zeros(datapoints,numgeofiles);
INT_C2K_CWF = zeros(datapoints,numgeofiles);
INT_C2K_CWQ = zeros(datapoints,numgeofiles);
INT_C2K_CWQ_Daily = zeros(numgeofiles,1);

%%Internal Learning Center
INT_LC_HWS = zeros(datapoints,numgeofiles);
INT_LC_HWR = zeros(datapoints,numgeofiles);
INT_LC_F = zeros(datapoints,numgeofiles);
INT_LC_Q = zeros(datapoints,numgeofiles);
INT_LC_Q_Daily = zeros(numgeofiles,1);

%%Internal Campus 4/5 Hot Water
INT_C45_HWS = zeros(datapoints,numgeofiles);
INT_C45_HWR = zeros(datapoints,numgeofiles);
INT_C45_F = zeros(datapoints,numgeofiles);
INT_C45_Q = zeros(datapoints,numgeofiles);
INT_C45_Q_Daily = zeros(numgeofiles,1);
```

```
%%Internal Campus 4/5  Chilled Water
INT_C45_CHWS = zeros(datapoints,numgeofiles);
INT_C45_CHWR = zeros(datapoints,numgeofiles);
INT_C45_CWF = zeros(datapoints,numgeofiles);
INT_C45_CWQ = zeros(datapoints,numgeofiles);
INT_C45_CWQ_Daily = zeros(numgeofiles,1);

%%Internal Farm Campus Hot Water
INT_DS_HWS = zeros(datapoints,numgeofiles);
INT_DS_HWR = zeros(datapoints,numgeofiles);
INT_DS_F = zeros(datapoints,numgeofiles);
INT_DS_Q = zeros(datapoints,numgeofiles);
INT_DS_Q_Daily = zeros(numgeofiles,1);
%%Internal Farm Campus  Chilled Water
INT_DS_CHWS = zeros(datapoints,numgeofiles);
INT_DS_CHWR = zeros(datapoints,numgeofiles);
INT_DS_CWF = zeros(datapoints,numgeofiles);
INT_DS_CWQ = zeros(datapoints,numgeofiles);
INT_DS_CWQ_Daily = zeros(numgeofiles,1);

%%Internal FARM Hot Water
INT_FARM_HWS = zeros(datapoints,numgeofiles);
INT_FARM_HWR = zeros(datapoints,numgeofiles);
INT_FARM_F = zeros(datapoints,numgeofiles);
INT_FARM_Q = zeros(datapoints,numgeofiles);
INT_FARM_Q_Daily = zeros(numgeofiles,1);
%%Internal FARM 4/5  Chilled Water
INT_FARM_CHWS = zeros(datapoints,numgeofiles);
INT_FARM_CHWR = zeros(datapoints,numgeofiles);
INT_FARM_CWF = zeros(datapoints,numgeofiles);
INT_FARM_CWQ = zeros(datapoints,numgeofiles);
INT_FARM_CWQ_Daily = zeros(numgeofiles,1);

%%Internal Campus UB3 Hot Water
INT_UB3_HWS = zeros(datapoints,numgeofiles);
INT_UB3_HWR = zeros(datapoints,numgeofiles);
INT_UB3_F = zeros(datapoints,numgeofiles);
INT_UB3_Q = zeros(datapoints,numgeofiles);
INT_UB3_Q_Daily = zeros(numgeofiles,1);
%%Internal Campus UB3  Chilled Water
INT_UB3_CHWS = zeros(datapoints,numgeofiles);
INT_UB3_CHWR = zeros(datapoints,numgeofiles);
INT_UB3_CWF = zeros(datapoints,numgeofiles);
INT_UB3_CWQ = zeros(datapoints,numgeofiles);
INT_UB3_CWQ_Daily = zeros(numgeofiles,1);
%%Campus UB3  Heat Exchangers
INT_UB3_HXS = zeros(datapoints,numgeofiles);
INT_UB3_HXR = zeros(datapoints,numgeofiles);
INT_UB3_HXF = zeros(datapoints,numgeofiles);
INT_UB3_HXQ = zeros(datapoints,numgeofiles);
INT_UB3_HXQ_Daily = zeros(numgeofiles,1);

%%Internal Pluto Hot Water
INT_PL_HWS = zeros(datapoints,numgeofiles);
INT_PL_HWR = zeros(datapoints,numgeofiles);
INT_PL_F = zeros(datapoints,numgeofiles);
```

```
INT_PL_Q = zeros(datapoints,numgeofiles);
INT_PL_Q_Daily = zeros(numgeofiles,1);
%%Internal Pluto Chilled Water
INT_PL_CHWS = zeros(datapoints,numgeofiles);
INT_PL_CHWR = zeros(datapoints,numgeofiles);
INT_PL_CWF = zeros(datapoints,numgeofiles);
INT_PL_CWQ = zeros(datapoints,numgeofiles);
INT_PL_CWQ_Daily = zeros(numgeofiles,1);


%%Predefine Campus Energy Variables
%%GeoBus'
GBA = zeros(datapoints,numgeofiles);
GBB = zeros(datapoints,numgeofiles);
GBC = zeros(datapoints,numgeofiles);
GBD = zeros(datapoints,numgeofiles);
GBF = zeros(datapoints,numgeofiles);
GBA_ME_Daily = zeros(numgeofiles,1);
GBB_ME_Daily = zeros(numgeofiles,1);
GBC_ME_Daily = zeros(numgeofiles,1);
GBD_ME_Daily = zeros(numgeofiles,1);
GBF_ME_Daily = zeros(numgeofiles,1);
GB_Total_Daily = zeros(numgeofiles,1);
%%Campus 1
C1CEP = zeros(datapoints,numgeofiles);
C1B1 = zeros(datapoints,numgeofiles);
C1B2 = zeros(datapoints,numgeofiles);
C1B3 = zeros(datapoints,numgeofiles);
C1B4 = zeros(datapoints,numgeofiles);
C1B5 = zeros(datapoints,numgeofiles);
C1B6 = zeros(datapoints,numgeofiles);
C1CEP_ME_Daily = zeros(numgeofiles,1);
C1B1_ME_Daily = zeros(numgeofiles,1);
C1B2_ME_Daily = zeros(numgeofiles,1);
C1B3_ME_Daily = zeros(numgeofiles,1);
C1B4_ME_Daily = zeros(numgeofiles,1);
C1B5_ME_Daily = zeros(numgeofiles,1);
C1B6_ME_Daily = zeros(numgeofiles,1);
C1_ME_Daily = zeros(numgeofiles,1);
%%Campus 2
C2_ME = zeros(datapoints,numgeofiles);
C2_ME_Daily = zeros(numgeofiles,1);
C2CEP = zeros(datapoints,numgeofiles);
C2H = zeros(datapoints,numgeofiles);
C2I = zeros(datapoints,numgeofiles);
C2J = zeros(datapoints,numgeofiles);
C2K = zeros(datapoints,numgeofiles);
%%Learning Campus/Voyager Hall
LC = zeros(datapoints,numgeofiles);
LC_ME_Daily = zeros(numgeofiles,1);
%%DeepSpace
DS = zeros(datapoints,numgeofiles);
DS_ME_Daily = zeros(numgeofiles,1);
%%Farm Campus
FARMCEP = zeros(datapoints,numgeofiles);
FARM_ME_Daily = zeros(numgeofiles,1);
```

```
%%C4
C4 = zeros(datapoints,numgeofiles);
C4_ME_Daily = zeros(numgeofiles,1);
%%UB3
UB3 = zeros(datapoints,numgeofiles);
UB3_ME_Daily = zeros(numgeofiles,1);
%%Total Mechanical Energy
Campus_Total_ME = zeros(numgeofiles,1);
%%Day Index
Day = zeros(numgeofiles,1);
%%Process Data Loop
for k=1:numgeofiles
%%Read Files
filename = ['E:\MCDAN FLASH\Research\GeoExchange\Epic Operations
Data\Operations\Geo Data\2017\Months\Apr\Geo_Data_2017-4-
',num2str(k),'.csv'];
X = xlsread(filename);
X(isnan(X)) = 0;
%%Borefield 1
BF1ST(:,k) = (X(:,1)-32).*(5/9);         %Supply Temp [C]
BF1RT(:,k) = (X(:,2)-32).*(5/9);         %Return Temp [C]
BF1F(:,k) = X(:,3).*6.30901964*10^-5;    %Flow [m3/s]
BF1Q(:,k) = BF1F(:,k).*Rho.*Cp.*(BF1RT(:,k)-BF1ST(:,k));    %Hourly Heat Flow
BF1(k) = mean(BF1Q(:,k))*24;             %%Vector that contains kWh for each
day.
BF2ST(:,k) = (X(:,4)-32).*(5/9);         %Supply Temp [C]
BF2RT(:,k) = (X(:,5)-32).*(5/9);         %Return Temp [C]
BF2F(:,k) = X(:,6).*6.30901964*10^-5;    %Flow [m3/s]
BF2Q(:,k) = BF2F(:,k).*Rho.*Cp.*(BF2RT(:,k)-BF2ST(:,k));    %Hourly Heat Flow
BF2(k) = mean(BF2Q(:,k))*24;             %%Vector that contains kWh for each
day.
BF3ST(:,k) = (X(:,12)-32).*(5/9);        %Supply Temp [C]
BF3RT(:,k) = (X(:,13)-32).*(5/9);        %Return Temp [C]
BF3F(:,k) = X(:,14).*6.30901964*10^-5;   %Flow [m3/s]
BF3Q(:,k) = BF3F(:,k).*Rho.*Cp.*(BF3RT(:,k)-BF3ST(:,k));    %Hourly Heat Flow
BF3(k) = mean(BF3Q(:,k))*24;         %%Vector that contains kWh for each day.
BF4ST(:,k) = (X(:,15)-32).*(5/9);    %Supply Temp [C]
BF4RT(:,k) = (X(:,16)-32).*(5/9);    %Return Temp [C]
BF4F(:,k) = X(:,17).*6.30901964*10^-5;   %Flow [m3/s]
BF4Q(:,k) = BF4F(:,k).*Rho.*Cp.*(BF4RT(:,k)-BF4ST(:,k));    %Hourly Heat Flow
BF4(k) = mean(BF4Q(:,k))*24;           %%Vector that contains kWh for each
day.
P10ST(:,k) = (X(:,7)-32).*(5/9);     %Supply Temp [C]
P10RT(:,k) = (X(:,8)-32).*(5/9);     %Return Temp [C]
P11ST(:,k) = (X(:,9)-32).*(5/9);     %Supply Temp [C]
P11RT(:,k) = (X(:,10)-32).*(5/9);    %Return Temp [C]
PF(:,k) = X(:,11).*6.30901964*10^-5;     %Flow [m3/s]
PQ(:,k) = (PF(:,k)/2).*Rho.*Cp.*(P10RT(:,k)-P10ST(:,k)) +
(PF(:,k)/2).*Rho.*Cp.*(P11RT(:,k)-P11ST(:,k)); %Hourly Heat Flow
Pond(k) = mean(PQ(:,k))*24; %%Vector that contains kWh for each day.
GeoHeat(k) = BF1(k)+ BF2(k) + BF3(k) + BF4(k) + Pond(k); %%Total Heat of
Borefield System for each day



%%Geowater to Outside of Buildings Section
```

```
%%Building 1
C1_B1_ST(:,k) = (X(:,19)-32).*(5/9);    %Supply Temp [C]
C1_B1_RT(:,k) = (X(:,20)-32).*(5/9);        %Return Temp [C]
C1_B1_F(:,k) = X(:,18).*6.30901964*10^-5;   %Flow [m3/s]
C1_B1_Q(:,k) = abs(C1_B1_F(:,k).*Rho.*Cp.*(C1_B1_RT(:,k)-C1_B1_ST(:,k)));
%Hourly Heat Flow
C1_B1_Q_Daily(k) = mean(C1_B1_Q(:,k))*24;    %%Daily kWh provided due to heat
flow
%%Building 2
C1_B2_ST(:,k) = (X(:,22)-32).*(5/9);    %Supply Temp [C]
C1_B2_RT(:,k) = (X(:,23)-32).*(5/9);        %Return Temp [C]
C1_B2_F(:,k) = X(:,21).*6.30901964*10^-5;   %Flow [m3/s]
C1_B2_Q(:,k) = abs(C1_B2_F(:,k).*Rho.*Cp.*(C1_B2_RT(:,k)-C1_B2_ST(:,k)));
%Hourly Heat Flow
C1_B2_Q_Daily(k) = mean(C1_B2_Q(:,k))*24;  %%Daily kWh provided due to heat
flow
%%UB3
C1_B3_ST(:,k) = (X(:,43)-32).*(5/9);    %Supply Temp [C]
C1_B3_RT(:,k) = (X(:,44)-32).*(5/9);        %Return Temp [C]
C1_B3_F(:,k) = X(:,42).*6.30901964*10^-5;   %Flow [m3/s]
C1_B3_Q(:,k) = abs(C1_B3_F(:,k).*Rho.*Cp.*(C1_B3_RT(:,k)-C1_B3_ST(:,k)));
%Hourly Heat Flow
C1_B3_Q_Daily(k) = mean(C1_B3_Q(:,k))*24;  %%Daily kWh provided due to heat
flow
%%Building 4
C1_B4_ST(:,k) = (X(:,25)-32).*(5/9);    %Supply Temp [C]
C1_B4_RT(:,k) = (X(:,26)-32).*(5/9);        %Return Temp [C]
C1_B4_F(:,k) = X(:,24).*6.30901964*10^-5;   %Flow [m3/s]
C1_B4_Q(:,k) = abs(C1_B4_F(:,k).*Rho.*Cp.*(C1_B4_RT(:,k)-C1_B4_ST(:,k)));
%Hourly Heat Flow
C1_B4_Q_Daily(k) = mean(C1_B4_Q(:,k))*24;  %%Daily kWh provided due to heat
flow
%%Building 5
C1_B5_ST(:,k) = (X(:,28)-32).*(5/9);    %Supply Temp [C]
C1_B5_RT(:,k) = (X(:,29)-32).*(5/9);        %Return Temp [C]
C1_B5_F(:,k) = X(:,27).*6.30901964*10^-5;   %Flow [m3/s]
C1_B5_Q(:,k) = abs(C1_B5_F(:,k).*Rho.*Cp.*(C1_B5_RT(:,k)-C1_B5_ST(:,k)));
%Hourly Heat Flow
C1_B5_Q_Daily(k) = mean(C1_B5_Q(:,k))*24;  %%Daily kWh provided due to heat
flow
%%Building 6
C1_B6_ST(:,k) = (X(:,31)-32).*(5/9);    %Supply Temp [C]
C1_B6_RT(:,k) = (X(:,32)-32).*(5/9);        %Return Temp [C]
C1_B6_F(:,k) = X(:,30).*6.30901964*10^-5;   %Flow [m3/s]
C1_B6_Q(:,k) = abs(C1_B6_F(:,k).*Rho.*Cp.*(C1_B6_RT(:,k)-C1_B6_ST(:,k)));
%Hourly Heat Flow
C1_B6_Q_Daily(k) = mean(C1_B6_Q(:,k))*24;  %%Daily kWh provided due to heat
flow
%%Campus Heat Flow
C1_Q(:,k) = C1_B1_Q(:,k) + C1_B2_Q(:,k) + C1_B3_Q(:,k) + C1_B4_Q(:,k) +
C1_B5_Q(:,k) + C1_B6_Q(:,k);
C1_Q_Daily(k) = mean(C1_Q(:,k))*24;  %%Daily kWh provided due to heat flow
%%Campus 2
C2_ST(:,k) = (X(:,34)-32).*(5/9);       %Supply Temp [C]
C2_RT(:,k) = (X(:,35)-32).*(5/9);        %Return Temp [C]
C2_F(:,k) = X(:,33).*6.30901964*10^-5;   %Flow [m3/s]
```

```
C2_Q(:,k) = abs(C2_F(:,k).*Rho.*Cp.*(C2_RT(:,k)-C2_ST(:,k)));   %Hourly Heat
Flow
C2_Q_Daily(k) = mean(C2_Q(:,k))*24;  %%Daily kWh provided due to heat flow
%%Learning Campus
LC_ST(:,k) = (X(:,51)-32).*(5/9);       %Supply Temp [C]
LC_RT(:,k) = (X(:,52)-32).*(5/9);        %Return Temp [C]
LC_F(:,k) = X(:,50).*6.30901964*10^-5;   %Flow [m3/s]
LC_Q(:,k) = abs(LC_F(:,k).*Rho.*Cp.*(LC_RT(:,k)-LC_ST(:,k)));   %Hourly Heat
Flow
LC_Q_Daily(k) = mean(LC_Q(:,k))*24;  %%Daily kWh provided due to heat flow
%% Deep Space
DS_ST(:,k) = (X(:,40)-32).*(5/9);       %Supply Temp [C]
DS_RT(:,k) = (X(:,41)-32).*(5/9);        %Return Temp [C]
DS_F(:,k) = X(:,39).*6.30901964*10^-5;   %Flow [m3/s]
DS_Q(:,k) = abs(DS_F(:,k).*Rho.*Cp.*(DS_RT(:,k)-DS_ST(:,k)));   %Hourly Heat
Flow
DS_Q_Daily(k) = mean(DS_Q(:,k))*24;  %%Daily kWh provided due to heat flow
%% FARM Campus
FARM_ST(:,k) = (X(:,48)-32).*(5/9);       %Supply Temp [C]
FARM_RT(:,k) = (X(:,49)-32).*(5/9);        %Return Temp [C]
FARM_F(:,k) = X(:,47).*6.30901964*10^-5;   %Flow [m3/s]
FARM_Q(:,k) = abs(FARM_F(:,k).*Rho.*Cp.*(FARM_RT(:,k)-FARM_ST(:,k)));
%Hourly Heat Flow
FARM_Q_Daily(k) = mean(FARM_Q(:,k))*24;  %%Daily kWh provided due to heat
flow
%%Total Heat Flow Daily to all Buildings
Buildings_Q_Daily(k) = FARM_Q_Daily(k) + DS_Q_Daily(k) + LC_Q_Daily(k) +
C2_Q_Daily(k) + C1_Q_Daily(k);



% Absolute Value Performance of UBend vs Rygan Comparison section



UBEND_ST(:,k) = (X(:,73)-32).*(5/9);       %Supply Temp [C]
UBEND_RT(:,k) = (X(:,74)-32).*(5/9);        %Return Temp [C]
UBEND_F(:,k) = X(:,72).*6.30901964*10^-5;   %Flow [m3/s]
UBEND_Q(:,k) = abs(UBEND_F(:,k).*Rho.*Cp.*(UBEND_RT(:,k)-UBEND_ST(:,k)));
%Hourly Heat Flow
UBEND_Q_Daily(k) = mean(UBEND_Q(:,k))*24;  %%Daily kWh provided due to heat
flow
UBEND_avgF_Daily(k) = mean(UBEND_F(:,k));      %%Average UBEND FLow
UBEND_running_ST((datapoints*(k-1))+1:datapoints*k) = UBEND_ST(:,k);
%%Running Compilation of UBEND return temperatures.
UBEND_running_RT((datapoints*(k-1))+1:datapoints*k) = UBEND_RT(:,k);
%%Running Compilation of UBEND return temperatures.
UBEND_F_running((datapoints*(k-1))+1:datapoints*k) = UBEND_F(:,k);
%%Running Compilation of UBEND Flow.

RYGAN_ST(:,k) = (X(:,76)-32).*(5/9);       %Supply Temp [C]
RYGAN_RT(:,k) = (X(:,77)-32).*(5/9);        %Return Temp [C]
RYGAN_F(:,k) = X(:,75).*6.30901964*10^-5;   %Flow [m3/s]
RYGAN_Q(:,k) = abs(RYGAN_F(:,k).*Rho.*Cp.*(RYGAN_RT(:,k)-RYGAN_ST(:,k)));
%Hourly Heat Flow
```

```
RYGAN_Q_Daily(k) = mean(RYGAN_Q(:,k))*24;  %%Daily kWh provided due to heat
flow
RYGAN_avgF_Daily(k) = mean(RYGAN_F(:,k));      %%Average Rygan FLow
RYGAN_running_ST((datapoints*(k-1))+1:datapoints*k) = RYGAN_ST(:,k);
%%Running Compilation of RYGAN supply temperatures.
RYGAN_running_RT((datapoints*(k-1))+1:datapoints*k) = RYGAN_RT(:,k);
%%Running Compilation of RYGAN  return temperatures.
RYGAN_F_running((datapoints*(k-1))+1:datapoints*k) = RYGAN_F(:,k);
%%Running Compilation of RYGAN  flow.


%Internal Building Heat Flow Section


%%Internal Campus 1 Building 1
INT_C1B1_HWS(:,k) = (X(:,78)-32).*(5/9);       %Hot Water Supply Temp [C]
INT_C1B1_HWR(:,k) = (X(:,79)-32).*(5/9);       %Hot Water Return Temp [C]
INT_C1B1_F(:,k) = X(:,80).*6.30901964*10^-5;      %Hot Water Flow [m3/s]
INT_C1B1_Q(:,k) = abs(INT_C1B1_F(:,k).*Rho.*Cp.*(INT_C1B1_HWR(:,k)-
INT_C1B1_HWS(:,k)));   %Hourly Heat Flow
INT_C1B1_Q_Daily(k) = mean(INT_C1B1_Q(:,k))*24;  %%Daily kWh provided due to
heat flow
%%Internal Campus 1 Building 2
INT_C1B2_HWS(:,k) = (X(:,81)-32).*(5/9);       %Hot Water Supply Temp [C]
INT_C1B2_HWR(:,k) = (X(:,82)-32).*(5/9);       %Hot Water Return Temp [C]
INT_C1B2_F(:,k) = X(:,83).*6.30901964*10^-5;      %Hot Water Flow [m3/s]
INT_C1B2_Q(:,k) = abs(INT_C1B2_F(:,k).*Rho.*Cp.*(INT_C1B2_HWR(:,k)-
INT_C1B2_HWS(:,k)));   %Hourly Heat Flow
INT_C1B2_Q_Daily(k) = mean(INT_C1B2_Q(:,k))*24;  %%Daily kWh provided due to
heat flow
%%Internal Campus 1 Building 4
INT_C1B4_HWS(:,k) = (X(:,84)-32).*(5/9);       %Hot Water Supply Temp [C]
INT_C1B4_HWR(:,k) = (X(:,85)-32).*(5/9);       %Hot Water Return Temp [C]
INT_C1B4_F(:,k) = X(:,86).*6.30901964*10^-5;      %Hot Water Flow [m3/s]
INT_C1B4_Q(:,k) = abs(INT_C1B4_F(:,k).*Rho.*Cp.*(INT_C1B4_HWR(:,k)-
INT_C1B4_HWS(:,k)));   %Hourly Heat Flow
INT_C1B4_Q_Daily(k) = mean(INT_C1B4_Q(:,k))*24;  %%Daily kWh provided due to
heat flow
%%Internal Campus 1 Building 5
INT_C1B5_HWS(:,k) = (X(:,87)-32).*(5/9);       %Hot Water Supply Temp [C]
INT_C1B5_HWR(:,k) = (X(:,88)-32).*(5/9);       %Hot Water Return Temp [C]
INT_C1B5_F(:,k) = X(:,89).*6.30901964*10^-5;      %Hot Water Flow [m3/s]
INT_C1B5_Q(:,k) = abs(INT_C1B5_F(:,k).*Rho.*Cp.*(INT_C1B5_HWR(:,k)-
INT_C1B5_HWS(:,k)));   %Hourly Heat Flow
INT_C1B5_Q_Daily(k) = mean(INT_C1B5_Q(:,k))*24;  %%Daily kWh provided due to
heat flow
%%Internal Campus 1 Building 6
INT_C1B6_HWS(:,k) = (X(:,90)-32).*(5/9);       %Hot Water Supply Temp [C]
INT_C1B6_HWR(:,k) = (X(:,91)-32).*(5/9);       %Hot Water Return Temp [C]
INT_C1B6_F(:,k) = X(:,92).*6.30901964*10^-5;      %Hot Water Flow [m3/s]
INT_C1B6_Q(:,k) = abs(INT_C1B6_F(:,k).*Rho.*Cp.*(INT_C1B6_HWR(:,k)-
INT_C1B6_HWS(:,k)));   %Hourly Heat Flow
INT_C1B6_Q_Daily(k) = mean(INT_C1B6_Q(:,k))*24;  %%Daily kWh provided due to
heat flow

%%Internal Campus 2 Total Hot Water
```

```
INT_C2TOT_HWS(:,k) = (X(:,93)-32).*(5/9);       %Hot Water Supply Temp [C]
INT_C2TOT_HWR(:,k) = (X(:,94)-32).*(5/9);       %Hot Water Return Temp [C]
INT_C2TOT_F(:,k) = X(:,95).*6.30901964*10^-5;      %Hot Water Flow [m3/s]
INT_C2TOT_Q(:,k) = abs(INT_C2TOT_F(:,k).*Rho.*Cp.*(INT_C2TOT_HWR(:,k)-
INT_C2TOT_HWS(:,k)));   %Hourly Heat Flow
INT_C2TOT_Q_Daily(k) = mean(INT_C2TOT_Q(:,k))*24;  %%Daily kWh provided due
to heat flow
%%Internal Campus 2 Total Chilled Water
INT_C2TOT_CHWS(:,k) = (X(:,99)-32).*(5/9);       %Hot Water Supply Temp [C]
INT_C2TOT_CHWR(:,k) = (X(:,100)-32).*(5/9);       %Hot Water Return Temp [C]
INT_C2TOT_CWF(:,k) = X(:,101).*6.30901964*10^-5;      %Hot Water Flow [m3/s]
INT_C2TOT_CWQ(:,k) = abs(INT_C2TOT_CWF(:,k).*Rho.*Cp.*(INT_C2TOT_CHWR(:,k)-
INT_C2TOT_CHWS(:,k)));   %Hourly Heat Flow
INT_C2TOT_CWQ_Daily(k) = mean(INT_C2TOT_CWQ(:,k))*24;  %%Daily kWh provided
due to heat flow
%%Internal Campus 2 Building K (Kouhotek) Hot Water
INT_C2K_HWS(:,k) = (X(:,96)-32).*(5/9);       %Hot Water Supply Temp [C]
INT_C2K_HWR(:,k) = (X(:,97)-32).*(5/9);       %Hot Water Return Temp [C]
INT_C2K_F(:,k) = X(:,98).*6.30901964*10^-5;      %Hot Water Flow [m3/s]
INT_C2K_Q(:,k) = abs(INT_C2K_F(:,k).*Rho.*Cp.*(INT_C2K_HWR(:,k)-
INT_C2K_HWS(:,k)));   %Hourly Heat Flow
INT_C2K_Q_Daily(k) = mean(INT_C2K_Q(:,k))*24;  %%Daily kWh provided due to
heat flow
%%Internal Campus 2 Building K (Kouhotek) Chilled Water
INT_C2K_CHWS(:,k) = (X(:,102)-32).*(5/9);       %Hot Water Supply Temp [C]
INT_C2K_CHWR(:,k) = (X(:,103)-32).*(5/9);       %Hot Water Return Temp [C]
INT_C2K_CWF(:,k) = X(:,104).*6.30901964*10^-5;      %Hot Water Flow [m3/s]
INT_C2K_CWQ(:,k) = abs(INT_C2K_CWF(:,k).*Rho.*Cp.*(INT_C2K_CHWR(:,k)-
INT_C2K_CHWS(:,k)));   %Hourly Heat Flow
INT_C2K_CWQ_Daily(k) = mean(INT_C2K_CWQ(:,k))*24;  %%Daily kWh provided due
to heat flow

%%Internal Learning Center
INT_LC_HWS(:,k) = (X(:,105)-32).*(5/9);       %Hot Water Supply Temp [C]
INT_LC_HWR(:,k) = (X(:,106)-32).*(5/9);       %Hot Water Return Temp [C]
INT_LC_F(:,k) = X(:,107).*6.30901964*10^-5;      %Hot Water Flow [m3/s]
INT_LC_Q(:,k) = abs(INT_LC_F(:,k).*Rho.*Cp.*(INT_LC_HWR(:,k)-
INT_LC_HWS(:,k)));   %Hourly Heat Flow
INT_LC_Q_Daily(k) = mean(INT_LC_Q(:,k))*24;  %%Daily kWh provided due to heat
flow

%%Internal Campus 4/5 Hot Water
INT_C45_HWS(:,k) = (X(:,108)-32).*(5/9);       %Hot Water Supply Temp [C]
INT_C45_HWR(:,k) = (X(:,109)-32).*(5/9);       %Hot Water Return Temp [C]
INT_C45_F(:,k) = X(:,110).*6.30901964*10^-5;      %Hot Water Flow [m3/s]
INT_C45_Q(:,k) = abs(INT_C45_F(:,k).*Rho.*Cp.*(INT_C45_HWR(:,k)-
INT_C45_HWS(:,k)));   %Hourly Heat Flow
INT_C45_Q_Daily(k) = mean(INT_C45_Q(:,k))*24;  %%Daily kWh provided due to
heat flow
%%Internal Campus 4/5 Chilled Water
INT_C45_CHWS(:,k) = (X(:,111)-32).*(5/9);       %Hot Water Supply Temp [C]
INT_C45_CHWR(:,k) = (X(:,112)-32).*(5/9);       %Hot Water Return Temp [C]
INT_C45_CWF(:,k) = X(:,113).*6.30901964*10^-5;      %Hot Water Flow [m3/s]
INT_C45_CWQ(:,k) = abs(INT_C45_CWF(:,k).*Rho.*Cp.*(INT_C45_CHWR(:,k)-
INT_C45_CHWS(:,k)));   %Hourly Heat Flow
```

```
INT_C45_CWQ_Daily(k) = mean(INT_C45_CWQ(:,k))*24;  %%Daily kWh provided due
to heat flow

%%Internal Deep Space Hot Water
INT_DS_HWS(:,k) = (X(:,114)-32).*(5/9);       %Hot Water Supply Temp [C]
INT_DS_HWR(:,k) = (X(:,115)-32).*(5/9);       %Hot Water Return Temp [C]
INT_DS_F(:,k) = X(:,116).*6.30901964*10^-5;      %Hot Water Flow [m3/s]
INT_DS_Q(:,k) = abs(INT_DS_F(:,k).*Rho.*Cp.*(INT_DS_HWR(:,k)-
INT_DS_HWS(:,k)));   %Hourly Heat Flow
INT_DS_Q_Daily(k) = mean(INT_DS_Q(:,k))*24;  %%Daily kWh provided due to heat
flow
%%Internal Deep Space Chilled Water
INT_DS_CHWS(:,k) = (X(:,117)-32).*(5/9);       %Hot Water Supply Temp [C]
INT_DS_CHWR(:,k) = (X(:,118)-32).*(5/9);       %Hot Water Return Temp [C]
INT_DS_CWF(:,k) = X(:,119).*6.30901964*10^-5;      %Hot Water Flow [m3/s]
INT_DS_CWQ(:,k) = abs(INT_DS_CWF(:,k).*Rho.*Cp.*(INT_DS_CHWR(:,k)-
INT_DS_CHWS(:,k)));   %Hourly Heat Flow
INT_DS_CWQ_Daily(k) = mean(INT_DS_CWQ(:,k))*24;  %%Daily kWh provided due to
heat flow

%%Internal Farm Campus Hot Water
INT_FARM_HWS(:,k) = (X(:,120)-32).*(5/9);       %Hot Water Supply Temp [C]
INT_FARM_HWR(:,k) = (X(:,121)-32).*(5/9);       %Hot Water Return Temp [C]
INT_FARM_F(:,k) = X(:,122).*6.30901964*10^-5;      %Hot Water Flow [m3/s]
INT_FARM_Q(:,k) = abs(INT_FARM_F(:,k).*Rho.*Cp.*(INT_FARM_HWR(:,k)-
INT_FARM_HWS(:,k)));   %Hourly Heat Flow
INT_FARM_Q_Daily(k) = mean(INT_FARM_Q(:,k))*24;  %%Daily kWh provided due to
heat flow
%%Internal Farm Campus Chilled Water
INT_FARM_CHWS(:,k) = (X(:,123)-32).*(5/9);       %Hot Water Supply Temp [C]
INT_FARM_CHWR(:,k) = (X(:,124)-32).*(5/9);       %Hot Water Return Temp [C]
INT_FARM_CWF(:,k) = X(:,125).*6.30901964*10^-5;      %Hot Water Flow [m3/s]
INT_FARM_CWQ(:,k) = abs(INT_FARM_CWF(:,k).*Rho.*Cp.*(INT_FARM_CHWR(:,k)-
INT_FARM_CHWS(:,k)));   %Hourly Heat Flow
INT_FARM_CWQ_Daily(k) = mean(INT_FARM_CWQ(:,k))*24;  %%Daily kWh provided due
to heat flow

%%Internal UB3 Hot Water
INT_UB3_HWS(:,k) = (X(:,126)-32).*(5/9);       %Hot Water Supply Temp [C]
INT_UB3_HWR(:,k) = (X(:,127)-32).*(5/9);       %Hot Water Return Temp [C]
INT_UB3_F(:,k) = X(:,128).*6.30901964*10^-5;      %Hot Water Flow [m3/s]
INT_UB3_Q(:,k) = abs(INT_UB3_F(:,k).*Rho.*Cp.*(INT_UB3_HWR(:,k)-
INT_UB3_HWS(:,k)));   %Hourly Heat Flow
INT_UB3_Q_Daily(k) = mean(INT_UB3_Q(:,k))*24;  %%Daily kWh provided due to
heat flow
%%Internal UB3 Chilled Water
INT_UB3_CHWS(:,k) = (X(:,129)-32).*(5/9);       %Hot Water Supply Temp [C]
INT_UB3_CHWR(:,k) = (X(:,130)-32).*(5/9);       %Hot Water Return Temp [C]
INT_UB3_CWF(:,k) = X(:,131).*6.30901964*10^-5;      %Hot Water Flow [m3/s]
INT_UB3_CWQ(:,k) = abs(INT_UB3_CWF(:,k).*Rho.*Cp.*(INT_UB3_CHWR(:,k)-
INT_UB3_CHWS(:,k)));   %Hourly Heat Flow
INT_UB3_CWQ_Daily(k) = mean(INT_UB3_CWQ(:,k))*24;  %%Daily kWh provided due
to heat flow
%%Internal UB3 Heat Exchangers
INT_UB3_HXS(:,k) = (X(:,136)-32).*(5/9);       %Hot Water Supply Temp [C]
INT_UB3_HXR(:,k) = (X(:,137)-32).*(5/9);       %Hot Water Return Temp [C]
```

```
INT_UB3_HXF(:,k) = X(:,138).*6.30901964*10^-5;      %Hot Water Flow [m3/s]
INT_UB3_HXQ(:,k) = abs(INT_UB3_HXF(:,k).*Rho.*Cp.*(INT_UB3_HXR(:,k)-
INT_UB3_HXS(:,k)));   %Hourly Heat Flow
INT_UB3_HXQ_Daily(k) = mean(INT_UB3_HXQ(:,k))*24;  %%Daily kWh provided due
to heat flow

%%Internal Pluto Hot Water
INT_PL_HWS(:,k) = (X(:,139)-32).*(5/9);       %Hot Water Supply Temp [C]
INT_PL_HWR(:,k) = (X(:,140)-32).*(5/9);       %Hot Water Return Temp [C]
INT_PL_F(:,k) = X(:,141).*6.30901964*10^-5;      %Hot Water Flow [m3/s]
INT_PL_Q(:,k) = abs(INT_PL_F(:,k).*Rho.*Cp.*(INT_PL_HWR(:,k)-
INT_PL_HWS(:,k)));   %Hourly Heat Flow
INT_PL_Q_Daily(k) = mean(INT_PL_Q(:,k))*24;  %%Daily kWh provided due to heat
flow
%%Internal Pluto Chilled Water
INT_PL_CHWS(:,k) = (X(:,142)-32).*(5/9);       %Hot Water Supply Temp [C]
INT_PL_CHWR(:,k) = (X(:,143)-32).*(5/9);       %Hot Water Return Temp [C]
INT_PL_CWF(:,k) = X(:,144).*6.30901964*10^-5;      %Hot Water Flow [m3/s]
INT_PL_CWQ(:,k) = abs(INT_PL_CWF(:,k).*Rho.*Cp.*(INT_PL_CHWR(:,k)-
INT_PL_CHWS(:,k)));   %Hourly Heat Flow
INT_PL_CWQ_Daily(k) = mean(INT_PL_CWQ(:,k))*24;  %%Daily kWh provided due to
heat flow



%%Building Mechanical Energy Section



GBA(:,k) = X(:,145);
GBA_ME_Daily(k) = sum(GBA(:,k));
GBB(:,k) = X(:,146);
GBB_ME_Daily(k) = sum(GBB(:,k));
GBC(:,k) = X(:,147);
GBC_ME_Daily(k) = sum(GBC(:,k));
GBD(:,k) = X(:,148);
GBD_ME_Daily(k) = sum(GBD(:,k));
GBF(:,k) = X(:,149);
GBF_ME_Daily(k) = sum(GBF(:,k));
GB_Total_Daily(k) = GBA_ME_Daily(k) + GBB_ME_Daily(k) + GBC_ME_Daily(k) +
GBD_ME_Daily(k) + GBF_ME_Daily(k);
%%Campus 1
C1CEP(:,k) = X(:,150);
C1CEP_ME_Daily(k) = sum(C1CEP(:,k));
C1B1(:,k) = X(:,151);
C1B1_ME_Daily(k) = sum(C1B1(:,k));
C1B2(:,k) = X(:,152);
C1B2_ME_Daily(k) = sum(C1B2(:,k));
C1B3(:,k) = X(:,153);
C1B3_ME_Daily(k) = sum(C1B3(:,k));
C1B4(:,k) = X(:,154);
C1B4_ME_Daily(k) = sum(C1B4(:,k));
C1B5(:,k) = X(:,155);
C1B5_ME_Daily(k) = sum(C1B5(:,k));
C1B6(:,k) = X(:,156);
```

```
C1B6_ME_Daily(k) = sum(C1B6(:,k));
C1_ME_Daily(k) = C1CEP_ME_Daily(k) + C1B6_ME_Daily(k) + C1B5_ME_Daily(k) +
C1B4_ME_Daily(k) + C1B3_ME_Daily(k) + C1B2_ME_Daily(k) + C1B1_ME_Daily(k);
%%Campus 2
C2CEP(:,k) = X(:,157);
C2H(:,k) = X(:,158);
C2I(:,k) = X(:,159);
C2J(:,k) = X(:,160);
C2K(:,k) = X(:,161);
C2_ME(:,k) = C2CEP(:,k) + C2H(:,k) + C2I(:,k) + C2J(:,k) + C2K(:,k);
C2_ME_Daily(k) = sum(C2_ME(:,k));
%%Learning Campus
LC(:,k) = X(:,162);
LC_ME_Daily(k) = sum(LC(:,k));
%%Deep Space
DS(:,k) = X(:,163);
DS_ME_Daily(k) = sum(DS(:,k));
%%Farm Campus
FARMCEP(:,k) = X(:,164);
FARM_ME_Daily(k) = sum(FARMCEP(:,k));
%%Campus 4
C4(:,k) = X(:,165);
C4_ME_Daily(k) = sum(C4(:,k));
%%UB3
UB3(:,k) = X(:,166);
UB3_ME_Daily(k) = sum(UB3(:,k));

%%Total
Campus_Total_ME(k) =
UB3_ME_Daily(k)+C4_ME_Daily(k)+FARM_ME_Daily(k)+DS_ME_Daily(k)+LC_ME_Daily(k)
+C2_ME_Daily(k)+C1_ME_Daily(k);

%%Day Index
Day(k) = k;
end


%Write Excel Document Summarizing Data
path = cd('E:\MCDAN FLASH\Research\GeoExchange\Epic Operations
Data\Operations\Geo Data\Matlab Processed Data\2017\Months\Apr\'); %%Change
path to desired folder of exported excel file - Change to Appropriate Month

warning('off','MATLAB:xlswrite:AddSheet') %%Turn off warning that alerts when
writing over a pre-existing excel file.

%%Borefield Heat Flow Tab
Borefield_Headers = {'Day','Borefield 1 Total Heat Transported
[kWh]','Borefield 2 Total Heat Transported [kWh]','Borefield 3 Total Heat
Transported [kWh]','Borefield 4 Total Heat Transported [kWh]','Pond Total
Heat Transported [kWh]','Overall Total Heat Transported [kWh]'};
xlswrite('Monthly Summary.xls',Borefield_Headers,'Borefield Heat Flow','A1');
Borefield_Summary = [Day,BF1,BF2,BF3,BF4,Pond,GeoHeat];
xlswrite('Monthly Summary.xls',Borefield_Summary,'Borefield Heat Flow','A2');

%%Geowater to External Building Sensors Tab
```

```
External_Building_GeoHeat_Headers = {'Day','Campus 1 Building 1 Heat Moved
[kWh]','Campus 1 Building 2 Heat Moved [kWh]','Campus 1 Building 3 Heat Moved
[kWh]','Campus 1 Building 4 Heat Moved [kWh]','Campus 1 Building 5 Heat Moved
[kWh]','Campus 1 Building 6 Heat Moved [kWh]','Campus 1 Total Heat Moved
[kWh]','Campus 2 Total Heat Moved [kWh]','Learning Center Total Heat Moved
[kWh]','Deep Space Total Heat Moved [kWh]','Farm Campus Total Heat Moved
[kWh]','Buildings Total Heat Moved [kWh]'};
xlswrite('Monthly Summary.xls',External_Building_GeoHeat_Headers,'External
Building GeoHeat Flow','A1');
External_GeoHeat_Summary =
[Day,C1_B1_Q_Daily,C1_B2_Q_Daily,C1_B3_Q_Daily,C1_B4_Q_Daily,C1_B5_Q_Daily,C1
_B6_Q_Daily,C1_Q_Daily,C2_Q_Daily,LC_Q_Daily,DS_Q_Daily,FARM_Q_Daily,Building
s_Q_Daily];
xlswrite('Monthly Summary.xls',External_GeoHeat_Summary,'External Building
GeoHeat Flow','A2');

%%UBEND vs Rygan Tab
GHX_comparison_Headers = {'Day','UBend Absolute Heat Moved [kWh]','Rygan
Absolute Heat Moved [kWh]','UBend Average Flow [m^3/s]','Rygan Average Flow
[m^3/s]',};
xlswrite('Monthly Summary.xls',GHX_comparison_Headers,'UBEND vs Rygan
Comparison','A1');
GHX_comparison_Summary =
[Day,UBEND_Q_Daily,RYGAN_Q_Daily,UBEND_avgF_Daily,RYGAN_avgF_Daily];
xlswrite('Monthly Summary.xls',GHX_comparison_Summary,'UBEND vs Rygan
Comparison','A2');

%%Internal Building Heat Flow Tab
Internal_Q_Headers = {'Day','C1B1 Heat Moved [kWh]','C1B2 Heat Moved
[kWh]','C1B4 Heat Moved [kWh]','C1B5 Heat Moved [kWh]','C1B6 Heat Moved
[kWh]','Campus 2 Total Hot Water Heat Moved [kWh]','Campus 2 Total Chilled
Water Heat Moved [kWh]','C2 Kohoutek Total Hot Water Heat Moved [kWh]','C2
Kohoutek Total Chilled Water Heat Moved [kWh]','Learning Center Heat Moved
[kWh]','Campus 4/5 Hot Water Heat Moved [kWh]','Campus 4/5 Hot Water Chilled
Moved [kWh]','Deep Space Hot Water Heat Moved [kWh]','Deep Space Chilled
Water Heat Moved [kWh]','FARM Hot Water Heat Moved [kWh]','FARM Chilled Water
Heat Moved [kWh]','UB3 Hot Water Heat Moved [kWh]','UB3 Chilled Water Heat
Moved [kWh]','UB3 Heat Exchanger Heat Moved [kWh]','Pluto Hot Water Heat
Moved [kWh]','Pluto Chilled Water Heat Moved [kWh]'};
xlswrite('Monthly Summary.xls',Internal_Q_Headers,'Internal Building Heat
Flows','A1');
Internal_Building_Heat_Summary =
[Day,INT_C1B1_Q_Daily,INT_C1B2_Q_Daily,INT_C1B4_Q_Daily,INT_C1B5_Q_Daily,INT_
C1B6_Q_Daily,INT_C2TOT_Q_Daily,INT_C2TOT_CWQ_Daily,INT_C2K_Q_Daily,INT_C2K_CW
Q_Daily,INT_LC_Q_Daily,INT_C45_Q_Daily,INT_C45_CWQ_Daily,INT_DS_Q_Daily,INT_D
S_CWQ_Daily,INT_FARM_Q_Daily,INT_FARM_CWQ_Daily,INT_UB3_Q_Daily,INT_UB3_CWQ_D
aily,INT_UB3_HXQ_Daily,INT_PL_Q_Daily,INT_PL_CWQ_Daily];
xlswrite('Monthly Summary.xls',Internal_Building_Heat_Summary,'Internal
Building Heat Flows','A2');

%%Mechanical Energy to Run Geothermal System Tab
Mechanical_Energy_Headers = {'Day','PumpHouse Mechanical Energy
[kWh]','Campus 1 CEP Mechanical Energy [kWh]','C1B1 Mechanical Energy
[kWh]','C1B2 Mechanical Energy [kWh]','C1B3 Mechanical Energy [kWh]','C1B4
Mechanical Energy [kWh]','C1B5 Mechanical Energy [kWh]','C1B5 Mechanical
Energy [kWh]','Campus 1 Total Mechanical Energy [kWh]','Campus 2 Total
```

```
Mechanical Energy [kWh]','Learning Center Mechanical Energy [kWh]','Deep
Space Mechanical Energy [kWh]','Farm Campus Mechanical Energy [kWh]','Campus
4 Mechanical Energy [kWh]','UB3 Mechanical Energy [kWh]','Overal Total Campus
Mechanical Energy [kWh]'};
xlswrite('Monthly Summary.xls',Mechanical_Energy_Headers,'Campus Mechanical
Energy','A1');
Mechanical_Energy_Summary =
[Day,GB_Total_Daily,C1CEP_ME_Daily,C1B1_ME_Daily,C1B2_ME_Daily,C1B3_ME_Daily,
C1B4_ME_Daily,C1B5_ME_Daily,C1B6_ME_Daily,C1_ME_Daily,C2_ME_Daily,LC_ME_Daily
,DS_ME_Daily,FARM_ME_Daily,C4_ME_Daily,UB3_ME_Daily,Campus_Total_ME];
xlswrite('Monthly Summary.xls',Mechanical_Energy_Summary,'Campus Mechanical
Energy','A2');
```

Appendix 2: Epic Campus Net Zero Calculations

Epic Systems is an extremely successful provider of healthcare software. Over half of the U.S. population that has healthcare is connected in some way to software developed by Epic (Epic Careers 2017). A significant portion of revenue from this success has been reinvested into the campus to create an attractive and welcoming destination for customers to learn about software as well as a whimsical environment to stimulate creative problem solving by software developers. This philosophy, pioneered by C.E.O. Judy Faulkner, primarily manifests itself in campus artwork and architecture. Office buildings themes include: a treehouse, a barnyard, Hogwarts, a medieval castle, and heaven, among many others.

In addition to the creation of a whimsical environment, Epic also has the goal of running a campus at as close to net-zero electrical energy as possible; meaning they produce as much as they consume. In an effort to accomplish this goal, Epic uses solar panels on the roof of their Zodiac parking garage, a 1.4 MW solar panel field, six 1.65-MW, Vestas V82 MK II wind turbines that are collectively known as the Galactic Wind Farm, and the geothermal exchange system that has been the main focus of this report. For the purpose of this research and analyzing Epic's performance towards the net-zero goal, data has been collected hourly since 01/15/2015 to the submission of this thesis on 05/05/2017. The collected data includes energy produced by solar panels and wind turbines, as well as on-site generators and electricity purchased by Epic from the local utility, Alliant Energy.

The majority of this data analysis has been performed by Max Brennan, who at the time was an undergraduate researcher on the Energy Geotechnics research team, and is now a master's degree candidate for the Mechanical Engineering Department at UW-Madison. Several of the following conclusions and figures are credited to his superb Fall 2015 and Spring 2016 end-of-semester reports.

Similar to the campus energy flow data discussed in Appendix 1, the net zero energy is collected by Epic's network utility software, Cimplicity, compiled daily, and emailed to almcdaniel@wisc.edu each morning at 01:00 with hourly data from the previous day. However, this data contains anomalies that represent infeasibly high or negative rates of power generation that must be corrected before the data can be analyzed. Particularly at the activation or termination of solar or wind generation, data points up to the magnitude of 30,000,000 kW are recorded. There are also strings of negative values or zeros in the midst of positive strings of power generation that suggest a faulty meter measurement more than an operational decision. The wind data was corrected by removing any spike in energy production over the rated capacity of Galactic Wind Farms (9.9 MW) and linear interpolation was used to replace zeros or negative values within positive energy production trends. Data representing Epic's purchased electrical energy from Alliant was initially collected and reported as nearly constant from 01/15/2015 to 03/10/2015. This was seen as a highly improbable operational condition, and when brought to Epic's attention, determined to be a measurement error. Replacement data was requested and received from Epic on 03/11/2015 that shows a much more variable purchasing pattern.

Solar data was analyzed from February to October 2015 to provide insight into daily and monthly production trends. Figure 40*: Average daily solar production at Epic.* displays a predictable trend of average daily use that mirrors the expected daily interaction of solar luminosity and the rotation of the earth. Figure 41*: Monthly total solar production in 2015.* shows a slightly less intuitive trend in monthly total solar energy produced at Epic. Total solar production stays relatively constant year-round between 200 and 250 MWh of energy per month. February and October totals are lower due to 2 weeks of curtailment in each month, and show a similar daily average as the other months when operational.

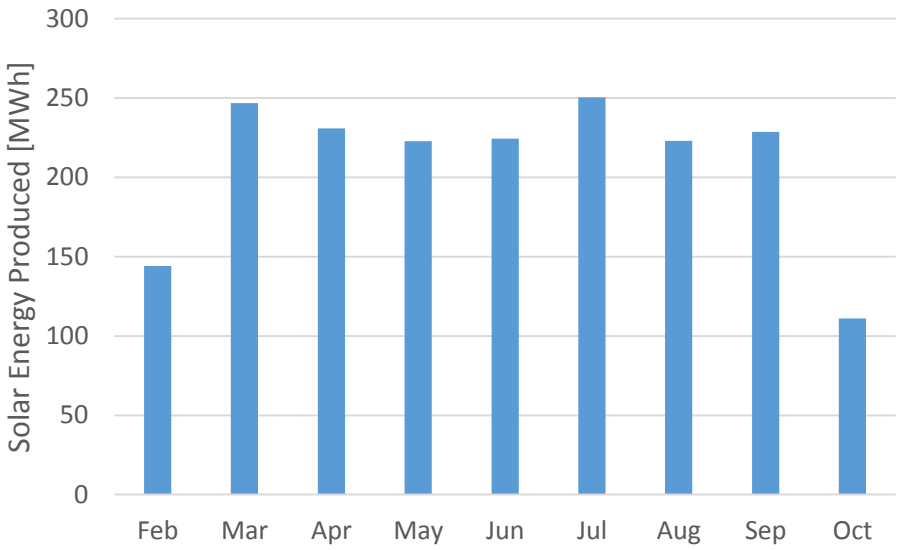

Figure 41: Monthly total solar production in 2015.

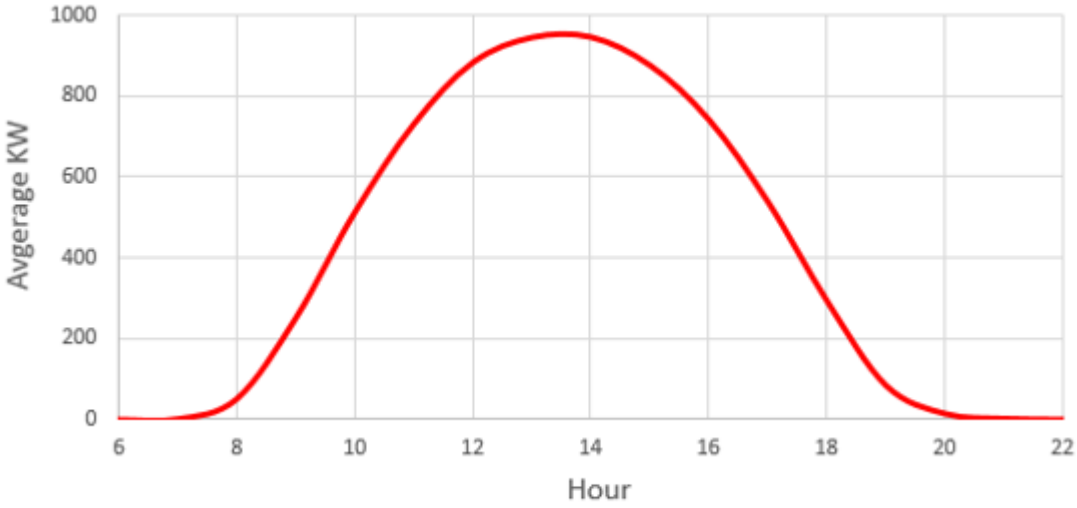

Figure 40: Average daily solar production at Epic.

Electricity purchased by Epic from Alliant Energy generally stays between 6,000 and 12,000 kW. There seems to be a base-line electrical need of approximately 6,000 kW to keep the campus operational, even when few employees are present. During the workday, the purchased electricity nearly doubles from employee presence. Weekends show a small increase from the base purchase, but to a much lesser extent than during the work week. Figure 42 shows this trend from Sunday, October 4th to Saturday October 10th, 2015. This weekly trend continues year-round, but varies in magnitude of base-load and employee load, as seen in Figure 43.

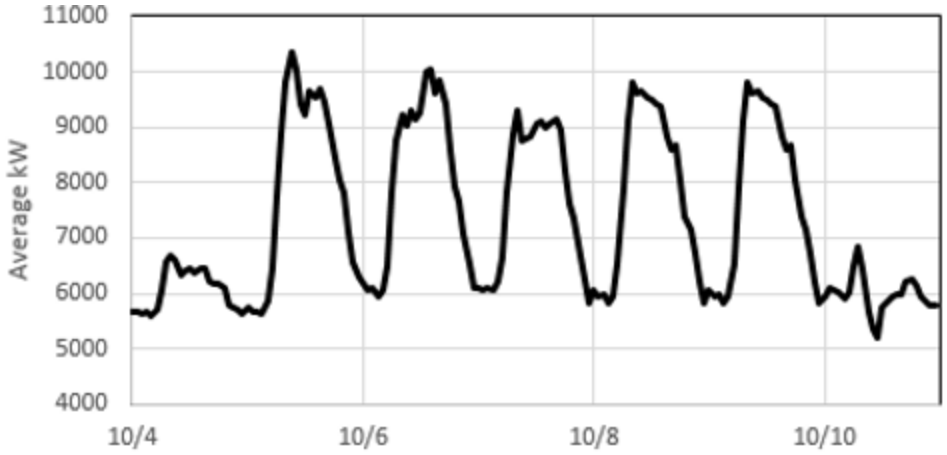

Figure 42: Typical week of electricity purchased by Epic.

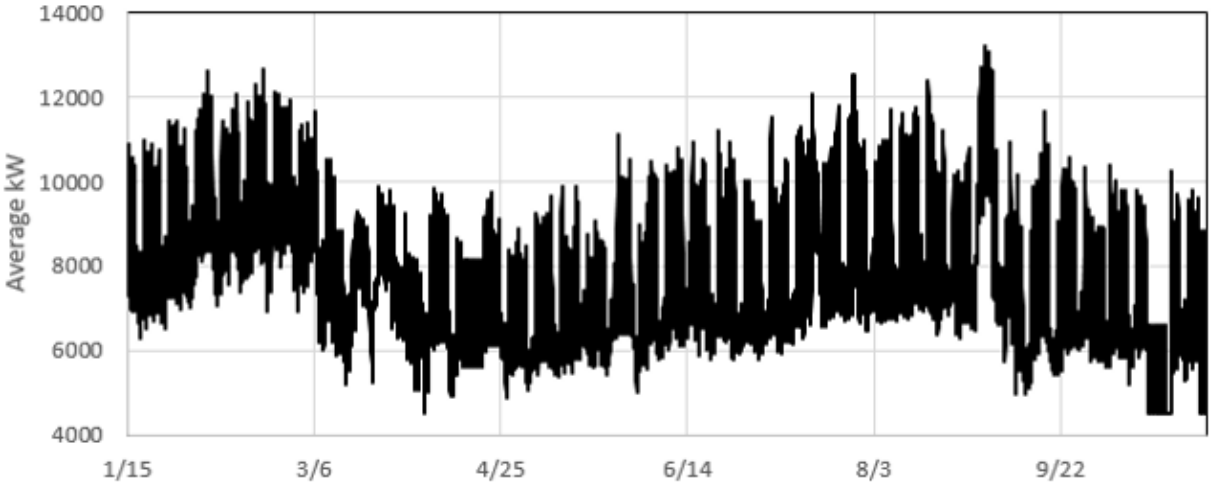

Figure 43: Long-term trends in electricity purchasing by Epic.

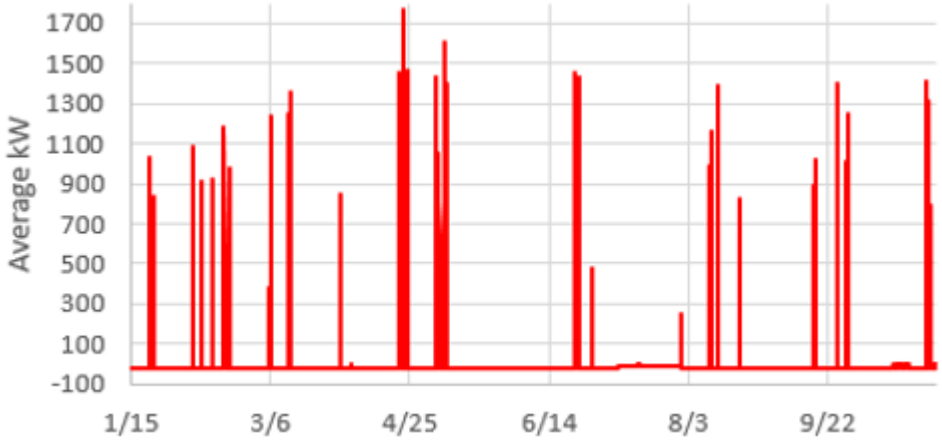

Figure 45: Backup generator usage in 2015.

From January to October 2015, Epic's generators idled 97.6% of the time, consuming an average base load of 22 kW, totally 143.2 MWh of energy consumption. When the generators were activated to provide additional electrical input to the campus (2.4% of the time), 131.4 MWh of energy was produced. Over this time period, there was a net energy loss for Epic to idle their generators; however, the generators provided a reliable backup source of electricity to keep vital data servers running when other forms of electricity fail to meet demand. Although costly, this is a vital component of the Epic business model and worth the investment.

Figure 44: Galactic Wind Farm site map.

The Galactic Wind Farm is located in Martinsville, WI, 20 miles north of Epic's Campus. As such, the electrical energy produced there is not directly used by Epic's campus, but rather is

sold to Madison Gas and Electric, the local utility. Produced power, consumed power, facing direction, wind speed, wind direction, and blade pitch datasets are collected from these turbines at 5 or 10 minute intervals for the entirety of 2015. Figure 44 shows a map view of the turbine layout, and the corresponding turbine numerical identification system.

The available wind resource at Galactic Wind farm was analyzed using wind speed and direction data and creating a wind rose (Figure 47: 2015 wind rose for turbine 1.) and energy rose (Figure 46) for each turbine in 2015. The most common wind at turbine 1 was 0 to 3 m s^{-1} from due north, followed by westerly winds from 3 to 9 m s^{-1}. This trend is generally observed in the wind roses for the other five turbines as well (not included). Turbine 1's energy rose (Figure 46) predictably shows the vast majority of energy production coming from westerly winds, with a notable increase from southwesterly winds 9 to 12 m s^{-1}. Turbines extract energy from the wind, and create wake losses for other turbines. Turbines 1, 2, and 3 are located in an east-west line that may significantly diminish production in turbines downwind of the predominately westerly winds. Turbines 4, 5, and 6 are more spread out in a pattern that will minimize the effect of

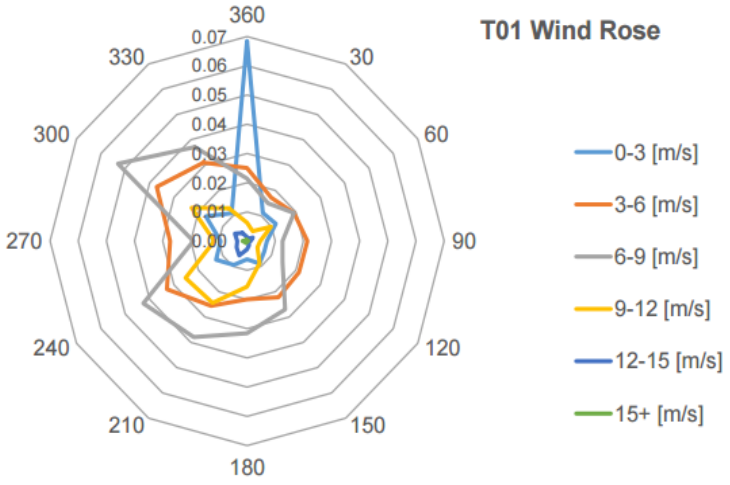

Figure 47: 2015 wind rose for turbine 1.

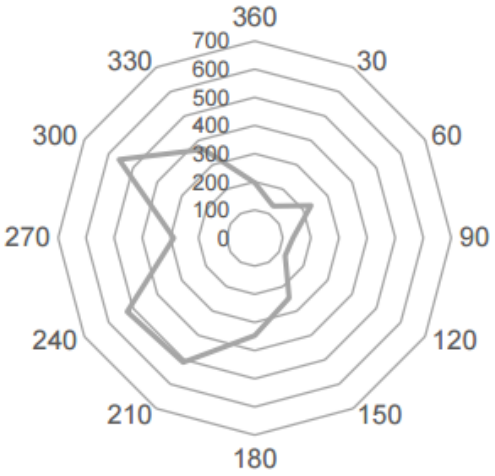

Figure 46: 2015 energy rose for turbine 1 [MWh].

westerly wake losses, but may diminish energy production from the southwesterly winds.

Galactic Wind Farm is affected by curtailment when Madison Gas and Electric cannot add the wind-produced electricity to the grid. Figure 48: Galactic Wind Farm curtailment on 05/17/2015. shows an example of one such instance on 05/17/2015. Several hours of energy production and wind resource were missed in the evening hours, most likely due to the decreased electrical demand overnight. The collected data shows many instances similar to this, many with much longer periods of curtailment. Additionally, the turbines were off-production for maintenance purposes for several periods during data collection. Despite these issues, Galactic Wind Farm operated at a 2015 capacity factor of 26.78%. Capacity factor did vary by month, as seen in Figure 49: Galactic Wind Farm 2015 Capacity Factor.. The summer months included the largest periods of turbine maintenance and may be artificially lower than otherwise possible if the turbines had been functioning properly.

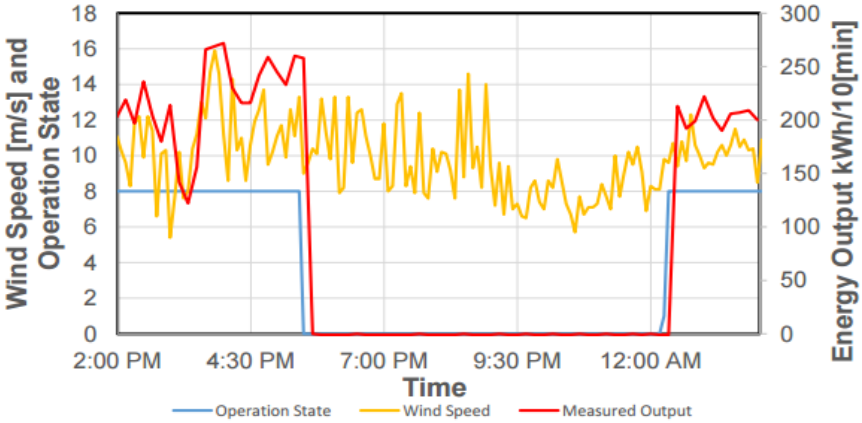

Figure 48: Galactic Wind Farm curtailment on 05/17/2015.

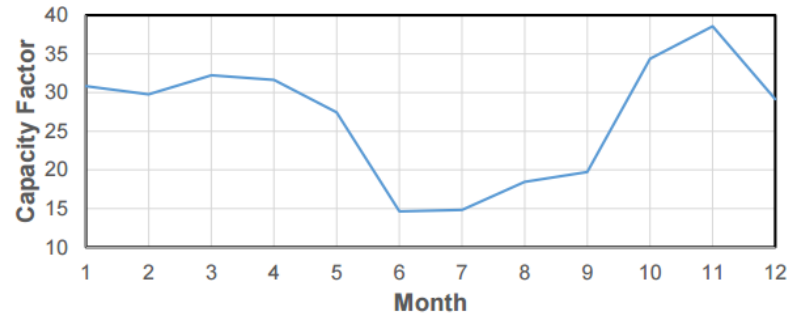

Figure 49: Galactic Wind Farm 2015 Capacity Factor.

When calculating a net-zero balance at Epic systems, there are several possibilities. However, I believe the most accurate reflection of reality is described by Eq. 17.

(17)

$$Solar\ Production + Wind\ Production - Alliant\ Purchased - Generators - Solar\ Production = 0$$

Appendix 3: U-pipe vs. Coaxial Ground Heat Exchanger Performance

All 6172 geothermal boreholes at Epic are equipped with single u-pipe GHXs. However, other piping configurations exist, including a double u-pipe and coaxial pipe-within-pipe orientation. Due to the significant number of GHX and potential for more future GHX, Epic was interested in the optimal piping configuration for their needs. An Oklahoma-based company, Rygan Corporation, designs a coaxial GHX that they claim is, "The highest performing well field system in geothermal, bar none". As they also charge higher prices for their system, Epic asked our research team to investigate the potential benefits from a coaxial GHX so that an informed decision could be made on future

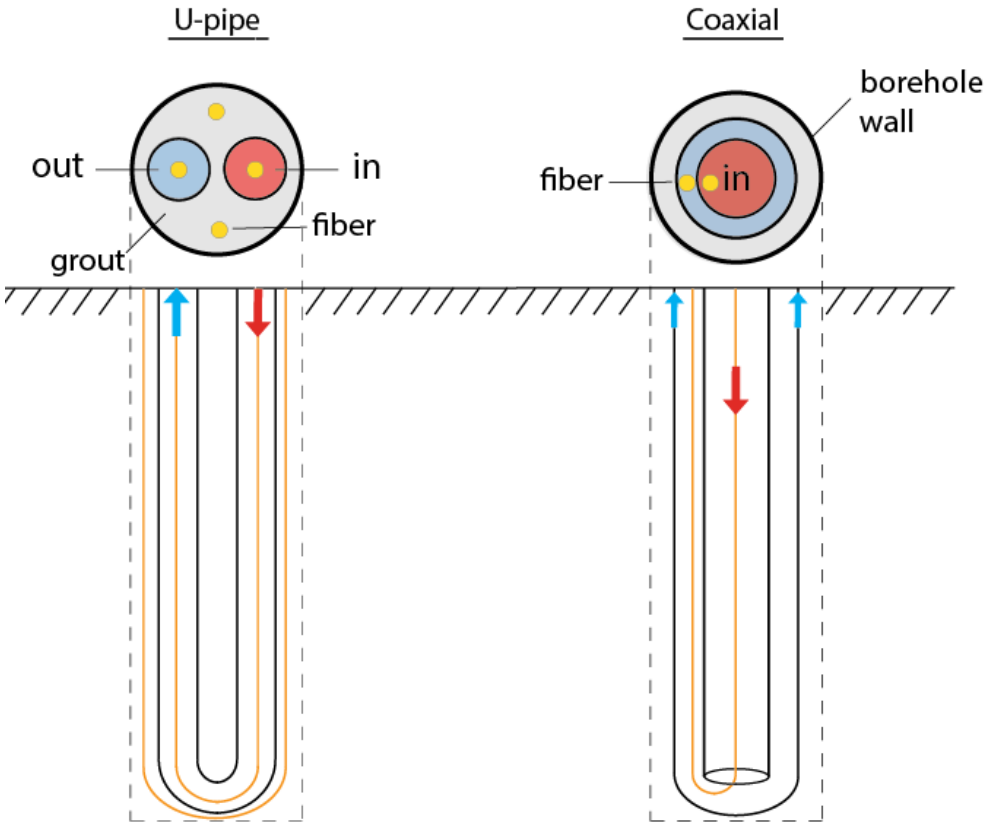

Figure 50: U-pipe and coaxial GHX configurations.

installations. One U-pipe and one coaxial GHX (Figure 50) were installed at the southeast corner of borefield 4, each instrumented with an ultrasonic flowmeter, in-pipe thermometers, and fiber optics for distributed temperature sensing.

The Rygan Corporation coaxial GHX has three main designs changes for greater heat transfer.

1) The center flow channel is made of thermally insulating nylon-reinforced Ethylene-Propylene to prevent thermal interaction between the supply and return streams.
2) Corrugated and ribbed rubber surrounding the center channel to create turbulent return flow.
3) The outer pipe is made of patented, low-thermal resistance composite material to increase heat transfer away from the borehole.

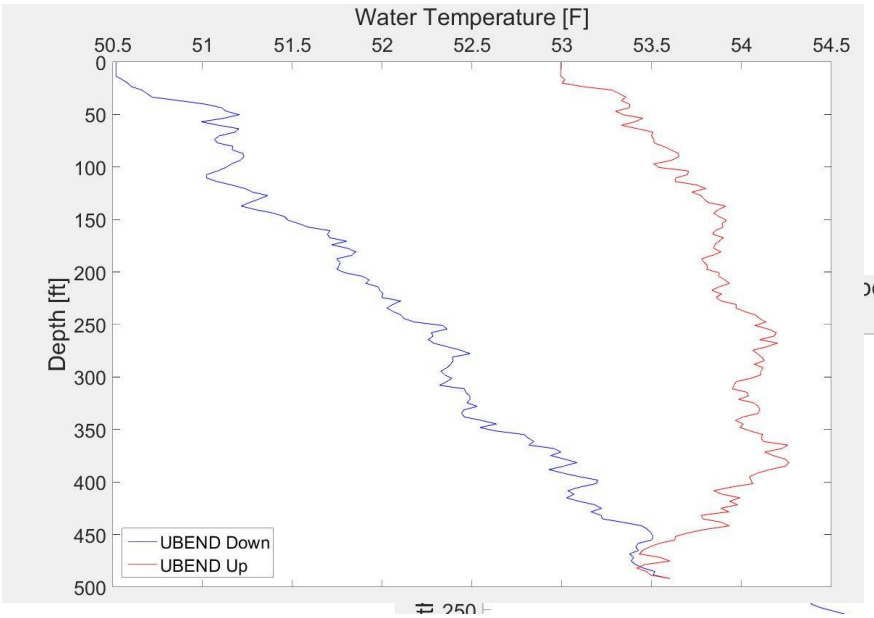

Figure 52: U-pipe DTS data in heating mode.

The fiber optics were installed to provide insight into the efficacy of the thermally insulating center flow channel by observing where the fluid temperature change occurs. The following four profiles are DTS data; Rygan (Figure 51) and U-pipe (Figure 52) in heating mode on 02/15/2017; and Rygan (Figure 53) and U-pipe (Figure 54) in cooling mode on 07/15/2015. It is observed that within the Rygan central flow channel, there is temperature change in both heating and cooling mode. It is difficult to surmise from 4 static profiles if there is less thermal interference in the coaxial GHX than the u-pipe, as Rygan claims. There are almost two years of DTS profiles from 05/13/2015 to the submittal of this thesis on 05/05/2017 that could be calibrated and used to more completely answer this research question. When the system is run in cooling mode, the controlling temperature gradient appears to consistently be between the hot exchange fluid and the relatively cold subsurface. This conclusion is drawn from Figure 53 and Figure 54, which show constant heat transfer away from both the supply and return streams by the 'V-shape' of the temperature profile. When the system

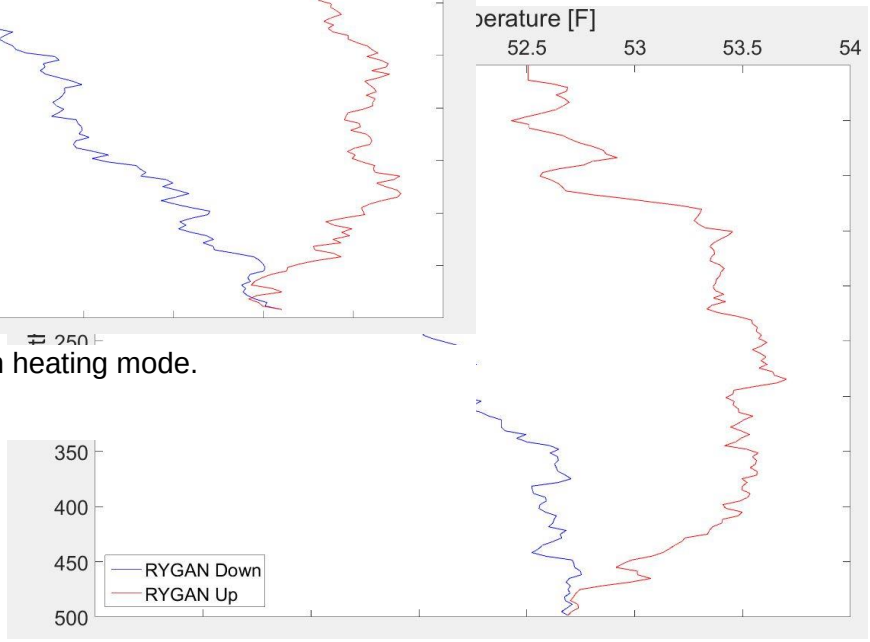

Figure 51: Rygan DTS data in heating mode.

is run in heating mode, and the supply water temperature is much lower, local gradients are thermal interference between pipes appears to play a larger role. Both the coaxial (Figure 51) and u-pipe (Figure 52) show water heating up during the entire supply path. However, both return paths show an approximate equal effect of heating near the bottom of the well and cooling near the top of the well. This suggests that in both cases, the hottest water about to leave the GHX is transferring heat to a relatively cool nearby subsurface or it is heating the supply stream when it is at its coldest.

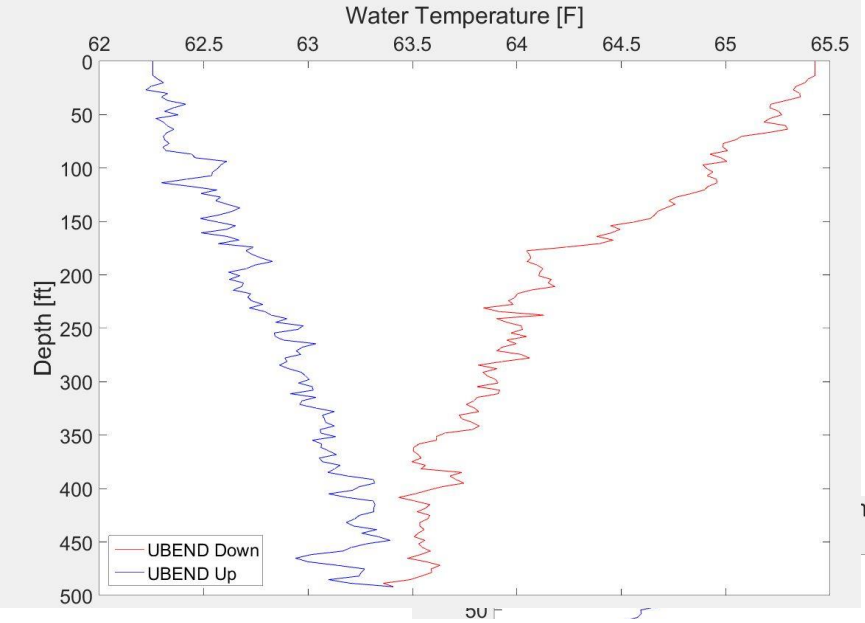

Figure 54: U-pipe DTS data in cooling mode.

This DTS data for both the coaxial and the u-pipe GHXs could be used as a DTRT, as presented in Chapter 5 of this thesis. The geology of borefield 4 is well documented (See Chapter 4), and 2 years of DTS data has monitored the distributed nature of the heating and cooling. Combined with the supply and return temperature and flow rate data, a conventional TRT analysis could also be done to provide

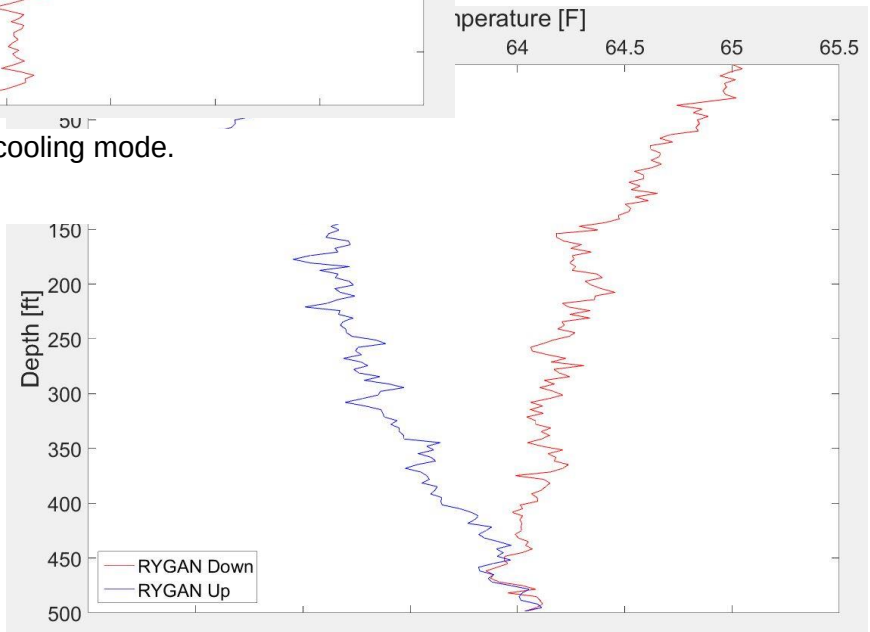

Figure 53: Rygan DTS data in cooling mode.

effective borehole parameters using the Raymond et al. (2011) analysis. One of the concerns of the Illinois DTRT presented in Chapter 5 was the true lack of true steady state conditions. After two years of operation, both the coaxial and the u-pipe should have reached study state conditions, and the Molz et al (1989) impeller method analogy should be used with little reservations.

The flowmeter and supply/return temperature measurements allow for the calculation of borehole heat transfer capacity for both wells, and a direct comparison of energy exchange performance. However, from the beginning of data collection on 1/15/2015, it was observed that the flowmeter measuring the flow of water through the coaxial well provided erratic measurements (Figure 55). The flow measurements for the U-pipe remained near a constant 4 gpm for the majority of the first nine months of measurement, after which the flow dropped to a near constant 2 gpm, which is a believable operational schedule. The coaxial GHX reported flows that varied by 2 to 4 gpm in a signal day, and displays results that appear more like a noisy signal than an operational pattern. The ultrasonic flow meter was installed on the return header pipe, which may

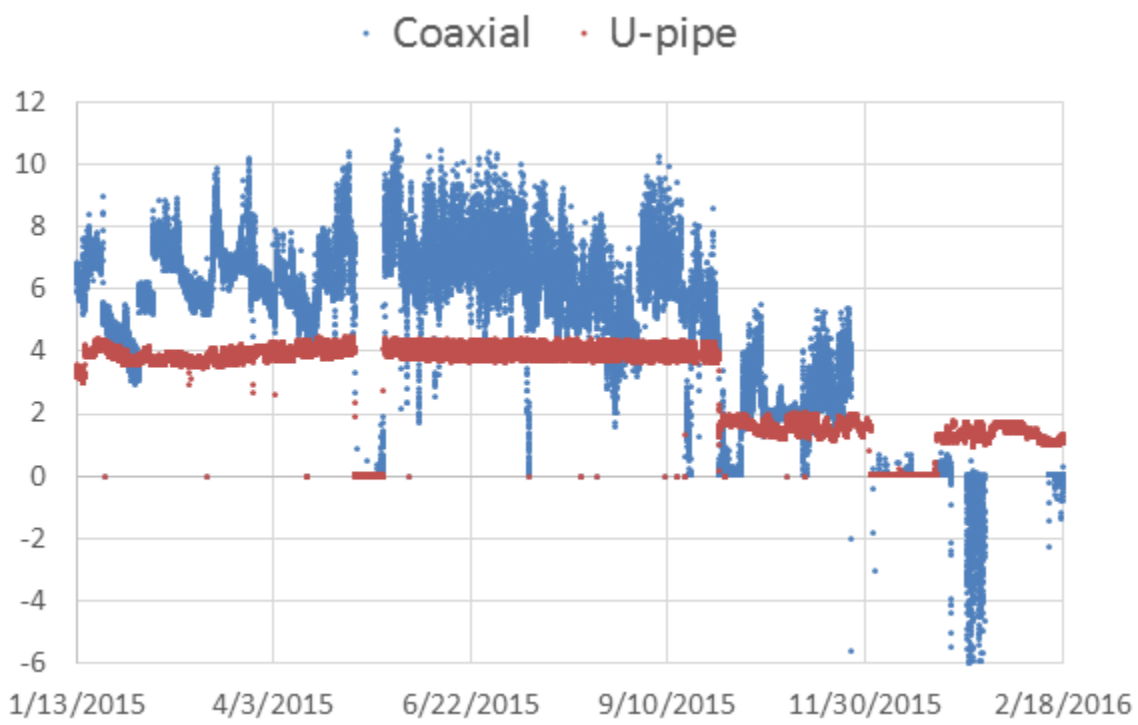

Figure 55: U-pipe vs. coaxial GHX flow comparison.

have been contributing to this noise, as the coaxial pipe does purposefully create turbulent flow. However, the flowmeter was moved to the supply header pipe, and the problem was not resolved. The true cause of the flowmeter malfunction was never determined, but the flowmeter was replaced on 04/14/2016, after which the flowmeter has been reading what have been determined to be accurate results. The data after the new flowmeter was installed has been collected, but has not yet be analyzed for heat flows. Without accurate flow data, the most useful measure of GHX heat transfer performance was the change in temperature accomplished by passage of water through the GHX piping. ΔT does not tell the whole story, as a higher flowrate can provide more energy transfer, even with a lower ΔT. Additionally, a higher ΔT could be because of higher fluid residence time in the subsurface and not necessarily due to better heat transfer design of the GHX. With those thoughts in mind, Figure 56 shows a side-by-side comparison of the ΔT accomplished by both wells. Interestingly, the u-pipe GHX consistently provides a greater ΔT than the coaxial well.

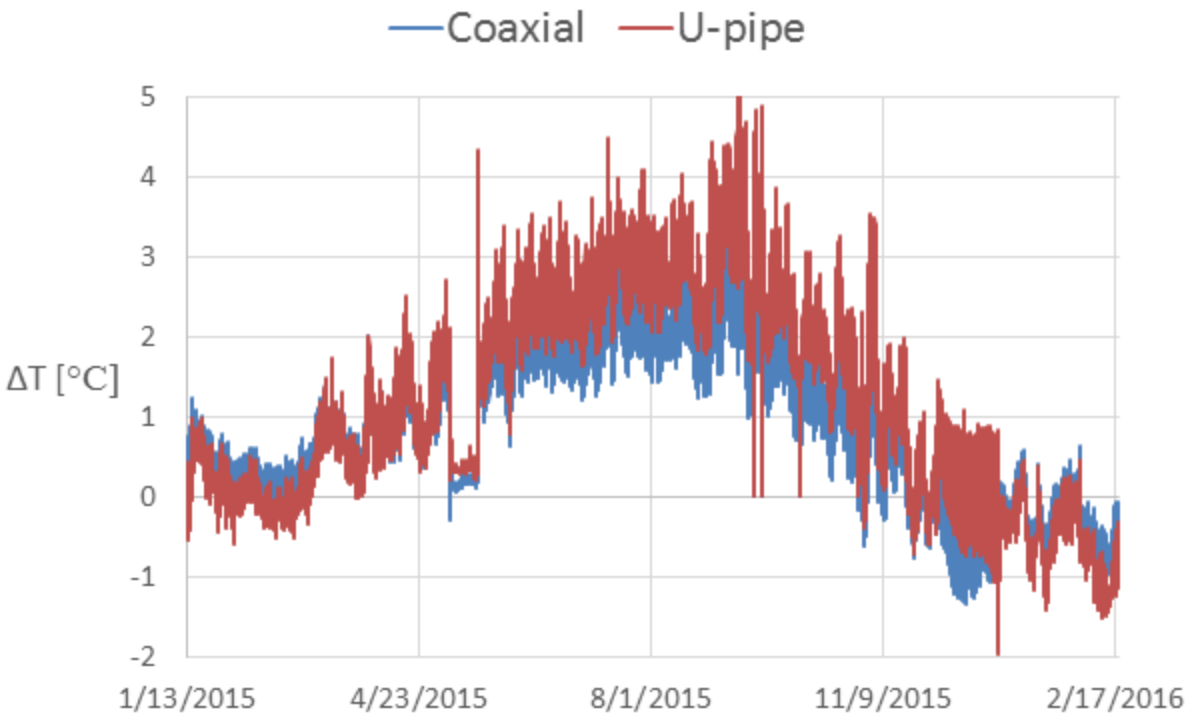

Figure 56: U-pipe vs. coaxial GHX temperature comparison.

After discussion of these results with the Rygan Corporation, they have provided insight that the true benefit of the coaxial design is apparent at higher flowrates, and it is not an accurate comparison to remove flowrates, or even to use flowrates in the analysis but to operational apply the same flowrate to both wells. Future work to improve this comparison would involve a higher pressure drop to the coaxial well, and increase the flowrate to an optimal performance window as prescribed by the Rygan Corporation.

It is my opinion that the coaxial well will indeed transfer heat away from the exchanger fluid to the near-field at higher rates than the standard u-pipe GHX. All of the design changes are correct ways to decrease thermal resistance and increase heat transfer rates. However, I do not believe that the coaxial well would fit well to Epic's application. The limiting factor in Epic's borefields is not peak load capacity, but rather sustaining capacity for the long-term. If a borefield of coaxial wells was installed by Epic, I suspect that the early performance of the field would surpass a u-pipe borefield equivalent. As a result, the subsurface would increase in temperature

more quickly, which would steadily decrease the coaxial well's performance over time. This performance feedback loop may decrease the efficiency gains of the coaxial well and bring into question the worth of the higher initial investment. If the piping is feasible, coaxial wells may provide a borefield remediation strategy. A borefield with mostly u-pipe wells injecting energy, and scattered coaxial wells extracting energy could provide more rapid borefield cooling. It is beyond my expertise to estimate the additional cost (and thus efficacy) of such a borefield piping.

Appendix 4: Wisconsin Institute for Discovery Geothermal Investigation

The Wisconsin Institutes for Discovery (WID) is a UW-Madison campus building that was designed as a multi-disciplinary research facility that encourages collaboration. The building itself was designed with an emphasis on reducing environmental impact, and was certified LEED Gold in 2010 when the building came into use. A significant component of the LEED certification and the building's sustainable footprint is an 82-borehole GSHP system with an estimated cooling capacity of 1000 kW (Herrera, 2016). 54 boreholes are oriented in a ring that outlines the WID building, and 21 boreholes surround the UW's Physical Plant across the street (Figure 57). Each borehole is approximately 91 m in depth. Due to plumbing issues early in the installation of the GSHP system, the system was converted to run only in cooling mode. This operational strategy of only injecting heat into the ground, and never extracting it fundamentally undermines that energy storage principles of a GSHP system, and instead treats the ground as an infinite constant temperature heat sink, which it is not.

Figure 57: WID borefield layout. (Kelly, 2009)

In May 2013, the geothermal system was ran at high capacity cooling mode for a period of several days in response to a limited supply of chilled water from the campus-wide HVAC system. The subsequent returning water temperature patterns can be seen in Figure 58. The concentrated heating load creating a substantial rise in water temperature returning from the

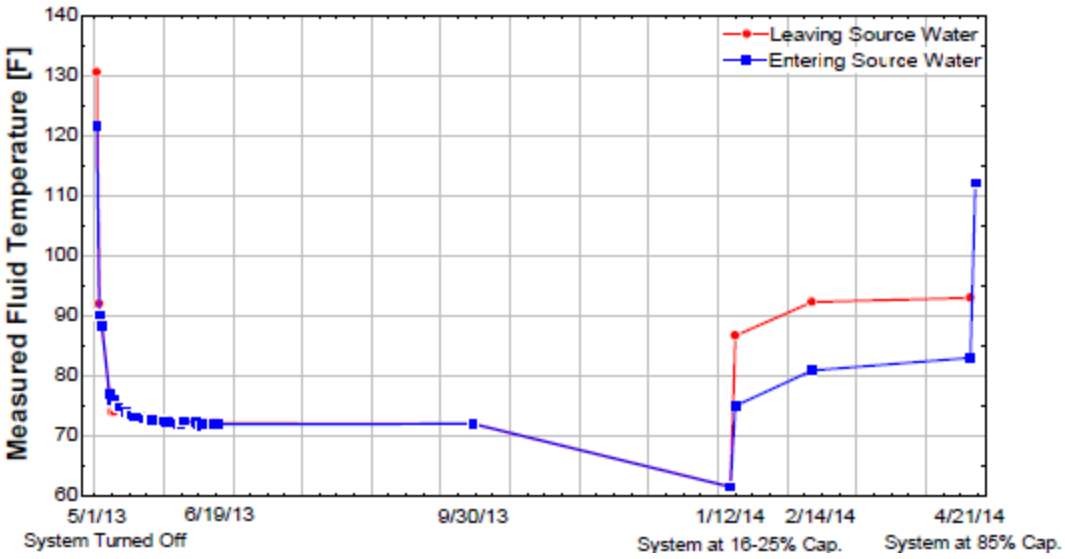

Figure 58: Returning temperature effects from WID borefield high capacity heat injection.

borefield, reporting temperatures as high as 50 °C (121 °F). During the nine days after this episode of high heat injection, the returning water temperature dropped to 24 °C (75 °F). However, the cooling of the borefield slowed significantly after this initial period, and never returned to expected undisturbed ground temperature of 11.7 °C (53 °F). In general, the GSHP was left to idle, occasionally circulating water to deter bacterial growth. In January 2014, the system was run at partial capacity, and again in April 2014 the system was activated to provide cooling at near full capacity. At both occasions, the outgoing fluid temperature rapidly spiked, causing low heat pump efficiencies.

In the fall of 2015, two GHXs were uncovered (Figure 59 and Figure 60), hydraulically separated from the rest of the borefield, and used to conduct a battery of tests to diagnose the cause of borefield overheating with the goal of designing a remediation strategy. The following tests were performed:

1) Vary pump flowrate and measure pressure drop to create a pumping curve.
2) Use submersible borescope to observe pipes, looking for fouling.
3) Use levelogger and FO-DTS in each GHX for borefield temperature profiles.

4) Sample grout and test for composition.

Figure 59: Uncovering the WID geofield.

The pumping test returned pumping curves with pressure drops nearly identical to manufacturing specifications. The borescope, after some difficulty, was able to record images of clean pipes on the supply and return side of both GHXs. A custom fishing pole was used to lower leveloggers (Solinst) down the GHXs to monitor temperature with depth. The fishing line was marked every 9 m (30 ft.) to allow the levelogger to equilibrate to its surroundings for 5 min at that depth before being lowered to the next depth. The results of this test on the southern GHX return side can be seen in Figure 61. These temperature profiles showed an unexpected temperature pattern. A depth window from 20 to 60 m bgs was the hottest portion of the field, and temperatures below 60 m bgs decreased significantly. When correlated to geology, a hypothesis was developed that the depths storing heat were also highly correlated with Wonewoc sandstone that makes up the shallow Madison aquifer that may have minimal groundwater flow.

Figure 60: Uncovered WID GHXs.

The bottom of the borefield just reaches Mt. Simon formation that is the top of the deeper aquifer that Madison municipal water is pumped from and will have significant groundwater flow.

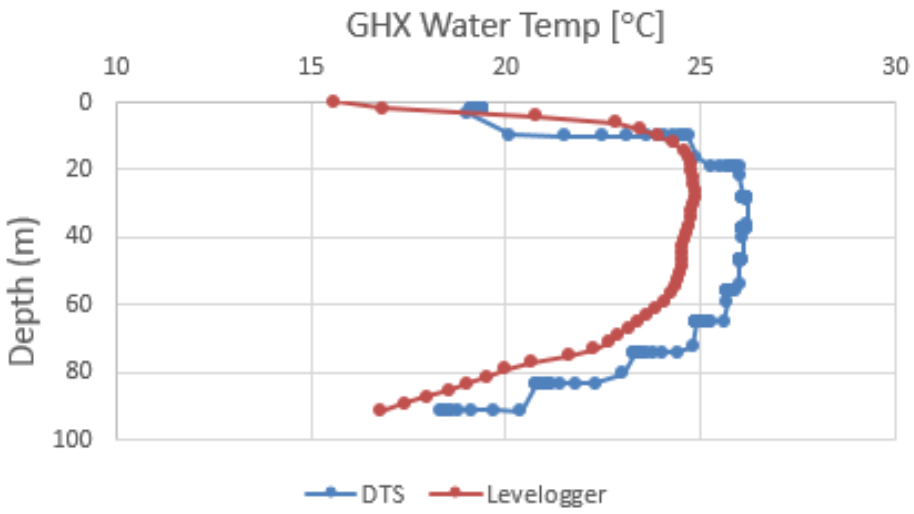

Figure 61: South GHX borehole return side temperature profiles.

When the boreholes were uncovered, voids were visible around the GHX piping that had been vacated by settling grout. If this continued the length of the GHX, the pockets of air would significantly increase thermal resistance and may play a part in borefield overheating. However, after digging for several meters, the voids disappeared and were judged to be only a factor in the top few meters of the borefield and not a significant cause of thermal resistance. The grout was sampled, dried,

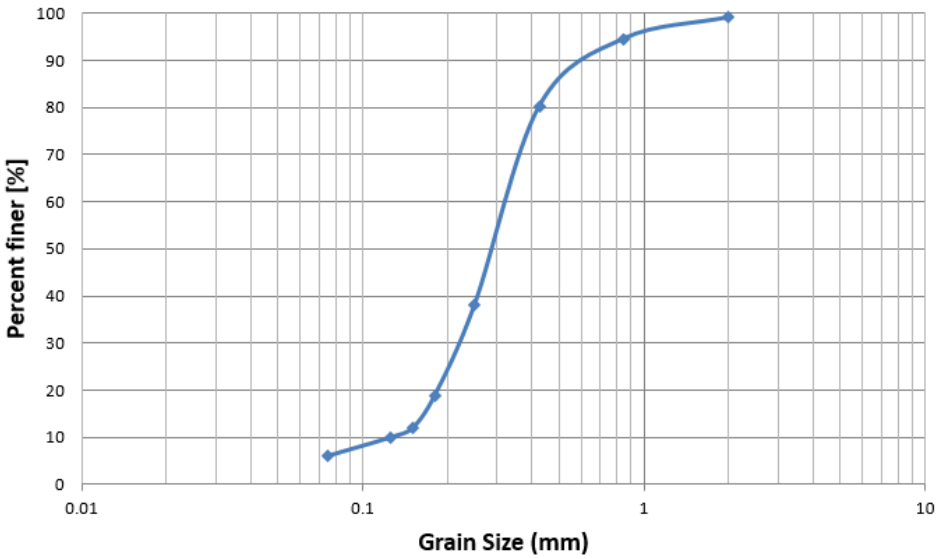

Figure 62: WID grout grain size distribution.

and run through sieves (ASTM D6913-04) for a grain size distribution (Figure 62). The percent fines (assumed bentonite) and percent coarse aggregate was within specifications, and it was determined the grout, although not highly thermally conductive, was not the cause of overheating.

A Distributed Thermal Response Test (Figure 63, DTRT) was conducted on the south uncovered GHX during the summer of 2016 to further investigate subsurface conditions. This DTRT used the same custom rig as outlined in Chapter 5 of this thesis. Because of the GHX was not previously installed with fiber optic cables, two single ended cables were lowered to the bottom of the GHX, on the supply and return sides, respectively. A Halo interrogator, and three calibration baths were used for the DTS calibration. Both fibers that were dropped into the GHX were previously configured in a double-ended configuration which allow pre-calculated of differential attenuation. A complete discussion of the methodology and results can be found in Herrera (2016). Distributed thermal conductivity values of the subsurface were calculated by subsurface lithologic formation. The Wonewoc formation yielded a thermal conductivity of 3.8 W m^{-1} K^{-1}, and the Mt. Simon yielded 3 W m^{-1} K^{-1}. This small difference in thermal conductivity is not enough to explain the spike in temperature between 20 and 60 m bgs. However, the hydraulic conductivity of the Wonewoc is also higher than the Mt. Simon (see Chapter 4), and the Madison municipal pumping in the deep aquifer will create high hydraulic gradients. It is my belief that stagnant groundwater flow is a primary contributor to slow thermal diffusivity near the top of the borefield, while advective heat flow from groundwater is cooling the bottom of the borefield.

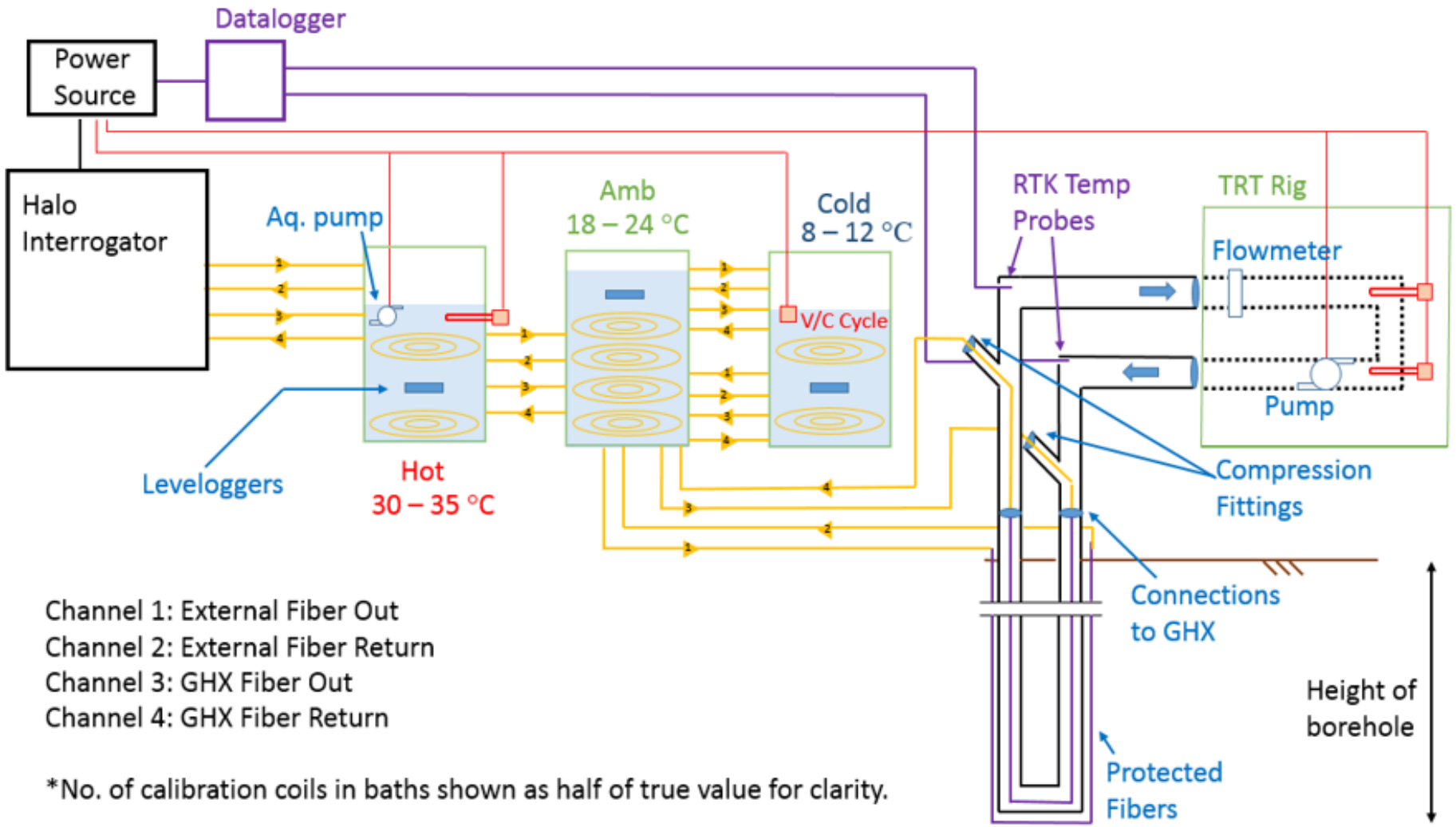

Figure 63: Schematic of DTRT used at the WID.

Appendix 5: Guided Tutorial of Epic Calibration Procedure

The following is a step-by-step guided tutorial of the process followed to calibrate data DTS data being collected by the Sentinel interrogator at Epic's borefield 4.

STEP 1: Retrieve the raw data files

There is only one computer (Figure 64) that can remote access the Sentinel interrogator in vault 14 at Epic. This computer has been assigned a static IP (provided and installed by CAE). That IP is the only exception in the firewall for the Epic server that the Sentinel is connected to. The password to log on to this computer is password_1.

Figure 64: Computer needed to retrieve Sentinel data.

Once on this computer, the Linux virtual machine much be launched. Run the program: VMware Workstation 12 Player. This program has an Ubuntu operating system installed that can be run simultaneously as the windows operating system. Upon launching the program, you will see Figure 65. Click on the Linux VM and then the green arrow "play virtual machine".

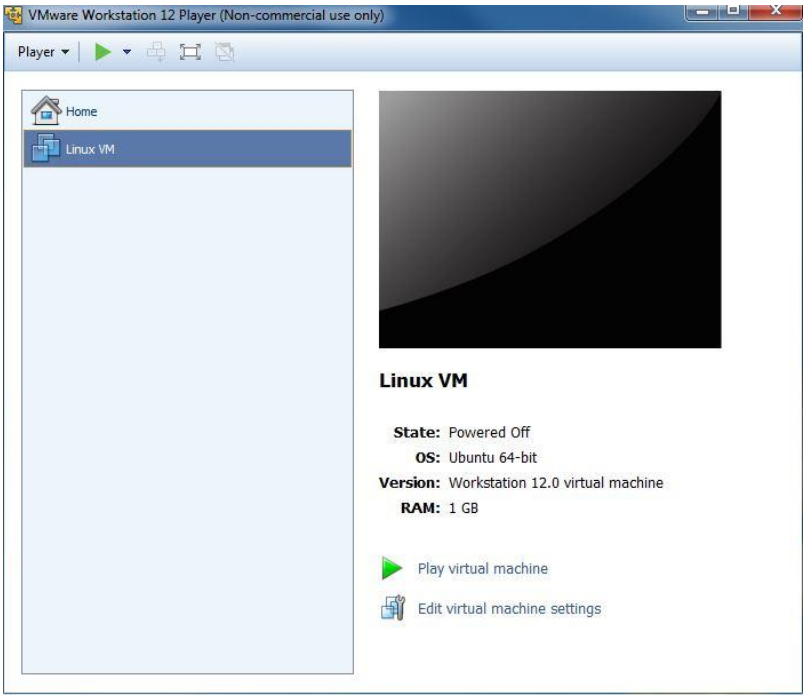

Figure 65: VMware Workstation 12 Player home screen.

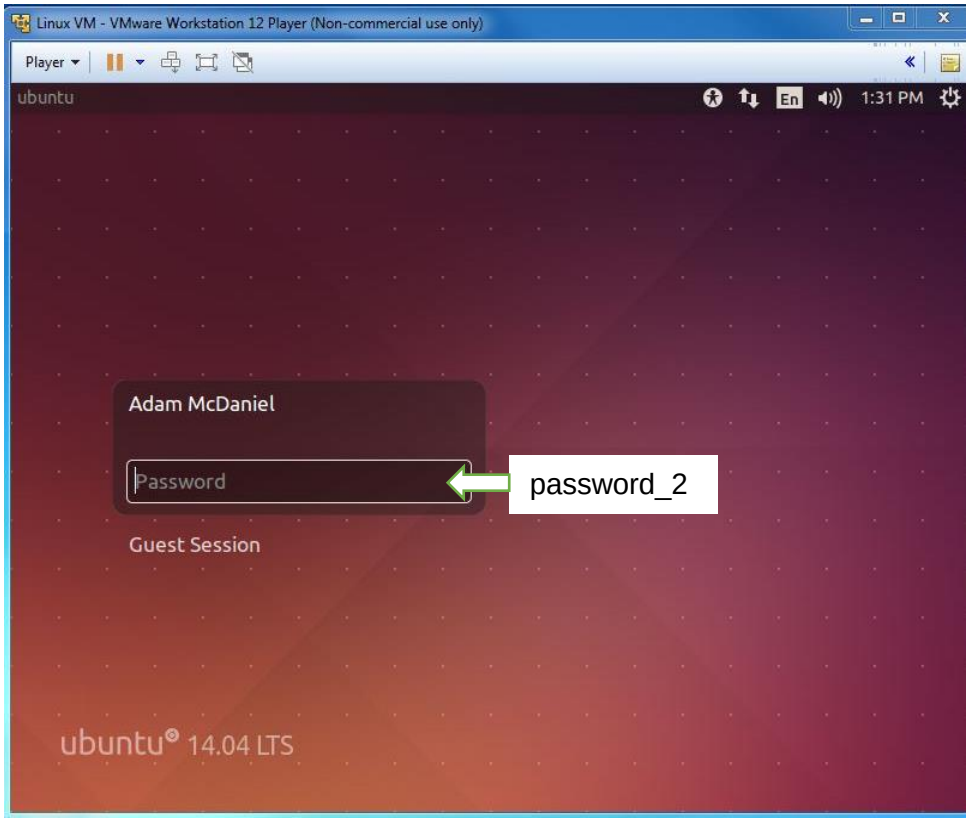

Figure 66: Ubuntu operating system login screen.

Enter password_2 to login to the Adam McDaniel account on the Ubuntu operating system. This account name and password should be changed once the successor has been chosen to maintain this data. Once logged in, launch the “Terminal” application from the task bar on the left side of the screen. From this terminal window, commands are given to the operating system via written code in the same way that clicking through windows explorer gives commands to a windows operating system. An excel file saved to the desktop of the windows operating system has a list of useful commands that may be entered. The command to initiate the connection to the Sentinel is:

ssh –nXC geocache.epic.com xtightvncviewer geo-field-4-collector-1.epic.com

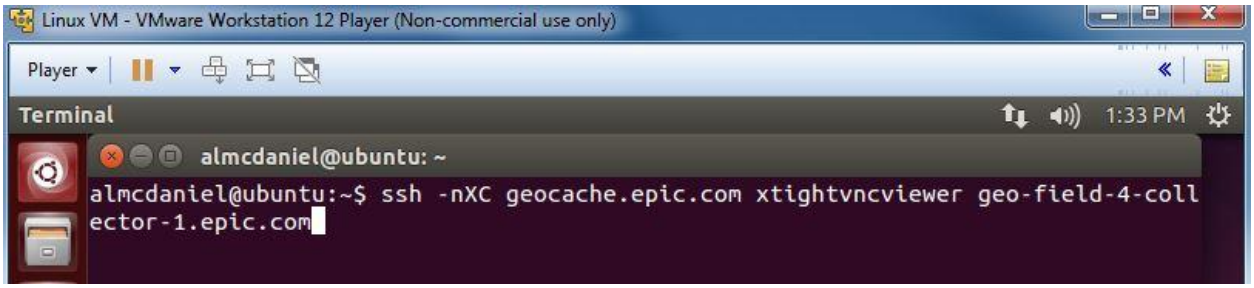

Figure 67: Command to initiate virtual connection with the Sentinel.

This command initiates a SSH (Secure Shell) tunnel to the Epic server that the Sentinel interrogator is connected to. A SSH tunnel is an encrypted method of remote connection and required by Epic as the most secure form of access. This command will then as for login to the Epic server. Password_3 is used here. Once logged in, the command already entered with immediately initialize the program “TightVNC” to have remote desktop control of the sentinel

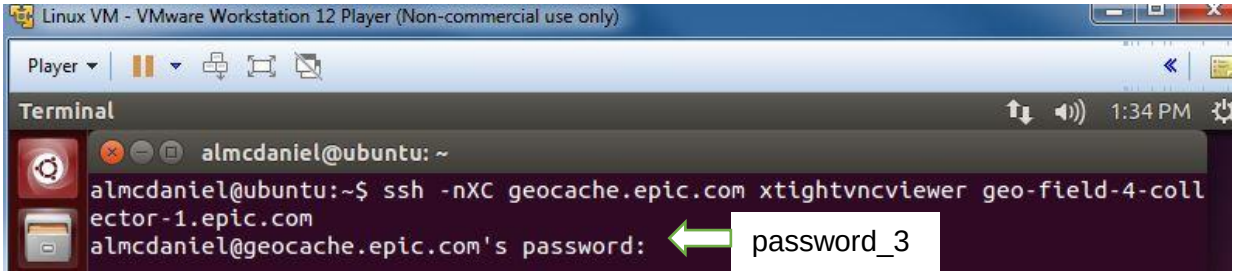

Figure 68: Login to account on Epic's server.

machine. “TightVNC” will require password authorization for login. Password_4 is used here. If completed correctly up to this point, the user will now be in control of the Sentinel interrogator. It is best practice to, at this point, check the current status of the Sentinel to ensure that data collection is occurring.

Data is stored on the Sentinel hard drive: Computer>Local Disk (D:)>Sensornet dts>data>all data. There you will found all of the data collected by the Sentinel in folders labeled by configuration name. Current data (as of the submittal of this thesis on 05/05/2017) is stored in “All Channels Green”. The Sentinel has wired internet access, as part of the Epic network, so data can be uploaded to UW-Madison’s box account. This intermediate step functions as backup for the data if something were to happen to the Sentinel’s data storage. Once uploaded, the files can be downloaded to a location of the user’s choosing for calibration.

Matlab scripts have been developed that will calibrate fiber data for TMW-1B & TMW-2B, TMW-3B & TMW-4B, TMW-5B & TMW-6B, and TMW-7B and TMW-8B. No Matlab scripts have been developed at this time to calibrate the u-pipe and coaxial fiber data. In general, these scripts use a function provided by CTEMPs called “Process_Sensornet” to read .ddf files (one or many) and compile the data in Matlab variables of appropriate labels. The Sentinel creates a new folder each month, so current practice has been to calibrate one month of data at a time.

The remainder of the Matlab script corrects for splices, calculates sectioned differential attenuation, reads calibration bath temperatures, and calibrates the forward and reverse signals based on all four calibration baths. The resulting calibration parameters are stored in variables for exporting to larger excel spreadsheets that keep track of longer periods of data collection. One Matlab script is used that allows gamma to vary with each recalibration. The gamma values from these calibrations are collected and averaged to find the optimal gamma over the desired period of calibration. This average gamma is inputted to a second Matlab script that will fix gamma (at

that value) and recalibrate only allowing C to vary. The temperatures of the two TMWs on that loop can then be pulled and stored elsewhere. When sufficient data has been collected that it may be visualized with a colorflood plot, a third Matlab script is used. The calibrated temperatures, and associated dates must be imported to this spreadsheet and saved as a set of variables. The Matlab script will then load those variables and plot the temperature data in a colorflood plot. An example of each type of Matlab script is included here for the loop of TMW-1B and TMW-2B.

Appendix 5.1 Variable Gamma Calibrating Matlab Script for TMW-1B & TMW-2B

```
%%Adam McDaniel
%%January 6th, 2016
%%Calibration and Outputting of TMW-1 & TMW-2 Temperature Data for Epic
%%Real Time Onservation
clear
close
clc

%%Input data files
Process_Sensornet('F:\MCDAN FLASH\Research\GeoExchange\Calibrating
Organization\Raw ddf Files\TMW1&2\2016\apr\',0,2031,'TMW12.mat');
load('TMW12.mat');

%%Move File into 'Used' Folder
% movefile('C:\Users\Adam\Desktop\Automation\Automation File Initial\channel
7 20160106 001 00001.ddf','C:\Users\Adam\Desktop\Automation\Automation File
End\');

%%Loop to run over multiple files
numfiles = size(Stokes,2);
%Prefine Multiple File Variables
GammaF = zeros(1,numfiles);
cF = zeros(1,numfiles);
GammaR = zeros(1,numfiles);
cR = zeros(1,numfiles);
DAsections = zeros(7,numfiles);
TMW1Keep = zeros(150,numfiles);
TMW1UncalibratedKeep = zeros(150,numfiles);
TMW2Keep = zeros(150,numfiles);
TMW1CimKeep = zeros(5,numfiles);
TMW2CimKeep = zeros(5,numfiles);
RMSEKeep = zeros(5,numfiles);
%
for x = 1:numfiles

%%Flip reverse light intensity data
```

```
AntiStokesR(:,x) = flipud(AntiStokesR(:,x)); %#ok<SAGROW>
StokesR(:,x) = flipud(StokesR(:,x)); %#ok<SAGROW>

%%Create raw local differential attenuation vector
indexend = length(distance);

EQ1 = zeros(indexend,1);
for i = 1:(indexend-1)
    EQ1(i) = (log(Stokes(i+1,x)/AntiStokes(i+1,x)) -
log(Stokes(i,x)/AntiStokes(i,x)) + log(StokesR(i,x)/AntiStokesR(i,x)) -
log(StokesR(i+1,x)/AntiStokesR(i+1,x)))/2;
end

%%Create raw cumulative differential attenuation vector
CumEQ1 = zeros(indexend,1);
for i = 2:(indexend-1)
   CumEQ1(i) = EQ1(i)+ CumEQ1(i-1);
end
CumEQ1(indexend) = CumEQ1(indexend-1);

%%Create vectors for natural log ratios forward and reverse
LnFor = log(Stokes(:,x)./AntiStokes(:,x));
LnRev = log(StokesR(:,x)./AntiStokesR(:,x));

% %%Splice indexing
SP1B = 1;
SP1A = 6;
SP2B = 33;
SP2A = 38;
SP3B = 271;
SP3A = 276;
SP4B = 643;
SP4A = 648;
SP5B = 995;
SP5A = 1000;
SP6B = 1361;
SP6A = 1366;
SP7B = 1952;
SP7A = 1957;
SP8B = 1981;
SP8A = 1991;

% %%Bath indexing
B1B = 14;       %Hot
B1A = 18;       %Hot
B2B = 24;       %Ambient
B2A = 29;       %Ambient
B3B = 1962;     %Ambient
B3A = 1966;     %Ambient
B4B = 1973;     %Hot
B4A = 1975;     %Hot

%%Forward Splice Corrections
%Splice 1
FC1 = LnFor(SP1A) - LnFor(SP1B);
```

```
LnFor(SP1B:SP1A,1) = LnFor(SP1B);
LnFor(SP1A+1:indexend) = LnFor(SP1A+1:indexend)- FC1;
%Splice 2
FC2 = LnFor(SP2A) - LnFor(SP2B);
LnFor(SP2B:SP2A,1) = LnFor(SP2B);
LnFor(SP2A+1:indexend) = LnFor(SP2A+1:indexend)- FC2;
%Splice 3
FC3 = LnFor(SP3A) - LnFor(SP3B);
LnFor(SP3B:SP3A,1) = LnFor(SP3B);
LnFor(SP3A+1:indexend) = LnFor(SP3A+1:indexend)- FC3;
%Splice 4
FC4 = LnFor(SP4A) - LnFor(SP4B);
LnFor(SP4B:SP4A,1) = LnFor(SP4B);
LnFor(SP4A+1:indexend) = LnFor(SP4A+1:indexend)- FC4;
%Splice 5
FC5 = LnFor(SP5A) - LnFor(SP5B);
LnFor(SP5B:SP5A,1) = LnFor(SP5B);
LnFor(SP5A+1:indexend) = LnFor(SP5A+1:indexend)- FC5;
%Splice 6
FC6 = LnFor(SP6A) - LnFor(SP6B);
LnFor(SP6B:SP6A,1) = LnFor(SP6B);
LnFor(SP6A+1:indexend) = LnFor(SP6A+1:indexend)- FC6;
%Splice 7
FC7 = LnFor(SP7A) - LnFor(SP7B);
LnFor(SP7B:SP7A,1) = LnFor(SP7B);
LnFor(SP7A+1:indexend) = LnFor(SP7A+1:indexend)- FC7;
%Splice 8
FC8 = LnFor(SP8A) - LnFor(SP8B);
LnFor(SP8B:SP8A,1) = LnFor(SP8B);

%%Reverse Splice Corrections
%Splice 8
RC8 = LnRev(SP8B) - LnRev(SP8A);
LnRev(SP8B:SP8A,1) = LnRev(SP8A);
LnRev(1:SP8B-1,1) = LnRev(1:SP8B-1) - RC8;
%Splice 7
RC7 = LnRev(SP7B) - LnRev(SP7A);
LnRev(SP7B:SP7A,1) = LnRev(SP7A);
LnRev(1:SP7B-1,1) = LnRev(1:SP7B-1) - RC7;
%Splice 6
RC6 = LnRev(SP6B) - LnRev(SP6A);
LnRev(SP6B:SP6A,1) = LnRev(SP6A);
LnRev(1:SP6B-1,1) = LnRev(1:SP6B-1) - RC6;
%Splice 5
RC5 = LnRev(SP5B) - LnRev(SP5A);
LnRev(SP5B:SP5A,1) = LnRev(SP5A);
LnRev(1:SP5B-1,1) = LnRev(1:SP5B-1) - RC5;
%Splice 4
RC4 = LnRev(SP4B) - LnRev(SP4A);
LnRev(SP4B:SP4A,1) = LnRev(SP4A);
LnRev(1:SP4B-1,1) = LnRev(1:SP4B-1) - RC4;
%Splice 3
RC3 = LnRev(SP3B) - LnRev(SP3A);
LnRev(SP3B:SP3A,1) = LnRev(SP3A);
LnRev(1:SP3B-1,1) = LnRev(1:SP3B-1) - RC3;
%Splice 2
RC2 = LnRev(SP2B) - LnRev(SP2A);
```

```
LnRev(SP2B:SP2A,1) = LnRev(SP2A);
LnRev(1:SP2B-1,1) = LnRev(1:SP2B-1) - RC2;
%Splice 1
RC1 = LnRev(SP1B) - LnRev(SP1A);
LnRev(SP1B:SP1A,1) = LnRev(SP1A);


%%Create corrected local differential attenuation vector
CorrectedEQ1 = zeros(indexend,1);
for i = 1:(indexend-1)
CorrectedEQ1(i) = (LnFor(i+1) - LnFor(i) + LnRev(i) - LnRev(i+1))/2;
end

%%Create corrected cumulative differential attenuation vector
CorrectedCumEQ1 = zeros(indexend,1);
for i = 2:(indexend-1)
   CorrectedCumEQ1(i) = CorrectedEQ1(i)+ CorrectedCumEQ1(i-1);
end
CorrectedCumEQ1(indexend) = CorrectedCumEQ1(indexend-1);


%%Find Sectional Differential Attenuations
A = CorrectedCumEQ1;
B = ones(indexend,2);
B(:,2) = distance;
DA = zeros(7,1);

%Section 1
A1 = A(SP1A:SP2B-1);
B1 = B(SP1A:SP2B-1,:);
X1 = B1\A1;
DA(1) = X1(2);
%Section 2
A2 = A(SP2A:SP3B-1);
B2 = B(SP2A:SP3B-1,:);
X2 = B2\A2;
DA(2) = X2(2);
%Section 3
A3 = A(SP3A:SP4B-1);
B3 = B(SP3A:SP4B-1,:);
X3 = B3\A3;
DA(3) = X3(2);
%Section 4
A4 = A(SP4A:SP5B-1);
B4 = B(SP4A:SP5B-1,:);
X4 = B4\A4;
DA(4) = X4(2);
%Section 5
A5 = A(SP5A:SP6B-1);
B5 = B(SP5A:SP6B-1,:);
X5 = B5\A5;
DA(5) = X5(2);
%Section 6
A6 = A(SP6A:SP7B-1);
B6 = B(SP6A:SP7B-1,:);
X6 = B6\A6;
```

```
DA(6) = X6(2);
%Section 7
A7 = A(SP7A:SP8B-1);
B7 = B(SP7A:SP8B-1,:);
X7 = B7\A7;
DA(7) = X7(2);


%%Creation of Piecewise Linear Function
PWF = zeros(indexend,1);
n = 1;
%Section 1 & 2
while n<=SP3B+2
PWF(n) = distance(n)*DA(2);
n = n+1;
end
%Section 3
while n<=SP4B+2
PWF(n) = PWF(SP3B+2)+ (distance(n)-distance(SP3B+2))*DA(3);
n = n+1;
end
%Section 4
while n<=SP5B+2
PWF(n) = PWF(SP4B+2)+ (distance(n)-distance(SP4B+2))*DA(4);
n = n+1;
end
%Section 5
while n<=SP6B+2
PWF(n) = PWF(SP5B+2)+ (distance(n)-distance(SP5B+2))*DA(5);
n = n+1;
end
%Section 6 & 7
while n<=indexend
PWF(n) = PWF(SP6B+2)+ (distance(n)-distance(SP6B+2))*DA(6);
n = n+1;
end


%%Determine Calibration Parameters
%Bath 1                              %Hot
T_1 = tref_1(1,x) + 273.15;
Ratio_1F = mean(LnFor(B1B:B1A));
Ratio_1R = mean(LnRev(B1B:B1A));
PWF_1 = mean(PWF(B1B:B1A));
%Bath 2                              %Ambient
T_2 = tref_2(1,x) + 273.15;
Ratio_2F = mean(LnFor(B2B:B2A));
Ratio_2R = mean(LnRev(B2B:B2A));
PWF_2 = mean(PWF(B2B:B2A));
%Bath 3                              %Ambient
T_3 = tref_2(1,x) + 273.15;
Ratio_3F = mean(LnFor(B3B:B3A));
Ratio_3R = mean(LnRev(B3B:B3A));
PWF_3 = mean(PWF(B3B:B3A));
%Bath 4
T_4 = tref_1(1,x) + 273.15;           %Hot
```

```
Ratio_4F = mean(LnFor(B4B:B4A));
Ratio_4R = mean(LnRev(B4B:B4A));
PWF_4 = mean(PWF(B4B:B4A));


%Forward
AF = [1,-T_1;1,-T_2;1,-T_3;1,-T_4];
BF = [T_1*(Ratio_1F-PWF_1);T_2*(Ratio_2F-PWF_2);T_3*(Ratio_3F-
PWF_3);T_4*(Ratio_4F-PWF_4)];
XF = AF\BF;
Gamma_Forward = XF(1);
C_Forward = XF(2);

%Reverse
AR = [1,-T_1;1,-T_2;1,-T_3;1,-T_4];
BR = [T_1*(Ratio_1R-PWF_1);T_2*(Ratio_2R-PWF_2);T_3*(Ratio_3R-
PWF_3);T_4*(Ratio_4R-PWF_4)];
XR = AR\BR;
Gamma_Reverse = XR(1);
C_Reverse = XR(2);


%%Calibrated Temperatures
%Forward
ForwardTemp = zeros(indexend,1);
for i = 1:indexend
ForwardTemp(i) = Gamma_Forward/(LnFor(i)+C_Forward-PWF(i)) - 273.15;
end

%Reverse
ReverseTemp = zeros(indexend,1);
LnRev2 = flipud(LnRev);
for i = 1:indexend
ReverseTemp(i) = Gamma_Reverse/(LnRev2(i)+C_Reverse-PWF(i)) - 273.15;
end
ReverseTemp = flipud(ReverseTemp);

%Average of Forward and Reverse Calibrations
CalTemp = (ReverseTemp+ForwardTemp)/2;

%Plot Calibated Temperatures
% figure
% plot(distance,ForwardTemp,'g',distance,ReverseTemp,'b',distance,tempC,'r');
% legend('ForwardTemp','ReverseTemp','tempC');
% title('TMW-1B & TMW-2B Comparison of Forward, Reverse, and Default
Calibrations');
% xlabel('Distance Along Fiber [m]');
% ylabel('Temperature [C]');



%%Create TMW-1B Temperature with Depth Orientation
%Pull Temperatures
TMW1Entry = 312;
TMW1Bottom = 461;
```

```
TMW1Exit = 610;
TMW1Down = CalTemp(TMW1Entry:TMW1Bottom,1);
TMW1Up = CalTemp(TMW1Bottom:TMW1Exit,1);            %May need to change
TMW1Bottom+1 / TMW1Bottom if the vectors are not the same size (perfectly
symmetrical).
TMW1Up = flipud(TMW1Up);
TMW1 = (TMW1Down+TMW1Up)/2;
TMW1F = TMW1*(9/5)+32;              %Convert Celcius temperatures into
Fahrenheight
%Apply appropriate depths to Temperatures
TMW1Depthm = distance(TMW1Entry:TMW1Bottom) - distance(TMW1Entry);
TMW1Depthft = TMW1Depthm .* 3.28084;    %Convert meters to feet

TMW1DownUnCalibrated = tempC(TMW1Entry:TMW1Bottom,x);
TMW1UpUnCalibrated = tempC(TMW1Bottom:TMW1Exit,x);
TMW1Uncalibrated = (TMW1DownUnCalibrated+TMW1UpUnCalibrated)/2;



% %Plot TMW-1B Calibrated Temperature
% figure
% plot(TMW1,TMW1Depthft,'b-',TMW1Up,TMW1Depthft,'r-',TMW1Down,TMW1Depthft,'g-
');
% legend('TMW-1B','TMW-1B Up','TMW-1B Down','Location','Southwest');
% title('TMW1 Temperature with Depth');
% xlabel('Temperature [C]');
% ylabel('Depth [ft]');
% set(gca,'XAxisLocation','top','YAxisLocation','left','ydir','reverse');

%%Find TMW-1B Temperatures at 100 ft intervals for Cimplicity
TMW1Cim = zeros(5,2);      %%Temperature Monitoring Well 1B Temperature with
Depth
i=1;
for n = 1:4
while TMW1Depthft(i)<=100*n
    i = i+1;
    TMW1Cim(n,2) = (TMW1F(i)+TMW1F(i+1)+TMW1F(i-1))/3;
    TMW1Cim(n,1) = TMW1Depthft(i);
end
end
%Bottom of the well values inputed into 500 ft vector
TMW1Cim(5,2) = TMW1F(length(TMW1));
TMW1Cim(5,1) = TMW1Depthft(length(TMW1));



%%Create TMW-2B Temperature with Depth Orientation
%Pull Temperatures
TMW2Entry = 1031;
TMW2Bottom = 1180;
TMW2Exit = 1330;
TMW2Down = CalTemp(TMW2Entry:TMW2Bottom,1);
TMW2Up = CalTemp(TMW2Bottom+1:TMW2Exit,1);
TMW2Up = flipud(TMW2Up);
TMW2 = (TMW2Down+TMW2Up)/2;
```

```
TMW2F = TMW2*(9/5)+32;              %Convert Temperatures from Celcius to
Fahrenheight
%Apply appropriate depths to Temperatures
TMW2Depthm = distance(TMW2Entry:TMW2Bottom) - distance(TMW2Entry);
TMW2Depthft = TMW2Depthm .* 3.28084;    %Convert meters to feet

% %Plot TMW-2B Calibrated Temperature
% figure
% plot(TMW2,TMW2Depthft,'b-',TMW2Up,TMW2Depthft,'r-',TMW2Down,TMW2Depthft,'g-
');
% legend('TMW-2B','TMW-2B Up','TMW-2B Down','Location','Southwest');
% title('TMW2 Temperature with Depth');
% xlabel('Temperature [C]');
% ylabel('Depth [ft]');
% set(gca,'XAxisLocation','top','YAxisLocation','left','ydir','reverse');


%%Find TMW-2B Temperatures at 100 ft intervals for Cimplicity
TMW2Cim = zeros(5,2);      %%Temperature Monitoring Well 2B Temperature with
Depth
i=1;
for n = 1:4
while TMW2Depthft(i)<=100*n
    i = i+1;
    TMW2Cim(n,2) = (TMW2F(i)+TMW2F(i+1)+TMW2F(i-1))/3;
    TMW2Cim(n,1) = TMW2Depthft(i);
end
end
%Bottom of the well values inputed into 500 ft vector
TMW2Cim(5,2) = TMW2F(length(TMW2));
TMW2Cim(5,1) = TMW2Depthft(length(TMW2));

CimMatrix = zeros(12,2);
CimMatrix(2:6,:) = TMW1Cim;
CimMatrix(8:12,:) = TMW2Cim;

% %Create File for Cimplicity Location
% csvwrite('cimplicityfiberfile.csv',CimMatrix);



%%Keep Track of Variables of Interest
GammaF(1,x) = Gamma_Forward;
cF(1,x) = C_Forward;
GammaR(1,x) = Gamma_Reverse;
cR(1,x) = C_Reverse;
for i = 1:7
DAsections(i,x) = DA(i);
end
TMW1CimKeep(:,x) = TMW1Cim(:,2);
TMW2CimKeep(:,x) = TMW2Cim(:,2);
TMW1Keep(:,x) = TMW1;
TMW1UncalibratedKeep(:,x) = TMW1Uncalibrated;
TMW2Keep(:,x) = TMW2;
```

```
%Calculate RMSE of Baths
Bath1Error = (CalTemp(B1B:B1A) - tref_2(1,x)).^2;
B1_RMSE = sqrt(sum(Bath1Error)/length(Bath1Error));

Bath2Error = (CalTemp(B2B:B2A) - tref_1(1,x)).^2;
B2_RMSE = sqrt(sum(Bath2Error)/length(Bath2Error));

Bath3Error = (CalTemp(B3B:B3A) - tref_1(1,x)).^2;
B3_RMSE = sqrt(sum(Bath3Error)/length(Bath3Error));

Bath4Error = (CalTemp(B4B:B4A) - tref_2(1,x)).^2;
B4_RMSE = sqrt(sum(Bath4Error)/length(Bath4Error));

AvgRMSE = (B1_RMSE+B2_RMSE+B3_RMSE+B4_RMSE)/4;
RMSE = [B1_RMSE;B2_RMSE;B3_RMSE;B4_RMSE;AvgRMSE];

%RMSE Keep Code
RMSEKeep(:,x) = RMSE;

end
```

Appendix 5.2 Fixed Gamma Calibrating Matlab Script for TMW-1B & TMW-2B

```
%%Adam McDaniel
clear
close
clc

%%Input data files
Process_Sensornet('E:\Research\Raw Data
Files\TMW1&2\mar\',0,2031,'TMW12.mat');
load('TMW12.mat');

%%Move File into 'Used' Folder
% movefile('C:\Users\Adam\Desktop\Automation\Automation File Initial\channel
7 20160106 001 00001.ddf','C:\Users\Adam\Desktop\Automation\Automation File
End\');

GammaF_Average = 481.4308677;
GammaR_Average = 482.1688619;

%%Loop to run over multiple files
numfiles = size(Stokes,2);
%Prefine Multiple File Variables
GammaF = zeros(1,numfiles);
cF = zeros(1,numfiles);
GammaR = zeros(1,numfiles);
cR = zeros(1,numfiles);
DAsections = zeros(7,numfiles);
TMW1Keep = zeros(150,numfiles);
TMW2Keep = zeros(150,numfiles);
TMW1CimKeep = zeros(5,numfiles);
TMW2CimKeep = zeros(5,numfiles);


for x = 1:numfiles

%%Flip reverse light intensity data
AntiStokesR(:,x) = flipud(AntiStokesR(:,x)); %#ok<SAGROW>
StokesR(:,x) = flipud(StokesR(:,x)); %#ok<SAGROW>

%%Create raw local differential attenuation vector
indexend = length(distance);

EQ1 = zeros(indexend,1);
for i = 1:(indexend-1)
    EQ1(i) = (log(Stokes(i+1,x)/AntiStokes(i+1,x)) -
log(Stokes(i,x)/AntiStokes(i,x)) + log(StokesR(i,x)/AntiStokesR(i,x)) -
log(StokesR(i+1,x)/AntiStokesR(i+1,x)))/2;
end

%%Create raw cumulative differential attenuation vector
CumEQ1 = zeros(indexend,1);
for i = 2:(indexend-1)
   CumEQ1(i) = EQ1(i)+ CumEQ1(i-1);
```

```
end
CumEQ1(indexend) = CumEQ1(indexend-1);

%%Create vectors for natural log ratios forward and reverse
LnFor = log(Stokes(:,x)./AntiStokes(:,x));
LnRev = log(StokesR(:,x)./AntiStokesR(:,x));

%%Splice indexing
SP1B = 1;
SP1A = 6;
SP2B = 33;
SP2A = 38;
SP3B = 271;
SP3A = 276;
SP4B = 643;
SP4A = 648;
SP5B = 995;
SP5A = 1000;
SP6B = 1361;
SP6A = 1366;
SP7B = 1952;
SP7A = 1957;
SP8B = 1981;
SP8A = 1991;

%%Bath indexing
B1B = 14;       %Hot
B1A = 18;       %Hot
B2B = 24;       %Ambient
B2A = 29;       %Ambient
B3B = 1962;     %Ambient
B3A = 1966;     %Ambient
B4B = 1973;     %Hot
B4A = 1975;     %Hot

%%Forward Splice Corrections
%Splice 1
FC1 = LnFor(SP1A) - LnFor(SP1B);
LnFor(SP1B:SP1A,1) = LnFor(SP1B);
LnFor(SP1A+1:indexend) = LnFor(SP1A+1:indexend)- FC1;
%Splice 2
FC2 = LnFor(SP2A) - LnFor(SP2B);
LnFor(SP2B:SP2A,1) = LnFor(SP2B);
LnFor(SP2A+1:indexend) = LnFor(SP2A+1:indexend)- FC2;
%Splice 3
FC3 = LnFor(SP3A) - LnFor(SP3B);
LnFor(SP3B:SP3A,1) = LnFor(SP3B);
LnFor(SP3A+1:indexend) = LnFor(SP3A+1:indexend)- FC3;
%Splice 4
FC4 = LnFor(SP4A) - LnFor(SP4B);
LnFor(SP4B:SP4A,1) = LnFor(SP4B);
LnFor(SP4A+1:indexend) = LnFor(SP4A+1:indexend)- FC4;
%Splice 5
FC5 = LnFor(SP5A) - LnFor(SP5B);
LnFor(SP5B:SP5A,1) = LnFor(SP5B);
LnFor(SP5A+1:indexend) = LnFor(SP5A+1:indexend)- FC5;
```

```
%Splice 6
FC6 = LnFor(SP6A) - LnFor(SP6B);
LnFor(SP6B:SP6A,1) = LnFor(SP6B);
LnFor(SP6A+1:indexend) = LnFor(SP6A+1:indexend)- FC6;
%Splice 7
FC7 = LnFor(SP7A) - LnFor(SP7B);
LnFor(SP7B:SP7A,1) = LnFor(SP7B);
LnFor(SP7A+1:indexend) = LnFor(SP7A+1:indexend)- FC7;
%Splice 8
FC8 = LnFor(SP8A) - LnFor(SP8B);
LnFor(SP8B:SP8A,1) = LnFor(SP8B);

%%Reverse Splice Corrections
%Splice 8
RC8 = LnRev(SP8B) - LnRev(SP8A);
LnRev(SP8B:SP8A,1) = LnRev(SP8A);
LnRev(1:SP8B-1,1) = LnRev(1:SP8B-1) - RC8;
%Splice 7
RC7 = LnRev(SP7B) - LnRev(SP7A);
LnRev(SP7B:SP7A,1) = LnRev(SP7A);
LnRev(1:SP7B-1,1) = LnRev(1:SP7B-1) - RC7;
%Splice 6
RC6 = LnRev(SP6B) - LnRev(SP6A);
LnRev(SP6B:SP6A,1) = LnRev(SP6A);
LnRev(1:SP6B-1,1) = LnRev(1:SP6B-1) - RC6;
%Splice 5
RC5 = LnRev(SP5B) - LnRev(SP5A);
LnRev(SP5B:SP5A,1) = LnRev(SP5A);
LnRev(1:SP5B-1,1) = LnRev(1:SP5B-1) - RC5;
%Splice 4
RC4 = LnRev(SP4B) - LnRev(SP4A);
LnRev(SP4B:SP4A,1) = LnRev(SP4A);
LnRev(1:SP4B-1,1) = LnRev(1:SP4B-1) - RC4;
%Splice 3
RC3 = LnRev(SP3B) - LnRev(SP3A);
LnRev(SP3B:SP3A,1) = LnRev(SP3A);
LnRev(1:SP3B-1,1) = LnRev(1:SP3B-1) - RC3;
%Splice 2
RC2 = LnRev(SP2B) - LnRev(SP2A);
LnRev(SP2B:SP2A,1) = LnRev(SP2A);
LnRev(1:SP2B-1,1) = LnRev(1:SP2B-1) - RC2;
%Splice 1
RC1 = LnRev(SP1B) - LnRev(SP1A);
LnRev(SP1B:SP1A,1) = LnRev(SP1A);


%%Create corrected local differential attenuation vector
CorrectedEQ1 = zeros(indexend,1);
for i = 1:(indexend-1)
CorrectedEQ1(i) = (LnFor(i+1) - LnFor(i) + LnRev(i) - LnRev(i+1))/2;
end

%%Create corrected cumulative differential attenuation vector
CorrectedCumEQ1 = zeros(indexend,1);
for i = 2:(indexend-1)
   CorrectedCumEQ1(i) = CorrectedEQ1(i)+ CorrectedCumEQ1(i-1);
```

```
end
CorrectedCumEQ1(indexend) = CorrectedCumEQ1(indexend-1);


%%Find Sectional Differential Attenuations
A = CorrectedCumEQ1;
B = ones(indexend,2);
B(:,2) = distance;
DA = zeros(7,1);

%Section 1
A1 = A(SP1A:SP2B-1);
B1 = B(SP1A:SP2B-1,:);
X1 = B1\A1;
DA(1) = X1(2);
%Section 2
A2 = A(SP2A:SP3B-1);
B2 = B(SP2A:SP3B-1,:);
X2 = B2\A2;
DA(2) = X2(2);
%Section 3
A3 = A(SP3A:SP4B-1);
B3 = B(SP3A:SP4B-1,:);
X3 = B3\A3;
DA(3) = X3(2);
%Section 4
A4 = A(SP4A:SP5B-1);
B4 = B(SP4A:SP5B-1,:);
X4 = B4\A4;
DA(4) = X4(2);
%Section 5
A5 = A(SP5A:SP6B-1);
B5 = B(SP5A:SP6B-1,:);
X5 = B5\A5;
DA(5) = X5(2);
%Section 6
A6 = A(SP6A:SP7B-1);
B6 = B(SP6A:SP7B-1,:);
X6 = B6\A6;
DA(6) = X6(2);
%Section 7
A7 = A(SP7A:SP8B-1);
B7 = B(SP7A:SP8B-1,:);
X7 = B7\A7;
DA(7) = X7(2);


%%Creation of Piecewise Linear Function
PWF = zeros(indexend,1);
n = 1;
%Section 1 & 2
while n<=SP3B+2
PWF(n) = distance(n)*DA(2);
n = n+1;
end
%Section 3
```

```
while n<=SP4B+2
PWF(n) = PWF(SP3B+2)+ (distance(n)-distance(SP3B+2))*DA(3);
n = n+1;
end
%Section 4
while n<=SP5B+2
PWF(n) = PWF(SP4B+2)+ (distance(n)-distance(SP4B+2))*DA(4);
n = n+1;
end
%Section 5
while n<=SP6B+2
PWF(n) = PWF(SP5B+2)+ (distance(n)-distance(SP5B+2))*DA(5);
n = n+1;
end
%Section 6 & 7
while n<=indexend
PWF(n) = PWF(SP6B+2)+ (distance(n)-distance(SP6B+2))*DA(6);
n = n+1;
end


%%Determine Calibration Parameters
%Bath 1                              %Hot
T_1 = tref_1(1,x) + 273.15;
Ratio_1F = mean(LnFor(B1B:B1A));
Ratio_1R = mean(LnRev(B1B:B1A));
PWF_1 = mean(PWF(B1B:B1A));
%Bath 2                              %Ambient
T_2 = tref_2(1,x) + 273.15;
Ratio_2F = mean(LnFor(B2B:B2A));
Ratio_2R = mean(LnRev(B2B:B2A));
PWF_2 = mean(PWF(B2B:B2A));
%Bath 3                              %Ambient
T_3 = tref_2(1,x) + 273.15;
Ratio_3F = mean(LnFor(B3B:B3A));
Ratio_3R = mean(LnRev(B3B:B3A));
PWF_3 = mean(PWF(B3B:B3A));
%Bath 4
T_4 = tref_1(1,x) + 273.15;           %Hot
Ratio_4F = mean(LnFor(B4B:B4A));
Ratio_4R = mean(LnRev(B4B:B4A));
PWF_4 = mean(PWF(B4B:B4A));


% %Forward
% AF = [1,-T_1;1,-T_2;1,-T_3;1,-T_4];
% BF = [T_1*(Ratio_1F-PWF_1);T_2*(Ratio_2F-PWF_2);T_3*(Ratio_3F-
PWF_3);T_4*(Ratio_4F-PWF_4)];
% XF = AF\BF;
% Gamma_Forward = XF(1);
% C_Forward = XF(2);

C_Forward1 = GammaF_Average/T_1 + PWF_1 - Ratio_1F;
C_Forward2 = GammaF_Average/T_2 + PWF_2 - Ratio_2F;
C_Forward3 = GammaF_Average/T_3 + PWF_3 - Ratio_3F;
C_Forward4 = GammaF_Average/T_4 + PWF_4 - Ratio_4F;
```

```
C_Forward = (C_Forward1 + C_Forward2 + C_Forward3 + C_Forward4)/4;

% %Reverse
% AR = [1,-T_1;1,-T_2;1,-T_3;1,-T_4];
% BR = [T_1*(Ratio_1R-PWF_1);T_2*(Ratio_2R-PWF_2);T_3*(Ratio_3R-
PWF_3);T_4*(Ratio_4R-PWF_4)];
% XR = AR\BR;
% Gamma_Reverse = XR(1);
% C_Reverse = XR(2);

C_Reverse1 = GammaR_Average/T_1 + PWF_1 - Ratio_1R;
C_Reverse2 = GammaR_Average/T_2 + PWF_2 - Ratio_2R;
C_Reverse3 = GammaR_Average/T_3 + PWF_3 - Ratio_3R;
C_Reverse4 = GammaR_Average/T_4 + PWF_4 - Ratio_4R;
C_Reverse = (C_Reverse1 + C_Reverse2 + C_Reverse3 + C_Reverse4)/4;


%%Calibrated Temperatures
%Forward
ForwardTemp = zeros(indexend,1);
for i = 1:indexend
ForwardTemp(i) = GammaF_Average/(LnFor(i)+C_Forward-PWF(i)) - 273.15;
end

%Reverse
ReverseTemp = zeros(indexend,1);
LnRev2 = flipud(LnRev);
for i = 1:indexend
ReverseTemp(i) = GammaR_Average/(LnRev2(i)+C_Reverse-PWF(i)) - 273.15;
end
ReverseTemp = flipud(ReverseTemp);

%Average of Forward and Reverse Calibrations
CalTemp = (ReverseTemp+ForwardTemp)/2;

% %Plot Calibated Temperatures
% figure
% plot(distance,ForwardTemp,'g',distance,ReverseTemp,'b',distance,tempC,'r');
% legend('ForwardTemp','ReverseTemp','tempC');
% title('TMW-1B & TMW-2B Comparison of Forward, Reverse, and Default
Calibrations');
% xlabel('Distance Along Fiber [m]');
% ylabel('Temperature [C]');



%%Create TMW-1B Temperature with Depth Orientation
%Pull Temperatures
TMW1Entry = 312;
TMW1Bottom = 461;
TMW1Exit = 610;
TMW1Down = CalTemp(TMW1Entry:TMW1Bottom,1);
TMW1Up = CalTemp(TMW1Bottom:TMW1Exit,1);            %May need to change
TMW1Bottom+1 / TMW1Bottom if the vectors are not the same size (perfectly
symmetrical).
```

```
TMW1Up = flipud(TMW1Up);
TMW1 = (TMW1Down+TMW1Up)/2;
TMW1F = TMW1*(9/5)+32;              %Convert Celcius temperatures into
Fahrenheight
%Apply appropriate depths to Temperatures
TMW1Depthm = distance(TMW1Entry:TMW1Bottom) - distance(TMW1Entry);
TMW1Depthft = TMW1Depthm .* 3.28084;    %Convert meters to feet

% %Plot TMW-1B Calibrated Temperature
% figure
% plot(TMW1,TMW1Depthft,'b-',TMW1Up,TMW1Depthft,'r-',TMW1Down,TMW1Depthft,'g-
');
% legend('TMW-1B','TMW-1B Up','TMW-1B Down','Location','Southwest');
% title('TMW1 Temperature with Depth');
% xlabel('Temperature [C]');
% ylabel('Depth [ft]');
% set(gca,'XAxisLocation','top','YAxisLocation','left','ydir','reverse');

%%Find TMW-1B Temperatures at 100 ft intervals for Cimplicity
TMW1Cim = zeros(5,2);      %%Temperature Monitoring Well 1B Temperature with
Depth
i=1;
for n = 1:4
while TMW1Depthft(i)<=100*n
    i = i+1;
    TMW1Cim(n,2) = (TMW1F(i)+TMW1F(i+1)+TMW1F(i-1))/3;
    TMW1Cim(n,1) = TMW1Depthft(i);
end
end
%Bottom of the well values inputed into 500 ft vector
TMW1Cim(5,2) = TMW1F(length(TMW1));
TMW1Cim(5,1) = TMW1Depthft(length(TMW1));



%%Create TMW-2B Temperature with Depth Orientation
%Pull Temperatures
TMW2Entry = 1031;
TMW2Bottom = 1180;
TMW2Exit = 1330;
TMW2Down = CalTemp(TMW2Entry:TMW2Bottom,1);
TMW2Up = CalTemp(TMW2Bottom+1:TMW2Exit,1);
TMW2Up = flipud(TMW2Up);
TMW2 = (TMW2Down+TMW2Up)/2;
TMW2F = TMW2*(9/5)+32;              %Convert Temperatures from Celcius to
Fahrenheight
%Apply appropriate depths to Temperatures
TMW2Depthm = distance(TMW2Entry:TMW2Bottom) - distance(TMW2Entry);
TMW2Depthft = TMW2Depthm .* 3.28084;    %Convert meters to feet

% %Plot TMW-2B Calibrated Temperature
% figure
% plot(TMW2,TMW2Depthft,'b-',TMW2Up,TMW2Depthft,'r-',TMW2Down,TMW2Depthft,'g-
');
% legend('TMW-2B','TMW-2B Up','TMW-2B Down','Location','Southwest');
% title('TMW2 Temperature with Depth');
```

```
% xlabel('Temperature [C]');
% ylabel('Depth [ft]');
% set(gca,'XAxisLocation','top','YAxisLocation','left','ydir','reverse');


%%Find TMW-2B Temperatures at 100 ft intervals for Cimplicity
TMW2Cim = zeros(5,2);      %%Temperature Monitoring Well 2B Temperature with
Depth
i=1;
for n = 1:4
while TMW2Depthft(i)<=100*n
    i = i+1;
    TMW2Cim(n,2) = (TMW2F(i)+TMW2F(i+1)+TMW2F(i-1))/3;
    TMW2Cim(n,1) = TMW2Depthft(i);
end
end
%Bottom of the well values inputed into 500 ft vector
TMW2Cim(5,2) = TMW2F(length(TMW2));
TMW2Cim(5,1) = TMW2Depthft(length(TMW2));

CimMatrix = zeros(12,2);
CimMatrix(2:6,:) = TMW1Cim;
CimMatrix(8:12,:) = TMW2Cim;

% %Create File for Cimplicity Location
% csvwrite('cimplicityfiberfile.csv',CimMatrix);



%%Keep Track of Variables of Interest
GammaF(1,x) = GammaF_Average;
cF(1,x) = C_Forward;
GammaR(1,x) = GammaR_Average;
cR(1,x) = C_Reverse;
for i = 1:7
DAsections(i,x) = DA(i);
end
TMW1CimKeep(:,x) = TMW1Cim(:,2);
TMW2CimKeep(:,x) = TMW2Cim(:,2);
TMW1Keep(:,x) = TMW1;
TMW2Keep(:,x) = TMW2;

end
```

Appendix 5.3 Colorflood Data Visualization for TMW-1B & TMW-2B

```
%%Data Visualization for TMW-1B and TMW-2B
%%Adam McDaniel

clear
close
clc
```

```
cd('F:\MCDAN FLASH\Research\GeoExchange\Calibrating Organization\FINAL\');

% load('WinterGammaFixedF.mat');          %Gamma Fixed, Winter, F
load('TMW12ALLFixeda.mat');              %Gamma Fixed, Start to End Nov 2017,


% TMW-1B Plot
startDate = datenum('5-13-2015');
endDate = datenum('3-28-2017');
xData = linspace(startDate,endDate,8);

% Interpolation
[TimeMesh,DepthMesh]=meshgrid([min(Time):0.0139:max(Time)],[min(Depth):max(De
pth)]);
TMW2Interp=griddata(Time,Depth,TMW1,TimeMesh,DepthMesh);

figure
contourf(TimeMesh,DepthMesh,TMW2Interp,50,'edgecolor','none');
set(findobj(gca,'color',[0,0,0]),'visible','off')
% pcolor(TMW1);
shading interp;
datetick('x','mm')

% figure
% contour(Time,Depth,TMW1);
% pcolor(TMW1);
% shading interp;

set(gca,'XAxisLocation','top','YAxisLocation','left','ydir','reverse','FontSi
ze',20);
ylabel('Depth [m]');
title('TMW-1B All Data');

% axis labeling %%COMMENT ME OUT IF NOT WORKING
ax = gca;
ax.XTick = xData;
datetick('x','mmm','keepticks');
ylim([0 150]);


% colorbar coloring
colormap jet
colorbar
caxis([9 18.5])

%%%%%%%%%%%%%%%%%%%%%%%%%%%%%%%%%%%%%%%%%%%%%%%%%%%%%%%%%%%%%%%%%%%%%%%%%%%%
%%%%%%%%%%%%%%%

% TMW-1B Plot
% startDate = datenum('5-13-2015');
% endDate = datenum('11-30-2016');
% xData = linspace(startDate,endDate,8);
```

```
%Interpolation
[TimeMesh,DepthMesh]=meshgrid([min(Time):0.0139:max(Time)],[min(Depth):max(De
pth)]);
TMW2Interp=griddata(Time,Depth,TMW2,TimeMesh,DepthMesh);

figure
contourf(TimeMesh,DepthMesh,TMW2Interp,200,'edgecolor','none');
% set(findobj(gca,'color',[0,0,0]),'visible','off')
% pcolor(TMW1);
shading interp;
datetick('x','mm')

% figure
% contour(Time,Depth,TMW1);
% pcolor(TMW1);
% shading interp;

set(gca,'XAxisLocation','top','YAxisLocation','left','ydir','reverse','FontSi
ze',20);
ylabel('Depth [m]');
title('TMW-2B All Data');

% axis labeling %%COMMENT ME OUT IF NOT WORKING
ax = gca;
ax.XTick = xData;
datetick('x','mmm','keepticks');
ylim([0 150]);


%colorbar coloring
colormap jet
colorbar
caxis([9 18.5])
```

References

Acuña, J., & Palm, B. (2013). Distributed thermal response tests on pipe-in-pipe borehole heat exchangers. Appl. Energy, 109, 312-320. doi:10.1016/j.apenergy.2013.01.024

American Society of Heating, Refrigerating and Air-Conditioning Engineers (ASHRAE), (2011)."Geothermal Energy." In 2011 ASHRAE Handbook - HVAC Applications." Ch. 34. American Society of Heating, Refrigerating and Air-Conditioning Engineers.

Arnon, A., Selker, J.S., & Lensky, N.G. (2016). Thermohaline stratification and double diffusion diapycnal fluxes in the hypersaline Dead Sea. Limnol. Oceanogr, 61(4), 1214-1231. doi: 10.1002/lno.10285

ASTM Standard D2216, 2010, “Standard Test Methods for Laboratory Determination of Water (Moisture) Content of Soil and Rock by Mass.”

ASTM Standard D6913, 2004, “Standard Test Methods for Particle-Size Distribution (Gradation) of Soils Using Sieve Analysis.”

ASTM Standard D7263, 2009, “Standard Test Methods for Laboratory Determination of Density (Unit Weight) of Soil Specimens.”

ASTM Standard E1225, 2009, “Standard Test Method for Thermal Conductivity of Solids Using the Guarded-Comparative-Longitudinal Heat Flow Technique.”

Bahr, J.M., Hart, D.J., & Leaf, A.T. (2011). Distributed temperature sensing (DTS) as a hydrostratigraphic characterization tool. Project Completion Report; Wisconsin Geological and Natural History Survey. Retrieved from http://ctemps.org/sites/ctemps.org/files/ctemps/bahr_2011.pdf

Bao, X., & Chen, L. (2012). Recent progress in distributed fiber optic sensors. Sensors, 12(7), 8601-8639. doi: 10.3390/s120708601

Beier, R.A., Acuña, J., Mogensen, P., & Palm, B. (2012). Vertical temperature profiles and borehole resistance in a u-tube borehole heat exchanger. Geothermics, 44, 23-32. doi: 10.1016/j.geothermics.2012.06.0

Bejan, A., Tsatsaronis, G., & Moran, M. (1996). Thermal Design and Optimization. New York, NY: John Wiley & Sons, Inc.

Bense, V.F., Read, T., & Verhoef, A. (2016). Using distributed temperature sensing to monitor field scale dynamics of ground surface temperature related substrate heat flux. Agric. For. Meteorol., 220, 207-215. doi: 10.1016/j.agrformet.2016.01.138

Bloom, E.F., and Tinjum, J.M. (2016). Fully instrumented life-cycle analyses for a residential geo-exchange system. ASCE GSP 270, pp. 114-124. Paper presented at the Geo-Chicago 2016 Conference. Chicago, IL. doi: 10.1061/9780784480137.012

Blum, P., Campillo, G., Münch, W., and Kölbel, T. (2010). CO_2 savings of ground source heat pump systems – A regional analysis. *Renew Energ*, *35*(1), pp. 112-127. doi: 10.1016/j.renene.2009.03.034

Blume, T., Krause, S., Meinikmann, K., & Lewandowski, J. (2013). Upscaling lacustrine groundwater discharge rates by fiber-optic distributed temperature sensing. Water Resour. Res., 49. doi: 10.1002/2012WR013215

Bugge, J., Kjær, S., and Blum, R. (2006). High-efficiency coal-fired power plants development and perspectives. Energy, 31(10-11). pp. 1437-1445. doi: 10.1016/j.energy.2005.05.025

Carslaw, H.S., and Jaeger, J.C. (1947). Conduction of Heat in Solids. Oxford, UKL Claremore Press.

Clauser, C. and Huenges, E. (2013). Thermal conductivity of rocks and minerals, in Rock Physics and Phase Relations, edited by T.J. Ahrens, pp. 105-126. Am. Geophys. Union, Washington D.C., 1995.

Cottingham, C., Vitale, M., Selker, J., Selker, F., & Lupton, S. (2013, August). Using fiber optics and vibrating wire piezometers to characterize an aquifer in preparation for ground and aquifer freezing. Paper presented at the International Mine Water Association 2013 Annual Conference, Golden, CO. Retrieved from http://www.mwen.info/docs/imwa_2013/IMWA2013_Cottingham_495.pdf

Curry, B., Grimley, D., & McKay, D. (2011). Quaternary glaciations in Illinois. Developments in Quaternary Science, 15 (2011), 467-487. doi: 10.1016/B978-0-444-53447-7.00036-2

Dehkordi, S.E. and Schincariol, R.A. (2014). Effect of thermal-hydrogeological and borehole heat exchanger properties on performance and impact of vertical closed-loop geothermal heat pump systems. *Hydrogeol. J. 22*(1). pp 189-203. doi:10.1007/s10040-013-1060-6

Diao, N., Li, Q., and Fang, Z. (2004). Heat transfer in ground heat exchangers with groundwater advection. *Int. J. Therm. Sci.*, *43*(12). pp. 1203-1211. doi: 10.1016/j.ijthermalsci.2004.04.009

Dott, Jr., R.H., and Attig, J.W., (2004). Roadside geology of Wisconsin. Missoula, Montana: Mountain Press Publishing Company.

Energy Center of Wisconsin, (2010). Achieving 25x'25 goals for energy independent communities: results from the 2009 pilot program. Retrieved from: https://www.seventhwave.org/sites/default/files/252-1.pdf

Energy Information Administration (EIA), (2009). "Residential Energy Consumption Survey (RECS)."

Energy Information Administration (EIA), (2016). "International Energy Outlook." U.S. Energy Information Administration (USEIA).

Environmental Protection Agency (EPA). 2013. "Draft Inventory of U.S. Greenhouse Gas Emissions and Sinks: 1990–2015." Washington D.C.

Epic Careers. (2017). Retrieved from: https://careers.epic.com/Home/WhatWeDo

Etheridge, D.M., Steele, L.P., Langenfelds, R.L., Francey, R.J., Barnola, J.M., and Morgan, V.I. (1996)."Natural and anthropogenic changes in atmospheric CO2 over the last 1000 years from air in Antarctic ice and firn." *Geophysical Research*, *101*(D2), 4115–4128.

Farahani, M.A., & Gogolla, T. (1999). Spontaneous raman scattering in optical fibers with modulated probe light for distributed temperature raman remote sensing. J. Lightwave Technol, 17(8), 1379-1391. doi: 10.1109/50.779159

Florea, L.J., Hart, D.J., Tinjum, J.M., and Choi, C. (2017). Potential impacts to groundwater from ground-coupled geothermal heat pumps in district scale. *Ground Water*, *55*(1). pp. 8-9. doi: 10.1111/gwat.12484

Fourier. J.B.J. (1822). Théorie Analytique de la Chaleur. Paris, France: Firmin Didot.

Freifeld, B.M., Finsterle, S., Onstott, T.C., Toole, P., & Pratt, L.M. (2008). Ground surface temperature reconstructions: Using in situ estimates for thermal conductivity acquired with a fiber-optic distributed thermal perturbation sensor. Geophysical Research Letters, 35(14). doi: 10.1029/2008GL034762

Fridleifsson, I.B., Bertani, R., Huenges, E., Lund, J.W., Ragnarsson, A., and Rybach, L. (2008). The possible role and contribution of geothermal energy to the mitigation of climate change. In: O. Hohmeyer and T. Trittin (Eds.), IPCC Scoping Meeting on Renewable Energy Sources, Proceedings, Luebeck, Germany, 20–25 January 2010, pp. 59–80.

Fujii, H., Okubo, H., Nishi, K., Itoi, R., Ohyama, K., & Shibata, K. (2009). An improved thermal response test for U-tube ground heat exchangers based on optical fiber thermometers. Geothermics, 38(4) 399-406. doi: 10.1016/j.geothermics.2009.06.002

Garber, D., Choudhary, R., & Soga, K. (2013). Risk based lifetime costs assessment of a ground source heat pump (GSHP) system design: Methodology and case study. Building and Environment, 60, 66-80. doi: 10.1016/j.buildenv.2012.11.011

Gehlin, C.E.S. (1996). A mobile equipment for thermal response test: Testing and evaluation (Doctoral dissertation). Luleå University of Technology, Luleå, Sweden.

Ground Loop Design (2016). Thermal Dynamics. Ontario, CA.

Hartog, A.H. (1983). A distributed temperature sensor based on liquid-core optical fibers. *J. Lightw. Technol. 1*(3). pp. 498-509. doi: 10.1109/JLT.1983.1072146

Hausner, M., Suárez, F., Glander, K., van de Giesen, N., Selker, J., & Tyler, S. (2011). Calibrating single-ended fiber-optic raman spectra distributed temperature sensing data. Sensors 11(11), 10859-10879. doi: 10.3390/s111110859

Hausner, M., & Kobs, S. (2016). Identifying and correcting step losses in single-ended fiber-optic distributed temperature sensing data. Journal of Sensors, 2016, 10 pages. doi: 10.1155/2016/7073619

Hecht-Méndez, J. de Paly, M., Beck, M. and Bayer, P. (2013). Optimization of energy extraction for vertical close-loop geothermal systems considering groundwater flow. *Energ. Convers. Manage. 66*(2013). pp. 1-10. doi: 10.1016/j.enconman.2012.09.019

Hellström, G. (1991). Ground heat storage: Thermal analysis of duct storage systems. Lund, Sweden: Part I Theory. University of Lund, Dpartment of Mathematical Physics.

Helmke, M.F., Wilson, J.A., Gatlin, D.C., and Moore, K.O. (2016). Thermogeologic performance of a large-scale district geoexchange system in southeast Pennsylvania. GSA Special Papers 519. doi: 10.1130/2016.2519(03)

Henninges, J., & Huenges, E. (2005). In situ thermal conductivity of gas-hydrate-bearing sediments of the Mallik 5L-38 well. Journal of Geophysical Research, 110(B11). doi: 10.1029/2005JB003734

Henderson, R.D., Day-Lewis, F.D., & Harvey, C.F. (2009). Investigation of aquifer-estuary interaction using wavelet analysis of fiber-optic temperature data. Geophys. Res. Lett., 36(6). doi: 10.1029/2008GL036926

Herrera, C. (2016). Modeling and Assessment of the Wisconsin Institutes for Discovery Ground-Coupled Heat Pump. (Master's thesis). University of Wisconsin-Madison, Madison, Wisconsin.

Hoes, O.A.C., Schilperoort, R.P.S., Luxemburg, W.M.J., Clemens, F.H.L.R., & van de Giesen N.C. (2009). Locating illicit connections in storm water sewers using fiber-optic distributed temperature sensing. Water Res., 43(20), 5187-5197. doi: 10.1016/j.watres.2009.08.020

Horai, K., and Simmons, G. (1969). Thermal conductivity of rock-forming minerals. Earth Planet. Sci. Lett. 6(1969). pp. 359-368. doi: 10.1016/0012-821X(69)90186-1

Ingersoll, L.R., Zobel, O.J., and Ingersoll, A.C. (1954). Heat Conduction with Engineering, Geological and Other Applications. New York: McGraw-Hill.

Ismail, A., & Stumpf, A.J. (2014). Seismic characterization of glacial sediments in central Illinois. Journal of Applied Geophysics, 101 (2014), 1-10. doi: 10.1016/j.jappgeo.2013.11.009.

Jenkins, D.P., Tucker, R., and Rawlings, R. (2009). Modelling the carbon-saving performance of domestic ground-source heat pumps. *Energ Buildings, 41*(6), pp. 587-595. doi: 10.1016/j.enbuild.2008.12.002

Kavanaugh, S. (1995). A design method for commercial ground-coupled heat pumps. American Society of Heating, Refrigerating and Air-Conditioning (ASHRAE) Transactions, 101(part 2), pp. 1088-1094.

Keller, C.A., Huwald, H., Vollmer, M.K., Wenger, A., Hill, M., Parlange, M.B., & Reimann, S. (2011). Fiber optic distributed temperature sensing for the determination of the nocturnal atmospheric boundary layer height. Atmos. Meas. Tech., 4, 143-149. doi: 10.5194/amt-4-143-2011

Kelly, J. (January 6, 2009). "Deep Drilling Begins for Wisconsin Institutes for Discovery Geothermal System." Retrieved from University of Wisconsin-Madison News: http://news.wisc.edu/deep-drilling-begins-for-wisconsin-institutes-for-discovery-geothermal-system/

Kersey, A.D. (2000). Optical Fiber Sensors for Permanent Downwell Monitoring Applications in the Oil and Gas Industry. IEICE Trans. Electron., E83-C(3), 400-404. Retrieved from http://search.ieice.org/bin/summary.php?id=e83-c_3_400

Knudson, R. (2013). Coupled heat pumps: Utilizing live building control data in the Wisconsin Institutes for Discovery (Master's thesis). University of Wisconsin-Madison, Madison, Wisconsin.

Krause, S. & Blume, T. (2013). Impact of seasonal variability and monitoring mode on the adequacy of fiber-optic distributed temperature sensing at aquifer-river interfaces. Water Resour. Res. 49, 2408-2423. doi: 10.1002/wrcr.0232

Li, S., Yang, W., and Zhang, X. (2009). Soil temperature distribution around a U-tube heat exchanger in a multi-function ground source heat pump system. *Appl. Therm. Eng. 29*(17-18). pp. 3679-3686. doi: 10.1016/j.applthermaleng.2009.06.025

Li, M. (2012). Life Cycle Assessment of Residential Heating and Cooling Systems in Minnesota. (Master's thesis). University of Minnesota, Minneapolis, Minnesota.

Lowry, C.S., Walker, J.F., Hunt, R.J., & Anderson, M.P. (2007). Identifying spatial variability of groundwater discharge in a wetland stream using a distributed temperature sensor. Water Resour. Res., 43(10). doi: 10.1029/2007WR006145

Lucas, R.G. Suárez, F., Tyler, S.W., Moran, J.E., & Conklin, M.H. (2016). Polymictic pool behavior in a montane meadow, Sierra Nevada, CA. Hydrol. Process, 30(18), 3274-3288. doi: 10.1002/hyp.10834

Luo, J., Rohn, J., Bayer, M., Priess, A., Wilkmann, L., and Xiang, W. (2015). Heating and cooling performance analysis of a ground source heat pump system in Southern Germany. Geothermics, 53(2015), 57-66. doi: 10.1016/j.geothermics.2014.04.0

Lund, J.W., & Boyd T.L. (2015). Direct utilization of geothermal energy 2015 worldwide review. Geothermics, 60, 66-93. doi: 10.1016/j.geothermics.2015.11.004

Madison Gas and Electric (April, 2017). Residential Electric Rates. https://www.mge.com/customer-service/home/elec-rates-res/

Magraner, T., Montero, À., Quilis, S., & Urchueguía, J.F. (2010). Comparison between design and actual energy performance of HVAC-ground coupled heat pump system in cooling and heating operation. Energy and Buildings, 42(9) 1394-1401. doi: 10.1016/j.enbuild.2010.03.008

McDaniel, A. Harper, M., Fratta, D., Tinjum, J., Choi, C., and Hart, D. 2016. Dynamic calibration of fiber-optic distributed temperature sensing at a district-scale geothermal exchange borefield. In Geo-Chicago 2016, 1-11. Chicago, IL. doi: 10.106I/9780784480137.001

McDaniel, A., Tinjum, J.M., Hart, D.J., and Fratta, D. (2017). Dynamic calibration and permanent distributed temperature sensing network. In Press.

Meyer, L. (2013). Thermophysical properties of Wisconsin rocks for application in geothermal energy (Master's thesis). University of Wisconsin-Madison, Madison, Wisconsin.

Molz, F.J., Morin, R.H., Hess, A.E., Melville, J.G., & Gűven, O. (1989). The impeller meter for measuring aquifer permeability variations: Evaluation and comparison with other tests. Water Resources Research, 25(7), 1677-1683. doi: 10.1029/WR025i007p01677

Montgomery, R.B. (1947). Viscosity and thermal conductivity of air and diffusivity of water vapor in air. *J. Atmos. Sci.*, vol. *6*. pp. 193-196. doi: 10.1175/15200469(1947)004<0193:VATCOA>2.0.CO;2

Nagano, K., Katsura, T., & Takeda, S. (2006). Development of a design and performance prediction tool for the ground source heat pump system. Applied Thermal Engineering, 26(14-15), 1578-1592. doi: 10.1016/j.applthermaleng.2005.12.003

Omer, A.M. (2006). Ground-source heat pumps systems and applications. *Renew. Sustainable Energy Rev*., *12*(2). pp. 344-371. doi: 10.1016/j.rser.2006.10.003

Özdoğan-Dölçek, A. (2015). Numerical modeling of heat transport for ground-coupled heat pump (GCHP) systems and associated life cycle assessments (Doctoral dissertation). University of Wisconsin-Madison, Madison, Wisconsin.

Parsen, M.J., Bradbury, K.R., Hunt, R.J., and Feinstein, D.T. (2016). The 2016 groundwater flow model for Dane County, Wisconsin. Bulletin 110. Wisconsin Geologic and Natural History Survey, Madison, Wisconsin.

Puttagunta, S., Aldrich, R.A., Owens, D., & Mantha, P. (2010). Residential ground-source heat pumps: In-field system performance and energy modeling. GRC Trans, 34(2010) 941-948. Retrieved from: http://www.carb-swa.com/Collateral/Documents/CARB-SWA/Research/Ground_Source_Heat_Pumps.pdf

Rafferty, K. (2015). A capital cost comparison of commercial ground-source heat pump systems. Geo-Heat Center. Oregon Institute of Technology. Retrieved from: http://www.oit.edu/docs/default-source/geoheat-center-documents/publications/heat-pump/tp38.pdf?sfvrsn=2

Ramires, M.L.V., Nieto de Castro, C.A., Nagasaka, Y., Nagashima, A., Assael, M.J., and Wakeham, W.A. (1995). Standard reference data for the thermal conductivity of water. *J. Phys. Chem. Ref. Data.*, vol. *24*. pp. 1377-1381. doi: 10.1063/1.555963

Raymond, J., Therrien, R., Gosselin, L., & Lefebvre, R. (2011). A review of thermal response test analysis using pumping test concepts. Ground Water, 49(6), 932-945. doi: 10.1111/j.1745-6584.2010.00791.x

Raymond, J., and Lamarche, L. (2013). Simulation of thermal response tests in a layered subsurface. *App. Eng. 109*(2013). pp. 293-301. doi: 10.1016/j.apenergy.2013.01.033

Read, T., Bour, O., Bense, V., Le Borgne, T., Goderniaux, P., Klepikova, M.V., Hochreutener, R., Lavenant, N. and Boschero, V. (2013). Characterizing groundwater flow and heat transport in fractured rock using fiber-optic distributed temperature sensing. Geophys. Res. Lett., 40(10), 2055-2059. doi: 10.1002/grl.50397

Rosenau, N.A., Tabor, N.J., Elrick, S.D., & Nelson, W.J. (2013). Polygenetic history of paleosols in middle-upper Pennsylvanian cyclothems of the Illinois basin, U.S.A.: Part 1. Characterization of paleosol types and interpretation of pedogenic processes. Journal of Sedimentary Research, 83(8), 606-636. doi: 10.2110/jsr.2013.50

Samuelson, A., Dowling, C.B., Neumann, K., and Bonneau, P. (2011). Baseline hydrogeologic characteristics of the first phase ground-source geothermal field at Ball State University (Muncie, IN), in 32nd Annual Indiana Water Resources Association Conference, Indiana Water Resources Association.

Sayde, C., Gregory, C., Gil-Rodriguez, M., Tufillaro, N., Tyler, S., van de Giesen, N., English, M., Cuenca, R., & Selker, J.S. (2010). Feasibility of soil moisture monitoring with heated fiber optics. Water Resour. Res., 46(6). doi: 10.1029/2009WR007846

Sayyaadi, H., Amlashi E.H., & Amidpour, M. (2009). Multi-objective optimization of a vertical ground source heat pump using evolutionary algorithm. Energy Conversion and Management, 50(8) 2035-2046. doi: 10.1016/j.enconman.2009.04.006

Schilperoort, R.P.S., & Clemens, F.H.L.R. (2009). Fibre-optic distributed temperature sensing in combined sewer systems. Water Sci. Technol., 60(5), 1127-1134. doi: 10.2166/wst.2009.467

Sensornet Ltd (2015). Sentinel DTS User Manual. Hertfordshire, UK.

Selker, J.S., Thévenaz, L., Huwald, H., Mallet, A., Luxemburg, W., van de Giesen, N., Stejskal, M., Zeman, J., Westhoff, M., & Parlange, M.B. (2006). Distributed fiber-optic temperature sensing for hydrologic systems. Water Resour. Res., 42, W12202, doi: 10.1029/2006WR005326

Seppänen, O. Fisk, W.J., and Lei, Q.H. (2006). Effect of Temperature on Task Performance in Office Environment. Ernest Orlando Lawrence Berkeley National Laboratory.

Siliski, A., Florea, L.J., Dowling, C.B., Neumann, K., Samuelson, A., and Dunn, M. (2016). Petrographic and hydrogeologic investigations for a district-scale ground-coupled heat pump-Ball State University, Indiana. GSA Special Papers 519. doi: 10.1130/2016.2519(04)

Silixa Ltd (2017). Ultima-DTS Datasheet. Hertfordshire, UK.

Slater, L.D., Ntarlagiannis, D., Day-Lewis, F., Mwakanyamale, K., Versteeg, R.J, Ward., A., Strickland, C., Johnson, C., & Lane, J.W. J. (2010). Use of electrical imaging and distributed temperature sensing methods to characterize surface water-groundwater exchange regulating uranium transport at the Handford 300 Area, Washington. Water Resour. Res., 46(10). doi: 10.1029./2010WR009110

Smith, E., Dent, G. (2005). “Modern raman spectrsocopy, a practical approach.Chapter three: the theroy of raman spectroscopy.” John Wiley & Sons, Ltd., Hoboken, N.J.

Steele-Dunne, S.C., Rutten, M.M., Krzeminska, D.M. Hausner, M., Tyler, S.W., Selker, J., Bogaard, T.A., & van de Giesen, N.C. (2010). Feasibility of soil moisture estimation using passive distributed temperature sensing. Water Resour. Res., 46(3). doi: 10.1029/2009WR008272

Striegl, A.M. & Loheide, S.P. (2012). Heated distributed temperature sensing for field scale soil moisture monitoring. Ground Water, 50(3), 340-347. doi: 10.1111/j.1745-6584.2012.00928.x

Suárez, F., Aravena, J.E., Hausner, M.B., Childress, A.E., & Tyler, S.W. (2011a). Assessment of a vertical high-resolution distributed-temperature-sensing system in a shallow thermohaline environment. Hydrol. Earth Syst. Sci. 15(3), 1081-1093. doi:10.5194/hess-15-1081-2011

Suárez, F., Hausner, M.B., Dozier, J., Selker, J.S., & Tyler, S.W. (2011b). Chapter 31: Heat transfer in the environment: Development and use of fiber-optic distributed temperature sensing. Developments in Heat Transfer (pp. 611-636), Rijeka, Croatia: InTech. doi: 10.5772/822

Tans, P., and Keeling, R. 2017. NOAA/ESRL (www.esrl.noaa.gov/gmd/ccgg/trends/) Scripps Institution of Oceanography.

Tarnawski, W.R., Leong, W.H., Momose, T., and Hamada, Y. (2009). Analysis of ground source heat pumps with horizontal ground heat exchangers for northern Japan. *Renew. Energy*, *34*(1). pp. 127–134. doi: 10.1016/j.renene.2008.03.026

Theis. C.V. (1952). The relation between the lowering of the piezometric surface and the rate and duration of discharge of a well using ground water storage. United States Department of the Interior, Geological Survey, Water Resources Division, Ground Water Branch: Washington D.C. doi: 10.1029/TR016i002p00519

Thomas, C.K., Kennedy, A.M., Selker, J.S., Moretti, A., Schroth, M.H., Smoot, A.R., Tufillaro, N.B., & Zeeman, M.J. (2011). High-resolution fibre-optic temperature sensing: A new tool to study the two-dimensional structure of atmospheric surface-layer flow. Bound.-Layer Meteorol., 142(2), 177-192. doi: 10.1007/s10546-011-9672-7

Tyler, S.W., Burak, S.A., McNamara, J.P., Lamontagne, A., Selker, J.S., & Dozier, J. (2008). Spatially distributed temperatures at the base of two mountain snowpacks measured with fiber-optic sensors. J. Glaciol., 54(187), 673-679. doi: 10.3189/002214308786570827

Tyler, S.W., Selker, J.S., Hausner, M.B., Hatch, C.E., Torgersen, T., Thodal, C.E., & Schladow, S.G. (2009). Environmental temperature sensing using Raman spectra DTS fiber-optic methods. Water Resour. Res., 45(4). doi: 10.1029/2008WR007052

van de Giesen, N., Steele-Dunne, S.C., Jansen, J., Hoes, O., Hausner, M.B., Tyler, S., & Selker, J.S. (2012). Double-ended calibration of fiber-optic raman sectra distributed temperature sensing data. Sensors, 12(5), 5471-5485. doi: 10.3390/s120505471

United States Geological Survey, (1920). “Geothermal Data of the United States: Including many original determinations of underground temperature” N.H. Darton, Washington D.C.

Walker, M.D., Meyer, L.L., Tinjum, J.M., & Hart, D.J. (2015). Thermal property measurements of stratigraphic units with modeled implications for expected performance of vertical ground source heat pumps. Geotech Geol Eng, 33(2), 223-238. doi: 10.1007/s10706-015-9847-y

Wisconsin Geological and Natrual History Survey (WGNHS). 2005. "Bedrock Geology of Wisconsin [map]”. http://wisconsingeologicalsurvey.org/pdfs/pgszpdf/bedrock_geology.pdf.

World Economic Forum (2012). "Global Competitiveness Report 2012-2013." http://www3.weforum.org/docs/WEF_GlobalCompetitivenessReport_2012-13.pdf.

Wu, R., Tinjum, J.M., and Likos, W.J. (2014). Coupled thermal conductivity dryout curve and soil–water characteristic curve in modeling of shallow horizontal geothermal ground loops*. Geotech. Geol. Eng.*, *33(*2). pp. 193-205. doi: 10.1007/s10706-014-9811-2

Xiang, H., Andrews, C., Selker, J.S., & Zheng, C. (2016). Assimilation of temperature and hydraulic gradients for quantifying the spatial variability of streambed hydraulics. Water Resour. Res., 52(8), 6419-6439. doi: 10.1002/2015WR018408

Yilmaz, G., & Karlik, S.E. (2006). A distributed optical fiber sensor for temperature detection in power cables. Sens. Actuators, A., 125(2), 148-155. doi: 10.1016/j.sna.2005.06.024

Zeng, H.Y., Diao, N.R., & Fang, Z.H. (2002). A finite line-source model for boreholes in geothermal heat exchangers. Heat Transfer: Asian Research, 31(7), 558-567. doi: 10.1002/htj.10057

Zimmerman, R.W. (1989). Thermal conductivity of fluid-saturated rocks. *J. Pet. Sci. Eng. 3*(3) pp. 219-227. doi: 10.1016/0920-4105(89)90019-3